DEVELOPMENTS IN WEATHER AND CLIMATE SCIENCE
SERIES EDITOR: PAUL D. WILLIAMS

7

AEROSOLS AND PRECIPITATION OVER AFRICA

Progress, Challenges, and Prospects

EDITED BY
AKINTOMIDE A. AKINSANOLA
ADEYEMI A. ADEBIYI

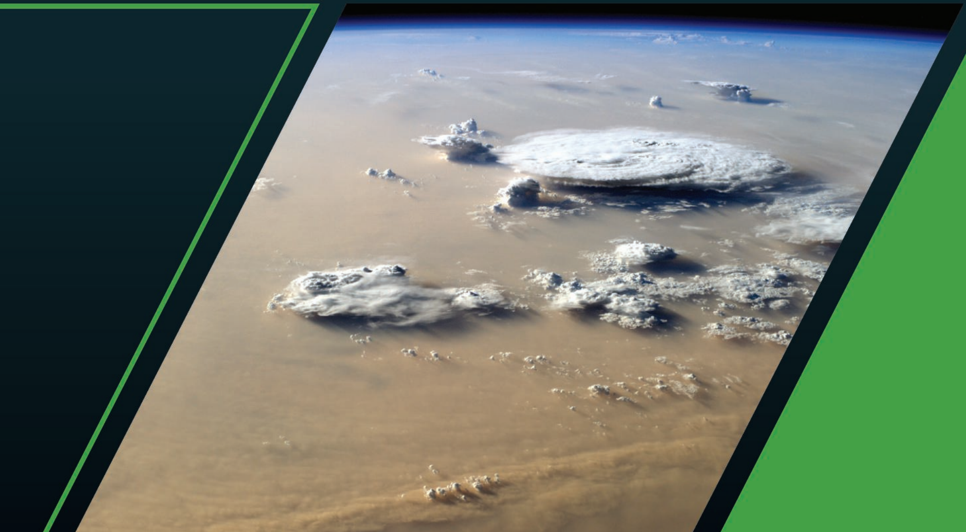

ELSEVIER

RMetS
Royal Meteorological Society

Aerosols and Precipitation Over Africa

Developments in Weather and Climate Science

Aerosols and Precipitation Over Africa

Progress, Challenges, and Prospects

Edited by

Akintomide A. Akinsanola

Adeyemi A. Adebiyi

Series editor

Paul D. Williams

ELSEVIER

RMetS
Royal Meteorological Society

Elsevier
Radarweg 29, PO Box 211, 1000 AE Amsterdam, Netherlands
125 London Wall, London EC2Y 5AS, United Kingdom
50 Hampshire Street, 5th Floor, Cambridge, MA 02139, United States

Copyright © 2025 Royal Meteorological Society. Published by Elsevier Inc. in cooperation with The Royal Meteorological Society. All rights are reserved, including those for text and data mining, AI training, and similar technologies.

For accessibility purposes, images in electronic versions of this book are accompanied by alt text descriptions provided by Elsevier. For more information, see https://www.elsevier.com/about/accessibility.

Publisher's note: Elsevier takes a neutral position with respect to territorial disputes or jurisdictional claims in its published content, including in maps and institutional affiliations.

No part of this publication may be reproduced or transmitted in any form or by any means, electronic or mechanical, including photocopying, recording, or any information storage and retrieval system, without permission in writing from the publisher. Details on how to seek permission, further information about the Publisher's permissions policies and our arrangements with organizations such as the Copyright Clearance Center and the Copyright Licensing Agency, can be found at our website: www.elsevier.com/permissions.

This book and the individual contributions contained in it are protected under copyright by the Publisher (other than as may be noted herein).

Notices

Knowledge and best practice in this field are constantly changing. As new research and experience broaden our understanding, changes in research methods, professional practices, or medical treatment may become necessary.

Practitioners and researchers must always rely on their own experience and knowledge in evaluating and using any information, methods, compounds, or experiments described herein. In using such information or methods they should be mindful of their own safety and the safety of others, including parties for whom they have a professional responsibility.

To the fullest extent of the law, neither the Publisher nor the authors, contributors, or editors, assume any liability for any injury and/or damage to persons or property as a matter of products liability, negligence or otherwise, or from any use or operation of any methods, products, instructions, or ideas contained in the material herein.

ISBN: 978-0-443-14050-1

For information on all Elsevier publications
visit our website at https://www.elsevier.com/books-and-journals

Publisher: Candice Janco
Acquisitions Editor: Jennette McClain
Editorial Project Manager: Ellie Barnett
Production Project Manager: Sruthi Satheesh
Cover Designer: Vicky Pearson Esser

Typeset by VTeX

ELSEVIER
Book Aid International
Working together
to grow libraries in
developing countries
www.elsevier.com • www.bookaid.org

Contents

5. Recent trends of clouds over Africa

Osinachi F. Ajoku, Mumin Abdulahi, and Oye Ideki

6. Future changes in precipitation distributions over Africa

Paul-Arthur Monerie, Hamida Ngoma Nadoya, Izidine Pinto, Alain T. Tamoffo, and Koffi Worou

7. Detection and attribution of climate change impacts in Africa

Shingirai S. Nangombe, Mohau J. Mateyisi, and Khetsiwe N. Khumalo

Contributors

Mumin Abdulahi, Department of Interdisciplinary Studies, Howard University, Washington D.C., United States

Adeyemi A. Adebiyi, Department of Life and Environmental Science, University of California Merced, Merced, CA, United States

Oluwafemi E. Adeyeri, Low-Carbon and Climate Impact Research Centre, School of Energy and Environment, City University of Hong Kong, Kowloon, Hong Kong Special Administrative Region

Osinachi F. Ajoku, Department of Earth, Environment and Equity, Howard University, Washington D.C., United States
Department of Interdisciplinary Studies, Howard University, Washington D.C., United States

Akintomide A. Akinsanola, Department of Earth and Environmental Sciences, University of Illinois Chicago, IL, United States
Environmental Science Division, Argonne National Laboratory, Lemont, IL, United States

Vishal Bobde, Department of Earth and Environmental Sciences, University of Illinois Chicago, IL, United States

Ian Chang, Department of Earth, Environmental, and Geographical Sciences, University of North Carolina at Charlotte, Charlotte, NC, United States

Claudia Di Biagio, Université Paris Cité and Univ Paris Est Creteil, CNRS, LISA, Paris, France

Paola Formenti, Université Paris Cité and Univ Paris Est Creteil, CNRS, LISA, Paris, France

Farnaz Hosseinpour, Desert Research Institute, Reno, NV, United States
University of Nevada Reno, Reno, NV, United States

Oye Ideki, Department of Interdisciplinary Studies, Howard University, Washington D.C., United States

Khetsiwe N. Khumalo, UNEP Copenhagen Climate Center, Copenhagen, Denmark

Mohau J. Mateyisi, Council for Scientific and Industrial Research, Pretoria, South Africa

Paul-Arthur Monerie, National Centre for Atmospheric Science, Reading, United Kingdom

Hamida Ngoma Nadoya, Department of Earth Sciences, University of Connecticut, Storrs, CT, United States

Shingirai S. Nangombe, Danish Meteorological Institute, Copenhagen, Denmark

Satyendra K. Pandey, Department of Life and Environmental Sciences, University of California Merced, Merced, CA, United States

Izidine Pinto, Royal Netherlands Meteorological Institute (KNMI), De Bilt, the Netherlands

Ibraheem Raji, Department of Earth and Environmental Sciences, University of Illinois Chicago, IL, United States

Fabien Solmon, LAERO OMP, CNRS, Toulouse University, Toulouse, France

Thierry N. Taguela, Department of Earth and Environmental Sciences, University of Illinois Chicago, IL, United States

Alain T. Tamoffo, Climate Service Center Germany (GERICS), Helmholtz-Zentrum Hereon, Hamburg, Germany

Koffi Worou, Swedish Centre for Impacts of Climate Extremes (CLIMES), Uppsala University, Uppsala, Sweden

Chapter 1

Aerosols over Africa: sources, properties, and distribution

Adeyemi A. Adebiyi[a], **Satyendra K. Pandey**[a], **Claudia Di Biagio**[b], **Ian Chang**[c], **Paola Formenti**[b], and **Akintomide A. Akinsanola**[d,e]

[a]*Department of Life and Environmental Sciences, University of California Merced, Merced, CA, United States,* [b]*Université Paris Cité and Univ Paris Est Creteil, CNRS, LISA, Paris, France,* [c]*Department of Earth, Environmental, and Geographical Sciences, University of North Carolina at Charlotte, Charlotte, NC, United States,* [d]*Department of Earth and Environmental Sciences, University of Illinois Chicago, IL, United States,* [e]*Environmental Science Division, Argonne National Laboratory, Lemont, IL, United States*

1.1 Introduction

Africa is an important continent for the global climate system (IPCC, 2023); Fig. 1.1. With about 1.4 billion people (~17% of the global population, United Nations, 2022), understanding climate-relevant atmospheric components, such as aerosols, over Africa is important to limit the potential effects of climate change, particularly on the under-resourced populations. This chapter introduces and synthesizes recent knowledge in our understanding of aerosols over Africa, focusing on the main aerosol species with climate-relevant consequences found over or near the continent. The remaining part of this section (Sections 1.1.1 & 1.1.2) broadly introduces aerosols over Africa, with more details about mineral dust aerosols (Section 1.2), carbonaceous aerosols (Section 1.3), marine aerosols (Section 1.4), and sulfate aerosols (Section 1.5) described later in the chapter.

1.1.1 Overview of aerosols

Aerosols are tiny suspended liquid or solid particles ubiquitous in the atmosphere. They differ from hydrometeors, such as cloud droplets or ice crystals, which typically have larger sizes than aerosol particles. Aerosol sizes can range from a few nanometers, approximately the size of a protein molecule, to several micrometers, about the diameter of human hair (Willeke and Whitby, 1975). This wide particle-size range varies among aerosol species, resulting in large spatial variability even when averaged over a long period (Prospero et al., 1983). Broadly speaking, key aerosol species in the atmosphere include mineral dust,

Aerosols and Precipitation Over Africa. https://doi.org/10.1016/B978-0-44-314050-1.00006-2

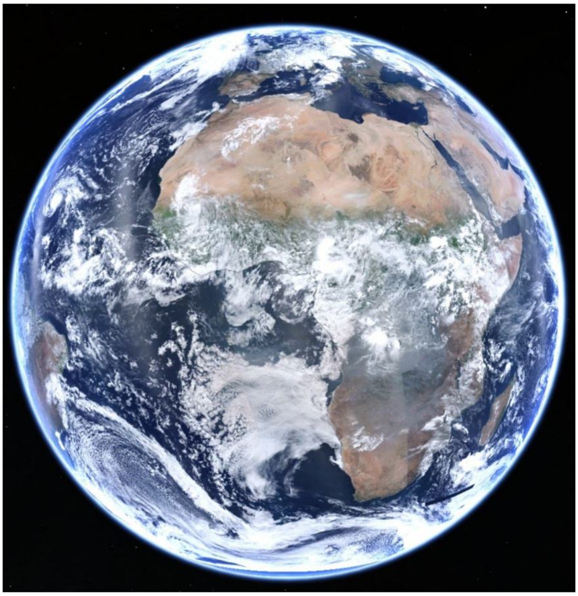

FIGURE 1.1 A true-color image on 2 September 2017 from the Visible Infrared Imaging Radiometer Suite (VIIRS) satellite showing the African continent.

carbonaceous aerosols (including organic and black carbon), marine aerosols (including sea salt), sulfate, and nitrate aerosols (Table 1.1).

Aerosols can be emitted directly or indirectly, often from natural or human-influenced anthropogenic sources (Boucher, 2015). Aerosols from direct emissions, also called primary aerosols, are produced by the effects of wind on oceanic and terrestrial surfaces, such as wind-blown sea spray and mineral dust aerosols. This source of aerosols also includes those produced during volcanic activities or combustion. In contrast, aerosols from indirect emissions, also called secondary aerosols, are aerosols that have not been emitted directly but are instead produced from the nucleation process (gas-to-particle conversion) involving a wide range of inorganic and organic gas-phase compounds derived from natural and anthropogenic sources. In addition to classification based on aerosol emission type, aerosols can also be classified according to their origin, whether natural or anthropogenic. Aerosols with the same emission type (direct or indirect) can have different origins. For example, mineral dust aerosols can be emitted from natural sources enhanced by wind erosion and anthropogenic sources through land-use and agricultural practices, such as tilling. Similarly, carbonaceous aerosols can be of natural origin, such as when lightning ignites fires in the forest and grasslands, or from anthropogenic sources, such as fossil-fuel combustion.

After emission, aerosol particles can stay in the atmosphere for several seconds to several days (Table 1.1). Because most aerosols in the atmosphere have

TABLE 1.1 Aerosol species over Africa, their main sources, lifetime in the atmosphere, and their key climate-relevant properties.

Aerosol species	Main sources	Lifetime	Key climate-relevant properties
Mineral Dust	• *Natural source*: Wind erosion, soil resuspension. • *Anthropogenic source*: Land use and agricultural practices, road and construction activities.	Few minutes to 1–2 weeks, depending on particle size.	• Can absorb and scatter both shortwave and longwave radiation. • Mostly cools the climate in shortwave and warms it in the longwave • Good ice-nucleating particle for cold clouds.
Carbonaceous Aerosols (including organic and black carbon)	• Combustion of fossil fuel, biofuel, and biomass. • Continental and marine ecosystems. • Some anthropogenic and biogenic non-combustion sources.	$\sim$ 1 week	• Can absorb some shortwave radiation. • Black carbon has larger shortwave mass-absorption efficiency than organic carbon. • Organic carbon enhances absorption when mixed with black carbon or when deposited as a coating on black carbon. • Good cloud-condensation nuclei (depending on aging and size).
Marine Aerosols (including sea salt)	Through wind erosion and breaking of air bubbles over the ocean.	Few minutes to 1 week, depending on particle size.	• Primarily scatters shortwave and longwave radiation. • Very hygroscopic. • Good cloud condensation nuclei.
Sulfate Aerosols	• *Primary source*: marine and volcanic emissions. • *Secondary source*: oxidation of SO_2 and other sulfur-based gases from natural and anthropogenic sources.	$\sim$ 1 week	• Primarily scatters solar radiation. • Very hygroscopic. • Enhances absorption when deposited as a coating on black carbon. • Good cloud-condensation nuclei.

short lifetimes, high aerosol concentrations are typically found near the source locations, with a progressive decline along the transport pathways and vertically with altitude. This spatial distribution of aerosols is primarily determined by the climatological patterns of atmospheric wind circulation, which transport aerosol particles for thousands of kilometers (e.g., Swap et al., 1996; Knippertz and Todd, 2012). In addition to changes in aerosol concentration, other aerosol properties can also change during transport through the atmosphere. Fundamentally, aerosols are defined by their properties, including size distribution, shapes, and chemical compositions, that establish the aerosol's physical and optical properties. During their transport through the atmosphere, aerosols are influenced by physicochemical processes that can substantially impact their properties. One way this process can occur is through the coagulation of particles of different chemical compositions, both outside and inside clouds, and by condensation of semi-volatile compounds on the aerosol particles. For example, aerosols, such as black carbon and mineral dust, can be covered by a coating of soluble species, which change their hygroscopicity—a property of aerosol particles that defines their ability to take up water and grow in size as ambient relative humidity increases (e.g., Deboudt et al., 2010). In addition, depositional processes, which include dry and wet deposition, can influence aerosol sizes, since bigger particles are deposited faster than smaller particles, resulting in a decline in the overall aerosol concentration along the transport pathways (Seinfeld and Pandis, 2006).

Depending on their physical and optical properties, aerosols in the atmosphere can scatter and/or absorb shortwave and/or longwave radiation. In the shortwave, absorbing aerosols are primarily black carbon, mineral dust, and organic carbon, while purely scattering aerosols are sulfates and sea salts (Li et al., 2022). While all aerosols in the atmosphere interact with radiation in the shortwave, only a few aerosol species with larger particle sizes (e.g., mineral dust and sea salt) can interact with radiation in the longwave. Specifically, mineral dust can absorb and scatter longwave radiation, however, sea salt aerosol mostly scatters longwave radiation (e.g., Yue and Liao, 2012; Adebiyi et al., 2023a; Kok et al., 2023). The amount of radiation extinguished (scattered and absorbed) by aerosols in the atmosphere is often determined by aerosol optical depth (AOD). This parameter measures the ability of aerosol to extinguish the radiation in the atmosphere and single scattering albedo that estimates the fraction of the radiation that is scattered rather than absorbed (Seinfeld and Pandis, 2006).

1.1.2 African aerosols

Relative to other continents, Africa accounts for a significant fraction of the major aerosol species in the atmosphere (Fig. 1.2). These major aerosols include mineral dust aerosols originating from the arid and semi-arid regions of the continent, such as the Sahara and Namibia Deserts, as well as carbonaceous aerosols (including black carbon and organic carbon) from West and

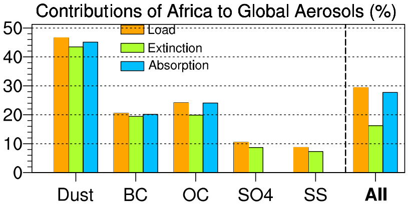

FIGURE 1.2 The percentage contributions of African aerosols, including mineral dust, carbonaceous aerosols (black carbon, BC, organic carbon, OC), sulfate aerosols (SO4), and sea salt (SS) to global aerosol load (orange), shortwave extinction (defined by aerosol optical depth at 550 nm wavelength; green bars), and shortwave absorption (defined by absorbing aerosol optical depth at 550 nm wavelength; blue bars). The rightmost column shows the percentage contributions for all aerosols (All). All contributions are estimated between 35°S–40°N and 30°W–50°E (Fig. 1.3). We used data between 1980 and 2023 obtained from the Modern-Era Retrospective Analysis for Research and Applications, Version 2 (MERRA-2) reanalysis dataset.

Central Africa. Specifically, African sources dominate the emitted mineral dust and carbonaceous aerosols, accounting for 49–52% of global estimates, respectively (Van Der Werf et al., 2010; Kok et al., 2021). Indeed, Africa's dominant contribution to mineral dust is expected since Africa has the world's largest dust-producing desert, the Sahara Desert, contributing substantially to global dust aerosols (Middleton and Goudie, 2001). Similarly, Africa has the second-largest contiguous forest after the Amazonia, contributing considerably to global carbonaceous aerosols (Mayaux et al., 2013). In the atmosphere, aerosols over Africa collectively account for 29% of the global aerosol load, about 16% of global aerosol shortwave extinction, and about 28% of global aerosol shortwave absorption (Fig. 1.2). Divided into individual aerosol species, African mineral dust contributes to more than 45% of the global dust load, shortwave extinction, and absorption. Although these estimates are obtained from a reanalysis dataset (Modern-Era Retrospective Analysis for Research and Applications, Version 2 (MERRA-2)) that relies, in part, on model simulation of atmospheric dust, they are largely consistent with estimates obtained with observationally informed constraints on dust properties (Kok et al., 2021). In addition to dust, Africa contributes a substantial fraction of the global carbonaceous aerosols, with more than ~20% of the global loading, extinction, and absorption of black and organic carbon. In contrast to mineral dust and carbonaceous aerosols, which are shortwave-absorbing aerosols, African sulfate aerosols from industrial sources and sea-salt aerosols from the surrounding oceans contribute generally less than 10% to global loading and shortwave extinction. Because these aerosols are purely scattering aerosols, they do not contribute to the absorption of shortwave radiation (Fig. 1.2).

Beyond Africa's contribution to global aerosols, the distribution of African aerosols extends across the continent and over the adjacent Atlantic Ocean (Fig. 1.3). Broadly, aerosol distribution over Africa is dominated by mineral dust in the north and carbonaceous aerosols in the south. Specifically, based

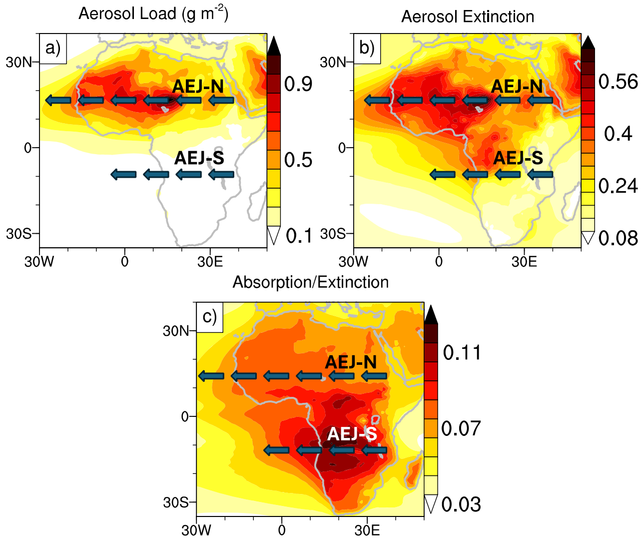

FIGURE 1.3 The climatological distribution of total aerosol burden (g m^{-2}), aerosol shortwave extinction (defined by extinction aerosol optical depth at 550 nm wavelength), and the ratio between aerosol shortwave absorption and extinction over Africa (absorption is defined by absorption aerosol optical depth at 550 nm wavelength). We used data between 1980 and 2023 obtained from the Modern-Era Retrospective Analysis for Research and Applications, Version 2 (MERRA-2) reanalysis dataset. The arrows show the approximate latitude of the Northern and Southern African Easterly Jets (AEJ-N & AEJ-S, respectively).

on the column mass loading, aerosol mass distribution over Africa is weighted to the north, where mineral dust dominates over the Sahara Desert (Fig. 1.3a). In contrast, because the carbonaceous aerosols substantially impact the overall extinction and absorption, they dominate in the central and southern parts of the continent (Fig. 1.3b & c). Indeed, of the five aerosol species, mineral dust accounts for 83% of the total aerosol load, 45% of the extinction, and 48% of the absorption over Africa (Fig. 1.4). Black carbon contributes minimally to the overall loading (0.5%) and extinction (4%) over the continent but substantially to the overall absorption, accounting for 47% of the absorption over Africa. Consequently, only two aerosol species, mineral dust and back carbon, account for about 95% of the overall shortwave aerosol absorption over Africa. In contrast, organic carbon contributes minimally about 5% of the continent's overall absorption by about 18% of the overall extinction.

On a climatological timescale, the distributions of African aerosols are primarily controlled by large-scale dynamical systems broadly similar over the Northern and Southern hemispheres of the continent. Specifically, mineral dust aerosols are predominantly transported westward in the north by the northern African easterly jet (AEJ-N), and in the south, the carbonaceous aerosols are transported westwardly by the southern African easterly jet (AEJ-S) (Adebiyi

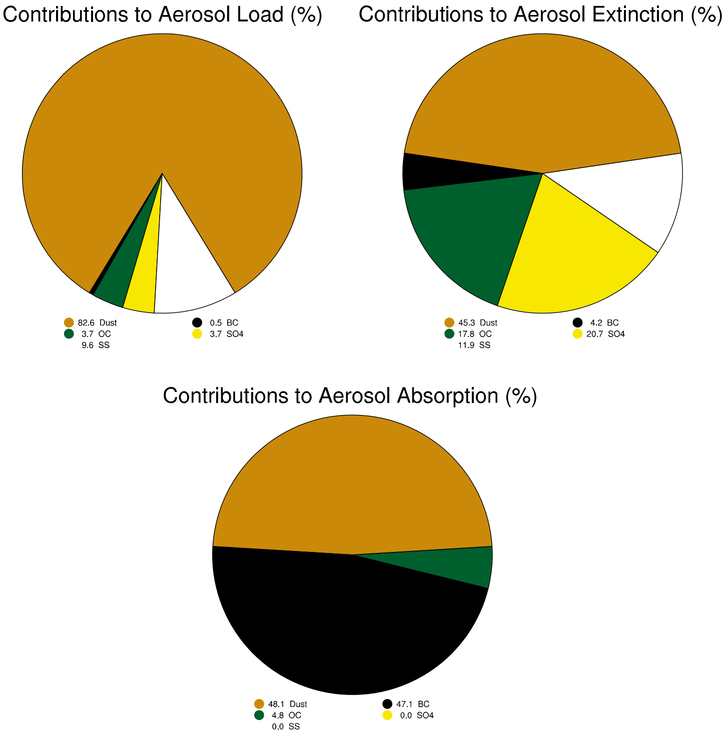

FIGURE 1.4 Percentage contributions of aerosol species, including mineral dust (brown), carbonaceous aerosol, including black carbon (BC; black) and organic carbon (OC; green), sulfate (SO4; yellow), and sea salt (SS; white) to the total aerosol load, aerosol shortwave extinction (defined by the extinction aerosol optical depth), and aerosol shortwave absorption (defined by the absorption aerosol optical depth). All contributions are estimated between 35°S–40°N and 30°W–50°E (Fig. 1.3). We used data between 1980 and 2023 obtained from the Modern-Era Retrospective Analysis for Research and Applications, Version 2 (MERRA-2) reanalysis dataset.

and Zuidema, 2016; Bercos-Hickey et al., 2017). These two jets occur in regions of strong mid-tropospheric easterly winds that reach as high as approximately 700 and 550 hPa and result from the surface temperature gradient between the poleward semiarid portions of the subcontinent and the humid vegetated equatorial region (Cook, 1999; Thorncroft and Blackburn, 1999; Adebiyi and Zuidema, 2016; Adebiyi et al., 2023b). While the AEJ-N occurs most of the year, they migrate latitudinally and amplify dust offshore transport during boreal spring and summer (Knippertz and Todd, 2012). Specifically, AEJ-N is found at approximately 3°–5°N during the boreal winter but migrates north to approximately 15°N during boreal spring and summer. In contrast, the AEJ-S maximizes during austral spring, corresponding to the maximum offshore transport of carbonaceous aerosols over the southeast Atlantic Ocean. On a shorter timescale, the variability of wind circulation determines the local variability of aerosol from emission to deposition. Specifically, the local wind variability influences the emission of natural aerosols, such as mineral dust and sea salt.

In the following section, we describe in detail the sources, properties, and distribution of each aerosol species. Section 1.2 focuses on mineral dust; Section 1.3 on carbonaceous aerosols; Section 1.4 on marine aerosols; and Section 1.5 on sulfate aerosols. Finally, we provide a summary and outlook of our understanding of African aerosols in Section 1.6.

1.2 Dust aerosols over Africa

Mineral dust aerosol is a key player in the climate system and a tracer of climate change (Petit et al., 1999; Knippertz and Stuut, 2014). When emitted from diverse sources, African arid and semi-arid regions contribute to about half of the global mineral dust aerosol emissions, loading, and AOD (Huneeus et al., 2011; Ginoux et al., 2012; Kok et al., 2021). Atmospheric dust is associated with episodic but frequent storm events capable of injecting substantial amounts of particles into the atmosphere, particularly close to source regions (Kandler et al., 2007; Rajot et al., 2008) and with size distribution of particles extending from hundreds of nanometers to hundreds of micrometers (Ryder et al., 2019; Adebiyi et al., 2023a; Formenti and Di Biagio, 2024). With a lifetime of a few days up to 1–2 weeks in the troposphere (Table 1.1), dust aerosols can be transported up to thousands of kilometers away from their sources before being deposited (Goudie and Middleton, 2001; Prospero et al., 2014; Zuidema et al., 2019). Dust aerosols influence the transfer of solar and infrared radiation in the atmosphere (the direct radiative effect), the cloud formation and properties (the indirect radiative effect), the oceanic and terrestrial biogeochemistry, the atmospheric chemistry, the air quality, the human health, and the solar energy production (Rosenfeld et al., 2001; Usher et al., 2003; Jickells et al., 2005; Slingo et al., 2006; Bristow et al., 2010; Atkinson et al., 2013; Kok et al., 2017; Rieger et al., 2017; Knippertz and Stuut, 2014). African dust has emerged as a major contributor to the direct and indirect radiative effects, biogeochemistry, and chemistry (di Sarra et al., 2011; Kok et al., 2023). In addition, it also has a socioeconomic impact on Europe, the Middle East, the Atlantic and the Southern Oceans, the Caribbean, the Amazon, the Arctic, and the Antarctic (Swap et al., 1992; Reid et al., 2003; Bristow et al., 2010; Prospero et al., 2014; Nabat et al., 2015; Han et al., 2018; Zuidema et al., 2019; Gili et al., 2022). Satellite images illustrating the strength of dust episodes from Africa are shown in Fig. 1.5 for dust plumes close to source areas during a dust storm in Algeria (Fig. 1.5a), Saharan dust off West Africa towards the tropical Atlantic Ocean (Fig. 1.5b), and a dust plume off the coast of Namibia towards the South Atlantic (Fig. 1.5c).

In recent decades, the scientific community has fostered tremendous efforts toward the experimental investigation of the properties and impacts of African dust aerosols (Miller et al., 2004; Washington et al., 2006; Slingo et al., 2006; Ansmann et al., 2011; Formenti et al., 2011b; Ryder et al., 2013b; Di Biagio

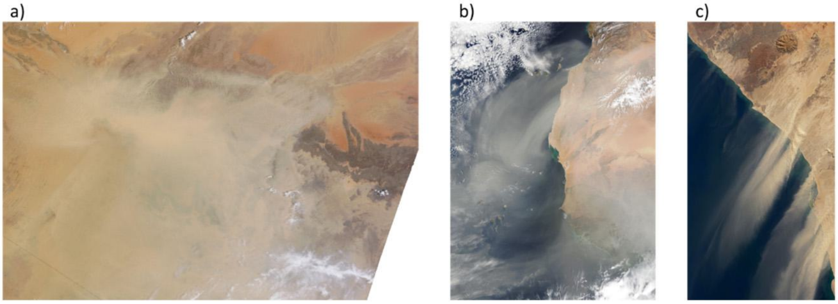

FIGURE 1.5 True-color images for (a) a dust storm over Algeria captured by the Moderate Resolution Imaging Spectroradiometer (MODIS) on board the Terra satellite on 15 July 2011); (b) Saharan dust off West Africa from MODIS Terra on 2 March 2000; (c) dust off the coast of Namibia from Landsat 8 Operational Land Imager on 17 July 2020. Images are obtained from NASA Worldview.

et al., 2017; Kok et al., 2017; Ryder et al., 2019; Kok et al., 2021; Adebiyi et al., 2023a; Mona et al., 2023). This effort has included several large international projects and intensive measurement campaigns, such as AMMA (African Monsoon Multidisciplinary Analysis; Rajot et al., 2008; Haywood et al., 2008; Reeves et al., 2010), DODO (Dust Outflow and Deposition to the Ocean; McConnell et al., 2008), DABEX (Dust and Biomass-burning Experiment; Haywood et al., 2008; Johnson et al., 2008), SAMUM (Saharan Mineral Dust Experiment; Ansmann et al., 2011), FENNEC (Ryder et al., 2013b), SHADE (Saharan Dust Experiment; Tanré et al., 2003), and SALTRACE (Saharan Aerosol Long-Range Transport and Aerosol–Cloud-Interaction Experiment; Weinzierl et al., 2017). As of today, the combination of the diverse sources of information available from advanced surface and satellite remote sensing observations, intensive field campaign studies, laboratory measurements, and numerical regional and global modeling enables an advanced understanding of the main emission processes and transport patterns of dust, as well as of the regional variability and large-scale evolution of dust properties relevant to their climatic, environmental, and health impacts.

Based on the available body of knowledge, this section discusses the sources, emissions, distribution, and properties of dust from Africa, the largest dust source in the world.

1.2.1 Sources and emission of dust aerosols

The emission of mineral dust into the atmosphere is due to wind erosion on arid and semiarid surfaces. The processes responsible for this emission are saltation and sandblasting of large soil aggregates, which depend on surface wind speed and soil properties, such as humidity, mineralogy, and surface roughness (Marticorena and Bergametti, 1995; Alfaro and Gomes, 2001; Prospero et al., 2002). The dust aerosol mobilization process has been parametrized through various schemes, usually associated with a threshold friction velocity, defined as the minimum wind velocity necessary to trigger dust emission (Alfaro and Gomes, 2001; Shao, 2001). The dynamical processes that generate strong wind speeds to surpass the threshold velocity, and thus initiate dust emission, span diverse spatial scales and include synoptic depressions, mesoscale convective systems, and microscale dynamical processes (Knippertz and Todd, 2012). Because most global models have a spatial resolution of hundreds of kilometers, they can only account for the larger synoptic and mesoscale processes. Thus, models usually do not resolve smaller-scale processes that influence dust emissions.

Main emission sources in Africa are associated with subtropical deserts in the Northern Hemisphere, where major sources such as the Sahara Desert and the Sahel are located, and the Southern Hemisphere, such as the Namib Desert. The Saharan Desert in Northern Africa is the largest source of mineral dust on Earth, injecting up to 1,600 Tg yr^{-1} of aerosol into the atmosphere, representing around 75% of the total emissions from Northern Africa (estimated at ∼2,100 Tg yr^{-1}) (Goudie and Middleton, 2001; Ginoux et al., 2012; Kok et al., 2021). A compilation of the available data on visibility, back trajectory analysis, satellite observations, and isotopic composition studies reveals the localization of major potential source areas (PSA) and emission hot spots in Northern Africa (PSA NAF), as summarized in Formenti et al. (2011b) and further partitioned into natural and anthropogenic sources by Ginoux et al. (2012). The PSA NAF-1 to NAF-6 (Fig. 1.6) predominantly contribute to dust emission and large-scale dust load from Northern Africa, which are mainly topographical lows, foothills of mountains, and ephemeral lakes, all relating mostly to natural sources. Those include the zone of Chotts in Tunisia and Northern Algeria (PSA NAF-1), the foothills of the Atlas Mountains and western coastal region (PSA NAF-2), the Mali-Algerian border region (PSA NAF-3), Central Libya (PSA NAF-4), the Bodélé depression (PSA NAF-5), and Southern Egypt, Northern Sudan (PSA NAF-6). In particular, the Bodélé depression in Western Chad is one of the world's most intense sources of dust (Prospero et al., 2002; Washington et al., 2006).

The semiarid Sahel region south of the Sahara Desert is also an important dust source area, accounting for about 25% of North African emissions (Kok et al., 2021). The Sahelian dust is mostly associated with anthropogenic activities (Ginoux et al., 2012), particularly land use changes, observations, and exhibits continuous increase in dust emissions since the 1950s (Gill, 1996). Dust transport from the Sahara and local emissions associated with the monsoon flow and mesoscale systems add to the land-use induced dust emission (Bou Karam et al., 2008; Ginoux et al., 2012).

Sources in Southern Africa are much less intense than in Northern Africa and account only for 2–5% of global dust emissions (Kok et al., 2021). Emitting areas are mainly located in Namibia, Botswana, and South Africa (Ginoux et

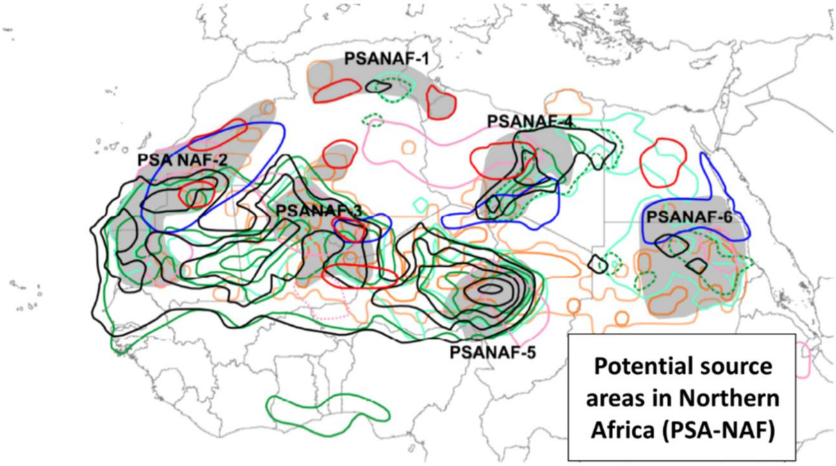

FIGURE 1.6 Regional distribution of potential source areas (PSA, shaded areas) in Northern Africa (PSA NAF). Various PSA indicates: PSA NAF-1: Zone of Chotts in Tunisia and Northern Algeria; PSA NAF-2: foothills of Atlas mountains (PSA NAF-2a) and western coastal region (PSA NAF-2b; Western Sahara, Western Mauritania); PSA NAF-3: Mali–Algerian border region; PSA NAF-4: Central Libya; PSA NAF-5: Bodélé depression (Western Chad); PSA NAF-6: Southern Egypt, Northern Sudan. The region with isolines represents the fraction of dust source activations (DSA). The figure is adapted from Formenti et al. (2011b).

al., 2012). Sources are associated with natural emissions from topographical lows, ephemeral lakes, ephemeral riverbeds, and gravel plains. Moreover, a few anthropogenic activities from mines also have been identified (Ginoux et al., 2012; Vickery et al., 2013; Holdt and Eckardt, 2018).

Together with those just noted, another emergent dust source observed to be of relevance for Africa is the one associated with post-wildfire emissions (Yu and Ginoux, 2022). This is due to dust mobilization occurring in the aftermath of large wildfires due to the reduced vegetation cover and reduced soil moisture. This phenomenon appears to be regionally relevant, particularly for savannahs in West Africa and the tropical forest area of the Congo–Zaire basin. This potential dust emission pathway is expected to increase in the next decades due to the strengthening of wildfire activity and the projected drought associated with climate change (Kok et al., 2023).

1.2.2 Climatological distribution of dust aerosols

The distribution of African dust aerosols in the atmosphere is controlled by the geographical distribution of sources across the continent and the meteorological fields determining emission and transport routes (e.g., Knippertz, 2014). Fig. 1.7 shows the climatological representation of dust based on observations from the Cloud-Aerosol Lidar with Orthogonal Polarization (CALIOP) and Moderate Resolution Imaging Spectroradiometer (MODIS). Dust from the Sahara Desert

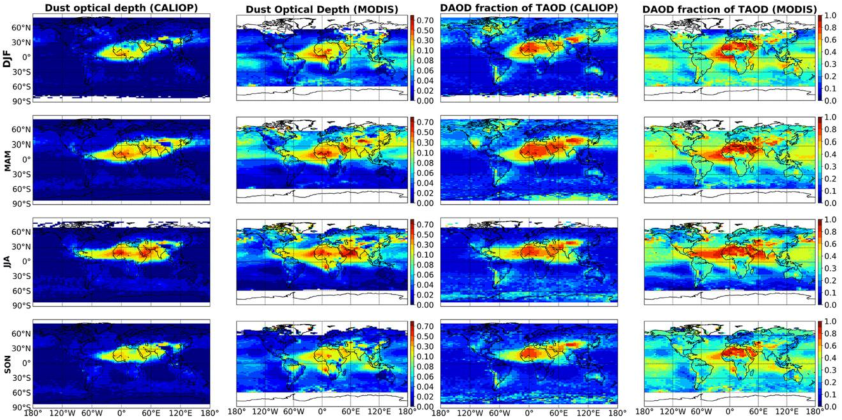

FIGURE 1.7 Spatial distribution of the seasonal mean CALIOP-based dust aerosol optical depth (DAOD), MODIS-based DAOD and the fraction of DAOD with respect to the total aerosol optical depth (TAOD) based on CALIOP and MODIS, respectively, for the globe at a 5° longitude × 2° latitude resolution based on 13-year (2007–2019) CALIOP measurements. DJF: December of the previous year–January–February; MAM: March–April–May; JJA: June–July–August; SON: September–October–November. Image adapted from Song et al. (2021).

and the Sahel in Northern Africa is transported toward the Atlantic Ocean. These dust plumes reach both North and South America, depending on the time of the year and the position of the intertropical convergence zone (ITCZ) (Swap et al., 1992; Reid et al., 2003; Prospero et al., 2014). Dust transport to the Mediterranean basin and towards continental Europe has also been documented (Pace et al., 2006; Di Mauro et al., 2019; Varga et al., 2021). Dust from North Africa is also identified in Arctic ice cores (Han et al., 2018; Újvári et al., 2022). Similarly, the contribution of sources in Southern Africa is documented in Antarctic sediments (Petit et al., 1999; Gili et al., 2022).

The cycle of global dust aerosols is strongly influenced by meteorology, causing strong seasonal, inter-annual, and decadal variability (Knippertz, 2014; Prospero and Lamb, 2003). Additional variability in the spatiotemporal distribution of dust may occur as a consequence of land-use changes or changing surface properties and meteorological fields, in turn modulating dust mobilization and transport (Hsu et al., 2012; Moulin and Chiapello, 2006). The distribution and temporal variability of African Dust are further influenced by large-scale climate patterns, such as the North Atlantic Oscillation (NAO) and the El-Niño/Southern Oscillation (ENSO), the latter particularly impacting the occurrence of droughts in the Sahel region (Prospero and Lamb, 2003; Chiapello et al., 2005; Hsu et al., 2012). In contrast, the Sahara is less affected by the year-to-year variability in precipitation.

1.2.3 Properties of dust aerosols

The fundamental physicochemical properties of dust aerosols, controlling their broad impact on the climate and the environment, are the size dstribution, the morphology, and the chamical composition (Formenti et al., 2011b; Knippertz and Stuut, 2014; Adebiyi et al., 2023a). These will be discussed in the following subsections, followed by a discussion on the dust optical properties, hygroscopicity and solubility, relevant for their interactions in the climate system.

1.2.3.1 Physical properties

The size distribution of mineral dust aerosols spans a wide range from hundreds of nanometers to hundreds of micrometers (Ryder et al., 2019; Adebiyi et al., 2023a; Formenti and Di Biagio, 2024). At emission and close to source regions, the dust volume size distribution is dominated by the coarse mode centered at diameters > 5 μm (Rajot et al., 2008; Rosenberg et al., 2014; Ryder et al., 2013a). The fine fraction below 2 μm has been shown to be potentially modulated by wind speed and to increase in importance with increasing wind intensity at emission (Sow et al., 2009). After injection into the atmosphere, the size distribution of dust then evolves principally due to gravitational settling that causes the depletion of the larger particles as the plume travels away from the source (Maring et al., 2003). Intensive experimental research over recent decades has made it possible to show that the coarse mode of dust aerosols is however conserved during transport due to processes such as convective mixing, atmospheric stratification, turbulence, and electrical levitation (Ryder et al., 2013b; Denjean et al., 2016a; Weinzierl et al., 2017; Adebiyi and Kok, 2020; Adebiyi et al., 2020; Adebiyi et al., 2023a). Compilation and harmonization of in situ surface and airborne field observations in the literature based on optical counters, electron microscopy, and aerodynamic sizing techniques have been recently provided by Formenti and Di Biagio (2024). This dataset confirms the conservation of coarse dust particles during transport in the atmosphere. Specifically, the main dust volume mode is located around 10 μm close to sources and decreases but still includes an important fraction of coarse particles after mid- and long-range transport in the atmosphere, where the modes are located at ∼5 μm and ∼2 μm, respectively (Fig. 1.8). In addition, Formenti and Di Biagio (2024) show that the submicron dust mode slightly increases after transport, possibly because of dust plumes mixing with polluted air masses.

Together with size distribution, another key physical property of dust is morphology. Mineral dust aerosols present a complex and irregular morphology, represented by the shape and roughness of the full aggregate of its constituents (Chou et al., 2008; Kandler et al., 2011). Particle morphology is important because it affects the optical behavior of dust and its lifetime by modulating its settling velocity (Huang et al., 2020). The aspect ratio (AR), a common parameter usually applied to describe the dust shape, is the ratio of the longer to the shorter axis of an ellipse that fits the irregular dust shape. Synthesis of AR for

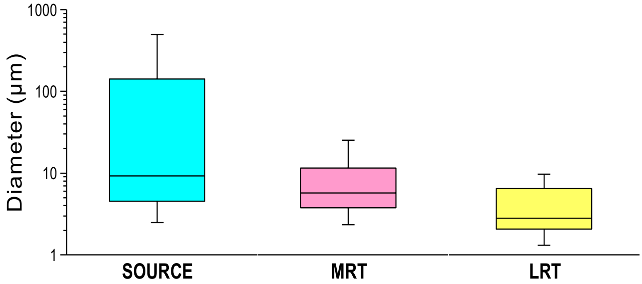

FIGURE 1.8 Range of variability of the volume mode diameter of dust aerosols sampled close to source regions (blue), after mid-range transport (MRT, 1–4 days of transport; pink) and after long-range transport (LRT, >4 days of transport; yellow). Data corresponds to the diameter at which the volume distribution of dust peaks. Data obtained from Formenti and Di Biagio (2024).

North African dust is provided in Huang et al. (2020), suggesting a mean mostly source-independent value of 1.72. Based on a literature synthesis, Huang et al. (2020) also identified an increase in AR during long-range transport (going up to 1.90), suggesting that dust becomes more aspherical when transported far away from its sources. This is explained by considering the higher settling velocity of spherical particles compared to aspherical ones. In addition to gravitational settling, dust morphology can modify due to the mixing with other aerosols species or reaction with gaseous constituents and water vapor, causing particles to become rounder, particularly if a coating forms or if water is adsorbed on the particle surface, potentially reducing the AR. However, the body of knowledge linking chemical and morphological changes of dust remains limited.

1.2.3.2 Chemical properties

Dust aerosol is composed of several minerals, such as clays (kaolinite, illite, smectite, chlorite), quartz, calcium-rich carbonates (calcite, dolomite), sulfates (gypsum), feldspars (orthose, albite), and iron and titanium oxides (Formenti et al., 2011b; Scheuvens et al., 2013; Formenti et al., 2014b). The composition of dust varies with the particle's origin and the diversity of surface soil composition (Caquineau et al., 2002; Formenti et al., 2011b; Journet et al., 2014). Additionally, the proportion of the different minerals depends on the dust size distribution at emission because quartz, feldspars, and calcium-rich species are commonly more abundant in the coarse-mode fraction, while clays dominate the fine-mode fraction (Kandler et al., 2009).

The composition of African dust, as identified by field and laboratory investigations, is dominated by clays, which can amount up to 50 to 90% in mass, with variable contents of quartz, calcite, dolomite, feldspars, and iron and titanium oxides (Caquineau et al., 2002; Kandler et al., 2009; Formenti et al., 2011b, 2014b; Scheuvens et al., 2013; Di Biagio et al., 2017). The major clay species are illite, kaolinite, smectite, and palygorskite. Illite and kaolinite are ubiquitous, while smectite and palygorskite are detected only in some regions, such as Algeria, Ethiopia, and Namibia and more generally the northwestern PSA (PSA NAF-1, PSA NAF-2a; see Fig. 1.6) (Formenti et al., 2011b; Di Biagio et al., 2017). Iron oxides can represent up to more than 70% of the total elemental iron in dust and within 1–6% of the total mass (Formenti et al., 2014b; Caponi et al., 2017). Goethite appears as the dominant iron oxide species for Saharan and Sahelian dust (Lafon et al., 2004; Formenti et al., 2014a), whereas the few data available suggest that hematite dominates over goethite for Namib dust (Di Biagio et al., 2017).

Collectively, past studies indicate general regional tendencies in the dust mineralogical composition, also providing mineralogical fingerprints for the different source areas (Formenti et al., 2011b; Scheuvens et al., 2013; Formenti et al., 2014b). On the scale of northern Africa, calcite is more abundant in northern Saharan samples (PSA NAF-1 to 3), reaching up to 50–70% in mass, and it decreases (or is not present) when moving towards the southern part of the Sahara and the Sahel. Similarly, the quartz content increases from the northern Sahara towards the Sahel (Caquineau et al., 2002). The illite to kaolinite ratio (I/K) is found to be the highest (>1) for dust from northwestern sources (PSA NAF-1 and 2) and lower than 1 for the other Northern African sources. Amongst elemental ratios, the calcium (Ca) to aluminium (Al) ratio (Ca/Al) shows regional variability and can be used to discern amongst the different source areas (Formenti et al., 2011b). An example illustrating the contrast of mineralogical composition between different African sources is shown in Fig. 1.9.

The composition of dust modifies after emission due to various processes. Gravitational settling and the associated progressive loss of coarse particles during dust transport in the atmosphere tend to reduce the quartz, feldspars, and calcium-rich species content (Pye, 1987; Kandler et al., 2011). Additionally, external or internal particle mixing with other species can occur when dust plumes mix with marine or continental air masses. Various field studies have documented the mixing of dust with pollution particles (e.g., Denjean et al., 2016a), sea salt, sulfates, and soot (e.g., Kandler et al., 2011), particularly affecting the sizes below about 0.5 μm. Heterogeneous reactions on the particle surface can also affect dust composition during transport and can determine the formation of a coating, notably sulfates or nitrates, on the particles (Usher et al., 2003). Heterogeneous reactions depend strongly on relative humidity and dust mineralogy, with sulfate (nitrate) formation favored on aluminum silicate (calcium carbonate) particles (Laskin et al., 2005; Fairlie et al., 2010). Therefore, the chemical aging of dust aerosols in the atmosphere depends on their origin and environmental conditions encountered during transport. While many field studies document this dust aging in the atmosphere, others show no chemical processing occurring during the process. As an example, Denjean et al. (2016b) observed Saharan dust transported across the continent to the Caribbean putting in evidence that dust particles how dust particles can remain chemically unprocessed and only externally mixed.

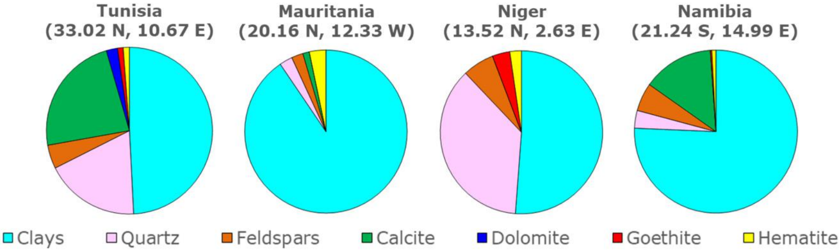

FIGURE 1.9 Mineralogy (% by mass) of four dust aerosol samples resuspended in the laboratory from parent soils originated in Tunisia, Mauritania, Niger, and Namibia. Data obtained from Di Biagio et al. (2017); Caponi et al. (2017); Di Biagio et al. (2019).

1.2.3.3 Optical properties

Because of their wide size distribution and characteristic mineralogical composition, dust aerosols interact with atmospheric radiation across the full spectral range, going from solar (shortwave) to infrared (longwave) wavelengths (Sokolik and Toon, 1999; Di Biagio et al., 2017, 2019; Adebiyi et al., 2023c). Scattering is the dominant process in the shortwave, while absorption mostly drives the interaction in the longwave. Nonnegligible scattering effects can nonetheless also contribute to longwave interactions at different wavelengths (Dufresne et al., 2002). Relative contributions of scattering and absorption to total extinction at different wavelengths are variable, depending mostly on the composition and, therefore, the origin of the dust.

Fig. 1.10 shows a literature-based synthesis of real and imaginary parts of spectral complex refractive index ($CRI = n - ik$) of dust aerosols in the shortwave and longwave parts of the spectrum as obtained from in situ and remote sensing field observations close to source areas and laboratory studies on chemically unaltered dust, all dealing with diverse African dust sources (Volz, 1972, 1973; Dubovik et al., 2002; Haywood et al., 2003; Sinyuk et al., 2003; Petzold et al., 2009; Wagner et al., 2012; Ryder et al., 2013b; Di Biagio et al., 2017; Rocha-Lima et al., 2018; Di Biagio et al., 2019). As evident from Fig. 1.10, the refractive index changes significantly both in magnitude and spectral variation from one source to another. Values range between 1.45 and 1.60 at 550 nm and between 1.2 and 3 at 10 µm for the real part (n), and between 0.0003 and 0.008 at 550 nm and between 0.1 and 0.9 at 10 µm for the imaginary part (k). In the shortwave range, the intensity of dust absorption, represented by the imaginary part k, is modulated by the dust content in iron oxides (Moosmüller et al., 2012; Caponi et al., 2017; Di Biagio et al., 2019). Based on laboratory simulation experiments on global dust sources (Fig. 1.10c), Di Biagio et al. (2019) found the largest imaginary CRI for dust from Niger (k = 0.0088 at 370 nm, 0.0048 at 520 nm) compared to dust from Tunisia, Algeria, Morocco, Mauritania and Mali. They also found the lowest shortwave absorption for dust from Bodélé (k = 0.0011 at 370 nm, 0.0006 at 520 nm) associated with the different content in iron oxides. Furthermore, Di Biagio et al. (2019) also identified

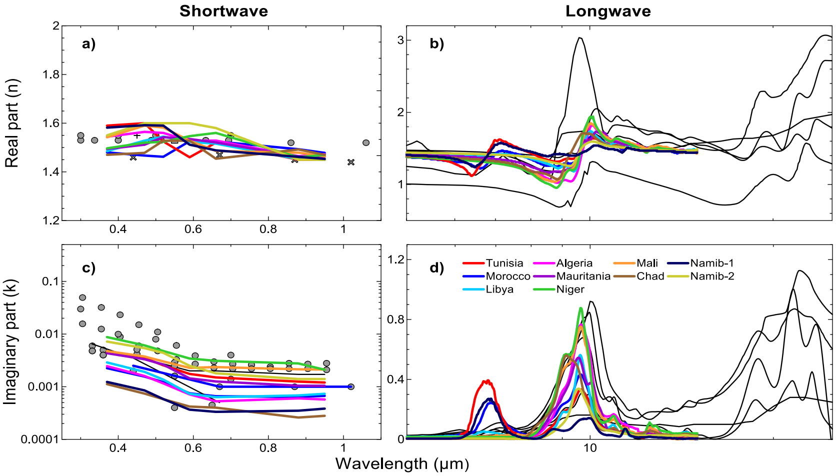

FIGURE 1.10 Literature-based synthesis of the spectral real and imaginary parts of the complex refractive index of dust aerosols in the shortwave part of the spectrum (a, c) and longwave part of the spectrum (b, d). Colored lines show results from laboratory simulation chamber experiments for chemically unaltered dust from various global-relevant regions in Africa, as reported in Di Biagio et al. (2019) for the shortwave and Di Biagio et al. (2017) for the longwave. The Namib-1 and Namib-2 indicate dust from two distinct areas of the Namib desert, one located at 21°S (Namib-1) and the other at 19°S (Namib-2). Grey dots and black lines show the compilation of data from in situ field observations and additional laboratory studies. Adapted from Di Biagio et al. (2017, 2019), where all references for literature studies reported in the figure can be found.

amongst the largest and smallest shortwave absorption for dust from Namibia (k = 0.0072 at 370 nm, 0.0044 at 520 nm for Namib-2, and k = 0.0012 at 370 nm, 0.0006 at 520 nm for Namib-1), supporting the potentially strong regional absorption variability of dust from Southern African sources. The laboratory study form Wagner et al. (2012) identified a strong absorption (i.e., the largest imaginary parts in Fig. 1.10c) for dust from Burkina Faso. In the longwave spectral range, the absorption of dust is modulated by the presence of diverse minerals, including quartz, clays, and calcite, all presenting specific absorption bands in this region (Sokolik and Toon, 1999; Di Biagio et al., 2014). The calcite's signature around 7 μm characterizes dust from Northern Africa, compared to Sahelian dusts, which are richer in kaolinite and quartz and show more pronounced absorption peaks at 9.2 and 12 μm (Fig. 1.10d). The few observations available for Namibian dust also support a strongly variable signature in the mid-infrared, associated with varying content of carbonate minerals (Di Biagio et al., 2017).

At mid-visible wavelengths (550 nm), the single scattering albedo (defined as relative fraction of aerosol scattering to extinction) of African dust obtained both from field and laboratory measurements ranges between 0.88 and 0.99 (Formenti et al., 2011a; Ryder et al., 2013b; Di Biagio et al., 2019; McConnell et al., 2008; Müller et al., 2010). Mie theory optical calculations, considering the iron oxide variability in Western Africa, indicate a dust asymmetry factor, g (representing the angular distribution of scattered light) between 0.76 and 0.8 and dust mass extinction coefficient (MEC) between 0.5 and 1.1 $m^2\,g^{-1}$ at 550 nm (Formenti et al., 2014a). In the longwave range, the single scattering albedo can be as low as 0.2 in the 8–12 µm atmospheric window, g around 0.5, and MEC within 0.1 to 0.25 $m^2\,g^{-1}$ (Di Biagio et al., 2014).

The optical properties of dust aerosols can be altered when particles age in the atmosphere. Based on laboratory studies performed under controlled conditions, it was found that the main intrinsic optical properties of the dust, the CRI, are not affected by changes in the size distribution and the weakening of the coarse particle's fraction during transport (Di Biagio et al., 2017, 2019). In contrast, properties such as the mass absorption and extinction coefficients (MAC, MEC), single scattering albedo, and g, which depend on the CRI and the size distribution, are expected to modify along transport due to size modification. Specifically, overall lower absorption is expected for smaller dust compared to coarser dust. A laboratory study (Caponi et al., 2017) retrieved nonetheless significantly higher MAC values for finer dust (PM2.5, 0.03–0.23 $m^2\,g^{-1}$ at 532 nm) than for coarser dust (PM10.6, 0.01–0.05 $m^2\,g^{-1}$), and they explained these different values using the fact that iron-containing minerals are more abundant in the clay fraction ($<$ 2.0 µm). These results suggest that the light absorption of dust can remain important during atmospheric transport because a reduction in dust concentration and coarse size fraction can be compensated by an increase in the absorption per unit of particle mass due to the size-dependency of composition. Together with size changes, external or internal mixing with non-absorbing (i.e., sulfate, nitrate) or absorbing (i.e., carbonaceous) species can also modify the dust's spectral optical properties during transport (Bauer et al., 2007). For African dust transported towards the tropical Atlantic Ocean or across the ocean towards the Mediterranean and the Americas, the measured single scattering albedo at 550 nm ranges within 0.90–1.00 (Jeong, 2008; Formenti et al., 2001; Ryder et al., 2013b; Denjean et al., 2016b,a), thus showing a general decrease of dust absorption during transport. The measured MEC for transported dust ranges between 0.2 and 1.5 $m^2\,g^{-1}$ at visible wavelengths (Ryder et al., 2013b; Denjean et al., 2016b), similar to the range of that estimated for dust close to sources. The role of chemical processing on the spectral optical properties of dust remains a matter of ongoing research, including the investigation of the impact of dust interaction with both inorganic and organic species (Liu et al., 2013).

1.2.3.4 Hygroscopicity and solubility

The African climate is dependent on water supplies from warm and cold clouds (Janicot et al., 2008; Spirig et al., 2019), and the primary productivity of the neighboring Atlantic, Indian, and Southern Oceans is dependent on the supply of limiting nutrients, such as iron, from the atmosphere (Jickells et al., 2005; Ito and Kok, 2017). While dust particles are mixtures of mostly insoluble minerals, their hygroscopicity and water solubility can influence precipitation and the primary productivity in the ocean. Clays, feldspars, and halite salts can adsorb water, and the coatings of sulfate and nitrate can form on dust particles by chemical aging and cloud-processing, influencing dust hygroscopicity and water solubility (Formenti et al., 2011a; Knippertz and Stuut, 2014). At trace levels, elements such as iron can be soluble depending on mineralogy and oxidation state and can be altered by atmospheric aging (Journet et al., 2008; Shi et al., 2012). While the adsorption of water at a relative humidity below saturation remains limited (Chen et al., 2020), in super-saturated conditions, dust particles can activate into droplets of liquid clouds, acting as giant cloud condensation nuclei (CCN) because of the large particle size (Köhler, 1936). At freezing temperatures, mineral dust particles can form ice crystals even at low supersaturations, depending on chemical composition and the presence of coatings (Koop et al., 2000).

Despite the importance of those processes on dust radiative budget, to the best of our knowledge, only a very few publications have reported measurements of the hygroscopicity of African mineral dust, possibly because of the difficulty in performing such measurements. During the African Monsoon Multidisciplinary Analysis (AMMA) project (Lebel et al., 2011), Matsuki et al. (2010) demonstrated the formation of secondary sulfates, nitrates, and chlorates found on dust particles processed by convective clouds, mostly on carbonates. Mixing with soluble secondary species was also observed by Twohy et al. (2009) in the eastern North Atlantic, where they measured relatively high concentrations of droplets containing dust in small clouds. They suggested that even submicron dust, when processed, can be as important as CCN, as well as ice nuclei (IN) in freezing conditions. Crumeyrolle et al. (2008) measured CCN profiles over West Africa prior to and after the passage of a dust-laden convective cloud to show the large enhancement of the CCN activity. Measurements of ice nucleation by African dust have been conducted mostly onboard aircraft to sample freezing conditions. The measurements of DeMott et al. (2003) and the more recent experiments by Boose et al. (2016) at a high-altitude mountain site show that aging with time can increase the IN capability of African dust within the Saharan dust layer. These measurements have been complemented and interpreted by mechanistic studies in the AIDA simulation chamber, highlighting the positive role of coarse potassium-rich feldspar and that of passivating concurrent processes, such as deactivation by acid coatings (Sullivan et al., 2010).

Schladitz et al. (2011) measured the physical properties and hygroscopicity of Saharan dust aerosols downwind of source regions at Cape Verde Island and showed that, in the submicron fraction, the external mixing of dust, sea spray, and secondary aerosols resulted in high hygroscopicity, while, at coarse fractions where dust particles dominated, particles remained almost hydrophobic. These results are supported by Denjean et al. (2015) in research that was conducted on Puerto Rico, downwind African sources, showing that mixing with soluble aerosols such as sea spray during long-range transport over the North

Atlantic Ocean remained minor and the hygroscopicity of mineral dust at subsaturated conditions was not significantly enhanced.

On the other hand, a very significant body of literature exists on the solubility of African dust, particularly concerning iron. The laboratory measurements of Journet et al. (2008) on pure mineral proxies have highlighted that the iron from oxides such as hematite and goethite have the lowest solubility. In contrast, iron trapped as an impurity in clays is most readily dissolved in water (0.003–5.25%). In the atmosphere, however, several processes contribute to increased iron solubility. For example, Paris et al. (2010) showed that iron solubility is modified by internal mixing in biomass-burning plumes. In addition, Desboeufs et al. (2024) showed that the solubility of iron in Namibian dust could be increased by marine biogenic emissions from the coastal Benguela upwelling.

1.3 Carbonaceous aerosols over Africa

Carbonaceous aerosols are one of the key products of biomass-burning and fossil fuel combustion, comprised primarily of light-scattering organic carbon (OC) and light-absorbing brown carbon (BrC) and black carbon (BC) (Andreae et al., 1998; Kirchstetter et al., 2003). Organic carbon is the carbon atom on the organic material (i.e., chained carbon atoms with hydrogen and other elements). In contrast, black carbon is a carbonaceous aerosol characterized by strong visible light absorption and resistance to chemical transformation (Petzold et al., 2013). Accurate measurements of carbonaceous aerosol are crucial for quantifying aerosol radiative effects. This section provides some background about the sources and emissions of carbonaceous aerosols, followed by their climatological distributions over Africa. Thereafter, we discuss their physical, chemical, and optical properties.

1.3.1 Sources and emission of carbonaceous aerosols

Carbonaceous aerosols in sub-Saharan Africa largely originate from wildfires and biomass-burning activities (Sedlacek et al., 2022). The primary fuel sources of carbonaceous aerosols include agricultural waste burning, charcoal burning, garbage burning, forest fires, savanna fires, and domestic and industrial biofuel use (Andreae and Merlet, 2001; Akagi et al., 2011). Savanna fires contribute to the world's largest biomass-burning emissions (Hao and Liu, 1994), which is shown by the high fire count in Fig. 1.11. Both BC and OC are generated during combustion. BC is typically produced in conditions where the required oxygen is limited for complete oxidation of carbonaceous fuel to CO_2 (Reid et al., 2005). The OC is produced during combustion and condensation of organic vapor onto existing particles. With adequate concentrations, organic vapors can create particles via nucleation.

Aerosol emissions are initiated by a mixture of combustion processes such as flaming and smoldering (Reid et al., 2005). Their relative contributions depend on the variability of the geometry, chemistry, growth phase, moisture in

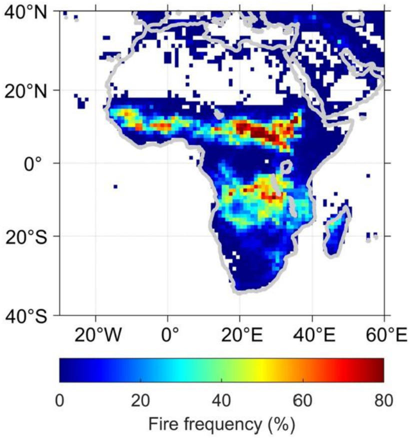

FIGURE 1.11 Fire frequency from the MODIS-Terra Active Fire product V005 (MOD14CM1) during 2001–2015.

fuels, and meteorological conditions such as wind characteristics (Akagi et al., 2011). The dry climate during winter and spring in southern Africa results in the burning of dry fuels that favor flaming combustion, which reaches a fire temperature of ~1400 K. In contrast, deforestation fires in the Amazon occur in a humid climate that favors smoldering combustion, reaching a fire temperature of ~1000 K (Holanda et al., 2023). BC-containing aerosols are primarily generated under flaming conditions, so the contributions of BC to the total aerosol loading are also higher in Africa. Section 1.3.3.2 will describe the chemical compositions of carbonaceous aerosols under the various dominating types of combustion.

1.3.2 Climatological distribution of carbonaceous aerosols

Carbonaceous aerosols are produced throughout the year with a seasonal shift from north to south of sub-Saharan Africa during the dry season of the year (Roberts et al., 2009). From the end of each year through the first few months of the following year (i.e., November to March), when the Northern Hemisphere experiences winter, the dry climate to the north of the Equator favors fire activities. Fig. 1.12 and Fig. 1.13 show the annual mean optical depth of BC and OC, respectively, over the African continent. The peak BC and OC loadings occur north of the Equator during the austral summer (December to February). Both carbonaceous aerosols reach a minimum during austral autumn (March to May) as the East African Monsoon prevails following the southward shift of the intertropical convergence zone. As the West African Monsoon prevails during the austral winter (June to August), southern Africa becomes dry with a wide distribution of fire activities. Hence, the BC and OC loadings peak during this time of the year. During austral spring (September to November), BC and OC loadings

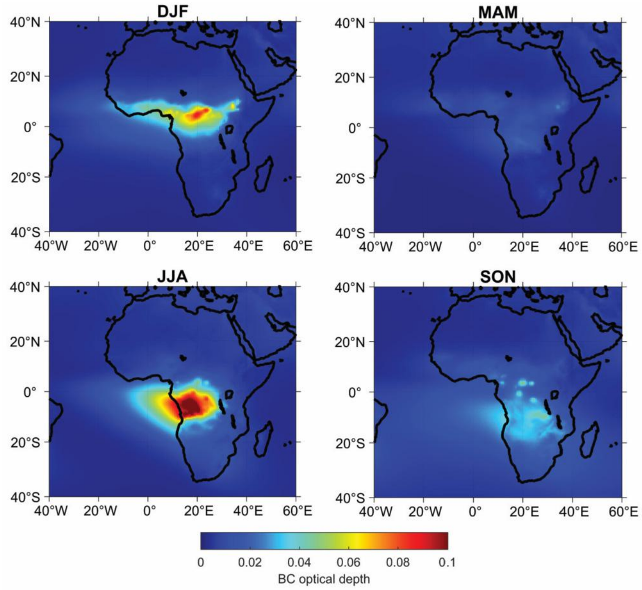

FIGURE 1.12 Seasonal mean black carbon optical depth over the African continent from MERRA-2 between 1980 and 2023.

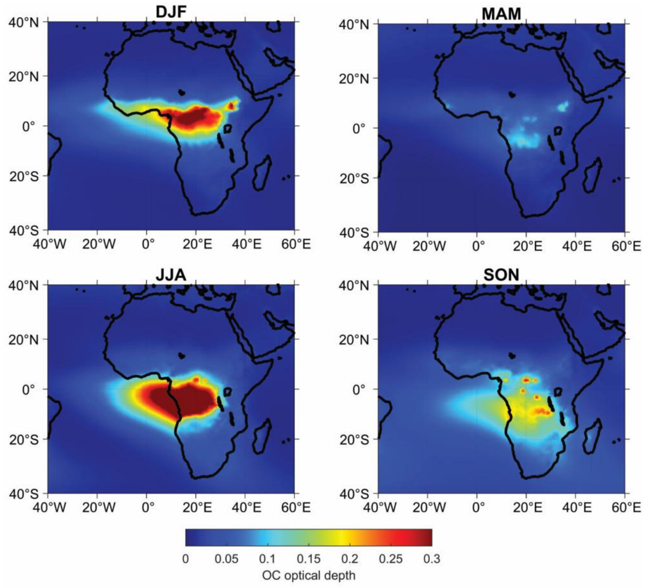

FIGURE 1.13 Seasonal mean organic carbon optical depth over the African continent from MERRA-2 between 1980 and 2023.

decrease with fire count as the southward ITCZ migration increases rainfall in the subcontinent.

Aerosols are mostly transported into the South Atlantic Ocean under the influence of the Southern African easterly jets (Adebiyi et al., 2015; Adebiyi and Zuidema, 2018, 2016). In contrast, aerosol emissions in the southern portion of Africa are subject to the predominant westerly winds, which readily transport carbonaceous aerosols into the Indian Ocean (Swap et al., 1996, 2003). Likewise, biomass-burning activities in Madagascar give rise to aerosols in the south Indian Ocean (Verreyken et al., 2020).

1.3.3 Properties of carbonaceous aerosols

1.3.3.1 Physical properties

Carbonaceous aerosols can be classified into three major particle types under transmission electron microscope, namely organic particles with inorganic inclusions, tar balls, and soot (Pósfai et al., 2003). The first type is the most abundantly present in biomass-burning activities and usually does not have distinct morphologies. Tar balls contain a greater concentration of carbon elements than the former. They are spherical and amorphous, and are commonly not aggregated with other particle types. Soot (also known as black carbon) comprises chain-like aggregates of 20–50 nm spherules (or monomers). Those formed from biomass-burning activities in southern Africa have more ordered microstructures than those originated from fossil fuel combustion. They could either be lacy or compact (Scarnato et al., 2013).

BC particles have geometric mean diameters of about 120 nm (Sedlacek et al., 2022). BCs generally make up to 30% of the total aerosol mass (Andreae and Merlet, 2001). Accumulation of large quantities of organic compounds via condensation create secondary organic aerosol (SOA) coatings within two hours with double the geometric diameter. Fig. 1.14 shows the lifecycle of carbonaceous aerosols. BC particles can also grow by coagulating with other BC particles or primary organic aerosols. After a few hours of emission, the growth of carbonaceous particles remains nearly constant due to limited condensable gases. After one to two days, coatings begin to drop, decreasing to about 30% of the maximum coating mass after ten days.

1.3.3.2 Chemical properties

Africa biomass burning aerosols tend to have a higher BC content than other regions (Reid et al., 2005). BC particles are typically 100 nm in mass-equivalent diameter and accumulate large quantities of organic compounds as coatings within a short period of time after biomass burning, forming secondary organic aerosols (SOA). The hygroscopic property depends on the mass ratio of the organic coating to BC. The mass ratio generally reaches 20 after a few hours and decreases to about five after ten days. Chemical reactions with nitrate can lead to the formation of brown carbon, which has wavelength-dependent absorption in

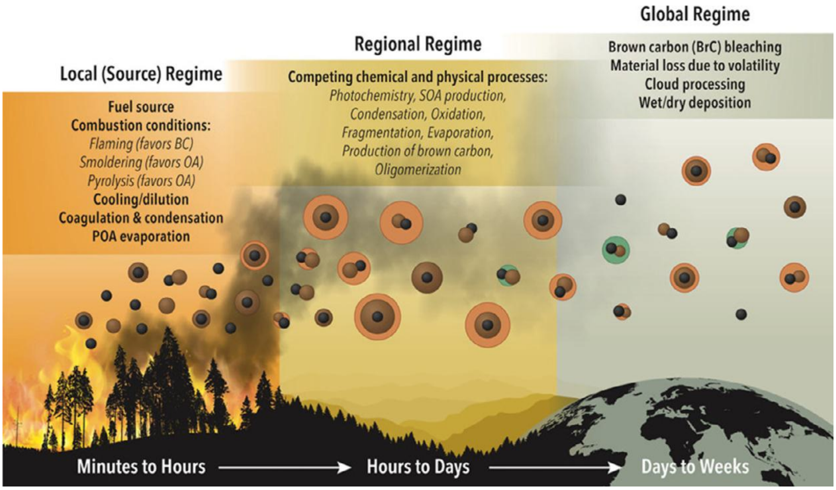

FIGURE 1.14 The evolution of carbonaceous aerosols at the local (i.e., source), regional (i.e., continental), and global regimes with corresponding time scales (Copyright with permission from Sedlacek et al., 2022).

the near-UV (300–400 nm) and visible wavelengths (400–700 nm) (Kirchstetter et al., 2004). Evaporation and chemical processes can remove the coating, whereas BCs' masses generally stay constant throughout their lifetime except near the fire emission source where aggregation and coagulation occur (Bond and Bergstrom, 2006; Reid et al., 2005). Coatings begin to decrease one or two days after emission (Sedlacek et al., 2022). Eventually, organic coatings are lost via either evaporation, heterogeneous oxidation, photolysis, aqueous-phase oxidation, dry deposition, or cloud processes.

Combustion types affect aging processes and the radiative impact of carbonaceous aerosols. Flaming combustion converts C, H, N, and S from the solid biomass fuel into highly oxidized gases such as CO_2, H_2O, NOx, and SO_2, respectively. BC particles are most abundantly produced by this type of combustion (Reid et al., 2005). The relative contribution of combustion type between flaming and smoldering can be defined as the modified combustion efficiency (MCE), which is quantified via ($CO_2/(CO+CO_2)$). In general, MCE > 0.9 corresponds to a dominance of flaming combustion, whereas MCE < 0.9 corresponds to the dominance of smoldering combustion. An MCE of 0.9 indicates an equal contribution of combustion from both. Smoldering combustion dominates over flaming combustion as the fire progresses via a combination of surface oxidation (i.e., glowing) and pyrolysis (i.e., the thermal breakdown of solid fuel into gases and particles). Smoldering generates most CO, CH_4, NMOC, and primary organic aerosol (Wu et al., 2020; Holanda et al., 2023).

1.3.3.3 Optical and radiative properties

BC is a major climate warming agent, and it is responsible for most of the light absorption in the atmosphere (Chung et al., 2012; Chung and Seinfeld, 2002). The single scattering albedo of the BC core generally increases from ∼0.45 near the source to ∼0.75 at maximum coating mass before dropping back ∼0.45. Thus, BCs strongly dictate the overall single-scattering albedo. The optical properties of the carbonaceous mixture also depend on the mass ratio of the organic coating to BC. Coating thickness results in a significantly greater increase in scattering than in absorption such that the single scattering albedo rapidly increases near the emission source and then drops down with age, ranging between 0.8 and 0.9 according to airborne field campaign measurements (Sedlacek et al., 2022). The higher mass absorption cross section (MAC) of uncoated BC particles is about 7.5 $m^2\ g^{-1}$, reaching a peak of ∼12.8 $m^2\ g^{-1}$ before returning down to ∼10.3 $m^2\ g^{-1}$. Lacy aggregates tend to have stronger absorption (lower single scattering albedo) than compact aggregates (higher single scattering albedo). The single scattering albedo of carbonaceous aerosols from flaming-dominated combustion tends to be lower than those from smoldering-dominated combustion, given the higher BC emission (Liu et al., 2014).

1.3.3.4 Radiative impacts

The climatic impact of carbonaceous aerosols is complex because aerosol–cloud–radiation interactions pose significant uncertainties in the predictions of changes to the Earth's climate system. Carbonaceous aerosols can impact Earth's energy balance by scattering and absorbing solar radiation, i.e., direct aerosol radiative effect (Coakley et al., 1983; McCormick and Ludwig, 1967) and via cloud interactions, i.e., indirect radiative effect (Twomey, 1977, 1974). Likewise, aerosols can alter the thermodynamic profiles of the atmosphere to rapidly adjust cloud radiative and physical properties, i.e., semi-direct radiative effect (Johnson et al., 2004). Aerosols over oceans reflect more radiation back into space than would occur in their absence (Myhre et al., 2007; Yu et al., 2006). When low-level marine liquid clouds exist beneath aerosols, however, aerosols can either enhance or diminish the magnitude of upward radiation depending on their coverage and radiative properties (Kacenelenbogen et al., 2019; Oikawa et al., 2018; Su et al., 2013; Zhang et al., 2016).

During each austral winter and spring, carbonaceous aerosols are readily transported westward from the African continent to the South Atlantic Ocean, where semipermanent low-level liquid clouds are abundantly present. In this ocean basin, aerosols above clouds generally result in slightly negative to large positive direct aerosol radiative effects due to the strong aerosol absorption of reflected radiation above clouds (Doherty et al., 2022). A simplified illustration of the direct aerosol radiative effects is shown in Fig. 1.15, which is computed as the TOA flux difference between the background condition and the aerosol

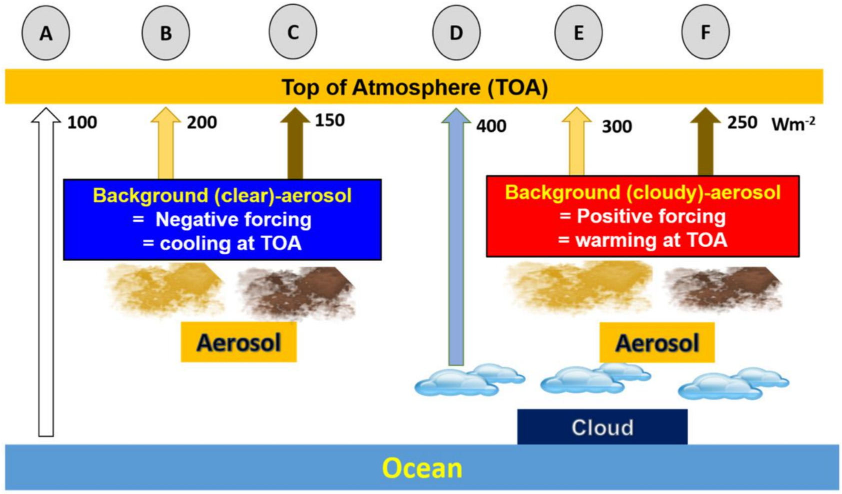

FIGURE 1.15 A simplified representation of the upward radiative fluxes at TOA in six scenarios. Aerosols in tan color scatter relatively more (i.e., weaker in absorption) than aerosols in dark brown colors. Scenarios A to F are arranged as clear-sky, weakly absorbing aerosol, strongly absorbing aerosol, cloud-only, weakly absorbing aerosol above cloud, and strongly absorbing aerosol above cloud. The numbers represent TOA fluxes in Wm^{-2}.

condition. Aerosols over dark surfaces (e.g., water bodies and vegetation) generally lead to radiative cooling at the TOA. As an example, aerosols over the ocean reflect more radiation back to space than the ocean because the ocean is darker, resulting in a cooling or negative forcing. Aerosols that scatter more (or have a higher single scattering albedo) result in a greater negative direct aerosol radiative effect (A minus B). For the same aerosol loading with greater aerosol absorption (i.e., lower single scattering albedo), the reflected fluxes back to space are smaller and cause a less negative direct aerosol radiative effect (A minus C).

The dominance of the sub-tropical high-pressure belt over the South Atlantic gives rise to abundant low-level stratocumulus clouds. Unlike the ocean, clouds reflect more solar radiation back into space. Adding clouds in the background (scenario D) increases TOA fluxes with the cloud optical thickness. When aerosols are transported over brighter backgrounds such as clouds, they can either enhance or reduce reflected TOA fluxes. Aerosols above optically thin clouds generally enhance upward TOA fluxes, leading to a negative direct radiative effect. Above opaque clouds, aerosols would diminish upward TOA fluxes to induce a positive direct aerosol radiative effect (D minus E). Aerosols with greater absorption, i.e., lower single scattering albedo, that reside above clouds would diminish even more upward TOA fluxes to induce a larger positive direct aerosol radiative effect (D minus F).

While the single scattering albedo plays a major role in driving the direct aerosol radiative effect, aerosol adjustment on cloud LWP dictates the sign and magnitude of the semidirect aerosol effects. In general, the semidirect radiative effect causes a negative radiative effect, especially when aerosols are near clouds (Adebiyi and Zuidema, 2018; Herbert et al., 2020; Wilcox, 2010). Large-eddy simulations indicated that this negative radiative effect weakens as the separation distance increases. At the surface of the African continent, aerosols induce both radiative and ambient cooling (Mallet et al., 2020). Thus, the lower tropospheric heating results in the weakening of the continental boundary-layer development.

Aerosol-cloud interactions present the largest uncertainty in aerosol–climate interactions. An observational-based study from satellites over the South Atlantic indicated that aerosols reduce cloud optical depth, cloud droplet radius, LWP, and precipitation efficiency. Optically-thin clouds tend to decrease their LWP due to evaporative dry-air entrainment, whereas optically-thick clouds tend to increase their LWP due to precipitation inhibition (Costantino and Bréon, 2013).

1.4 Marine aerosols near Africa

Marine aerosols are *ocean-derived* particles that are suspended in the atmosphere and can have sizes ranging from approximately 100 nanometers (nm) to several tens of micrometers (μm) (Cavalli et al., 2004). Marine aerosols typically originate from the surrounding ocean and can be transported inland by winds. Similar to mineral dust (section 1.2), marine aerosols also contribute to the global aerosol mass and constitute a substantial fraction of the mass of particulate matter close to the surface (Lewis and Schwartz, 2004). Whether over ocean or land, marine aerosols can substantially impact the regional climate in Africa particularly because they are very good cloud-condensation nuclei—a key ingredient in cloud formation (Gantt and Meskhidze, 2013). Previous studies have shown that marine aerosols have a non-negligible influence on our understanding of the current climate, especially in assessing anthropogenic aerosol forcings (Hoose et al., 2009). That is because estimates of anthropogenic aerosol forcings rely on an accurate representation of the pre-industrial atmosphere, which is primarily composed of aerosols from natural sources, such as marine aerosols. In addition to their impacts on climate, marine aerosols also have a biogeochemical impact by depositing nutrients and other compounds over the ocean and land (Ito et al., 2023). For example, marine aerosols can carry essential nutrients like nitrogen and phosphorus and, when deposited over coastal terrestrial ecosystems, can potentially enhance primary productivity and influence biogeochemical cycles (e.g., Myriokefalitakis et al., 2010). Overall, our understanding of the sources, emissions, distribution, and properties of marine aerosols is crucial for assessing their impact on regional climate and ecosystems. Therefore, this section provides an overview of marine aerosols over or near the African continent.

1.4.1 Source and emission of marine aerosols

The primary source of marine aerosols over Africa is the surrounding oceans, including the Atlantic Ocean to the west, the Indian Ocean to the east, the Mediterranean Sea to the north, and the Southern Ocean to the south. Two main types of marine aerosols are emitted from these ocean surfaces: sea spray aerosols (SSA) and primary organic aerosols (POA).

Sea spray aerosols (SSA) are generated primarily through bubble-bursting and wave-breaking mechanisms over the ocean surface. While details of SSA emissions can be found in Grythe et al. (2014), the emission of SSA can occur through four different mechanisms, which may produce particles of varying sizes (see Fig. 1.16). First, when bubbles over the ocean burst, they leave filaments above the water surface, resulting in film droplets with a typical particle radius of less than 1 μm. Second, the void left at the ocean surface by the bursting bubbles could produce jets with a typical radius of ∼1–10 μm. Third, stronger winds could produce a spume as it is torn off the wave crests with sizes typically larger than 10 μm in radius. Finally, splash drops could also be considered part of sea spray aerosols, although they are much larger in size than jets. As a result, larger marine aerosols produced by the third and fourth mechanics typically have shorter lifetimes in the atmosphere. The relatively smaller aerosols are elevated up into the atmosphere, where they evaporate and concentrate their sea salt components (Lewis and Schwartz, 2004; O'Dowd and de Leeuw, 2007). Additionally, most of the dissolved or particulate matter that constitutes SSA is NaCl. Specifically, 90% of the salt dissolved in the oceans is NaCl, and only a small fraction are SO_4^{2-}, Mg^{2+}, Ca^{2+} or K^+. Overall, sea spray aerosols contribute a substantial fraction of the marine aerosols in the atmosphere (O'Dowd et al., 1997).

In addition, the ocean is also a source of primary organic aerosols (POA), which are related to the biological activities of marine organisms. Similar to SSA, POA can be produced by breaking waves that scavenge surface-active organic matter and materials before being injected into the atmosphere (Barger and Garrett, 1970, 1976). Examples of organic matter at the surface may include bacteria, viruses, and detritus. In addition, POA can also be produced through the oxidation of phytoplankton-emitted volatile organic compounds (VOCs), such as DMS (dimethyl sulfide), aliphatic amines, isoprene, and monoterpenes, which can form secondary organic aerosols (SOA) over the ocean (Myriokefalitakis et al., 2010). Previous studies have shown the fine mode fractions (diameter, $D \leq \sim 0.2$ μm) of the size distribution for POA are often independent of sea salt aerosols, while the coarse mode fractions ($D \geq 1$ μm) are likely internally mixed with sea salt (Gantt and Meskhidze, 2013). Because the surface concentrations of POA are reported to be small, on average, previous studies have paid little attention to understanding their climate impacts separate from SSA. In fact, some studies have suggested that the definition of SSA be expanded to include both sea salt and primary organic matter (e.g., Gantt and Meskhidze, 2013).

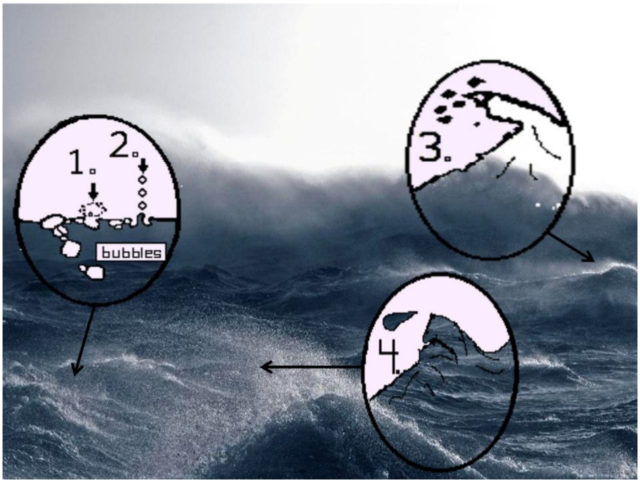

FIGURE 1.16 Sea spray aerosols are generated primarily through wind-breaking waves over the oceans. This figure shows the different mechanisms by which it occurs. Figure adapted from Grythe et al. (2014).

In addition to sources over the ocean, marine aerosols can also be influenced by emissions from the continent, including natural and anthropogenic aerosols. Aerosols from continental sources, such as mineral dust, sulfate, and carbonaceous aerosols, can be transported over the ocean and influence marine environments, changing the chemical composition of marine aerosols (Fitzgerald, 1991; O'Dowd and de Leeuw, 2007). For example, sulfate and nitrate aerosols can contribute to the acidification of marine aerosols, altering their hygroscopic properties. In addition, continental emissions from biomass burning, fossil-fuel combustion, and biogenic sources can contribute to the POA in the marine atmosphere, influencing the overall hygroscopicity, cloud condensation nuclei ability, and light-absorbing properties.

Various factors influence marine aerosol emission rates, including wind speed, sea surface temperature, salinity, and ocean biological productivity (Grythe et al., 2014). Generally, marine aerosol production is represented in most models by a source function that varies by size (see Grythe et al. (2014) for more details):

$$\frac{dF(D_p, U_{10}, T, S, O)}{dD_p} = W(U_{10}, D_p) \cdot \frac{dF_N D_p}{dD_p} \cdot T_w(T, D_p) \cdot S_w(S, D_p) \cdot O_w(O, D_p)$$

where W is the magnitude of production generally representing the whitecap fraction of the ocean, and it is a function of the 10-m wind speed, U_{10}, and the dry diameter, D_p; T_w, S_w, O_w are the weighting function representing the ocean temperature (T), salinity (S) and sea state (O), respectively; and $\frac{dF_N}{dD_p}$ is

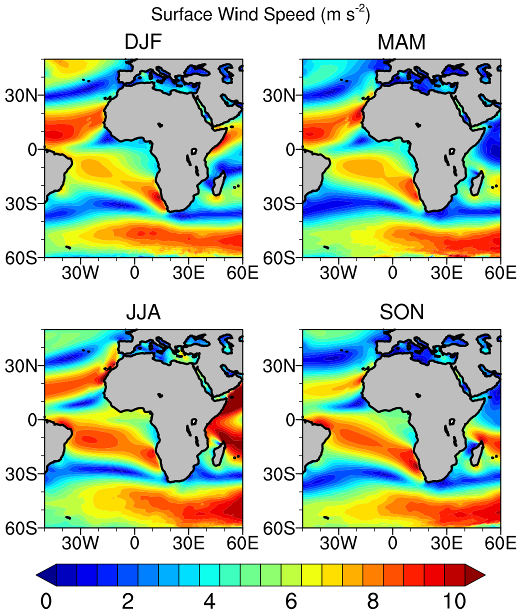

FIGURE 1.17 The spatial distribution of seasonal surface wind speed for DJF (December–January–February), MAM (March–April–May), JJA (June–July–August), and SON (September–October–November) from the MERRA-2 reanalysis (1980–2023).

the shape function of the number size distribution. Generally, stronger winds can generate larger waves, leading to more bubbles bursting and higher sea spray emissions (Fig. 1.17). Previous studies have also indicated that this relationship between wind speed and emissions is nonlinear, with emissions increasing exponentially with wind speed (Garratt, 1977; Gong, 2003). Part of the pathways by which this can occur includes the generation of strong turbulence at the surface that can induce strong vertical motion, pushing the particles past the reference height, which is typically taken to be at ~10 m above the ocean surface (Grythe et al., 2014; Reid et al., 2001). Thus, most models represent the whitecap fraction as a power law relationship where $W \propto U_{10}^{2} - U_{10}^{3.5}$ or $W \propto U_{10}^{3.41}$ (Monahan and Muircheartaigh, 1980; Grythe et al., 2014). In addition to strong surface winds, sea surface temperature (SST) can influence emissions, where warmer ocean surfaces enhance bubble formation and organic matter production, leading to higher aerosol emissions (Demarcq et al., 2003; Jaeglé et al., 2011). However, some other studies have found contrasting results on the influence of SST on SSA emission. For example, Zábori et al. (2012) showed that SSA concentration increases with decreasing temperature and Mårtensson et al. (2003) showed that the influence of SSA may also be size-dependent. Furthermore, the salinity of the ocean may influence the emission of SSA over the ocean, which occurs because the surface tension and density of the water are influenced by ocean salinity, which may, in turn, affect the bubble-bursting processes (Zábori et al., 2012). This may be an important factor in the Mediterranean Sea, for example, which typically has higher salinity than the Atlantic or Indian Oceans. Given the differences in the characteristics of the ocean surrounding the African continent, the ocean sources emit different amounts of marine aerosols that result in substantial spatiotemporal distribution in the atmosphere.

1.4.2 Climatological distribution of marine aerosols

After emission, marine aerosols in the atmosphere substantially vary in concentration over Africa's nearby oceans, primarily influenced by ocean biological activity and general wind patterns (Vignati et al., 2010). We show in Fig. 1.18 the spatial distribution of seasonal chlorophyll-a concentration from SeaWiFS (Sea-viewing Wide Field-of-view Sensor) and sea salt aerosols loading from MERRA-2 (Modern-Era Retrospective analysis for Research and Applications, Version 2) reanalysis dataset. The chlorophyll-a concentration (upper panel in Fig. 1.18) represents biological activity in the ocean, and previous studies have shown that it correlates with emitted water-insoluble organic carbon, a proxy for POA (Yoon et al., 2007). In addition, when combined with surface winds, regions of high biological activities represented by chlorophyll-a also serve as a proxy for sea spray generation at the ocean surface. High chlorophyll-a concentrations are typically found near the coastal regions, in areas with strong upwelling and surface winds (O'Dowd et al., 2004). For example, high concentrations are found near the Benguela Current, close to the coast of Angola–Namibia, in the southern Atlantic Ocean, and in the North Atlantic Ocean off the coast of West Africa. The chlorophyll-a concentration in the Indian Ocean is highest close to the Arabian Peninsula in the summer. Over the open ocean, high chlorophyll-a concentrations are over the Southern Ocean and the equatorial Atlantic and Indian Oceans. In contrast, minimum chlorophyll-a concentration occurs around and at the center of the ocean gyre, where wind speeds are generally low.

When averaged over the atmospheric column, the distribution of the sea salt aerosol loads is broadly consistent with the distributions of chlorophyll-a concentrations and the surface winds (lower panel in Fig. 1.18), with the maximum sea salt aerosols occurring downstream of the high ocean chlorophyll-a concentration. Specifically, the trade winds, which are easterly winds that blow from the subtropical high-pressure zones towards the equatorial low-pressure region, play a crucial role in transporting marine aerosols over the Atlantic and Indian Oceans. As such, high concentration of sea salt aerosols occurs over the tropical Atlantic and Indian Oceans. In addition, the strong winds associated with the mid-latitude westerly winds over the Southern Ocean lead to higher sea salt aerosol concentrations over the eastern parts of the basin than the western parts (see south of ∼30°S).

Seasonal migration of these winds also impacts the seasonal variation of chlorophyll-a and sea salt aerosols. Over the northern Atlantic Ocean, the maxi-

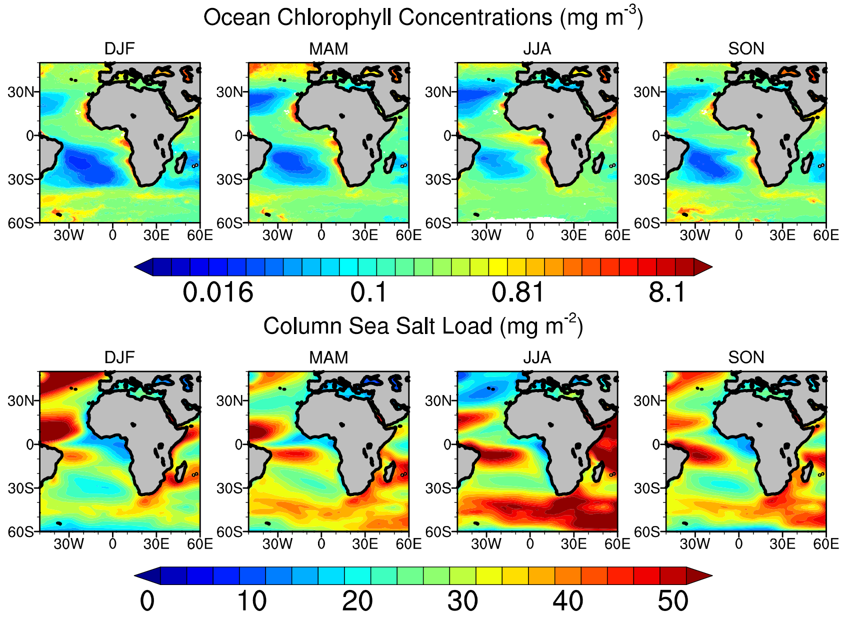

FIGURE 1.18 Seasonal variation in ocean chlorophyll from SeaWiFS (Sea-viewing Wide Field-of-view Sensor) and column-integrated sea salt load from MERRA-2 (Modern-Era Retrospective analysis for Research and Applications, Version 2) reanalysis dataset (1980–2023).

mum chlorophyll-a concentration and sea salt aerosols occur in the winter (DJF in Fig. 1.18) and reach a minimum in the summer (JJA in Fig. 1.18). The opposite is true over the South Atlantic and Indian Ocean, which exhibit its maximum values in the summer. In addition, seasonal variation also influences the transport of marine aerosols inland. For example, the seasonal variability of the West African Monsoon system controls the transport of sea salt over the West African region, which maximizes in the summer.

1.4.3 Properties of marine aerosols

Marine aerosols, including sea spray aerosols (SSA) and primary organic aerosols (POA), exhibit diverse physical, chemical, and optical properties influenced by their sources, atmospheric processing, and transport mechanisms. For chemical composition, SSAs are predominantly composed of sea salt ions derived from the fragmentation of seawater droplets during bubble-bursting and wave-breaking events (Fitzgerald, 1991). Most sea salt aerosols are sodium chloride (NaCl), accounting for approximately 85–90% of its dry mass (Grythe et al., 2014). Other inorganic salts present in smaller quantities include magnesium chloride ($MgCl_2$), sulfates (e.g., Na_2SO_4, $MgSO_4$), bromides, and carbonates. In addition, SSA can also contain trace amounts of metals such as iron, copper, zinc, and manganese, which play important roles in various biogeochemical processes. For example, dust particles that are transported from the Sahara Desert contain a substantial fraction of iron and, when deposited over the North Atlantic Ocean, contribute to the trace elements in the ocean (Jickells et al., 2005; Johnson and Meskhidze, 2013). Further, POAs consist of organic compounds emitted directly from marine organisms, including lipids, proteins, carbohydrates, and other biogenic materials (Gantt and Meskhidze, 2013). While inorganic salts are broadly represented as sea salts, POAs are often represented in components of soluble or insoluble water.

Both SSAs and POAs are hygroscopic, meaning they can uptake water vapor from the atmosphere, influencing their size, composition, and optical properties (Randles et al., 2004). Hygroscopic growth is more pronounced for SSAs due to their inorganic composition than for POAs, in which some organic compounds may exhibit hydrophobic behavior (Prisle et al., 2010; Ovadnevaite et al., 2011). Similarly, organic species in sea salt particles can significantly reduce hygroscopic growth in subsaturated conditions (Ming and Russell, 2001). As particles grow through their hygroscopic process, they increase in size and mass, changing their scattering and absorption characteristics (Randles et al., 2004). Overall, the hygroscopicity of marine aerosols and the consequent changes in particle size influence their ability to act as cloud condensation nuclei (CCN), thereby impacting cloud formation over the ocean.

In addition to chemical composition and hygroscopicity, marine aerosols span a wide range of particle sizes, from ultrafine or Aiken particles (< 0.1 μm) to coarse particles (> 1 μm), with various parts of the distribution dominated by SSAs or POAs (O'Dowd and de Leeuw, 2007). Given the different mechanisms in the generation of marine aerosols (Fig. 1.16), previous studies have shown that they have a trimodal size distribution, with modes centered around 0.02–0.05 μm, 0.1–0.2 μm and 2–3 μm (Clarke et al., 2006; Fuentes et al., 2010). Over the North Atlantic Ocean, sea salt aerosols dominate the coarse mode of size distribution, but their contributions vary depending on the biological activities in the part of the ocean (Fig. 1.18). In contrast, POA size distributions are in the Aiken mode and accumulation mode (diameter between 0.1–1 μm), with the majority having less than a 0.5 μm diameter (O'Dowd et al., 2004). O'Dowd et al. (2004) showed that the contributions of sea salt and POAs as a function of size, measured over the North Atlantic Ocean near Mace Head in 2002. For low biological activity periods, sea salt dominates the size distribution, accounting for at least 74% in the accumulation mode and about 98% in the coarse mode. In contrast, the POAs dominate the Aiken mode for biological activity periods and account for a substantial fraction of the accumulation mode. Specifically, about 83% of the Aiken mode is composed of POAs. In addition, the contribution of sea salt and POAs to each size bin also varies depending on the season. For example, the contribution of POAs is higher during winter, contributing broadly to the Aiken and accumulation model, whereas the contribution of POAs in the summer has a higher fraction in the Aiken mode than accumulation mode.

Furthermore, marine aerosols' particle shapes can vary from spherical to nonspherical, depending on the particle size and relative humidity (Pilinis and Li, 1998). Previous studies have suggested that sea salt aerosols, which contain mostly NaCl, appear spherical and largely homogeneous at high relative humidity, such as greater than 95% (Bi et al., 2018). When these sea salts crystallize at low relative humidity, typically between 46–58%, their shape becomes nonspherical, depending on their composition (Zeng et al., 2013). Therefore, spherical approximation at low relative humidity can result in large uncertainties in estimating sea salt optical properties, including phase matrix, backscattering linear depolarization ratio, and scattering coefficients (Chamaillard et al., 2003). However, close to the surface of the ocean, relative humidity is generally very high, and a spherical approximation for the shape of sea salt is possible. Whereas marine aerosols over land or at higher altitudes can have ambient relative humidity that can result in crystallization and subsequent nonsphericity of the sea salt aerosols, their contribution to the overall contribution to number and mass of marine aerosols is small. As a result, almost all climate models assume a spherical approximation for sea salt aerosols in estimating their optical properties.

Because marine aerosols are dominated by SSAs, they are considered to be primarily scattering aerosols. Due to their large size and refractive index contrast with air, SSAs efficiently scatter light in the visible and near-infrared spectra. In addition, POAs can exhibit both scattering and absorption properties, depending on their chemical composition and the presence of light-absorbing compounds like humic-like substances (Gantt and Meskhidze, 2013).

1.5 Sulfate aerosols over Africa

Sulfate (SO_4^{2-}) aerosols are solid or liquid particles composed of various sulfate compounds. These aerosols are generally formed from sulfur-containing gases such as sulfur dioxide (SO_2), Hydrogen sulfide (H_2S), carbonyl sulfide (OCS), and dimethyl sulfate (DMS; (CH3)2SO4) and largely come under secondary aerosols. In addition, crustal sulfate-containing compounds such as CaSO4, magnesium sulfate, sodium sulfate, and so on, are directly rejected into the atmosphere, albeit in smaller amounts compared to secondary aerosols. Sulfate aerosols are known to scatter incoming solar radiation and are thus considered a cooling agent for climate forcing. Sulfate aerosols also attract water vapor, thereby acting as efficient cloud-condensate nuclei influencing cloud formation and precipitation processes. In addition to impacts on climate, sulfate aerosols also affect visibility, air quality, and human health. In this section, we describe the anthropogenic and natural sources of sulfate aerosols and their precursor gases. Followed by the spatial pattern and variability, and we elaborate on the physicochemical properties of sulfate aerosols over Africa.

TABLE 1.2 Sulfate compounds commonly found in the atmosphere.

Compound	Chemical formula	Phase state	Formation mechanism
Sulfuric Acid	H_2SO_4	Liquid	Oxidation of SO_2 in the presence of water vapor
Ammonium Sulfate	$(NH_4)_2SO_4$	Solid	Ammonia reacts with sulfuric acid SO_2 reacts with NH_3 and Water Vapor
Ammonium Bisulfate	NH_4HSO_4	Solid	
Triammonium Hydrogen sulfate (Letovicite)	$(NH_4)_3H(SO_4)_2$	Solid	
Methanesulfonic Acid	CH_3SO_3H	Liquid	Oxidation of DMS
Magnesium Sulfate	$MgSO_4$	Solid	Mostly primary particles emitted directly into the atmosphere
Calcium Sulfate	$CaSO_4$	Solid	
Sodium Sulfate	Na_2SO_4	Solid	
Zinc Sulfate	$ZnSO_4$	Solid	
Ammonium Zinc Sulfate	$(NH_4)_2Zn(SO_4)_2$	Solid	

1.5.1 Sources and emission of sulfate aerosols

Sulfur is an essential element abundant across all spheres of the Earth's system, including the lithosphere, biosphere, hydrosphere, and atmosphere. Despite its ubiquity, the atmosphere contains the least amount of sulfur, with a burden of 5 Tg (S), in comparison to the vast amounts found in other reservoirs, such as 2×10^{10} Tg (S) in the lithosphere and 1.3×10^{9} Tg (S) in the oceans. Major compounds that are part of atmospheric sulfate aerosols are listed in Table 1.2. Particles containing liquid sulfuric acid are the most common sulfate aerosols. Sulfuric acid is the primary component of the natural stratospheric aerosol and is composed of an aqueous sulfuric acid solution of 60–80% sulfuric acid for temperatures from −80 to −45 °C (Shen et al., 1995).

Aqueous-phase and gas-phase oxidation of SO_2 are involved in the sulfate concentration in the atmosphere. The aqueous-phase pathway is responsible for more than half of the ambient concentration and reaming from gas-phase oxidation of SO_2 by OH radicals. SO_2 reacts with oxygen in the air and forms SO_3:

$$2SO_2 + O_2 \rightarrow 2SO_3.$$

However, the rate of reaction is slow under normal tropospheric conditions and is generally not considered a primary source of SO_3. The dominant gas-phase reaction involves OH radicals that produce sulfur trioxide, namely,

$$SO_2 + OH^{\cdot} + M \rightarrow HOSO_2^{\cdot} + M$$
$$HOSO_2^{\cdot} + O_2 \rightarrow HO_2^{\cdot} + SO_3$$

which, in the presence of water vapor, converts rapidly into sulfuric acid.

$$SO_3 + H_2O + M \rightarrow H_2SO_4 + M$$

Other dominant sulfate particles are due to the reaction of SO_2 with NH_3 in the presence of water vapor (Renard et al., 2004) or when sulfuric acid reacts with NH_3 by following reactions:

$$2NH_3 + H_2O + SO_3 \rightarrow (NH_4)_2\,SO_4$$
$$H_2SO_4 + 2NH_3 \rightarrow (NH_4)_2\,SO_4$$
$$NH_3 + SO_3 + H_2O \rightarrow NH_4HSO_4$$
$$H_2SO_4 + NH_3 \rightarrow NH_4HSO_4.$$

The prevalent particles that emerge out of the above reactions are ammonium sulfate ($(NH_4)_2SO_4$) and ammonium bisulfate (NH_4HSO_4) (Chen et al., 2018; Cheng et al., 2019). Ammonium sulfate is soluble in water, an almost unreactive material, and the most stable ammoniated compound forms as secondary aerosols in well-aged air masses (Charlson et al., 1978). Additionally, various other ammoniated particles are detected in the atmosphere, including triammonium hydrogen sulfate, known as letovicite ($(NH_4)_3H(SO_4)_2$). Letovicite is the most abundant solid ammoniated particle that is understudied for its effectiveness as a cloud condensation nucleus (CCN) and its role as a scatterer of solar radiation (Colberg et al., 2003).

Methanesulfonic acid (MSA; CH3SO3H) arises from the oxidation of DMS within the atmospheric boundary layer (Hodshire et al., 2019). This process occurs primarily through OH radicals during the day and NO_3 radicals at night (Lv et al., 2019). MSA, in conjunction with sulfuric acid, constitutes the principal byproduct of DMS oxidation, contributing to the formation of non-sea salt sulfate aerosols. These aerosols serve as crucial sources of cloud condensation nuclei (CCN) over oceanic regions.

Various other sulfate aerosols, including magnesium sulfate ($MgSO_4$), calcium sulfate ($CaSO_4$), sodium sulfate (Na_2SO_4), zinc sulfate ($ZnSO_4$), and zinc ammonium sulfate ($(NH_4)_2Zn(SO_4)_2$), are predominantly inorganic compounds emitted into the atmosphere through primary sources. For instance, $MgSO_4$ originates largely with sea salt when high winds impact onshore waters, constituting approximately 5.7% of total global sea salt emissions by weight. $CaSO_4$, primarily comprising coarse mode particles (with a particle size greater than 1–2 μm), is emitted through wind erosion over gypsum beds. Sodium sulfate (Na_2SO_4) is generated as a byproduct during waste incineration, notably within the paper industry, where it contributes to decreased visibility in surrounding areas. $ZnSO_4$ and $(NH_4)_2Zn(SO_4)_2$ result from specific metal processing activities, with $ZnSO_4$ displaying comparable water solubility to NH_4SO_4, while ammonium zinc sulfate exhibits significantly lower water solubility. It is important to note that, while the list in Table 1.2 is indicative, it is not exhaustive;

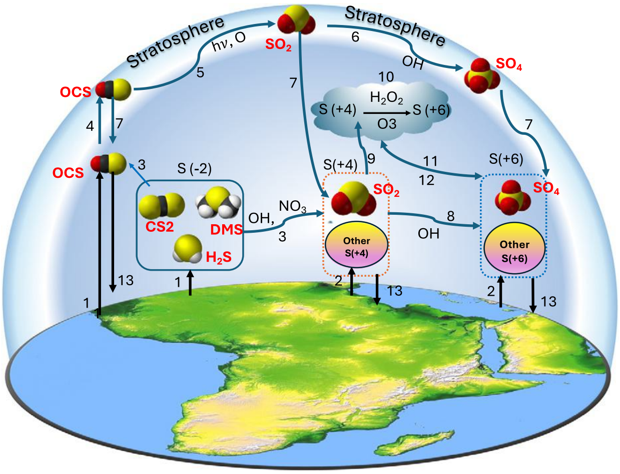

FIGURE 1.19 Atmospheric component of the sulfur cycle and formation of sulfate. The paths are labeled according to the processes: (1) emission of DMS, H_2S, CS_2, and OCS; (2) emission of S(+4) and S(+6); (3) oxidation of DMS, H_2S, and CS_2 by OH, and DMS, by NO_3 in the troposphere; (4) transport of OCS into the stratosphere; (5) photolysis of OCS or reaction with O atoms to form SO_2 in the stratosphere; (6) oxidation of SO_2 in the stratosphere; (7) transport of stratospheric OCS, SO_2, and sulfate back into the troposphere; (8) oxidation of SO_2 and other S(+4) products by OH in the troposphere; (9) absorption of S(+4), mainly SO_2, into hydrosols (cloud/fog/rain droplets, moist aerosol particles); (10) liquid phase oxidation of S(+4) by H_2 O_2(aq) in hydrosols (and by O_2 in the presence of elevated levels of catalytic metal ions); (11) absorption/growth of S(+6) aerosol—mainly sulfate—into hydrosols; (12) evaporation of cloud-water leaving residual S(+6) aerosol; (13) deposition of OCS, S(+4), and S(+6). Where S(+4) and S(+6) denote the compound with sulfur oxidation states 4 and 6, respectively, such as sulfite ion (SO_3^{2-}) and sulfuric acid (H_2 SO_4). Image adapted from Seinfeld and Pandis (2006).

interested readers are encouraged to consult Charlson et al. (1978) or Seinfeld and Pandis (2006) for further information.

From the previous discussion, it is evident that the formation of sulfur-containing aerosol particles involves the oxidation of SO_2 and other precursor gases such as CS_2, DMS, H_2S, and OCS. It is also worth noting that the transformation to sulfate particles involves SO_2 at different stages of the reaction. For example, directly emitted SO_2 may be oxidized to become SO_4^{2-} ion, the most stable sulfur-containing forms in the atmosphere, or gas like OCS may be transformed into SO_2 by photolysis, which eventually are converted into the sulfate ion. The detailed pathway of the processes involved, from the emission of precursor gases to the formation of various stable compounds that can be part of aerosol particles, is depicted in Fig. 1.19. These precursor gases, in addition to primary sulfate particles, are emitted into the atmosphere from both marine and continental regions, as indicated by arrows 1 and 2 in Fig. 1.19.

Starting from OCS, which can be directly emitted into the troposphere or oxidized from DMS or CS_2, this goes on to serve as the largest source of stratospheric sulfate aerosols. The chain of involved transformation is indicated by arrows 1, 4, 5, and 6 in Fig. 1.19 (Brühl et al., 2012). Similarly, within the troposphere, the oxidation of these gases leads to the production of SO_2, which subsequently undergoes conversion into sulfate ions (SO_4^{2-}). For example, DMS, which mainly originates from phytoplankton, other than a few terrestrial sources, undergoes oxidation to SO_2 primarily by hydroxyl radicals (OH) during the day and by nitrate radicals (NO_3) at night (Jardine et al., 2015; Chen et al., 2018). Subsequently, SO_2 is further oxidized to sulfate through gaseous-phase and aqueous-phase reactions. Cloud-mediated aqueous oxidation of SO_2 accounts for more than half of the ambient sulfate concentration (Venkatram et al., 1992; Dennis et al., 1993) in the troposphere. The remaining sulfate comes from gaseous phase reactions, such as the direct formation of sulfuric acid from organic sulfur gases (Berndt et al., 2023).

Thus, globally, sulfate aerosols in the atmosphere may come from diverse sources but are mainly dominated by SO_2. The SO_2 emissions from fossil fuel combustion contribute about 72% global sulfate aerosol burden. This is followed by approximately 19% from natural emissions like DMS, released by phytoplankton, while volcanic activities contribute about 7%, and biomass burning adds around 2% to the sulfate aerosol burden (Forster et al., 2007).

Quantifying ambient sulfate concentration over Africa is challenging due to the scarcity of ground-based measurements (Tiitta et al., 2014; Bowdalo et al., 2024). Unlike the United States' IMPROVE (Interagency Monitoring of Protected Visual Environments) and China's EANET (Acid Deposition Monitoring Network in East Asia) networks, which monitor ambient sulfate concentrations, most African air quality monitoring networks measure only SO_2, along with other criteria air pollutants. Satellite-based remote sensing observations of SO_2 are widely accepted and prove valuable for monitoring sulfate aerosols over regions such as Africa. This is because sulfate concentration correlates directly with the presence of SO_2 in the atmosphere, as previously discussed. In addition, tracking of SO_2 by satellite also enables the identification of potential point sources that contribute to the ambient sulfate concentrations (McLinden et al., 2016). For example, Fioletov et al. (2016) have devised a method to monitor and locate point sources, including large volcanic emissions, from satellites (see https://so2.gsfc.nasa.gov/).

Using this data and global emission inventory (Emissions Database for Global Atmospheric Research, versions 6.1; EDGARv6.1) (Crippa et al., 2022), Fig. 1.20a shows the point sources and other sources, such as ship tracks, of SO_2. Major anthropogenic sources of SO_2 in Africa and adjacent regions include industrial activities, smelting, oil and gas refineries, and shipping emissions.

The dominant SO_2 emission source over continental Africa is power plants, followed by the smelting industry. Power plants emit about 1.65 Tg $Year^{-1}$ while smelting 0.30 Tg $Year^{-1}$. Power plants situated in South Africa account for almost 80% ($\sim$1.39 Tg $Year^{-1}$) of total SO_2 emissions emanating from all power plants over continental Africa (Fig. 1.21). Northwestern, mid-African regions show few point sources of emissions. However, transport from Middle

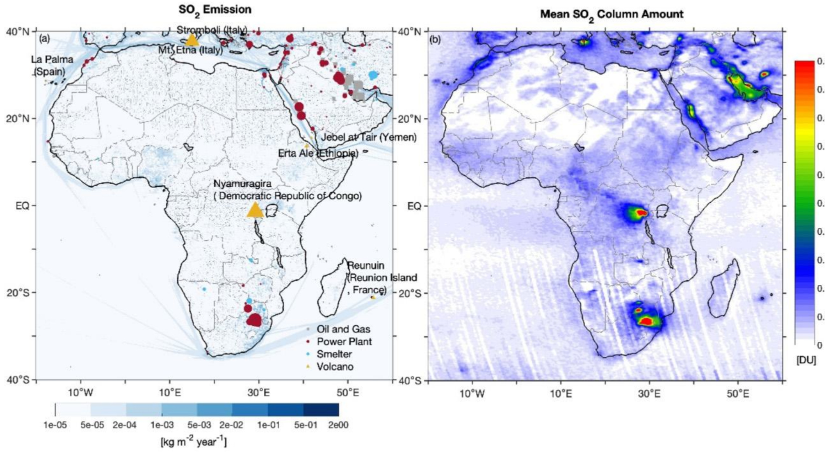

FIGURE 1.20 The emission of SO_2 over Africa and adjacent oceanic regions, along with the column burden, is depicted. Point sources such as oil and gas fields, power plants, smelters, and major volcanic locations are emphasized. The size of markers in (a) denotes relative source strengths. Volcanic emissions are denoted by yellow triangles, with their respective names adjacent to each location. (1 DU = 2.69 · 1016 molecules/cm^2).

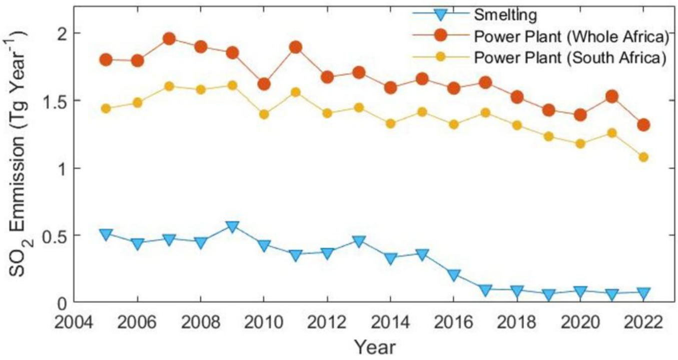

FIGURE 1.21 Year-to-year variation of SO_2 emissions over Africa due to power plants and smelting activity.

Eastern oil fields may contribute to the SO_2 burden in Africa. Apart from these point sources, emissions from shipping lanes in the Red Sea and the Mediterranean stemming from the Cape Town port and western coastal regions are evident.

Dominant natural sources of SO_2 over continental Africa are volcanic emissions from one of the major active volcanic regions comprising the Nyamuragira and Nyiragongo volcanoes in the Democratic Republic of Congo. This volcanic region contributes ~1 Tg Year^{-1} of SO_2 emissions (Campion, 2014). Years between 2012 and 2015 were the most active year in recent years, emitting about 2–3Tg SO_2 per year (see Fig. 1.22b). The most recent significant eruption hap-

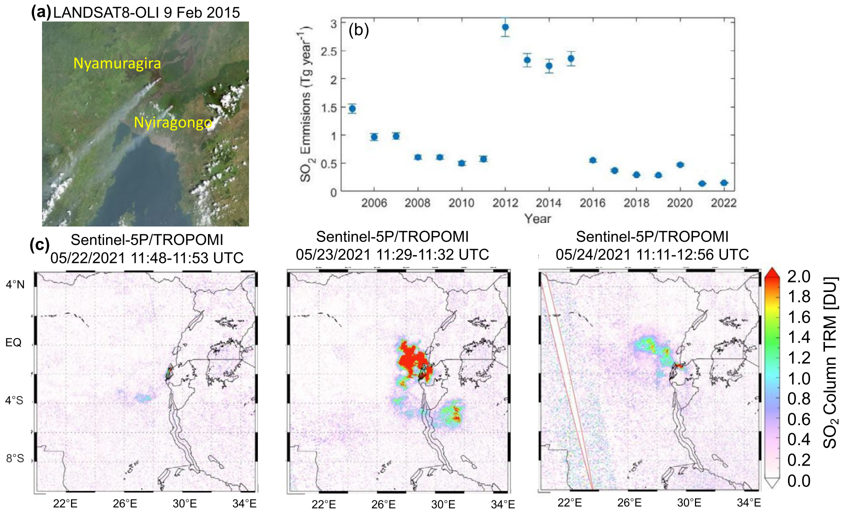

FIGURE 1.22 (a) Natural color image from Landsat-8 showing plumes from dual volcanoes (Nyamuragira and Nyiragongo) in the Democratic Republic of Congo; (b) annual emissions rate of SO_2 showing year-to-year variations; (c) SO_2 plumes due to Nyiragongo volcanic eruption of 2021, before (22 May 2021), during (23 May 2021), and after (24 May 2021) eruption–images are derived from Sentinel-5P's TROPOMI (TROPOspheric Monitoring Instrument) sensor, archived at global sulfur dioxide monitoring webpage (https://so2.gsfc.nasa.gov).

pened on 23 May 2021, when 0.007 Tg of SO_2 was emitted in one day (see Fig. 1.22c). Other volcanoes, such as Erta Al and Reunion Island, emit about 0.05 & 0.06 Tg Year^{-1}, respectively.

Numerical model simulation offers an alternative means to estimate the concentration of sulfate aerosols over Africa, which is limited by the unavailability of direct measurements. Global reanalysis products, such as NASA's MERRA2 (Modern-Era Retrospective Analysis for Research and Applications, Version 2) and Copernicus Atmosphere Monitoring Service (CAMS) reanalysis of atmospheric composition (Inness et al., 2019) provide concentration as well as optical depth of total aerosol along with aerosol type. In the next section, we describe the observed spatiotemporal variation of sulfate over Africa using CAMS datasets.

1.5.2 Climatological distribution of sulfate aerosols

The annual mean spatial pattern of sulfate AOD (Fig. 1.23a) and column burden (Fig. 1.23b) resemble the SO_2 pattern shown in Fig. 1.20b. Relatively higher sulfate optical depth and column burden are evident near point sources. In addition, the coastal regions, especially the eastern coast, show relatively higher values. The annual mean sulfate AOD value for continental Africa is 0.04 (± 0.009), which is $\sim 14\%$ of total AOD (0.28 ± 0.06; see also Fig. 1.4). In general, the

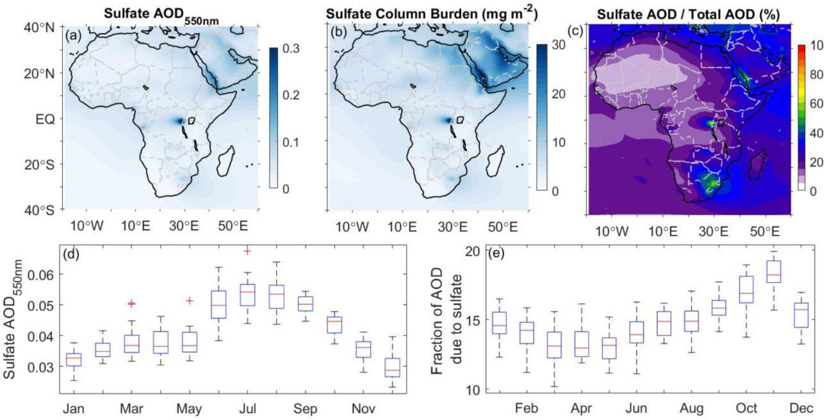

FIGURE 1.23 Spatial pattern of annual mean (2003–2021) sulfate aerosol optical depth (a), column burden (b), and ratio of sulfate AOD to total AOD (c). Seasonality of sulfate AOD over continental Africa (d) and fraction of total sulfate AOD to total AOD (e).

contribution of sulfate AOD to total AOD is larger in the eastern part compared to the western (Fig. 1.23c). In the vicinity of point sources in South Africa and the Democratic Republic of Congo, almost 70% of total column AOD is due to sulfate (see Fig. 1.23c).

Over continental Africa, seasonality in sulfate AOD and their relative contribution to total AOD is shown in Fig. 1.23d & e. Whereas the largest values of sulfate AOD are observed from June to October, the relative contribution to total AOD is highest for October and November. The lowest mean value of sulfate AOD is for December (0.029), which amounts to a 28% lesser value than the annual mean. Conversely, the highest value is observed for July at 0.053, marking a 30% increase over the annual mean. However, there is very little variation in the relative contribution of sulfate AOD to total AOD, which varies from a minimum of 13% in March to a maximum of 18% in November.

1.5.3 Properties of sulfate aerosols

The physiochemical and optical properties of aerosols determine their interaction with radiation, clouds, and other atmospheric constituents. These properties depend on the chemical composition and sources from where these particles originate. For example, particles that may form in the atmosphere from gas to particle conversion are generally much smaller than those that are emitted as primary particles in the atmosphere. As discussed, sulfate aerosols are predominantly secondary aerosols formed from precursor gases (Khoder, 2002). Therefore, before discussing other properties of sulfate aerosols, we explain the processes involved in their formation.

From gaseous elements, such as SO_2 or gaseous H_2SO_4, an initial molecular cluster forms, which, after reaching a critical size, can nucleate to form ultra-

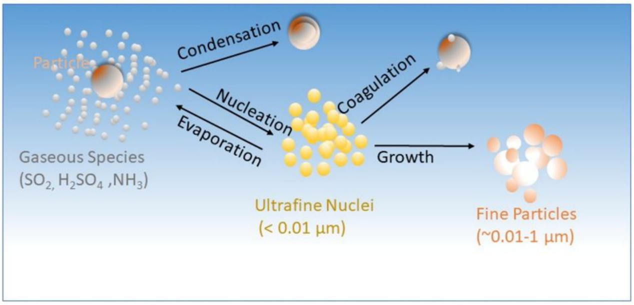

FIGURE 1.24 Schematic showing the formation of aerosol particles from gaseous elements due to successive processes such as nucleation, condensation, and coagulation.

fine particles that subsequently grow into fine particles (Fig. 1.24). For example, the molecule of H_2SO_4 with water molecules can form an initial cluster, which, with the help of available water vapor, grows into nanodroplets of aqueous sulfuric acid. Additionally, condensation and coagulation help create fine sulfate particles. Therefore, this interplay between nucleation, condensation, and coagulation determines the size distribution of sulfate aerosols (Penner et al., 1998).

Due to variations in sources, formation mechanisms, and the presence of other aerosol types in the ambient environment, the size of sulfate particles varies significantly. While fresh aqueous spherical sulfate particles can have a size of 0.01 μm, those produced by secondary processes in the atmosphere or directly emitted as primary particles can be as high as 2 μm. Therefore, the size distribution of sulfate aerosols, in general, is described by a log-normal distribution like other aerosols (Hansen and Travis, 1974).

$$\frac{dN_i(r)}{d(\ln(r))} = \frac{1}{\sqrt{2\pi}\,\ln(\sigma_i)}\frac{1}{r}\exp\left(\frac{-(\ln(r)-\ln(r_i))^2}{2(\ln(\sigma_i))2}\right)$$

Distribution parameters r_i (μm) is the median radius σ_i is the spread of the distribution. These distribution parameters for H_2SO_4 droplets (0.0695, 1.86), sulfate aerosols (0.0695, 2.03), and volcanic aerosols (0.217, 1.77) are listed by d'Almeida et al. (1991) for dry particles. Many of the sulfate particles are produced by the aqueous phase reaction. Also, newly formed particles can consume available water for cluster growth. Therefore, both the size and number concentration of sulfate aerosols are sensitive to the ambient humidity of the atmosphere.

The sulfate aerosols are known for their light scattering property, and they reflect much of the solar radiation back to space. Across the solar spectrum, single scattering albedo for sulfate aerosols is nearly 1, except for the near-infrared region where it is slightly absorbing (Penner et al., 2001). The refractive index of the pure H_2SO_4 is m = 1.43 – 0.0i, for 500 nm. However, the overall refractive index of the sample depends on the other particles present in the analyzed sample. For example, over the South African region, the sample was dominated by the $(NH_4)_2SO_4$, and the fractional number concentration of sulfate aerosol was 82%. The estimated refractive index was $m = 1.47 - 0.05i$, and the single scattering albedo was 0.87 (Gwaze et al., 2007).

1.6 Summary

Aerosols over (and near) Africa account for approximately 30% of the global aerosol concentration, 16% of global shortwave extinction, and 28% of global aerosol absorption. As such, African aerosols are critical to understanding our current climate system and how it will change in the future. Major aerosol species over Africa include mineral dust, carbonaceous aerosols (black carbon and organic carbon), marine aerosols, and sulfate aerosols. Because these aerosols include major scattering aerosols (e.g., sulfate) and absorbing aerosols (e.g., black carbon) in the shortwave and longwave spectra (e.g., mineral dust), Africa contributes a substantial fraction of the global aerosol radiative effects. Relative to other continents, African sources dominate the emitted mineral dust and carbonaceous aerosols, accounting for about 49% and 52% of global estimates, respectively. African dust also accounts for more than 45% of the global dust load, shortwave extinction, and absorption, and its carbonaceous aerosols account for more than 19% of the global loading, extinction, and absorption of black and organic carbon. Furthermore, African sulfate and marine aerosols also contribute a nonnegligible fraction of global loading and shortwave extinction. Because of Africa's influence and contribution to global aerosols and climate, this chapter provides the background knowledge of aerosols over Africa, synthesizing current progress in our understanding of the sources, distribution, and properties of the four main aerosol species over Africa.

First, mineral dust is a *land-derived* aerosol generated by wind erosion on arid and semiarid surfaces. Dust entrainment into the atmosphere is caused by saltation and sandblasting of large soil aggregates, which depend on surface wind speed and soil properties, such as its dry size distribution, humidity, mineralogy, and surface roughness. The dynamical processes responsible for dust emission include synoptic depressions, mesoscale convective systems, and microscale dynamics. The main African dust sources are the Sahara Desert and the Sahel in the Northern Hemisphere and the gravel plains and alluvial sources in Namibia, South Africa, and Botswana in the Southern Hemisphere. The Sahara Desert is the largest source of mineral dust on Earth. African dust is transported toward the Atlantic Ocean, reaching the North and South Americas, the Mediterranean basin, and continental Europe. It has also been identified in Arctic and Antarctic ice cores. Dust mobilization and transport are affected by seasonal, interannual, and decadal variability, modulated by meteorology and large-scale climate patterns, such as the North Atlantic and the El-Niño Southern Oscillations.

These dust aerosols span sizes from hundreds of nanometers to hundreds of micrometers, showing a complex and irregular morphology. The composition of African dust is either enriched in carbonates, quartz, or iron oxides, depending on the sources. The composition of African dust, its size distribution, and morphology are modified during transport towards the Mediterranean basin, the Atlantic, and Southern Oceans. These changes in properties are due to gravitational settling, external or internal particle mixing with other species, and heterogeneous reactions with gaseous compounds, potentially leading to the formation of inorganic and organic coatings on the dust surface. The size distribution of dust, mainly evolving with gravitational settling along transport, shows a volume size mode that locates around 10 μm close to sources and decreases to ~5 μm and ~2 μm after mid- and long-range transport. Through their interactions with atmospheric radiation, mineral dust strongly affects the radiative budget of the African continent and its surrounding oceanic and continental areas. Scattering is dominant in the shortwave, where the single scattering albedo ranges between 0.88 and 0.99, while absorption is dominant in the longwave, with a single scattering albedo as low as 0.2 in the 8–12 μm atmospheric window. Dust aerosols can also act as cloud condensation nuclei, particularly in supersaturated conditions, and can be efficient ice nuclei even at low supersaturations, depending on chemical composition and the presence of coatings. African dust provides additionally an important source of iron into the oceans, affecting primary productivity in the Atlantic, Indian, and Southern Oceans.

Second, in sub-Saharan Africa, carbonaceous aerosols are mostly produced by wildfire and biomass-burning activities. The peak carbonaceous aerosol loadings occur north of the Equator during the austral summer (December to February). Both carbonaceous aerosols reach a minimum during austral autumn (March to May) as the East African Monsoon prevails following the southward shift of the intertropical convergence zone. As the West African Monsoon prevails during the austral winter (June to August), southern Africa becomes dry with wide distributions of fire activities. In addition, carbonaceous aerosols are comprised primarily of light-scattering organic carbon (OC) and light-absorbing black carbon (BC). BC particles are about 120 nm in geometric mean diameter and constitute up to 30% of the total aerosol mass. BC particles can grow by coagulating with other BC particles or primary organic aerosols and then drop to about 30% of the maximum coating mass after ten days via either evaporation, heterogeneous oxidation, photolysis, aqueous-phase oxidation, dry deposition, and cloud processes. Chemical reactions with nitrate can lead to the formation of brown carbon, which has wavelength-dependent absorption in the near-UV (300–400 nm) and visible wavelengths (400–700 nm). Evaporation and chemical processes can eliminate the coating, whereas BCs' masses remain constant throughout their lifetime except near the fire emission source where aggregation and coagulation occur. BC is typically produced in environments where oxygen is limited for the complete oxidation of carbonaceous fuel to CO_2, whereas OC is produced during combustion and condensation of organic vapor onto existing particles.

Carbonaceous aerosol emissions are initiated by a mixture of combustion processes such as flaming and smoldering. The dry climate during the winter and spring seasons in southern Africa results in the burning of dry fuels that favor flaming combustion (reaching a fire temperature of ~1400 K). Deforestation fires in the Amazon, in contrast, occur in a humid climate that favors smoldering combustion (reaching a fire temperature of ~1000 K). BC particles are primarily generated under flaming conditions, so the contributions of BC to the total aerosol loading are also higher in Africa. Flaming combustion converts C, H, N, and S from solid biomass fuel into highly oxidized gases such as CO_2, H_2O, NO_X, and SO_2, respectively. Smoldering combustion dominates over flaming combustion as the fire progresses via a combination of surface oxidation and pyrolysis. Smoldering generates the majority of CO, CH_4, NMOC, and primary organic aerosol. Coating thickness results in a significantly greater increase in scattering than in absorption, such that the single scattering albedo rapidly increases near the emission source and then drops down with age, ranging between 0.8 and 0.9. In cloud-free conditions, aerosols that are more scattering (i.e., higher single scattering albedo) result in a greater negative direct aerosol radiative effect than aerosols that are more absorbing (i.e., lower single scattering albedo). Aerosols above clouds could affect the sign and magnitude of the direct aerosol radiative effects depending on the amount, aerosol absorption, and complex relationships among them.

Third, marine aerosols are *ocean-derived* particles with sizes spanning from nanometers to several tens of micrometers. The primary source of marine aerosols over Africa is the surrounding oceans, including the Atlantic Ocean to the west, the Indian Ocean to the east, the Mediterranean Sea to the north, and the Southern Ocean to the south. Emitted marine aerosols can generally be divided into sea spray aerosols (SSA) and primary organic aerosols (POA). Unlike SSAs, which are primarily sea salts, such as NaCl, POAs are related to the biological activities of marine organisms in the ocean. Despite the differences, both types of marine aerosols are emitted through similar bubble-bursting and wave-breaking mechanisms over the ocean surface, although POA often includes surface-active organic matter and/or materials, such as bacteria, viruses, and detritus. In addition, POA can also be produced through the oxidation of phytoplankton-emitted volatile organic compounds, such as dimethyl sulfide, aliphatic amines, isoprene, and monoterpenes, which can form secondary organic aerosols (SOA) over the ocean. Regardless of the source ocean and emission mechanism, factors influencing marine aerosols' emission rate include surface wind speed, sea surface temperature, salinity, and ocean biological productivity. Generally, stronger surface winds can generate larger waves, leading to more bubbles bursting and higher sea spray emissions, but this relationship is nonlinear, with emissions increasing exponentially with wind speed. In addition, ocean surface tension and density are influenced by ocean salinity and warmer ocean surfaces, and both can affect the bubble-bursting processes and organic matter production, influencing aerosol emissions over the ocean. Given the variability of these emission factors and differences in the characteristics of the ocean surrounding the African continent, the ocean sources emit different amounts of marine aerosols that result in substantial spatiotemporal distribution in the atmosphere. Specifically, high concentrations of marine aerosol, aided by strong surface winds, often occur downstream of the regions of high oceanic biological activities represented by chlorophyll-a concentration. For example, high concentrations of chlorophyll-a are found over the southern Atlantic Ocean near the Benguela Current (off the coasts of Angola and Namibia) and over the North Atlantic Ocean off the coast of West Africa. In these cases, high concentrations of sea salts are indicated downstream. Overall, a high concentration of sea salt aerosols occurs over the tropical Atlantic and Indian Ocean basins, aided by the trade winds, and over the Southern Ocean basin, aided by mid-latitude westerly winds. Regardless of the ocean basin, the size distributions of marine aerosols are dominated by SSA for the coarse mode fraction ($D \geq 1$ μm), while the POA contributes a substantial fraction of the fine mode fraction. In addition, hygroscopic growth is more pronounced for SSAs due to their inorganic composition than for POAs, in which some organic compounds may exhibit hydrophobic behavior. As particles grow through their hygroscopic processes, they increase in size and mass, changing their scattering and absorption characteristics. Because SSAs dominate marine aerosol concentrations, they are considered to be primarily scattering aerosols.

Fourth, sulfate aerosols are composed of various sulfate compounds and play a significant role in atmospheric processes, impacting climate, visibility, air quality, and human health. Understanding their diverse sources, physiochemical properties, and spatial distribution is crucial for effective mitigation and modeling efforts. The sulfate aerosols predominantly form from sulfur-containing gases by gas-to-particle conversion as secondary aerosols. Additionally, inorganic compounds like magnesium sulfate, calcium sulfate, and sodium sulfate are emitted from primary sources. The sulfur-containing gases can be emitted by anthropogenic sources such as industrial processes, transportation, shipping, biomass burning, or natural sources such as volcanic emissions and marine biota. Sulfur dioxide emissions from fossil fuel combustion constitute around 72% of global sulfate aerosols, with natural emissions such as DMS from the ocean and volcanic activities contributing to the rest. The formation of sulfate aerosols involves complex chemical processes, including gas-phase oxidation of SO_2 and aqueous-phase reactions leading to the production of sulfuric acid droplets. Ammoniated particles, such as ammonium sulfate and ammonium bisulfate, and other compounds like MSA are also common constituents.

Quantifying sulfate aerosol concentrations over Africa is challenging due to limited ground-based measurements. Satellite-based remote sensing, along with global emission inventories (e.g., EDGAR) and reanalysis products (such as MERRA-2 and CAMS), provide valuable insights into their spatial distribution and sources. Industrial activities, power plants, and smelting are major anthropogenic point sources over continental Africa, while volcanic emissions contribute significantly to certain regions like the Democratic Republic of Congo and Reunion Island. In addition, other anthropogenic sources such as vehicular emissions or biomass burning also significantly contribute to total sulfate loading over Africa. The spatial distribution of sulfate aerosols over Africa shows higher concentrations near point sources and coastal regions, with seasonality observed in their relative contributions to total AOD. The physicochemical properties of sulfate aerosols, including their formation mechanisms, particle size distribution, and optical properties, influence their interaction with radiation and other atmospheric constituents. Sulfate aerosols are dominantly scattering particles with single scattering albedo close to 1 across the solar spectrum, reflecting solar radiation and impacting radiative forcing. Their refractive index varies depending on the chemical composition of the aerosols. However, the imaginary part of the complex refractive index is zero for almost all pure sulfate-containing aerosols. Sulfate particles are often found adjacent to other aerosol species and modulate their optical and physical characteristics. The particle size distribution of sulfates generally can be expressed by log-normal distribution with distribution parameters 0.695 μm as the mean effective diameter and 2.03 μm as the spread of the distribution. The size and ambient tropospheric concentration of sulfate aerosols are greatly influenced by ambient humidity.

Although these aerosols over Africa exhibit diverse sources, distribution, and properties, they have substantial influences on several aspects of the regional climate, including the energy balance and precipitation (the subject of this book). Specifically, the distribution of precipitation over Africa is affected locally and regionally on the timescale of hours to days by changes in cloud microphysical processes triggered by aerosol-induced changes in droplet and ice particle concentrations. The total amount of precipitation is also affected on the timescale of days to months by changes in the energy balance in the atmosphere, which determines the amount of water that can condense. Ultimately, on the timescale of decades to centuries, aerosol-induced changes in surface temperature further alter the hydrological cycle and precipitation. A good example of aerosols' impact on regional precipitation is the impact on the West African monsoon (WAM) system. Mineral dust over North Africa and carbonaceous aerosols over West and Central Africa have substantial impacts on WAM by perturbing the meridional energy gradients, resulting in a shift of the meridional precipitation distribution. In addition, aerosols over Africa also have impacts on the African easterly jet and the African easterly wave system, which consequently impacts their resulting influence on tropical cyclones over the North Atlantic Ocean. Overall, aerosol over Africa remains an important continent in our current climate system and requires a deeper understanding of their sources, distribution, and properties to accurately estimate their impact on future climate.

Author contributions

A.A.A. conceptualize, lead, and synthesize the chapter. In addition, A.A.A. also wrote section 1.1, C.D.B. and P.F. wrote section 1.2, I.C. wrote section 1.3, and S.K.P. wrote section 1.4. All authors contribute comments and edit the chapter.

References

Adebiyi, A., Kok, J.F., Murray, B.J., Ryder, C.L., Stuut, J.-B.W., Kahn, R.A., Knippertz, P., Formenti, P., Mahowald, N.M., Pérez García-Pando, C., Klose, M., Ansmann, A., Samset, B.H., Ito, A., Balkanski, Y., Di Biagio, C., Romanias, M.N., Huang, Y., Meng, J., 2023a. A review of coarse mineral dust in the Earth system. Aeolian Research 60, 100849. https://doi.org/10.1016/j.aeolia.2022.100849.

Adebiyi, A.A., Akinsanola, A.A., Ajoku, O.F., 2023b. The misrepresentation of the Southern African easterly jet in models and its implications for aerosol, clouds, and precipitation distributions. Journal of Climate 36, 7785–7809. https://doi.org/10.1175/JCLI-D-23-0083.1.

Adebiyi, A.A., Huang, Y., Samset, B.H., Kok, J.F., 2023c. Observations suggest that North African dust absorbs less solar radiation than models estimate. Communications Earth & Environment 4, 1–13. https://doi.org/10.1038/s43247-023-00825-2.

Adebiyi, A.A., Kok, J.F., 2020. Climate models miss most of the coarse dust in the atmosphere. Science Advances 6, eaaz9507. https://doi.org/10.1126/sciadv.aaz9507.

Adebiyi, A.A., Kok, J.F., Wang, Y., Ito, A., Ridley, D.A., Nabat, P., Zhao, C., 2020. Dust Constraints from joint Observational-Modelling-experiMental analysis (DustCOMM): comparison with measurements and model simulations. Atmospheric Chemistry and Physics 20, 829–863. https://doi.org/10.5194/acp-20-829-2020.

Adebiyi, A.A., Zuidema, P., 2018. Low cloud cover sensitivity to biomass-burning aerosols and meteorology over the southeast Atlantic. Journal of Climate 31, 4329–4346. https://doi.org/10.1175/JCLI-D-17-0406.1.

Adebiyi, A.A., Zuidema, P., 2016. The role of the southern African easterly jet in modifying the southeast Atlantic aerosol and cloud environments. Quarterly Journal of the Royal Meteorological Society 142, 1574–1589. https://doi.org/10.1002/qj.2765.

Adebiyi, A.A., Zuidema, P., Abel, S.J., 2015. The convolution of dynamics and moisture with the presence of shortwave absorbing aerosols over the southeast Atlantic. Journal of Climate 28, 1997–2024. https://doi.org/10.1175/JCLI-D-14-00352.1.

Akagi, S.K., Yokelson, R.J., Wiedinmyer, C., Alvarado, M.J., Reid, J.S., Karl, T., Crounse, J.D., Wennberg, P.O., 2011. Emission factors for open and domestic biomass burning for use in atmospheric models. Atmospheric Chemistry and Physics 11, 4039–4072. https://doi.org/10.5194/acp-11-4039-2011.

Alfaro, S.C., Gomes, L., 2001. Modeling mineral aerosol production by wind erosion: emission intensities and aerosol size distributions in source areas. Journal of Geophysical Research. Atmospheres 106, 18075–18084. https://doi.org/10.1029/2000JD900339.

Andreae, M.O., Andreae, T.W., Annegarn, H., Beer, J., Cachier, H., Le Canut, P., Elbert, W., Maenhaut, W., Salma, I., Wienhold, F.G., Zenker, T., 1998. Airborne studies of aerosol emissions from savanna fires in southern Africa: 2. Aerosol chemical composition. Journal of Geophysical Research. Atmospheres 103, 32119–32128. https://doi.org/10.1029/98JD02280.

Andreae, M.O., Merlet, P., 2001. Emission of trace gases and aerosols from biomass burning. Global Biogeochemical Cycles 15, 955–966. https://doi.org/10.1029/2000GB001382.

Ansmann, A., Petzold, A., Kandler, K., Tegen, I., Wendisch, M., Müller, D., Weinzierl, B., Müller, T., Heintzenberg, J., 2011. Saharan Mineral Dust Experiments SAMUM–1 and SAMUM–2: what have we learned? Tellus. Series B, Chemical and Physical Meteorology 63, 403–429. https://doi.org/10.1111/j.1600-0889.2011.00555.x.

Atkinson, J.D., Murray, B.J., Woodhouse, M.T., Whale, T.F., Baustian, K.J., Carslaw, K.S., Dobbie, S., O'Sullivan, D., Malkin, T.L., 2013. The importance of feldspar for ice nucleation by mineral dust in mixed-phase clouds. Nature 498, 355–358. https://doi.org/10.1038/nature12278.

Barger, W.R., Garrett, W.D., 1970. Surface active organic material in the marine atmosphere. Journal of Geophysical Research 1896–1977 (75), 4561–4566. https://doi.org/10.1029/JC075i024p04561.

Barger, W.R., Garrett, W.D., 1976. Surface active organic material in air over the Mediterranean and over the eastern equatorial Pacific. Journal of Geophysical Research 1896–1977 (81), 3151–3157. https://doi.org/10.1029/JC081i018p03151.

Bauer, S.E., Mishchenko, M.I., Lacis, A.A., Zhang, S., Perlwitz, J., Metzger, S.M., 2007. Do sulfate and nitrate coatings on mineral dust have important effects on radiative properties and climate modeling? Journal of Geophysical Research. Atmospheres 112. https://doi.org/10.1029/2005JD006977.

Bercos-Hickey, E., Nathan, T.R., Chen, S.-H., 2017. Saharan dust and the African easterly jet–African easterly wave system: structure, location and energetics. Quarterly Journal of the Royal Meteorological Society 143, 2797–2808. https://doi.org/10.1002/qj.3128.

Berndt, T., Hoffmann, E.H., Tilgner, A., Stratmann, F., Herrmann, H., 2023. Direct sulfuric acid formation from the gas-phase oxidation of reduced-sulfur compounds. Nature Communications 14, 4849. https://doi.org/10.1038/s41467-023-40586-2.

Bi, L., Lin, W., Wang, Z., Tang, X., Zhang, X., Yi, B., 2018. Optical modeling of sea salt aerosols: the effects of nonsphericity and inhomogeneity. Journal of Geophysical Research. Atmospheres 123, 543–558. https://doi.org/10.1002/2017JD027869.

Bond, T.C., Bergstrom, R.W., 2006. Light absorption by carbonaceous particles: an investigative review. Aerosol Science and Technology 40, 27–67. https://doi.org/10.1080/02786820500421521.

Boose, Y., Sierau, B., García, M.I., Rodríguez, S., Alastuey, A., Linke, C., Schnaiter, M., Kupiszewski, P., Kanji, Z.A., Lohmann, U., 2016. Ice nucleating particles in the Saharan Air Layer. Atmospheric Chemistry and Physics 16, 9067–9087. https://doi.org/10.5194/acp-16-9067-2016.

Bou Karam, D., Flamant, C., Knippertz, P., Reitebuch, O., Pelon, J., Chong, M., Dabas, A., 2008. Dust emissions over the Sahel associated with the West African monsoon intertropical discontinuity region: a representative case-study. Quarterly Journal of the Royal Meteorological Society 134, 621–634. https://doi.org/10.1002/qj.244.

Boucher, O., 2015. Atmospheric aerosols. In: Boucher, O. (Ed.), Atmospheric Aerosols: Properties and Climate Impacts. Springer, Netherlands, Dordrecht, pp. 9–24.

Bowdalo, D., Basart, S., Guevara, M., Jorba, O., Pérez García-Pando, C., Jaimes Palomera, M., Rivera Hernandez, O., Puchalski, M., Gay, D., Klausen, J., Moreno, S., Netcheva, S., Tarasova, O., 2024. GHOST: a globally harmonised dataset of surface atmospheric composition measurements. Earth System Science Data Discussions, 1–137. https://doi.org/10.5194/essd-2023-397.

Bristow, C.S., Hudson-Edwards, K.A., Chappell, A., 2010. Fertilizing the Amazon and equatorial Atlantic with West African dust. Geophysical Research Letters 37. https://doi.org/10.1029/2010GL043486.

Brühl, C., Lelieveld, J., Crutzen, P.J., Tost, H., 2012. The role of carbonyl sulphide as a source of stratospheric sulphate aerosol and its impact on climate. Atmospheric Chemistry and Physics 12, 1239–1253. https://doi.org/10.5194/acp-12-1239-2012.

Campion, R., 2014. New lava lake at Nyamuragira volcano revealed by combined ASTER and OMI SO2 measurements. Geophysical Research Letters 41, 7485–7492. https://doi.org/10.1002/2014GL061808.

Caponi, L., Formenti, P., Massabó, D., Di Biagio, C., Cazaunau, M., Pangui, E., Chevaillier, S., Landrot, G., Andreae, O.M., Kandler, K., Piketh, S., Saeed, T., Seibert, D., Williams, E., Balkanski, Y., Prati, P., Doussin, J.F., 2017. Spectral- and size-resolved mass absorption efficiency of mineral dust aerosols in the shortwave spectrum: a simulation chamber study. Atmospheric Chemistry and Physics 17, 7175–7191. https://doi.org/10.5194/acp-17-7175-2017.

Caquineau, S., Gaudichet, A., Gomes, L., Legrand, M., 2002. Mineralogy of Saharan dust transported over northwestern tropical Atlantic Ocean in relation to source regions. Journal of Geophysical Research. Atmospheres 107, AAC 4-1–AAC 4-12. https://doi.org/10.1029/2000JD000247.

Cavalli, F., Facchini, M.C., Decesari, S., Mircea, M., Emblico, L., Fuzzi, S., Ceburnis, D., Yoon, Y.J., O'Dowd, C.D., Putaud, J.-P., Dell'Acqua, A., 2004. Advances in characterization of size-resolved organic matter in marine aerosol over the North Atlantic. Journal of Geophysical Research. Atmospheres 109. https://doi.org/10.1029/2004JD005137.

Chamaillard, K., Jennings, S.G., Kleefeld, C., Ceburnis, D., Yoon, Y.J., 2003. Light backscattering and scattering by nonspherical sea-salt aerosols. Journal of Quantitative Spectroscopy and Radiative Transfer, Electromagnetic and Light Scattering by Non-Spherical Particles 79–80, 577–597. https://doi.org/10.1016/S0022-4073(02)00309-6.

Charlson, R.J., Covert, D.S., Larson, T.V., Waggoner, A.P., 1978. Chemical properties of tropospheric sulfur aerosols. In: Proceedings of the International Symposium. Atmospheric Environment (1967) 12, 39–53. https://doi.org/10.1016/0004-6981(78)90187-7.

Chen, L., Peng, C., Gu, W., Fu, H., Jian, X., Zhang, H., Zhang, G., Zhu, J., Wang, X., Tang, M., 2020. On mineral dust aerosol hygroscopicity. Atmospheric Chemistry and Physics 20, 13611–13626. https://doi.org/10.5194/acp-20-13611-2020.

Chen, S., Zhao, Y., Zhang, R., 2018. Formation mechanism of atmospheric ammonium bisulfate: hydrogen-bond-promoted nearly barrierless reactions of SO3 with NH3 and H2O. ChemPhysChem 19, 967–972. https://doi.org/10.1002/cphc.201701333.

Cheng, T., Luo, L., Yang, L., Fan, H., Wu, H., 2019. Formation and emission characteristics of ammonium sulfate aerosols in flue gas downstream of selective catalytic reduction. Energy & Fuels 33, 7861–7868. https://doi.org/10.1021/acs.energyfuels.9b01436.

Chiapello, I., Moulin, C., Prospero, J.M., 2005. Understanding the long-term variability of African dust transport across the Atlantic as recorded in both Barbados surface concentrations and large-scale Total Ozone Mapping Spectrometer (TOMS) optical thickness. Journal of Geophysical Research. Atmospheres 110. https://doi.org/10.1029/2004JD005132.

Chou, C., Formenti, P., Maille, M., Ausset, P., Helas, G., Harrison, M., Osborne, S., 2008. Size distribution, shape, and composition of mineral dust aerosols collected during the African monsoon multidisciplinary analysis special observation period 0: dust and biomass-burning experiment field campaign in Niger, January 2006. Journal of Geophysical Research 113, 00C10. https://doi.org/10.1029/2008JD009897.

Chung, ChulE, Lee, K., Müller, D., 2012. Effect of internal mixture on black carbon radiative forcing. Tellus. Series B, Chemical and Physical Meteorology 64, 10925. https://doi.org/10.3402/tellusb.v64i0.10925.

Chung, S.H., Seinfeld, J.H., 2002. Global distribution and climate forcing of carbonaceous aerosols. Journal of Geophysical Research. Atmospheres 107, AAC 14-1–AAC 14-33. https://doi.org/10.1029/2001JD001397.

Clarke, A.D., Owens, S.R., Zhou, J., 2006. An ultrafine sea-salt flux from breaking waves: implications for cloud condensation nuclei in the remote marine atmosphere. Journal of Geophysical Research. Atmospheres 111. https://doi.org/10.1029/2005JD006565.

Coakley, J.A., Cess, R.D., Yurevich, F.B., 1983. The effect of tropospheric aerosols on the Earth's radiation budget: a parameterization for climate models. Journal of the Atmospheric Sciences 40, 116–138. https://doi.org/10.1175/1520-0469(1983)040<0116:TEOTAO>2.0.CO;2.

Colberg, C.A., Luo, B.P., Wernli, H., Koop, T., Peter, T., 2003. A novel model to predict the physical state of atmospheric $H_2SO_4/NH_3/H_2O$ aerosol particles. Atmospheric Chemistry and Physics 3, 909–924. https://doi.org/10.5194/acp-3-909-2003.

Cook, K.H., 1999. Generation of the African easterly jet and its role in determining West African precipitation. Journal of Climate 12, 1165–1184. https://doi.org/10.1175/1520-0442(1999)012<1165:GOTAEJ>2.0.CO;2.

Costantino, L., Bréon, F.-M., 2013. Satellite-based estimate of aerosol direct radiative effect over the South-East Atlantic. Atmospheric Chemistry and Physics Discussions 13, 23295–23324. https://doi.org/10.5194/acpd-13-23295-2013.

Crippa, M., Guizzardi, D., Muntean, M., Schaaf, E., Monforti-Ferrario, F., Banja, M., Pagani, F., Solazzo, E., others, 2022. EDGAR v6. 1 global air pollutant emissions.

Crumeyrolle, S., Gomes, L., Tulet, P., Matsuki, A., Schwarzenboeck, A., Crahan, K., 2008. Increase of the aerosol hygroscopicity by cloud processing in a mesoscale convective system: a case study from the AMMA campaign. Atmospheric Chemistry and Physics 8, 6907–6924. https://doi.org/10.5194/acp-8-6907-2008.

d'Almeida, G.A., Koepke, P., Shettle, E.P., 1991. Atmospheric Aerosols: Global Climatology and Radiative Characteristics. A. Deepak, Hampton. 561 pp.

Deboudt, K., Flament, P., Choël, M., Gloter, A., Sobanska, S., Colliex, C., 2010. Mixing state of aerosols and direct observation of carbonaceous and marine coatings on African dust by individual particle analysis. Journal of Geophysical Research. Atmospheres 115. https://doi.org/10.1029/2010JD013921.

Demarcq, H., Barlow, R.G., Shillington, F.A., 2003. Climatology and variability of sea surface temperature and surface chlorophyll in the Benguela and Agulhas ecosystems as observed by satellite imagery. African Journal of Marine Science 25, 363–372. https://doi.org/10.2989/18142320309504022.

DeMott, P.J., Sassen, K., Poellot, M.R., Baumgardner, D., Rogers, D.C., Brooks, S.D., Prenni, A.J., Kreidenweis, S.M., 2003. African dust aerosols as atmospheric ice nuclei. Geophysical Research Letters 30. https://doi.org/10.1029/2003GL017410.

Denjean, C., Caquineau, S., Desboeufs, K., Laurent, B., Maille, M., Quiñones Rosado, M., Vallejo, P., Mayol-Bracero, O.L., Formenti, P., 2015. Long-range transport across the Atlantic in summertime does not enhance the hygroscopicity of African mineral dust. Geophysical Research Letters 42, 7835–7843. https://doi.org/10.1002/2015GL065693.

Denjean, C., Cassola, F., Mazzino, A., Triquet, S., Chevaillier, S., Grand, N., Bourrianne, T., Momboisse, G., Sellegri, K., Schwarzenbock, A., Freney, E., Mallet, M., Formenti, P., 2016a. Size distribution and optical properties of mineral dust aerosols transported in the western Mediterranean. Atmospheric Chemistry and Physics 16, 1081–1104. https://doi.org/10.5194/acp-16-1081-2016.

Denjean, Cyrielle, Formenti, P., Desboeufs, K., Chevaillier, S., Triquet, S., Maillé, M., Cazaunau, M., Laurent, B., Mayol-Bracero, O.L., Vallejo, P., Quiñones, M., Gutierrez-Molina, I.E., Cassola, F., Prati, P., Andrews, E., Ogren, J., 2016b. Size distribution and optical properties of African mineral dust after intercontinental transport. Journal of Geophysical Research. Atmospheres 121, 7117–7138. https://doi.org/10.1002/2016JD024783.

Dennis, R.L., McHenry, J.N., Barchet, W.R., Binkowski, F.S., Byun, D.W., 1993. Correcting RADM's sulfate underprediction: discovery and correction of model errors and testing the corrections through comparisons against field data. Atmospheric Environment. Part A. General Topics, European Monitoring and Evaluation Program Workshop on the Combined Analysis of Measurements and Model Results with Special Emphasis on NO/VOC/Oxidants 27, 975–997. https://doi.org/10.1016/0960-1686(93)90012-N.

Desboeufs, K., Formenti, P., Torres-Sánchez, R., Schepanski, K., Chaboureau, J.-P., Andersen, H., Cermak, J., Feuerstein, S., Laurent, B., Klopper, D., Namwoonde, A., Cazaunau, M., Chevaillier, S., Feron, A., Mirande-Bret, C., Triquet, S., Piketh, S.J., 2024. Fractional solubility of iron in mineral dust aerosols over coastal Namibia: a link to marine biogenic emissions? Atmospheric Chemistry and Physics 24, 1525–1541. https://doi.org/10.5194/acp-24-1525-2024.

Di Biagio, C., Boucher, H., Caquineau, S., Chevaillier, S., Cuesta, J., Formenti, P., 2014. Variability of the infrared complex refractive index of African mineral dust: experimental estimation and implications for radiative transfer and satellite remote sensing. Atmospheric Chemistry and Physics 14, 11093–11116. https://doi.org/10.5194/acp-14-11093-2014.

Di Biagio, C., Formenti, P., Balkanski, Y., Caponi, L., Cazaunau, M., Pangui, E., Journet, E., Nowak, S., Andreae, M.O., Kandler, K., Saeed, T., Piketh, S., Seibert, D., Williams, E., Doussin, J.-F., 2019. Complex refractive indices and single-scattering albedo of global dust aerosols in the shortwave spectrum and relationship to size and iron content. Atmospheric Chemistry and Physics 19, 15503–15531. https://doi.org/10.5194/acp-19-15503-2019.

Di Biagio, C., Formenti, P., Balkanski, Y., Caponi, L., Cazaunau, M., Pangui, E., Journet, E., Nowak, S., Caquineau, S., Andreae, M.O., Kandler, K., Saeed, T., Piketh, S., Seibert, D., Williams, E., Doussin, J.-F., 2017. Global scale variability of the mineral dust long-wave refractive index: a new dataset of in situ measurements for climate modeling and remote sensing. Atmospheric Chemistry and Physics 17, 1901–1929. https://doi.org/10.5194/acp-17-1901-2017.

Di Mauro, B., Garzonio, R., Rossini, M., Filippa, G., Pogliotti, P., Galvagno, M., Morra di Cella, U., Migliavacca, M., Baccolo, G., Clemenza, M., Delmonte, B., Maggi, V., Dumont, M., Tuzet, F., Lafaysse, M., Morin, S., Cremonese, E., Colombo, R., 2019. Saharan dust events in the European Alps: role in snowmelt and geochemical characterization. The Cryosphere 13, 1147–1165. https://doi.org/10.5194/tc-13-1147-2019.

di Sarra, A., Di Biagio, C., Meloni, D., Monteleone, F., Pace, G., Pugnaghi, S., Sferlazzo, D., 2011. Shortwave and longwave radiative effects of the intense Saharan dust event of 25–26 March 2010 at Lampedusa (Mediterranean Sea). Journal of Geophysical Research. Atmospheres 116. https://doi.org/10.1029/2011JD016238.

Doherty, S.J., Saide, P.E., Zuidema, P., Shinozuka, Y., Ferrada, G.A., Gordon, H., Mallet, M., Meyer, K., Painemal, D., Howell, S.G., Freitag, S., Dobracki, A., Podolske, J.R., Burton, S.P., Ferrare, R.A., Howes, C., Nabat, P., Carmichael, G.R., da Silva, A., Pistone, K., Chang, I., Gao, L., Wood, R., Redemann, J., 2022. Modeled and observed properties related to the direct aerosol radiative effect of biomass burning aerosol over the southeastern Atlantic. Atmospheric Chemistry and Physics 22, 1–46. https://doi.org/10.5194/acp-22-1-2022.

Dubovik, O., Holben, B., Eck, T.F., Smirnov, A., Kaufman, Y.J., King, M.D., Tanré, D., Slutsker, I., Dubovik, O., Holben, B., Eck, T.F., Smirnov, A., Kaufman, Y.J., King, M.D., Tanré, D., Slutsker, I., Sciences, G.E., Directorate, E.S., 2002. Variability of absorption and optical properties of key aerosol types observed in worldwide locations. Journal of the Atmospheric Sciences 59, 590–608. https://doi.org/10.1175/1520-0469(2002)059<0590:VOAAOP>2.0.CO;2.

Dufresne, J.-L., Gautier, C., Ricchiazzi, P., Fouquart, Y., 2002. Longwave scattering effects of mineral aerosols. Journal of the Atmospheric Sciences 59, 1959–1966. https://doi.org/10.1175/1520-0469(2002)059<1959:LSEOMA>2.0.CO;2.

Fairlie, T.D., Jacob, D.J., Dibb, J.E., Alexander, B., Avery, M.A., van Donkelaar, A., Zhang, L., 2010. Impact of mineral dust on nitrate, sulfate, and ozone in transpacific Asian pollution plumes. Atmospheric Chemistry and Physics 10, 3999–4012. https://doi.org/10.5194/acp-10-3999-2010.

Fioletov, V.E., McLinden, C.A., Krotkov, N., Li, C., Joiner, J., Theys, N., Carn, S., Moran, M.D., 2016. A global catalogue of large SO_2 sources and emissions derived from the Ozone Monitoring Instrument. Atmospheric Chemistry and Physics 16, 11497–11519. https://doi.org/10.5194/acp-16-11497-2016.

Fitzgerald, J.W., 1991. Marine aerosols: a review. Atmospheric Environment. Part A, General Topics 25, 533–545. https://doi.org/10.1016/0960-1686(91)90050-H.

Formenti, P., Andreae, M.O., Lange, L., Roberts, G., Cafmeyer, J., Rajta, I., Maenhaut, W., Holben, B.N., Artaxo, P., Lelieveld, J., 2001. Saharan dust in Brazil and Suriname during the Large-Scale Biosphere-Atmosphere Experiment in Amazonia (LBA) – Cooperative LBA Regional Experiment (CLAIRE) in March 1998. Journal of Geophysical Research. Atmospheres 106, 14919–14934. https://doi.org/10.1029/2000JD900827.

Formenti, P., Caquineau, S., Chevaillier, S., Klaver, A., Desboeufs, K., Rajot, J.L., Belin, S., Briois, V., 2014a. Dominance of goethite over hematite in iron oxides of mineral dust from Western Africa: quantitative partitioning by X-ray absorption spectroscopy. Journal of Geophysical Research. Atmospheres 119, 12,740–12,754. https://doi.org/10.1002/2014JD021668.

Formenti, P., Caquineau, S., Desboeufs, K., Klaver, A., Chevaillier, S., Journet, E., Rajot, J.L., 2014b. Mapping the physico-chemical properties of mineral dust in western Africa: mineralogical composition. Atmospheric Chemistry and Physics 14, 10663–10686. https://doi.org/10.5194/acp-14-10663-2014.

Formenti, P., Di Biagio, C., 2024. Large synthesis of in situ field measurements of the size distribution of mineral dust aerosols across their lifecycle. Earth System Science Data Discussions 1 (16). https://doi.org/10.5194/essd-2023-481.

Formenti, P., Rajot, J.L., Desboeufs, K., Saïd, F., Grand, N., Chevaillier, S., Schmechtig, C., 2011a. Airborne observations of mineral dust over western Africa in the summer Monsoon season: spatial and vertical variability of physico-chemical and optical properties. Atmospheric Chemistry and Physics 11, 6387–6410. https://doi.org/10.5194/acp-11-6387-2011.

Formenti, P., Schütz, L., Balkanski, Y., Desboeufs, K., Ebert, M., Kandler, K., Petzold, A., Scheuvens, D., Weinbruch, S., Zhang, D., 2011b. Recent progress in understanding physical and chemical properties of African and Asian mineral dust. Atmospheric Chemistry and Physics 11, 8231–8256. https://doi.org/10.5194/acp-11-8231-2011.

Forster, P., Ramaswamy, V., Artaxo, P., Berntsen, T., Betts, R., Fahey, D.W., Haywood, J., Lean, J., Lowe, D.C., Myhre, G., Nganga, J., Prinn, R., Raga, G., Schulz, M., Van Dorland, R., 2007. Changes in atmospheric constituents and in radiative forcing. Chapter 2.

Fuentes, E., Coe, H., Green, D., de Leeuw, G., McFiggans, G., 2010. Laboratory-generated primary marine aerosol via bubble-bursting and atomization. Atmospheric Measurement Techniques 3, 141–162. https://doi.org/10.5194/amt-3-141-2010.

Gantt, B., Meskhidze, N., 2013. The physical and chemical characteristics of marine primary organic aerosol: a review. Atmospheric Chemistry and Physics 13, 3979–3996. https://doi.org/10.5194/acp-13-3979-2013.

Garratt, J.R., 1977. Review of drag coefficients over oceans and continents. Monthly Weather Review 105, 915–929. https://doi.org/10.1175/1520-0493(1977)105<0915:RODCOO>2.0.CO;2.

Gili, S., Vanderstraeten, A., Chaput, A., King, J., Gaiero, D.M., Delmonte, B., Vallelonga, P., Formenti, P., Di Biagio, C., Cazanau, M., Pangui, E., Doussin, J.-F., Mattielli, N., 2022. South African dust contribution to the high southern latitudes and East Antarctica during interglacial stages. Communications Earth & Environment 3, 1–12. https://doi.org/10.1038/s43247-022-00464-z.

Gill, T.E., 1996. Eolian sediments generated by anthropogenic disturbance of playas: human impacts on the geomorphic system and geomorphic impacts on the human system. Geomorphology, Response of Aeolian Processes to Global Change 17, 207–228. https://doi.org/10.1016/0169-555X(95)00104-D.

Ginoux, P., Prospero, J.M., Gill, T.E., Hsu, N.C., Zhao, M., 2012. Global-scale attribution of anthropogenic and natural dust sources and their emission rates based on MODIS Deep Blue aerosol products. Reviews of Geophysics 50. https://doi.org/10.1029/2012RG000388.

Gong, S.L., 2003. A parameterization of sea-salt aerosol source function for sub- and super-micron particles. Global Biogeochemical Cycles 17. https://doi.org/10.1029/2003GB002079.

Goudie, A.S., Middleton, N.J., 2001. Saharan dust storms: nature and consequences. Earth-Science Reviews 56, 179–204. https://doi.org/10.1016/S0012-8252(01)00067-8.

Grythe, H., Ström, J., Krejci, R., Quinn, P., Stohl, A., 2014. A review of sea-spray aerosol source functions using a large global set of sea salt aerosol concentration measurements. Atmospheric Chemistry and Physics 14, 1277–1297. https://doi.org/10.5194/acp-14-1277-2014.

Gwaze, P., Helas, G., Annegarn, H.J., Huth, J., Piketh, S.J., 2007. Physical, chemical and optical properties of aerosol particles collected over Cape Town during winter haze episodes. South African Journal of Science 103, 35–43.

Han, C., Do Hur, S., Han, Y., Lee, K., Hong, S., Erhardt, T., Fischer, H., Svensson, A.M., Steffensen, J.P., Vallelonga, P., 2018. High-resolution isotopic evidence for a potential Saharan provenance of Greenland glacial dust. Scientific Reports 8, 15582. https://doi.org/10.1038/s41598-018-33859-0.

Hansen, J.E., Travis, L.D., 1974. Light scattering in planetary atmospheres. Space Science Reviews 16, 527–610.

Hao, W.M., Liu, M.-H., 1994. Spatial and temporal distribution of tropical biomass burning. Global Biogeochemical Cycles 8, 495–503. https://doi.org/10.1029/94GB02086.

Haywood, J., Francis, P., Osborne, S., Glew, M., Loeb, N., Highwood, E.J., Tanré, D., Myhre, G., Formenti, P., Hirst, E., 2003. Radiative properties and direct effect of Saharan dust measured by the C-130 aircraft during Saharan Dust Experiment (SHADE): 2. Terrestrial spectrum. Journal of Geophysical Research 108, 8578. https://doi.org/10.1029/2002JD002552.

Haywood, J.M., Pelon, J., Formenti, P., Bharmal, N., Brooks, M., Capes, G., Chazette, P., Chou, C., Christopher, S., Coe, H., Cuesta, J., Derimian, Y., Desboeufs, K., Greed, G., Harrison, M., Heese, B., Highwood, E.J., Johnson, B., Mallet, M., Marticorena, B., Marsham, J., Milton, S., Myhre, G., Osborne, S.R., Parker, D.J., Rajot, J.-L., Schulz, M., Slingo, A., Tanré, D., Tulet, P., 2008. Overview of the dust and biomass-burning experiment and African monsoon multidisciplinary analysis special observing period-0. Journal of Geophysical Research. Atmospheres 113. https://doi.org/10.1029/2008JD010077.

Herbert, R.J., Bellouin, N., Highwood, E.J., Hill, A.A., 2020. Diurnal cycle of the semi-direct effect from a persistent absorbing aerosol layer over marine stratocumulus in large-eddy simulations. Atmospheric Chemistry and Physics 20, 1317–1340. https://doi.org/10.5194/acp-20-1317-2020.

Hodshire, A.L., Campuzano-Jost, P., Kodros, J.K., Croft, B., Nault, B.A., Schroder, J.C., Jimenez, J.L., Pierce, J.R., 2019. The potential role of methanesulfonic acid (MSA) in aerosol formation and growth and the associated radiative forcings. Atmospheric Chemistry and Physics 19, 3137–3160. https://doi.org/10.5194/acp-19-3137-2019.

Holanda, B.A., Franco, M.A., Walter, D., Artaxo, P., Carbone, S., Cheng, Y., Chowdhury, S., Ditas, F., Gysel-Beer, M., Klimach, T., Kremper, L.A., Krüger, O.O., Lavric, J.V., Lelieveld, J., Ma, C., Machado, L.A.T., Modini, R.L., Morais, F.G., Pozzer, A., Saturno, J., Su, H., Wendisch, M., Wolff, S., Pöhlker, M.L., Andreae, M.O., Pöschl, U., Pöhlker, C., 2023. African biomass burning affects aerosol cycling over the Amazon. Communications Earth & Environment 4, 1–15. https://doi.org/10.1038/s43247-023-00795-5.

Holdt, J.R. von, Eckardt, F.D., 2018. Dust activity and surface sediment characteristics of the dustiest river in southern Africa: the Kuiseb River, Central Namib. South African Geographical Journal.

Hoose, C., Kristjánsson, J.E., Iversen, T., Kirkevåg, A., Seland, Ø., Gettelman, A., 2009. Constraining cloud droplet number concentration in GCMs suppresses the aerosol indirect effect. Geophysical Research Letters 36. https://doi.org/10.1029/2009GL038568.

Hsu, N.C., Gautam, R., Sayer, A.M., Bettenhausen, C., Li, C., Jeong, M.J., Tsay, S.-C., Holben, B.N., 2012. Global and regional trends of aerosol optical depth over land and ocean using SeaWiFS measurements from 1997 to 2010. Atmospheric Chemistry and Physics 12, 8037–8053. https://doi.org/10.5194/acp-12-8037-2012.

Huang, Y., Kok, J.F., Kandler, K., Lindqvist, H., Nousiainen, T., Sakai, T., Adebiyi, A., Jokinen, O., 2020. Climate models and remote sensing retrievals neglect substantial desert dust asphericity. Geophysical Research Letters 47. https://doi.org/10.1029/2019GL086592.

Huneeus, N., Schulz, M., Balkanski, Y., Griesfeller, J., Prospero, J., Kinne, S., Bauer, S., Boucher, O., Chin, M., Dentener, F., Diehl, T., Easter, R., Fillmore, D., Ghan, S., Ginoux, P., Grini, a., Horowitz, L., Koch, D., Krol, M.C., Landing, W., Liu, X., Mahowald, N., Miller, R., Morcrette, J.J., Myhre, G., Penner, J., Perlwitz, J., Stier, P., Takemura, T., Zender, C.S., 2011. Global dust model intercomparison in AeroCom phase i. Atmospheric Chemistry and Physics 11, 7781–7816. https://doi.org/10.5194/acp-11-7781-2011.

Inness, A., Ades, M., Agustí-Panareda, A., Barré, J., Benedictow, A., Blechschmidt, A.-M., Dominguez, J.J., Engelen, R., Eskes, H., Flemming, J., Huijnen, V., Jones, L., Kipling, Z., Massart, S., Parrington, M., Peuch, V.-H., Razinger, M., Remy, S., Schulz, M., Suttie, M., 2019. The CAMS reanalysis of atmospheric composition. Atmospheric Chemistry and Physics 19, 3515–3556. https://doi.org/10.5194/acp-19-3515-2019.

IPCC, 2023. AR6 Synthesis Report: Climate Change 2023 — IPCC.

Ito, A., Kok, J.F., 2017. Do dust emissions from sparsely vegetated regions dominate atmospheric iron supply to the Southern Ocean? Journal of Geophysical Research. Atmospheres 122, 3987–4002. https://doi.org/10.1002/2016JD025939.

Ito, A., Miyazaki, Y., Taketani, F., Iwamoto, Y., Kanaya, Y., 2023. Marine aerosol feedback on biogeochemical cycles and the climate in the Anthropocene: lessons learned from the Pacific Ocean. Environmental Science: Atmospheres 3, 782–798. https://doi.org/10.1039/D2EA00156J.

Jaeglé, L., Quinn, P.K., Bates, T.S., Alexander, B., Lin, J.-T., 2011. Global distribution of sea salt aerosols: new constraints from in situ and remote sensing observations. Atmospheric Chemistry and Physics 11, 3137–3157. https://doi.org/10.5194/acp-11-3137-2011.

Janicot, S., Thorncroft, C.D., Ali, A., Asencio, N., Berry, G., Bock, O., Bourles, B., Caniaux, G., Chauvin, F., Deme, A., Kergoat, L., Lafore, J.-P., Lavaysse, C., Lebel, T., Marticorena, B., Mounier, F., Nedelec, P., Redelsperger, J.-L., Ravegnani, F., Reeves, C.E., Roca, R., de Rosnay, P., Schlager, H., Sultan, B., Tomasini, M., Ulanovsky, A., ACMAD forecasters team, 2008. Large-scale overview of the summer monsoon over West Africa during the AMMA field experiment in 2006. Annales Geophysicae 26, 2569–2595. https://doi.org/10.5194/angeo-26-2569-2008.

Jardine, K., Yañez-Serrano, A.M., Williams, J., Kunert, N., Jardine, A., Taylor, T., Abrell, L., Artaxo, P., Guenther, A., Hewitt, C.N., House, E., Florentino, A.P., Manzi, A., Higuchi, N., Kesselmeier, J., Behrendt, T., Veres, P.R., Derstroff, B., Fuentes, J.D., Martin, S.T., Andreae, M.O., 2015. Dimethyl sulfide in the Amazon rain forest. Global Biogeochemical Cycles 29, 19–32. https://doi.org/10.1002/2014GB004969.

Jeong, G.Y., 2008. Bulk and single-particle mineralogy of Asian dust and a comparison with its source soils. Journal of Geophysical Research. Atmospheres 113. https://doi.org/10.1029/2007JD008606.

Jickells, T.D., An, Z.S., Andersen, K.K., Baker, A.R., Bergametti, C., Brooks, N., Cao, J.J., Boyd, P.W., Duce, R.A., Hunter, K.A., Kawahata, H., Kubilay, N., LaRoche, J., Liss, P.S., Mahowald, N., Prospero, J.M., Ridgwell, A.J., Tegen, I., Torres, R., 2005. Global iron connections between desert dust, ocean biogeochemistry, and climate. Science 308, 67–71. https://doi.org/10.1126/science.1105959.

Johnson, B.T., Osborne, S.R., Haywood, J.M., Harrison, M.A.J.J., 2008. Aircraft measurements of biomass burning aerosol over West Africa during DABEX. Journal of Geophysical Research. Atmospheres 113, 1–15. https://doi.org/10.1029/2007JD009451.

Johnson, B.T., Shine, K.P., Forster, P.M., 2004. The semi-direct aerosol effect: impact of absorbing aerosols on marine stratocumulus. Quarterly Journal of the Royal Meteorological Society 130, 1407–1422. https://doi.org/10.1256/qj.03.61.

Johnson, M.S., Meskhidze, N., 2013. Atmospheric dissolved iron deposition to the global oceans: effects of oxalate-promoted Fe dissolution, photochemical redox cycling, and dust mineralogy. Geoscientific Model Development 6, 1137–1155. https://doi.org/10.5194/gmd-6-1137-2013.

Journet, E., Balkanski, Y., Harrison, S.P., 2014. A new data set of soil mineralogy for dust-cycle modeling. Atmospheric Chemistry and Physics 14, 3801–3816. https://doi.org/10.5194/acp-14-3801-2014.

Journet, E., Desboeufs, K.V., Caquineau, S., Colin, J.-L., 2008. Mineralogy as a critical factor of dust iron solubility. Geophysical Research Letters 35. https://doi.org/10.1029/2007GL031589.

Kacenelenbogen, M.S., Vaughan, M.A., Redemann, J., Young, S.A., Liu, Z., Hu, Y., Omar, A.H., LeBlanc, S., Shinozuka, Y., Livingston, J., Zhang, Q., Powell, K.A., 2019. Estimations of global shortwave direct aerosol radiative effects above opaque water clouds using a combination of A-Train satellite sensors. Atmospheric Chemistry and Physics 19, 4933–4962. https://doi.org/10.5194/acp-19-4933-2019.

Kandler, K., Benker, N., Bundke, U., Cuevas, E., Ebert, M., Knippertz, P., Rodríguez, S., Schütz, L., Weinbruch, S., 2007. Chemical composition and complex refractive index of Saharan Mineral Dust at Izaña, Tenerife (Spain) derived by electron microscopy. Atmospheric Environment 41, 8058–8074. https://doi.org/10.1016/J.ATMOSENV.2007.06.047.

Kandler, K., Lieke, K., Benker, N., Emmel, C., Küpper, M., Müller-Ebert, D., Ebert, M., Scheuvens, D., Schladitz, A., Schütz, L., Weinbruch, S., 2011. Electron microscopy of particles collected at Praia, Cape Verde, during the Saharan Mineral Dust Experiment: particle chemistry, shape, mixing state and complex refractive index. Tellus. Series B, Chemical and Physical Meteorology 63, 475–496. https://doi.org/10.1111/j.1600-0889.2011.00550.x.

Kandler, K., Schütz, L., Deutscher, C., Ebert, M., Hofmann, H., Jäckel, S., Jaenicke, R., Knippertz, P., Lieke, K., Massling, A., Petzold, A., Schladitz, A., Weinzierl, B., Wiedensohler, A., Zorn, S., Weinbruch, S., 2009. Size distribution, mass concentration, chemical and mineralogical composition and derived optical parameters of the boundary layer aerosol at Tinfou, Morocco, during SAMUM 2006. Tellus. Series B, Chemical and Physical Meteorology 61, 32–50. https://doi.org/10.1111/j.1600-0889.2008.00385.x.

Khoder, M.I., 2002. Atmospheric conversion of sulfur dioxide to particulate sulfate and nitrogen dioxide to particulate nitrate and gaseous nitric acid in an urban area. Chemosphere 49, 675–684. https://doi.org/10.1016/S0045-6535(02)00391-0.

Kirchstetter, T.W., Novakov, T., Hobbs, P.V., 2004. Evidence that the spectral dependence of light absorption by aerosols is affected by organic carbon. Journal of Geophysical Research. Atmospheres 109. https://doi.org/10.1029/2004JD004999.

Kirchstetter, T.W., Novakov, T., Hobbs, P.V., Magi, B., 2003. Airborne measurements of carbonaceous aerosols in southern Africa during the dry biomass burning season. Journal of Geophysical Research. Atmospheres 108. https://doi.org/10.1029/2002JD002171.

Knippertz, P., 2014. Meteorological aspects of dust storms. In: Knippertz, P., Stuut, J.-B.W. (Eds.), Mineral Dust: A Key Player in the Earth System. Springer, Netherlands, Dordrecht, pp. 121–147.

Knippertz, P., Stuut, J.-B.W. (Eds.), 2014. Mineral Dust: A Key Player in the Earth System. Springer, Netherlands, Dordrecht.

Knippertz, P., Todd, M.C., 2012. Mineral dust aerosols over the Sahara: meteorological controls on emission and transport and implications for modeling. Reviews of Geophysics 50, RG1007. https://doi.org/10.1029/2011RG000362.

Köhler, H., 1936. The nucleus in and the growth of hygroscopic droplets. Transactions of the Faraday Society 32, 1152–1161. https://doi.org/10.1039/TF9363201152.

Kok, J.F., Adebiyi, A.A., Albani, S., Balkanski, Y., Checa-Garcia, R., Chin, M., Colarco, P.R., Hamilton, D.S., Huang, Y., Ito, A., Klose, M., Li, L., Mahowald, N.M., Miller, R.L., Obiso, V., Pérez García-Pando, C., Rocha-Lima, A., Wan, J.S., 2021. Contribution of the world's main dust source regions to the global cycle of desert dust. Atmospheric Chemistry and Physics 21, 8169–8193. https://doi.org/10.5194/acp-21-8169-2021.

Kok, J.F., Ridley, D.A., Zhou, Q., Miller, R.L., Zhao, C., Heald, C.L., Ward, D.S., Albani, S., Haustein, K., 2017. Smaller desert dust cooling effect estimated from analysis of dust size and abundance. Nature Geoscience 10, 274–278. https://doi.org/10.1038/ngeo2912.

Kok, J.F., Storelvmo, T., Karydis, V.A., Adebiyi, A.A., Mahowald, N.M., Evan, A.T., He, C., Leung, D.M., 2023. Mineral dust aerosol impacts on global climate and climate change. Nature Reviews Earth & Environment 1 (16). https://doi.org/10.1038/s43017-022-00379-5.

Koop, T., Luo, B., Tsias, A., Peter, T., 2000. Water activity as the determinant for homogeneous ice nucleation in aqueous solutions. Nature 406, 611–614. https://doi.org/10.1038/35020537.

Lafon, S., Rajot, J.L., Alfaro, S.C., Gaudichet, A., 2004. Quantification of iron oxides in desert aerosol. Atmospheric Environment 38, 1211–1218. https://doi.org/10.1016/j.atmosenv.2003.11.006.

Laskin, A., Iedema, M.J., Ichkovich, A., Graber, E.R., Taraniuk, I., Rudich, Y., 2005. Direct observation of completely processed calcium carbonate dust particles. Faraday Discussions 130, 453–468. https://doi.org/10.1039/B417366J.

Lebel, T., Parker, D.J., Flamant, C., Höller, H., Polcher, J., Redelsperger, J.-L., Thorncroft, C., Bock, O., Bourles, B., Galle, S., Marticorena, B., Mougin, E., Peugeot, C., Cappelaere, B., Descroix, L., Diedhiou, A., Gaye, A., Lafore, J.-P., 2011. The AMMA field campaigns: accomplishments and lessons learned. Atmospheric Science Letters 12, 123–128. https://doi.org/10.1002/asl.323.

Lewis, E.R., Schwartz, S.E., 2004. Sea Salt Aerosol Production: Mechanisms, Methods, Measurements, and Models. American Geophysical Union.

Li, J., Carlson, B.E., Yung, Y.L., Lv, D., Hansen, J., Penner, J.E., Liao, H., Ramaswamy, V., Kahn, R.A., Zhang, P., Dubovik, O., Ding, A., Lacis, A.A., Zhang, L., Dong, Y., 2022. Scattering and absorbing aerosols in the climate system. Nature Reviews Earth & Environment 3, 363–379. https://doi.org/10.1038/s43017-022-00296-7.

Liu, C., Chu, B., Liu, Y., Ma, Q., Ma, J., He, H., Li, J., Hao, J., 2013. Effect of mineral dust on secondary organic aerosol yield and aerosol size in α-pinene/NOx photo-oxidation. Atmospheric Environment 77, 781–789. https://doi.org/10.1016/j.atmosenv.2013.05.064.

Liu, S., Aiken, A.C., Arata, C., Dubey, M.K., Stockwell, C.E., Yokelson, R.J., Stone, E.A., Jayarathne, T., Robinson, A.L., DeMott, P.J., Kreidenweis, S.M., 2014. Aerosol single scattering albedo dependence on biomass combustion efficiency: laboratory and field studies. Geophysical Research Letters 41, 742–748. https://doi.org/10.1002/2013GL058392.

Lv, G., Zhang, C., Sun, X., 2019. Understanding the oxidation mechanism of methanesulfinic acid by ozone in the atmosphere. Scientific Reports 9, 322. https://doi.org/10.1038/s41598-018-36405-0.

Mallet, M., Solmon, F., Nabat, P., Elguindi, N., Waquet, F., Bouniol, D., Sayer, A.M., Meyer, K., Roehrig, R., Michou, M., Zuidema, P., Flamant, C., Redemann, J., Formenti, P., 2020. Direct and semi-direct radiative forcing of biomass-burning aerosols over the southeast Atlantic (SEA) and its sensitivity to absorbing properties: a regional climate modeling study. Atmospheric Chemistry and Physics 20, 13191–13216. https://doi.org/10.5194/acp-20-13191-2020.

Maring, H., Savoie, D.L., Izaguirre, M.A., Custals, L., Reid, J.S., 2003. Mineral dust aerosol size distribution change during atmospheric transport. Journal of Geophysical Research 108, 8592. https://doi.org/10.1029/2002JD002536.

Mårtensson, E.M., Nilsson, E.D., de Leeuw, G., Cohen, L.H., Hansson, H.-C., 2003. Laboratory simulations and parameterization of the primary marine aerosol production. Journal of Geophysical Research. Atmospheres 108. https://doi.org/10.1029/2002JD002263.

Marticorena, B., Bergametti, G., 1995. Modeling the atmospheric dust cycle: 1. Design of a soil-derived dust emission scheme. Journal of Geophysical Research 100, 16415. https://doi.org/10.1029/95JD00690.

Matsuki, A., Quennehen, B., Schwarzenboeck, A., Crumeyrolle, S., Venzac, H., Laj, P., Gomes, L., 2010. Temporal and vertical variations of aerosol physical and chemical properties over West Africa: AMMA aircraft campaign in summer 2006. Atmospheric Chemistry and Physics 10, 8437–8451. https://doi.org/10.5194/acp-10-8437-2010.

Mayaux, P., Pekel, J.-F., Desclée, B., Donnay, F., Lupi, A., Achard, F., Clerici, M., Bodart, C., Brink, A., Nasi, R., Belward, A., 2013. State and evolution of the African rainforests between 1990 and 2010. Philosophical Transactions of the Royal Society B: Biological Sciences 368, 20120300. https://doi.org/10.1098/rstb.2012.0300.

McConnell, C.L., Highwood, E.J., Coe, H., Formenti, P., Anderson, B., Osborne, S., Nava, S., Desboeufs, K., Chen, G., Harrison, M.A.J., 2008. Seasonal variations of the physical and optical characteristics of Saharan dust: results from the Dust Outflow and Deposition to the Ocean (DODO) experiment. Journal of Geophysical Research 113, 14S05. https://doi.org/10.1029/2007JD009606.

McCormick, R.A., Ludwig, J.H., 1967. Climate modification by atmospheric aerosols. Science 156, 1358–1359. https://doi.org/10.1126/science.156.3780.1358.

McLinden, C.A., Fioletov, V., Shephard, M.W., Krotkov, N., Li, C., Martin, R.V., Moran, M.D., Joiner, J., 2016. Space-based detection of missing sulfur dioxide sources of global air pollution. Nature Geoscience 9, 496–500. https://doi.org/10.1038/ngeo2724.

Middleton, N.J., Goudie, A.S., 2001. Saharan dust: sources and trajectories. Transactions of the Institute of British Geographers 26, 165–181. https://doi.org/10.1111/1475-5661.00013.

Miller, R.L., Tegen, I., Perlwitz, J., 2004. Surface radiative forcing by soil dust aerosols and the hydrologic cycle. Journal of Geophysical Research. Atmospheres 109. https://doi.org/10.1029/2003jd004085.

Ming, Y., Russell, L.M., 2001. Predicted hygroscopic growth of sea salt aerosol. Journal of Geophysical Research. Atmospheres 106, 28259–28274. https://doi.org/10.1029/2001JD000454.

Mona, L., Amiridis, V., Cuevas, E., Gkikas, A., Trippetta, S., Vandenbussche, S., Benedetti, A., Dagsson-Waldhauserova, P., Formenti, P., Haefele, A., Kazadzis, S., Knippertz, P., Laurent, B., Madonna, F., Nickovic, S., Papagiannopoulos, N., Pappalardo, G., García-Pando, C.P., Popp, T., Rodríguez, S., Sealy, A., Sugimoto, N., Terradellas, E., Vimic, A.V., Weinzierl, B., Basart, S., 2023. Observing mineral dust in northern Africa, the Middle East, and Europe: current capabilities and challenges ahead for the development of dust services. Bulletin of the American Meteorological Society 104, E2223–E2264. https://doi.org/10.1175/BAMS-D-23-0005.1.

Monahan, E.C., Muircheartaigh, I., 1980. Optimal power-law description of oceanic whitecap coverage dependence on wind speed. Journal of Physical Oceanography 10, 2094–2099. https://doi.org/10.1175/1520-0485(1980)010<2094:OPLDOO>2.0.CO;2.

Moosmüller, H., Engelbrecht, J.P., Skiba, M., Frey, G., Chakrabarty, R.K., Arnott, W.P., 2012. Single scattering albedo of fine mineral dust aerosols controlled by iron concentration. Journal of Geophysical Research. Atmospheres 117. https://doi.org/10.1029/2011JD016909.

Moulin, C., Chiapello, I., 2006. Impact of human-induced desertification on the intensification of Sahel dust emission and export over the last decades. Geophysical Research Letters 33. https://doi.org/10.1029/2006GL025923.

Müller, K., Lehmann, S., van Pinxteren, D., Gnauk, T., Niedermeier, N., Wiedensohler, A., Herrmann, H., 2010. Particle characterization at the Cape Verde atmospheric observatory during the 2007 RHaMBLe intensive. Atmospheric Chemistry and Physics 10, 2709–2721. https://doi.org/10.5194/acp-10-2709-2010.

Myhre, G., Bellouin, N., Berglen, T.F., Berntsen, T.K., Boucher, O., Grini, A., Ivar, S.A.M., Johnsrud, I., Michael, I.M., Stordal, F., Tanrée, D., 2007. Comparison of the radiative properties and direct radiative effect of aerosols from a global aerosol model and remote sensing data over ocean. Tellus. Series B, Chemical and Physical Meteorology 59, 115–129. https://doi.org/10.1111/j.1600-0889.2006.00238.x.

Myriokefalitakis, S., Vignati, E., Tsigaridis, K., Papadimas, C., Sciare, J., Mihalopoulos, N., Facchini, M.C., Rinaldi, M., Dentener, F.J., Ceburnis, D., Hatzianastasiou, N., O'Dowd, C.D., van Weele, M., Kanakidou, M., 2010. Global modeling of the oceanic source of organic aerosols. Advances in Meteorology 2010, e939171. https://doi.org/10.1155/2010/939171.

Nabat, P., Somot, S., Mallet, M., Michou, M., Sevault, F., Driouech, F., Meloni, D., di Sarra, A., Di Biagio, C., Formenti, P., Sicard, M., Léon, J.-F., Bouin, M.-N., 2015. Dust aerosol radiative effects during summer 2012 simulated with a coupled regional aerosol–atmosphere–ocean model over the Mediterranean. Atmospheric Chemistry and Physics 15, 3303–3326. https://doi.org/10.5194/acp-15-3303-2015.

O'Dowd, C.D., de Leeuw, G., 2007. Marine aerosol production: a review of the current knowledge. Philosophical Transactions of the Royal Society A: Mathematical, Physical and Engineering Sciences 365, 1753–1774. https://doi.org/10.1098/rsta.2007.2043.

O'Dowd, C.D., Facchini, M.C., Cavalli, F., Ceburnis, D., Mircea, M., Decesari, S., Fuzzi, S., Yoon, Y.J., Putaud, J.-P., 2004. Biogenically driven organic contribution to marine aerosol. Nature 431, 676–680. https://doi.org/10.1038/nature02959.

O'Dowd, C.D., Smith, M.H., Consterdine, I.E., Lowe, J.A., 1997. Marine aerosol, sea-salt, and the marine sulphur cycle: a short review. Atmospheric Environment 31, 73–80. https://doi.org/10.1016/S1352-2310(96)00106-9.

Oikawa, E., Nakajima, T., Winker, D., 2018. An evaluation of the shortwave direct aerosol radiative forcing using CALIOP and MODIS observations. Journal of Geophysical Research. Atmospheres 123, 1211–1233. https://doi.org/10.1002/2017JD027247.

Ovadnevaite, J., Ceburnis, D., Martucci, G., Bialek, J., Monahan, C., Rinaldi, M., Facchini, M.C., Berresheim, H., Worsnop, D.R., O'Dowd, C., 2011. Primary marine organic aerosol: a dichotomy of low hygroscopicity and high CCN activity. Geophysical Research Letters 38. https://doi.org/10.1029/2011GL048869.

Pace, G., di Sarra, A., Meloni, D., Piacentino, S., Chamard, P., 2006. Aerosol optical properties at Lampedusa (Central Mediterranean). 1. Influence of transport and identification of different aerosol types. Atmospheric Chemistry and Physics 6, 697–713. https://doi.org/10.5194/acp-6-697-2006.

Paris, R., Desboeufs, K.V., Formenti, P., Nava, S., Chou, C., 2010. Chemical characterisation of iron in dust and biomass burning aerosols during AMMA-SOP0/DABEX: implication for iron solubility. Atmospheric Chemistry and Physics 10, 4273–4282. https://doi.org/10.5194/acp-10-4273-2010.

Penner, J.E., et al., 2001. Aerosols, their direct and indirect effects. In: Houghton, J.T., et al. (Eds.), Climate Change 2001: The Scientific Basis. Cambridge Univ. Press, New York, pp. 289–348.

Penner, J.E., Chuang, C.C., Grant, K., 1998. Climate forcing by carbonaceous and sulfate aerosols. Climate Dynamics 14, 839–851. https://doi.org/10.1007/s003820050259.

Petit, J.R., Jouzel, J., Raynaud, D., Barkov, N.I., Barnola, J.-M., Basile, I., Bender, M., Chappellaz, J., Davis, M., Delaygue, G., Delmotte, M., Kotlyakov, V.M., Legrand, M., Lipenkov, V.Y., Lorius, C., PÉpin, L., Ritz, C., Saltzman, E., Stievenard, M., 1999. Climate and atmospheric history of the past 420,000 years from the Vostok ice core, Antarctica. Nature 399, 429–436. https://doi.org/10.1038/20859.

Petzold, A., Ogren, J.A., Fiebig, M., Laj, P., Li, S.-M., Baltensperger, U., Holzer-Popp, T., Kinne, S., Pappalardo, G., Sugimoto, N., Wehrli, C., Wiedensohler, A., Zhang, X.-Y., 2013. Recommendations for reporting "black carbon" measurements. Atmospheric Chemistry and Physics 13, 8365–8379. https://doi.org/10.5194/acp-13-8365-2013.

Petzold, A., Rasp, K., Weinzierl, B., Esselborn, M., Hamburger, T., Dörnbrack, A., Kandler, K., Schuütz, L., Knippertz, P., Fiebig, M., Virkkula, A., 2009. Saharan dust absorption and refractive index from aircraft-based observations during SAMUM 2006. Tellus. Series B, Chemical and Physical Meteorology 61, 118–130. https://doi.org/10.1111/j.1600-0889.2008.00383.x.

Pilinis, C., Li, X., 1998. Particle shape and internal inhomogeneity effects on the optical properties of tropospheric aerosols of relevance to climate forcing. Journal of Geophysical Research. Atmospheres 103, 3789–3800. https://doi.org/10.1029/97JD02792.

Pósfai, M., Simonics, R., Li, J., Hobbs, P.V., Buseck, P.R., 2003. Individual aerosol particles from biomass burning in southern Africa: 1. Compositions and size distributions of carbonaceous particles. Journal of Geophysical Research. Atmospheres 108. https://doi.org/10.1029/2002JD002291.

Prisle, N.L., Raatikainen, T., Laaksonen, A., Bilde, M., 2010. Surfactants in cloud droplet activation: mixed organic-inorganic particles. Atmospheric Chemistry and Physics 10, 5663–5683. https://doi.org/10.5194/acp-10-5663-2010.

Prospero, J.M., Charlson, R.J., Mohnen, V., Jaenicke, R., Delany, A.C., Moyers, J., Zoller, W., Rahn, K., 1983. The atmospheric aerosol system: an overview. Reviews of Geophysics 21, 1607–1629. https://doi.org/10.1029/RG021i007p01607.

Prospero, J.M., Collard, F.-X., Molinié, J., Jeannot, A., 2014. Characterizing the annual cycle of African dust transport to the Caribbean Basin and South America and its impact on the environment and air quality. Global Biogeochemical Cycles 28, 757–773. https://doi.org/10.1002/2013GB004802.

Prospero, J.M., Ginoux, P., Torres, O., Nicholson, S.E., Gill, T.E., 2002. Environmental characterization of global sources of atmospheric soil dust identified with the Nimbus 7 Total Ozone Mapping Spectrometer (TOMS) absorbing aerosol product. Reviews of Geophysics 40, 2–1-2–31. https://doi.org/10.1029/2000RG000095.

Prospero, J.M., Lamb, P.J., 2003. African droughts and dust transport to the Caribbean: climate change implications. Science 302, 1024–1027. https://doi.org/10.1126/science.1089915.

Pye, K., 1987. Aeolian Dust and Dust Deposits. Elsevier. https://doi.org/10.1016/C2013-0-05007-4.

Rajot, J.L., Formenti, P., Alfaro, S., Desboeufs, K., Chevaillier, S., Chatenet, B., Gaudichet, A., Journet, E., Marticorena, B., Triquet, S., Maman, A., Mouget, N., Zakou, A., 2008. AMMA dust experiment: an overview of measurements performed during the dry season special observation period (SOP0) at the Banizoumbou (Niger) supersite. Journal of Geophysical Research. Atmospheres 113. https://doi.org/10.1029/2008JD009906@10.1002/(ISSN)2169-8996.DABEX1.

Randles, C.A., Russell, L.M., Ramaswamy, V., 2004. Hygroscopic and optical properties of organic sea salt aerosol and consequences for climate forcing. Geophysical Research Letters 31. https://doi.org/10.1029/2004GL020628.

Reeves, C.E., Formenti, P., Afif, C., Ancellet, G., Attié, J.-L., Bechara, J., Borbon, A., Cairo, F., Coe, H., Crumeyrolle, S., Fierli, F., Flamant, C., Gomes, L., Hamburger, T., Jambert, C., Law, K.S., Mari, C., Jones, R.L., Matsuki, A., Mead, M.I., Methven, J., Mills, G.P., Minikin, A., Murphy, J.G., Nielsen, J.K., Oram, D.E., Parker, D.J., Richter, A., Schlager, H., Schwarzenboeck, A., Thouret, V., 2010. Chemical and aerosol characterisation of the troposphere over West Africa during the monsoon period as part of AMMA. Atmospheric Chemistry and Physics 10, 7575–7601. https://doi.org/10.5194/acp-10-7575-2010.

Reid, E.A., Reid, J.S., Meier, M.M., Dunlap, M.R., Cliff, S.S., Broumas, A., Perry, K., Maring, H., 2003. Characterization of African dust transported to Puerto Rico by individual particle and size segregated bulk analysis. Journal of Geophysical Research 108, 8591. https://doi.org/10.1029/2002JD002935.

Reid, J.S., Eck, T.F., Christopher, S.A., Koppmann, R., Dubovik, O., Eleuterio, D.P., Holben, B.N., Reid, E.A., Zhang, J., 2005. A review of biomass burning emissions part III: intensive optical properties of biomass burning particles. Atmospheric Chemistry and Physics 5, 827–849. https://doi.org/10.5194/acp-5-827-2005.

Reid, J.S., Jonsson, H.H., Smith, M.H., Smirnov, A., 2001. Evolution of the vertical profile and flux of large sea-salt particles in a coastal zone. Journal of Geophysical Research. Atmospheres 106, 12039–12053. https://doi.org/10.1029/2000JD900848.

Renard, J.J., Calidonna, S.E., Henley, M.V., 2004. Fate of ammonia in the atmosphere—a review for applicability to hazardous releases. Journal of Hazardous Materials 108, 29–60. https://doi.org/10.1016/j.jhazmat.2004.01.015.

Rieger, D., Steiner, A., Bachmann, V., Gasch, P., Förstner, J., Deetz, K., Vogel, B., Vogel, H., 2017. Impact of the 4 April 2014 Saharan dust outbreak on the photovoltaic power generation in Germany. Atmospheric Chemistry and Physics 17, 13391–13415. https://doi.org/10.5194/acp-17-13391-2017.

Roberts, G., Wooster, M.J., Lagoudakis, E., 2009. Annual and diurnal African biomass burning temporal dynamics. Biogeosciences 6, 849–866. https://doi.org/10.5194/bg-6-849-2009.

Rocha-Lima, A., Martins, J.V., Remer, L.A., Todd, M., Marsham, J.H., Engelstaedter, S., Ryder, C.L., Cavazos-Guerra, C., Artaxo, P., Colarco, P., Washington, R., 2018. A detailed characterization of the Saharan dust collected during the Fennec campaign in 2011: in situ ground-based and laboratory measurements. Atmospheric Chemistry and Physics 18, 1023–1043. https://doi.org/10.5194/acp-18-1023-2018.

Rosenberg, P.D., Parker, D.J., Ryder, C.L., Marsham, J.H., Garcia-Carreras, L., Dorsey, J.R., Brooks, I.M., Dean, A.R., Crosier, J., McQuaid, J.B., Washington, R., 2014. Quantifying particle size and turbulent scale dependence of dust flux in the Sahara using aircraft measurements. Journal of Geophysical Research. Atmospheres 119, 7577–7598. https://doi.org/10.1002/2013JD021255.

Rosenfeld, D., Rudich, Y., Lahav, R., 2001. Desert dust suppressing precipitation: a possible desertification feedback loop. Proceedings of the National Academy of Sciences 98, 5975–5980. https://doi.org/10.1073/pnas.101122798.

Ryder, C.L., Highwood, E.J., Lai, T.M., Sodemann, H., Marsham, J.H., 2013a. Impact of atmospheric transport on the evolution of microphysical and optical properties of Saharan dust. Geophysical Research Letters 40, 2433–2438. https://doi.org/10.1002/grl.50482.

Ryder, C.L., Highwood, E.J., Rosenberg, P.D., Trembath, J., Brooke, J.K., Bart, M., Dean, A., Crosier, J., Dorsey, J., Brindley, H., Banks, J., Marsham, J.H., McQuaid, J.B., Sodemann, H., Washington, R., 2013b. Optical properties of Saharan dust aerosol and contribution from the coarse mode as measured during the Fennec 2011 aircraft campaign. Atmospheric Chemistry and Physics 13, 303–325. https://doi.org/10.5194/acp-13-303-2013.

Ryder, C.L., Highwood, E.J., Walser, A., Seibert, P., Philipp, A., Weinzierl, B., 2019. Coarse and giant particles are ubiquitous in Saharan dust export regions and are radiatively significant over the Sahara. Atmospheric Chemistry and Physics 19, 15353–15376. https://doi.org/10.5194/acp-19-15353-2019.

Scarnato, B.V., Vahidinia, S., Richard, D.T., Kirchstetter, T.W., 2013. Effects of internal mixing and aggregate morphology on optical properties of black carbon using a discrete dipole approximation model. Atmospheric Chemistry and Physics 13, 5089–5101. https://doi.org/10.5194/acp-13-5089-2013.

Scheuvens, D., Schütz, L., Kandler, K., Ebert, M., Weinbruch, S., 2013. Bulk composition of northern African dust and its source sediments — a compilation. Earth-Science Reviews 116, 170–194. https://doi.org/10.1016/j.earscirev.2012.08.005.

Schladitz, A., Müller, T., Nowak, A., Kandler, K., Lieke, K., Massling, A., Wiedensohler, A., 2011. In situ aerosol characterization at Cape Verde. Tellus. Series B, Chemical and Physical Meteorology 63, 531–548. https://doi.org/10.1111/j.1600-0889.2011.00569.x.

Sedlacek, A.J.I., Lewis, E.R., Onasch, T.B., Zuidema, P., Redemann, J., Jaffe, D., Kleinman, L.I., 2022. Using the black carbon particle mixing state to characterize the lifecycle of biomass burning aerosols. Environmental Science & Technology 56, 14315–14325. https://doi.org/10.1021/acs.est.2c03851.

Seinfeld, J.H., Pandis, S.N., 2006. Atmospheric Chemistry and Physics: From Air Pollution to Climate Change. John Wiley & Sons.

Shao, Y., 2001. A model for mineral dust emission. Journal of Geophysical Research. Atmospheres 106, 20239–20254. https://doi.org/10.1029/2001JD900171.

Shen, T.-L., Wooldridge, P.J., Molina, M.J., 1995. Stratospheric pollution and ozone depletion. In: Composition, Chemistry, and Climate of the Atmosphere, pp. 394–442.

Shi, Z., Krom, M.D., Jickells, T.D., Bonneville, S., Carslaw, K.S., Mihalopoulos, N., Baker, A.R., Benning, L.G., 2012. Impacts on iron solubility in the mineral dust by processes in the source region and the atmosphere: a review. Aeolian Research 5, 21–42. https://doi.org/10.1016/j.aeolia.2012.03.001.

Sinyuk, A., Torres, O., Dubovik, O., 2003. Combined use of satellite and surface observations to infer the imaginary part of refractive index of Saharan dust. Geophysical Research Letters 30. https://doi.org/10.1029/2002GL016189.

Slingo, A., Ackerman, T.P., Allan, R.P., Kassianov, E.I., McFarlane, S.A., Robinson, G.J., Barnard, J.C., Miller, M.A., Harries, J.E., Russell, J.E., Dewitte, S., 2006. Observations of the impact of a major Saharan dust storm on the atmospheric radiation balance. Geophysical Research Letters 33, L24817. https://doi.org/10.1029/2006GL027869.

Sokolik, I.N., Toon, O.B., 1999. Incorporation of mineralogical composition into models of the radiative properties of mineral aerosol from UV to IR wavelengths. Journal of Geophysical Research. Atmospheres 104, 9423–9444. https://doi.org/10.1029/1998JD200048.

Song, Q., Zhang, Z., Yu, H., Ginoux, P., Shen, J., 2021. Global dust optical depth climatology derived from CALIOP and MODIS aerosol retrievals on decadal timescales: regional and interannual variability. Atmospheric Chemistry and Physics 21, 13369–13395. https://doi.org/10.5194/acp-21-13369-2021.

Sow, M., Alfaro, S.C., Rajot, J.L., Marticorena, B., 2009. Size resolved dust emission fluxes measured in Niger during 3 dust storms of the AMMA experiment. Atmospheric Chemistry and Physics 9, 3881–3891. https://doi.org/10.5194/acp-9-3881-2009.

Spirig, R., Vogt, R., Larsen, J.A., Feigenwinter, C., Wicki, A., Franceschi, J., Parlow, E., Adler, B., Kalthoff, N., Cermak, J., Andersen, H., Fuchs, J., Bott, A., Hacker, M., Wagner, N., Maggs-Kölling, G., Wassenaar, T., Seely, M., 2019. Probing the fog life cycles in the Namib Desert. Bulletin of the American Meteorological Society 100, 2491–2507. https://doi.org/10.1175/BAMS-D-18-0142.1.

Su, W., Loeb, N.G., Schuster, G.L., Chin, M., Rose, F.G., 2013. Global all-sky shortwave direct radiative forcing of anthropogenic aerosols from combined satellite observations and GOCART simulations. Journal of Geophysical Research. Atmospheres 118, 655–669. https://doi.org/10.1029/2012JD018294.

Sullivan, R.C., Petters, M.D., DeMott, P.J., Kreidenweis, S.M., Wex, H., Niedermeier, D., Hartmann, S., Clauss, T., Stratmann, F., Reitz, P., Schneider, J., Sierau, B., 2010. Irreversible loss of ice nucleation active sites in mineral dust particles caused by sulphuric acid condensation. Atmospheric Chemistry and Physics 10, 11471–11487. https://doi.org/10.5194/acp-10-11471-2010.

Swap, R., Garstang, M., Greco, S., Talbot, R., Kallberg, P., 1992. Saharan dust in the Amazon Basin. Tellus 44B, 133–149.

Swap, R., Garstang, M., Macko, S.A., Tyson, P.D., Maenhaut, W., Artaxo, P., Kållberg, P., Talbot, R., 1996. The long-range transport of southern African aerosols to the tropical South Atlantic. Journal of Geophysical Research. Atmospheres 101, 23777–23791. https://doi.org/10.1029/95JD01049.

Swap, R.J., Annegarn, H.J., Suttles, J.T., King, M.D., Platnick, S., Privette, J.L., Scholes, R.J., 2003. Africa burning: a thematic analysis of the Southern African Regional Science Initiative (SAFARI 2000). Journal of Geophysical Research. Atmospheres 108. https://doi.org/10.1029/2003JD003747.

Tanré, D., Haywood, J., Pelon, J., Léon, J.F., Chatenet, B., Formenti, P., Francis, P., Goloub, P., Highwood, E.J., Myhre, G., 2003. Measurement and modeling of the Saharan dust radiative impact: overview of the Saharan Dust Experiment (SHADE). Journal of Geophysical Research. Atmospheres 108. https://doi.org/10.1029/2002JD003273.

Thorncroft, C.D., Blackburn, M., 1999. Maintenance of the African easterly jet. Quarterly Journal of the Royal Meteorological Society 125, 763–786. https://doi.org/10.1002/qj.49712555502.

Tiitta, P., Vakkari, V., Croteau, P., Beukes, J.P., van Zyl, P.G., Josipovic, M., Venter, A.D., Jaars, K., Pienaar, J.J., Ng, N.L., Canagaratna, M.R., Jayne, J.T., Kerminen, V.-M., Kokkola, H., Kulmala, M., Laaksonen, A., Worsnop, D.R., Laakso, L., 2014. Chemical composition, main sources and temporal variability of PM_1 aerosols in southern African grassland. Atmospheric Chemistry and Physics 14, 1909–1927. https://doi.org/10.5194/acp-14-1909-2014.

Twohy, C.H., Coakley, J.A., Tahnk, W.R., 2009. Effect of changes in relative humidity on aerosol scattering near clouds. Journal of Geophysical Research. Atmospheres 114, 1–12. https://doi.org/10.1029/2008JD010991.

Twomey, S., 1974. Pollution and the planetary albedo. Atmospheric Environment 1967 (8), 1251–1256. https://doi.org/10.1016/0004-6981(74)90004-3.

Twomey, S., 1977. The influence of pollution on the shortwave albedo of clouds. Journal of the Atmospheric Sciences 34, 1149–1152. https://doi.org/10.1175/1520-0469(1977)034<1149:TIOPOT>2.0.CO;2.

Újvári, G., Klötzli, U., Stevens, T., Svensson, A., Ludwig, P., Vennemann, T., Gier, S., Horschinegg, M., Palcsu, L., Hippler, D., Kovács, J., Di Biagio, C., Formenti, P., 2022. Greenland ice core record of last glacial dust sources and atmospheric circulation. Journal of Geophysical Research. Atmospheres 127, e2022JD036597. https://doi.org/10.1029/2022JD036597.

United Nations, 2022. World Population Prospects [WWW Document]. URL https://population.un.org/wpp/. (Accessed 3 August 2024).

Usher, C.R., Michel, A.E., Grassian, V.H., Usher, Courtney R., Michel, Amy E., Grassian, Vicki H., 2003. Reactions on mineral dust. Chemical Reviews 103, 4883–4939.

Van Der Werf, G.R., Randerson, J.T., Giglio, L., Collatz, G.J., Mu, M., Kasibhatla, P.S., Morton, D.C., Defries, R.S., Jin, Y., Van Leeuwen, T.T., 2010. Global fire emissions and the contribution of deforestation, savanna, forest, agricultural, and peat fires (1997–2009). Atmospheric Chemistry and Physics 10, 11707–11735. https://doi.org/10.5194/acp-10-11707-2010.

Varga, G., Dagsson-Waldhauserová, P., Gresina, F., Helgadottir, A., 2021. Saharan dust and giant quartz particle transport towards Iceland. Scientific Reports 11, 11891. https://doi.org/10.1038/s41598-021-91481-z.

Venkatram, A., Karamchandani, P., Kuntasal, G., Misra, P.K., Davies, D.L., 1992. The development of the acid deposition and oxidant model (ADOM). Environmental Pollution, Physical and Chemical Processes in Acidic Deposition 2 Networks, Models and Mechanisms 75, 189–198. https://doi.org/10.1016/0269-7491(92)90039-D.

Verreyken, B., Amelynck, C., Brioude, J., Müller, J.-F., Schoon, N., Kumps, N., Colomb, A., Metzger, J.-M., Lee, C.F., Koenig, T.K., Volkamer, R., Stavrakou, T., 2020. Characterisation of African biomass burning plumes and impacts on the atmospheric composition over the south-west Indian Ocean. Atmospheric Chemistry and Physics 20, 14821–14845. https://doi.org/10.5194/acp-20-14821-2020.

Vickery, K.J., Eckardt, F.D., Bryant, R.G., 2013. A sub-basin scale dust plume source frequency inventory for southern Africa, 2005–2008. Geophysical Research Letters 40, 5274–5279. https://doi.org/10.1002/grl.50968.

Vignati, E., Facchini, M.C., Rinaldi, M., Scannell, C., Ceburnis, D., Sciare, J., Kanakidou, M., Myriokefalitakis, S., Dentener, F., O'Dowd, C.D., 2010. Global scale emission and distribution of sea-spray aerosol: sea-salt and organic enrichment. Atmospheric Environment 44, 670–677. https://doi.org/10.1016/j.atmosenv.2009.11.013.

Volz, F.E., 1972. Infrared refractive index of atmospheric aerosol substances. Applied Optics AO 11, 755–759. https://doi.org/10.1364/AO.11.000755.

Volz, F.E., 1973. Infrared optical constants of ammonium sulfate, Sahara dust, volcanic pumice, and flyash. Applied Optics 12, 564. https://doi.org/10.1364/AO.12.000564.

Wagner, R., Ajtai, T., Kandler, K., Lieke, K., Linke, C., Müller, T., Schnaiter, M., Vragel, M., 2012. Complex refractive indices of Saharan dust samples at visible and near UV wavelengths: a laboratory study. Atmospheric Chemistry and Physics 12, 2491–2512. https://doi.org/10.5194/acp-12-2491-2012.

Washington, R., Todd, M.C., Engelstaedter, S., Mbainayel, S., Mitchell, F., 2006. Dust and the low-level circulation over the Bodélé Depression, Chad: observations from BoDEx 2005. Journal of Geophysical Research 111, D03201. https://doi.org/10.1029/2005JD006502.

Weinzierl, B., Ansmann, A., Prospero, J.M., Althausen, D., Benker, N., Chouza, F., Dollner, M., Farrell, D., Fomba, W.K., Freudenthaler, V., Gasteiger, J., Groß, S., Haarig, M., Heinold, B., Kandler, K., Kristensen, T.B., Mayol-Bracero, O.L., Müller, T., Reitebuch, O., Sauer, D., Schäfler, A., Schepanski, K., Spanu, A., Tegen, I., Toledano, C., Walser, A., Weinzierl, B., Ansmann, A., Prospero, J.M., Althausen, D., Benker, N., Chouza, F., Dollner, M., Farrell, D., Fomba, W.K., Freudenthaler, V., Gasteiger, J., Groß, S., Haarig, M., Heinold, B., Kandler, K., Kristensen, T.B., Mayol-Bracero, O.L., Müller, T., Reitebuch, O., Sauer, D., Schäfler, A., Schepanski, K., Spanu, A., Tegen, I., Toledano, C., Walser, A., 2017. The Saharan aerosol long-range transport and aerosol–cloud-interaction experiment: overview and selected highlights. Bulletin of the American Meteorological Society 98, 1427–1451. https://doi.org/10.1175/BAMS-D-15-00142.1.

Wilcox, E.M., 2010. Stratocumulus cloud thickening beneath layers of absorbing smoke aerosol. Atmospheric Chemistry and Physics 10, 11769–11777. https://doi.org/10.5194/acp-10-11769-2010.

Willeke, K., Whitby, K.T., 1975. Atmospheric aerosols: size distribution interpretation. Journal of the Air Pollution Control Association 25, 529–534. https://doi.org/10.1080/00022470.1975.10470110.

Wu, Y., Cheng, T., Pan, X., Zheng, L., Shi, S., Liu, H., 2020. The role of biomass burning states in light absorption enhancement of carbonaceous aerosols. Scientific Reports 10, 12829. https://doi.org/10.1038/s41598-020-69611-w.

Yoon, Y.J., Ceburnis, D., Cavalli, F., Jourdan, O., Putaud, J.P., Facchini, M.C., Decesari, S., Fuzzi, S., Sellegri, K., Jennings, S.G., O'Dowd, C.D., 2007. Seasonal characteristics of the physicochemical properties of North Atlantic marine atmospheric aerosols. Journal of Geophysical Research. Atmospheres 112. https://doi.org/10.1029/2005JD007044.

Yu, H., Kaufman, Y.J., Chin, M., Feingold, G., Remer, L.A., Anderson, T.L., Balkanski, Y., Bellouin, N., Boucher, O., Christopher, S., DeCola, P., Kahn, R., Koch, D., Loeb, N., Reddy, M.S., Schulz, M., Takemura, T., Zhou, M., 2006. A review of measurement-based assessments of the aerosol direct radiative effect and forcing. Atmospheric Chemistry and Physics 6, 613–666. https://doi.org/10.5194/acp-6-613-2006.

Yu, Y., Ginoux, P., 2022. Enhanced dust emission following large wildfires due to vegetation disturbance. Nature Geoscience 15, 878–884. https://doi.org/10.1038/s41561-022-01046-6.

Yue, X., Liao, H., 2012. Climatic responses to the shortwave and longwave direct radiative effects of sea salt aerosol in present day and the last glacial maximum. Climate Dynamics 39, 3019–3040. https://doi.org/10.1007/s00382-012-1312-5.

Zábori, J., Krejci, R., Ekman, A.M.L., Mårtensson, E.M., Ström, J., de Leeuw, G., Nilsson, E.D., 2012. Wintertime Arctic Ocean sea water properties and primary marine aerosol concentrations. Atmospheric Chemistry and Physics 12, 10405–10421. https://doi.org/10.5194/acp-12-10405-2012.

Zeng, J., Zhang, G., Long, S., Liu, K., Cao, L., Bao, L., Li, Y., 2013. Sea salt deliquescence and crystallization in atmosphere: an in situ investigation using x-ray phase contrast imaging. Surface and Interface Analysis 45, 930–936. https://doi.org/10.1002/sia.5184.

Zhang, Z., Meyer, K., Yu, H., Platnick, S., Colarco, P., Liu, Z., Oreopoulos, L., 2016. Shortwave direct radiative effects of above-cloud aerosols over global oceans derived from 8 years of CALIOP and MODIS observations. Atmospheric Chemistry and Physics 16, 2877–2900. https://doi.org/10.5194/acp-16-2877-2016.

Zuidema, P., Alvarez, C., Kramer, S.J., Custals, L., Izaguirre, M., Sealy, P., Prospero, J.M., Blades, E., 2019. Is Summer African Dust Arriving Earlier to Barbados? The Updated Long-Term In Situ Dust Mass Concentration Time Series from Ragged Point, Barbados, and Miami, Florida. Bulletin of the American Meteorological Society 100, 1981–1986. https://doi.org/10.1175/BAMS-D-18-0083.1.

Chapter 2

Aerosol impacts on the West African Monsoon

Fabien Solmon
LAERO OMP, CNRS, Toulouse University, Toulouse, France

2.1 Introduction

This chapter aims at drawing a general picture regarding the interaction of major natural and anthropogenic aerosols with the West African Monsoon system (WAM). After recalling some key fundamental notions of aerosol–climate interaction and modeling in Section 2.2, the chapter will discuss in more detail the particular cases of regional dust and biomass-burning aerosol impacting the WAM (Section 2.3). The discussion will be structured by considering various mechanisms as well as various spatial and temporal scales of interactions. The impact of other anthropogenic aerosol sources, affecting the WAM through regional or global connections, as well a discussion regarding recent and future trends in aerosol relevant to the long-term variability and the future of the WAM will be proposed (Section 2.4).

2.2 Climatic effects of aerosols

2.2.1 Aerosol interactions with radiation and cloud microphysics

Aerosol particles in the atmosphere exhibit a great diversity of chemical compositions, shapes, and sizes. Observed aerosol-size distributions typically range from 10^{-3} (for nucleating particles) to 10^{2} μm (for super-coarse dust particles), i.e., a relevant scale for interaction with atmospheric radiative-transfer and cloud-formation processes. Aerosol interaction with solar and thermal radiation is formalized through the Mie theory, which describes the scattering and absorption of incident radiation by particles assumed to be spherical and homogeneous (Irvine, 1965). Climate-relevant aerosol optical properties derived from Mie theory include the aerosol mass-extinction efficiency (MEE), which quantifies the ability of the particle to attenuate incident radiation through absorption and backward scattering, the single scattering albedo (SSA), which quantifies how much absorbing vs diffusive a particle is, and the asymmetry parameter (alternatively the back-scattered fraction), which quantifies how much forward vs. backward scattering occurs. Aerosol optical properties are very much depen-

Aerosols and Precipitation Over Africa. https://doi.org/10.1016/B978-0-44-314050-1.00007-4

dent on particle size relative to the incident wavelength (with maximum MEE occurring when particle size is close to the wavelength), and particle refractive indices determined by chemical composition (for instance, SSA at 530 nm vary from less than 0.5 for highly absorbing particles such as fresh soot to 0.98 for almost purely scattering sulfate particles). The actual shape of aerosol particles can also differ substantially from the spherical assumption with a significant impact on optical properties. Extensions of the Mie theory have been proposed to account for these effects.

Aerosols are also essential in cloud-formation processes. Hygroscopic particles reduce the level of water-vapor supersaturation required for thermodynamical stabilization and spontaneous growth of cloud droplets. The activation of aerosol to cloud-condensation nuclei (CCN) and the ensuing initial cloud-droplet growth is described by the Koehler theory (Köhler, 1936). The efficiency with which a given dry particle can grow and activate CCN is usually quantified through the κ hygroscopic parameter (Petters and Kreidenweis, 2007) ranging from ~ 0 for nonhygroscopic species like pure soot to 1.4 for very hygroscopically active salts. As for optical properties, size, and chemical composition evolution determine κ values during atmospheric transport. Regarding the formation of ice and mixed-phase clouds, homogeneous freezing of previously nucleated liquid-cloud droplets normally occurs at about −38 °C. However, freezing can be triggered at warmer temperatures in the presence of solid aerosol particles which thermodynamically facilitate liquid water crystallization (Knopf and Alpert, 2023) and can act as ice nuclei (IN). There are various paths identified for heterogenous nucleation (contact, immersion, condensation, and deposition freezing) depending on conditions like temperature, supersaturation (with regards to ice), and the nature of aerosol particles. Examples of identified IN include desert dust, soot, organic matter, bacteria, pollen, fungal spores, and volcanic ash, among others. These IN particles have experimentally been shown to enable heterogenous nucleation for various onset temperatures (Hoose and Möhler, 2012), making them more or less "efficient IN", although a considerable variability and associated uncertainties remain.

2.2.2 Aerosol perturbation and feedbacks in a simple atmospheric-column framework

Let's consider first as a reference an idealized cloud-free column representing a stable atmosphere overlying a given terrestrial surface type. This column is characterized by a neutral potential temperature profile (Fig. 2.1), and radiatively by net (downward–upward) solar shortwave (SW) and terrestrial longwave (LW) fluxes at the Top Of the Atmosphere (TOA) and at the surface. Let's assume that this column is perturbed by an aerosol layer at a given altitude. Depending on particle concentration and optical properties, this layer absorbs and scatters SW radiation and, for large particles like coarse dust, enhances the layer LW emissivity and scattering. Without considering any atmospheric (temperature, humidity, etc.) adjustment, the changes in TOA and surface net radiation induced by the aerosol layer are called the aerosol instantaneous radiative forcing (IRF in $W.m^{-2}$, Fig. 2.1). In climate and meteorological models, the TOA IRF can be for instance diagnosed using a double call to the radiative transfer scheme, including or not aerosol radiative effects (Fig. 2.2). At the surface, the SW IRF is always negative as a result of surface incoming solar-radiation extinction and is associated with radiative cooling. The amplitude of the extinction is usually quantified by the aerosol optical depth (AOD) calculated from the vertical integration of concentration and MEE. The SW TOA IRF can be negative or positive, depending both on aerosol SSA and the SW reflectivity of the column segment beneath the aerosol layer. The SW reflectivity is determined first by the surface albedo, but also by the possible presence of lower-level cloudy layers. Note that taking into account or not the presence of cloudy layers in the reference state for IRF calculation results in all-sky vs clear-sky TOA IRF. Seen from the TOA, the SW IRF will be negative, meaning a radiative cooling for the column, if the aerosol layer induces an increase of the "planetary albedo" (including surface and lower cloud contributions) and positive if the aerosol layer enhances a decrease of the planetary albedo, associated with a net absorption and radiative warming. For a given planetary albedo, there is a critical value of aerosol SSA (depending on particle-mixture composition) for which the sign of SW TOA IRF reverses from positive to negative (Liao and Seinfeld, 1998). Highly scattering aerosol has, in general, a cooling effect, while the picture is regionally more complex for more absorbing aerosol such as dust and biomass-burning particles, as will be discussed in Section 2.3.2. Strongly absorbing aerosols, such as pure black carbon particle, have a warming effect. The contribution of LW forcing is much smaller and, in general, neglected for fine particles. However, the LW radiative forcing can be significant and must be accounted for in regions dominated by coarse dust, for example. The LW IRF is always positive at the surface, and both the TOA and surface LW IRF are sensitive to the aerosol layer height and burden (Liao and Seinfeld, 1998).

The radiative perturbation associated with the aerosol layer will induce some adjustments in the cloud-free column-state variables through the so-called *direct effect*: (i) The surface temperature will generally tend to decrease as a result of efficient surface SW extinction, although nighttime temperature increase due to LW warming can be significant in cases of large burdens of coarse particles. The timing and amplitude of the surface temperature response, occurring through surface-energy budget and flux adjustments, depend on the nature of the surface (e.g., land vs ocean, as discussed in 2.2.3). Associated feedback can then propagate into the atmosphere, for instance, through boundary layer turbulence and convection. (ii) In the atmospheric aerosol layer, the potential temperature profile is also directly impacted by the local diabatic heating induced by aerosol SW absorption notably. The combination of these effects is likely to induce a relative stabilization of the atmosphere beneath the aerosol layer and a relative destabilization above as illustrated in Fig. 2.1.

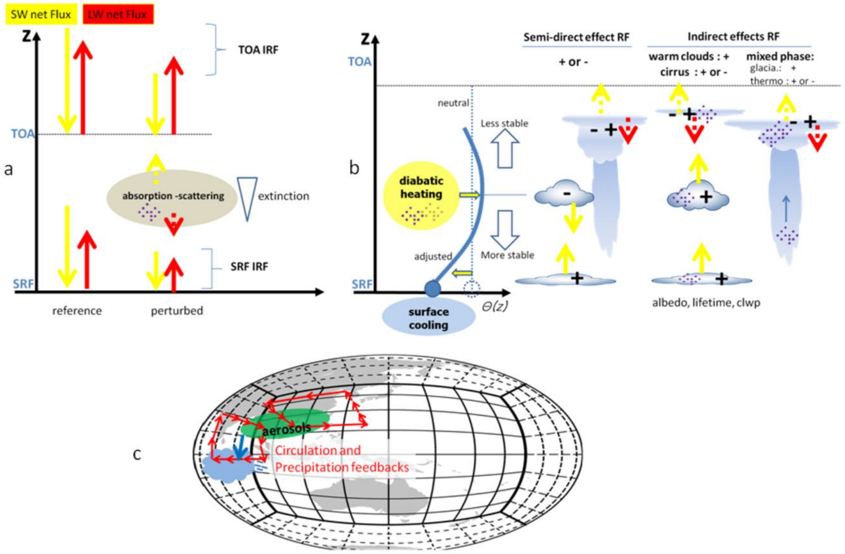

FIGURE 2.1 Single-column representation of aerosol radiative interaction. a) Instantaneous radiative forcing. b) Column adjustment, semidirect, and indirect effect radiative forcings. c) Regional-to-global adjustments.

If clouds are present in the column, they will also adjust to aerosol IRF, which in turn can quickly and significantly impact the column radiative budget. The radiative signature of this adjustment, called the *semidirect effect* (SDE), can potentially enhance or compensate the IRF, depending on cloud response and cloud types. In the columnar framework (Fig. 2.1.b), low clouds can be enhanced as a result of the relative stabilization beneath the aerosol layer and cloud coexisting with an absorbing aerosol layer can be reduced as a result of local diabatic heating and drying, while instability above the aerosol layer can be promoted with impacts on upper-level cloudiness (enhancement). However, in the case of convective clouds, the effective SDE is not straightforward since both stabilizing and destabilizing effects can compete with each other, as will be discussed further in Section 2.2.3.

Cloud response is not limited to SDE since aerosol can also perturb cloud microphysics, with ensuing impacts on radiative forcing through the so-called *indirect effects*. To put it briefly, for liquid phase clouds, an enhanced CCN number concentration at a constant cloud-liquid water path induces smaller cloud-droplet effective radii and increased cloud albedo (*first indirect effect*, Twomey, 1974). The reduction of droplet radius can also decrease precipitation rates and potentially enhance liquid-water path, cloud lifetime, and cloud fraction (the second aerosol indirect effect, Albrecht, 1989). On stratiform low clouds, these effects result in an *additional negative* SW radiative forcing both at the surface and TOA, while the LW RF effect remains small. The prevalence of first vs second indirect effects in the effective cloud adjustment is still a matter of intense discussion (e.g., Yuan et al., 2023). The picture becomes more complex regarding the perturbation of ice clouds, such as cirrus. Ice nucleation pathways might be competitive with regards to available humidity (Kärcher et al., 2022). This results in various impacts on macrophysical cloud characteristics (thickness, altitude, lifetime, etc.) which in turn affect LW and SW radiative-forcing components in various ways. Thus. the net radiative impact of IN interacting with cirrus clouds is very uncertain and a matter of intense research. In the case of convective mixed phase clouds, an increased CCN concentration in lower layers results in smaller ascending cloud droplets which, considered alone, would translate into a negative radiative forcing. However, these smaller droplets are also likely to freeze and release latent heat at higher altitudes, potentially invigorating updrafts and increasing cloud-top heights and anvils. Taken alone, this invigoration is likely associated with net positive TOA radiative forcing owing to a reduced outgoing LW radiation. As a result, the so-called thermodynamic indirect effect can be positive or negative and remains uncertain. As discussed for cirrus clouds, the picture gets even more complex if significant concentrations of IN are also transported in the convective updrafts. For instance, an additional glaciation indirect effect can occur (Lohmann and Feichter, 2005), by which more ice nuclei promote precipitation and cloudiness reduction, translating into a positive radiative forcing.

For both semidirect and indirect effects, the cloud environment (thermodynamic, dynamic, background aerosol conditions, etc.) plays a major role in modulating the cloud-effective response to a given aerosol perturbation. The environment can, for instance, determine competitive and buffering mechanisms occurring at small dynamical scales (compared to the column scale) that limit the cloud feedback and associated radiative-forcing response (Fons et al., 2023). In the case of an induced convective invigoration, Zang et al. (2023) argue that, since convection strongly influences its tropospheric environment, there are also synergies between the primary aerosol impact on convection and the meteorological modification associated with convection perturbation.

2.2.3 Aerosol perturbation and feedbacks at regional to global scales, effective radiative forcing

Stepping away from a simple columnar view, aerosol “local” radiative and microphysical perturbation will propagate to neighboring atmospheric columns and induce atmospheric responses and adjustments at larger spatial scales (Fig. 2.1). The study of such connections can be addressed using atmospheric models ranging from high-resolution cloud-resolving models and large eddy simulations (LES), to mesoscale meteorological models, to climate and Earth system models. For instance, aerosols have been shown to influence surface-pressure and temperature patterns, induce spatial and temporal shift in precipitation, etc. Section 2.2.3 will actually propose a discussion of such effects specific to the African monsoon region. In the latest IPCC assessments, potential aerosol climatic impact is quantified using the *effective radiative forcing* (ERF) metric (Bellouin et al., 2020; Smith et al., 2020). Determined through model sensitivity experiments, the ERF includes the radiative signatures of the direct effect, aerosol induced direct modification of surface albedo (e.g., snow darkening, not discussed here), and 'fast' atmospheric adjustments including semidirect and indirect effects as well as circulation and thermodynamic changes. "Fast" refers here to the fact that the slow-component, ocean and ice-sheet, adjustments are not considered in ERF calculation (Smith et al., 2020).

2.3 Aerosol impacts on the West African Monsoon (WAM) system

2.3.1 The WAM system

The WAM is connected to a meridional pressure gradient between higher pressure over the Atlantic cold tongue, which develops at the end of boreal spring, and the Saharan heat low following an enhanced insulation during boreal summer (Caniaux et al., 2011). The WAM has been theoretically described in terms of a thermal circulation for moist atmospheres, where the gradient of boundary-layer entropy determines the strength of the monsoon (Eltahir and Gong, 1996). In this framework, the entropy meridional gradient's variability is connected not only to large-scale climate fluctuations (notably Atlantic SST), but also to regional factors impacting the distribution of diabatic and humidity sources and sinks (Mohtadi et al., 2016). Saharan heat low activity (Lavaysse et al., 2015), land use changes (Paeth et al., 2009), soil humidity feedbacks (Douville et al., 2006), low level clouds (Kniffka et al., 2019), and, as will be developed further, aerosols are an example of such factors. Moist convection, which occurs at diverse degrees of organization depending on the regional environment, is a key player for diabatic and moisture redistribution and is connected to many aspects and scales of the WAM system. In particular, the nonlinear nature of convective processes and their capacity to potentially amplify, from an energetic point of view, "small" perturbations is determinant for understanding WAM sensitivity to environmental changes. In the following sections, we will review how natural and anthropogenic aerosol particles interact with the WAM and its variability. The discussion will mostly, but not only, focus on the role of regional dust and biomass-burning particles, which are major aerosol species in Africa.

2.3.2 Dust aerosol and WAM interactions

Forty-sixty percent of the global dust burden originates from the numerous sources of the Sahara (Engelstaedter et al., 2006), from which emissions peak during boreal summer coinciding with the WAM (Prospero et al., 2002; Schepanski et al., 2007). Maximum dust concentrations are generated in Saharan arid dust-source regions such as Erg El Djouf (Western Sahara) or the Bodele de-

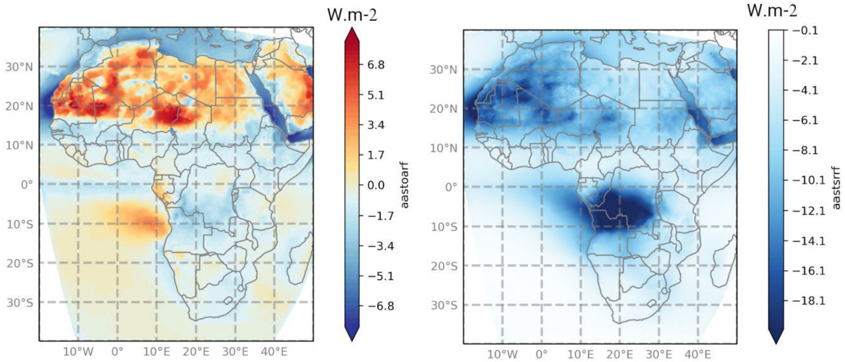

FIGURE 2.2 Example of simulated TOA (a) and surface (b) instantaneous, all-sky radiative forcing for Africa, JJAS 2001. Simulation made with the RegCM5 regional climate model, forced here by MERRA-2 aerosol reanalysis. The contributions of Saharan dust and biomass-burning particles are clearly visible. Change of TOA RF is notably dependent on surface albedo, and the presence of low clouds over the south Eastern Atlantic.

pression and, to a lesser but still significant extent, from the Sahelian sources (see Ginoux et al., 2012 for active sources identification). During boreal summer, significant amount of dust are transported westward and southward, above the monsoon layer, as part of the Saharan Air Layer. Over the Sahel, monsoon bursts, convective activity, and cold-pool-induced dust emission and transport are also closely connected (see, for instance Knippertz and Todd, 2012 for a detailed overview).

2.3.2.1 Dust climatic impact on the WAM

Since the late 1990s, global and regional climate models have progressively evolved to include online representation of dust emission, transport, and removal processes as well interaction with radiation (Miller and Tegen, 1998; Zender et al., 2003; Liu et al., 2003; Yoshioka et al., 2007; Zakey et al., 2006, ...). Although imperfect in many regards, such models have made it possible to progressively assess the causality chains linking dust radiative forcing (Fig. 2.2) to monsoon dynamic and precipitation responses.

Based on GCM experiments, Lau et al. (2009) have proposed a conceptual framework for interpreting dust impacts on WAM, namely, the elevated heat pump effect (EHP), which is illustrated in Fig. 2.3. Note that the EHP was first introduced to describe the impact of anthropogenic aerosol on the Indian monsoon system. Keeping the mechanisms described in Section 2.2.2 in mind, the EHP essentially states that the strong diabatic warming induced by dust absorption in the lower-to-mid troposphere over the Sahara and Sahel promotes continental convection over Sahel. Further away from the sources, the transported elevated dust layers tend, on the contrary, to promote stabilization and lower-level cloudiness. The resulting dust-induced zonal and meridional circulation anomaly that develops tends to increase the low-level monsoon humidity-flow fueling convection, while shifting the convective belt precipitation northward (Fig. 2.3).

While dust diabatic warming is put forward as the primary engine of the EHP, the dust-induced surface solar extinction and cooling is also at play, with, if considered alone, a tendency to increase static stability and reduce continental convection. The efficiency and validity of the EHP depend thus on competitive mechanisms, which explains why other studies have come with contrasting results, outlining, on the contrary, a negative circulation and precipitation feedback associated with a predominant stabilizing effect of dust over the Sahel, notably (Yoshioka et al., 2007; Miller and Tegen, 1998; Solmon et al., 2008; Pausata et al., 2016, ...). It quickly became clear that the competition between stabilizing vs convective enhancement was very much dependent on dust SSA (Solmon et al., 2008; Lau et al., 2009; Zhao et al., 2011), and that this sensitivity was robust among various modeling systems (Miller et al., 2014). Along with surface albedo, the SSA strongly determines the sign of dust TOA radiative forcing and the relative strength of surface-vs-atmospheric forcing, to which moist convection is very sensitive. Models that consider medium-to-high absorbing dust (SSA < 0.9 at 550 nm) show in general larger positive TOA radiative forcing over the bright Sahara and a weaker negative, or even slightly positive, TOA RF over the Sahel, associated with an effective EHP. On the contrary, when dusts are weakly absorbing (SSA > 0.95 at 550 nm), the EHP mechanism might not be triggered with an opposite effect on mean WAM circulation and precipitation shifted to the south (Figs. 2.3 and 2.4).

As mentioned previously, the SSA depends on particle-size distribution and refractive indices, which for dust are tied to source mineralogy (e.g., hematite content). Historically, it has been very challenging to constrain dust SSA at regional and global scales. In situ measurements generally indicate a higher shortwave absorption than satellite-based estimates (Haywood et al., 2003; Kaufman et al., 2001; Di Biagio et al., 2019), and the range of effective SSA considered in models can vary roughly from 0.84 to 0.98, which most likely encompass the critical value for ‘EHP reversal’. Recent advances based on field measurements (Adebiyi et al., 2023a; Di Biagio et al., 2019) outline the need to consider higher proportions of super-coarse particles in dust emission-size distributions, as well as a regionally varying hematite content for the specification of optical properties. Balkanski et al. (2021) shows that, when considered in a particular GCM, these new constraints tend to produce a very effective EHP associated with a significant enhancement, and northward shift, of monsoon precipitation (Fig. 2.4). Note also that optical properties considered in climate models can be affected by compensating errors in emission size distribution and refractive indices (Adebiyi et al., 2023a).

In addition to optical properties, other environmental factors are likely to impact at various degrees the WAM response to dust radiative forcing at climatic scale. In term of modeling, the surface and boundary layer schemes will determine surface albedo, surface flux adjustments, the presence of low clouds,

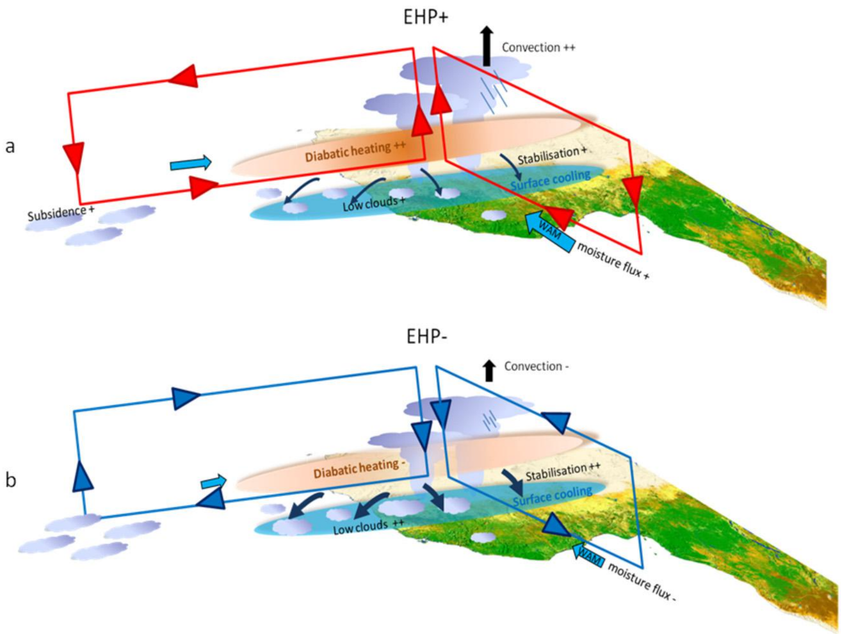

FIGURE 2.3 a) Schematic representation of the Elevated Heat Pump Effect, adapted from (Lau et al., 2009). b) Schematic representation of a model where EHP is not as effective, due to more diffusive dust particle.

etc. The convective scheme will be key in determining the ‘model sensitivity’ to dust perturbation (Solmon et al., 2012). Given the complexity of interdependent processes and the diversity of models at play, an exhaustive discussion is beyond the scope of this chapter. However, one aspect that deserves perhaps more attention is the role of SST adjustment to the dust radiative perturbation. Historically and for computing resources reasons, a number of dust-impact studies have been based on atmosphere only GCM or RCM, using prescribed SST. Since dust forcing is significant both on the surface and in the atmosphere (2.2.2), not considering any SST adjustment results in an energy imbalance that sensibly affect the regional precipitation response over the ocean and also inland (Miller and Tegen, 1998; Yue et al., 2011; Solmon et al., 2012; Jordan et al., 2018). Dust surface radiative forcing can induce a cooling reaching typically 0.5 to 1 K in the eastern Atlantic. This cooling induces a stabilization and a reduction of evaporation and moisture convergence, which can dampen the EHP and the positive precipitation feedback (in a model where EHP is effective) or increase furthermore the Sahelian drying (in a model where EHP is not effective). The dust-induced SST cooling is also of prime importance regarding the impact of dust on cyclonic activity over the Atlantic (Evan et al., 2009). The importance, mechanisms, and time scales tied to aerosol-induced regional SST

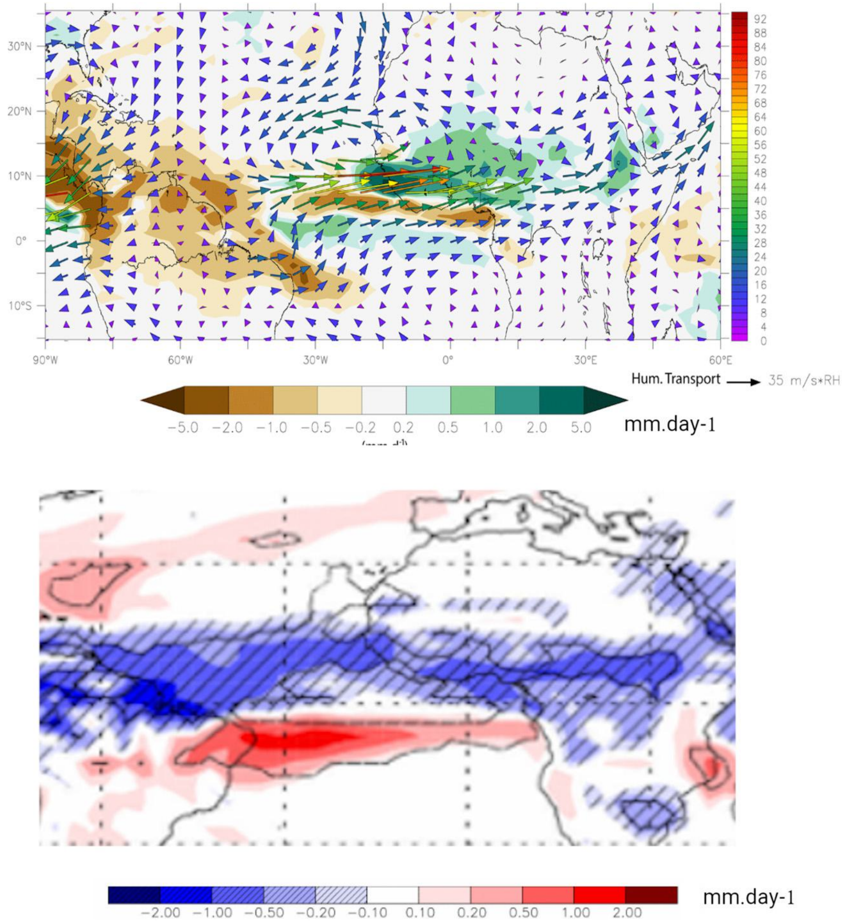

FIGURE 2.4 a) Examples of GCM simulated dust-induced WAM precipitation anomalies when a) the EHP is effective (taken form Balkanski et al., 2021) and b) the EHP is not effective (taken from Yoshioka et al., 2007).

adjustments will be also discussed in the case of biomass-burning aerosol impact (Section 2.3.3).

2.3.2.2 Dust, African easterly waves, and mesoscale convective system interactions

African Easterly Waves (AEW) are synoptic-scale atmospheric disturbances with a preferred wavelength in the 2000–4000-km range and are a key component of the WAM system, modulating daily to seasonal precipitation variability over West Africa and the Sahel. AEWs are both energetically connected to the African Easterly Jet (AEJ) disturbances and to organized mesoscale convective systems (MCS) (Berry and Thorncroft, 2012). Diabatic heating is an important factor for the growth of AEWs over West Africa (Russell et al., 2020).

During the monsoon, AEWs are often connected to large dust-emission events producing significant daily AOD enhancements over continental Africa and the Atlantic basin. To a large extent, the previously discussed dust-mean climatic impacts reflect the average signature of interactions occurring at the spatial and temporal scale of AEW and embedded MCS. Several studies analyzing AEW energetics, whether based on reanalyzes or modeling experiments, show that the diabatic heating associated with dust absorption is significant enough to positively impact AEW developments (Grogan and Thorncroft, 2019; Bercos-Hickey et al., 2022). The dust-induced increase in mid-troposphere meridional temperature gradients tends to strengthen baroclinicity and results in the enhanced conversion of potential to eddy kinetic-energy fueling AEWs. It is suggested that anomalous heating could potentially even trigger disturbances in the AEJ–AEW coupled system (Hosseinpour and Wilcox, 2024). AEWs developing along the "northern track" tends to be more impacted relative to those following the "southern track" (Diedhiou et al., 1998), most likely due to a closer vicinity with large dust sources. Incidentally, this might be a source of intraseasonal variability in dust–monsoon interactions. For both tracks, dust heating can induce a northward shift of AEW, in association with a northward shift of the AEJ (Bercos-Hickey et al., 2017). Note that, when extrapolated to longer time scales, these results and mechanisms tend to be consistent with the EHP. Similar to the previous EHP discussion, other studies have argued for an opposite (weakening) effect of dust on AEW activity linked to a reduction of convective activity consecutive to the dust-induced lower troposphere stabilization (Jury and Santiago, 2010). Bangalath et al. (2023) shows the importance of dust absorption properties (and associated uncertainties) to the AEW feedback, which is again consistent with the "EHP sensitivity" to dust absorption.

As mentioned already, dusts not only modulates regional radiative forcing and temperature gradients, but they also have an impact at the convective scale through radiative–cloud-microphysics interactions. These connections are important for WAM intraseasonal variability, precipitation intensity, and feedback to the AEW. For a one week a case study, Martínez and Chaboureau (2018) show that the dust radiative effect reduces the number of simulated MCS and average precipitation via low-level stabilization, while promoting more organized and vigorous MCS when they actually do form. Regarding microphysical effects, dust particles are efficient IN and, with much uncertainty, could also act as CCN and giant CCNs. High-resolution studies exploring these effects produce varied results, sometime contradictory: For instance, Min et al. (2014) reported that an increase of IN generate a competition for moisture, which tends to reduce total rainfall formation and anvil cloud extent; Gibbons et al. (2018) argue that IN impact on MCS precipitation could be negative in convective cores vs positive in stratiform detraining anvils: Seigel et al. (2013) suggested that by acting as CCN and giant CCN, dust might enhance convective warm-rain production and overall weaken convection. When both radiative and microphysic effects are considered, Huang et al. (2019) indicate that dust radiation effect tends to be more influential than dust–cloud interactions and that nonlinear synergies exist between the direct, semidirect, and indirect effects contributing to the overall MCS response. In a specific case study, they show that the overall dust impact is to delay the formation of the MCS while increasing its organization. Overall, understanding fine dust-induced convective-cloud adjustments, their dependence on variable environmental conditions (themselves impacted by regional dust forcing), and their effective impact on WAM variability at climatic scale, is still very challenging.

2.3.3 Biomass-burning aerosol and WAM interactions

African biomass-burning emissions, resulting primarily from agricultural activities, are a major source of carbonaceous aerosol worldwide. During the WAM season, these sources are mostly active over central and southern Africa, i.e., relatively far away from West Africa and the WAM core. Large concentrations of biomass-burning aerosols are, on average, transported westward over the southern Atlantic Ocean (SEA) at altitudes between two and four km, relative to the southern African Easterly jet (SAEJ) activity (Adebiyi et al., 2023b; Mari et al., 2008). However, as part of the regional dynamical variability, intermittent transequatorial transport of biomass-burning aerosols toward southern West Africa can also be observed (Ajoku et al., 2020; Menut et al., 2018; Mari et al., 2008). These aerosols can further be entrained in the lower monsoon layer by turbulent and cloud venting processes (Dajuma et al., 2020). In the following discussion, and to reflect the outcomes of various studies, we will distinguish the potential impact of biomass-burning aerosol transported to the WAM domain from the climatic impact of the southern core of the mean aerosol outflow inducing a disturbance on the WAM system. Of course, in reality, both of these interactions are at play.

2.3.3.1 'Local' effects of transported biomass-burning aerosol

As part of the Dynamics-Aerosol-Chemistry-Cloud Interactions in West Africa DACCIWA program (Knippertz et al., 2015), observation and regional modeling studies targeting the West African coastal region have suggested that northwardly transported aerosol tends to promote a "local" stabilization and a reduction of precipitation, both due to direct and indirect effects on warm low clouds (Taylor et al., 2019; Dajuma et al., 2021). Based on a detailed LES case study, Delbeke et al. (2023) showed that the low-cloud diurnal evolution and macrophysical adjustment to direct, semidirect, and indirect effects induced by observed aerosol profiles is however not straightforward and depends strongly on the diurnal cloud-development stage. The competition of indirect effects, inducing a SW surface cooling, with the in-cloud semidirect effect of absorbing particles, which locally reduce cloud-water inducing surface SW warming, is also important.

As for West African convective systems and AEW, which could also potentially be “locally” impacted by biomass-burning aerosols transported within the WAM layer, there is a clear lack of equivalent high-resolution studies, so far. Biomass-burning aerosol impact studies on convection carried out in other tropical regions suggest that indirect effects on warm microphysics could lead to significant cloud invigoration and precipitation enhancement (Zang et al., 2023; Takeishi and Wang, 2021). As mentioned earlier and as described in more detail hereafter, convection within the WAM might also be strongly influenced by larger-scale aerosol-induced environmental modifications.

2.3.3.2 Biomass burning outflow perturbing the WAM

At larger scales, the WAM system is likely to be dynamically connected to the strong radiative perturbation occurring in the core of the Southern Hemisphere source and biomass-burning aerosol outflow, existing approximately between 20°S and the equator. In terms of mean radiative forcing, biomass-burning aerosol show in general negative TOA IRF in the continental source regions of central and southern Africa (Fig. 2.2) and up to the Gulf of Guinean for transported particles. One of the particularities of the African biomass-burning outflow is that the mean TOA IRF sharply reverses to positive in the South Eastern Atlantic (SEA) region dominated by a reflective semipermanent stratocumulus deck as shown, for example, in (Schulz et al., 2006; Brown et al., 2021; Mallet et al., 2020) and in Fig. 2.2. Note that the representation of this regional contrast is quite variable among climate models reflecting uncertainties relative to smoke optical properties (Mallet et al., 2021), aerosol injection height, aerosol vertical transport, and the simulation of low-cloud dynamics and albedo. In recent years, the SEA biomass-burning aerosol outflow region has received much scientific attention, notably through the Aerosol RadiatiOn and CLOuds in Southern Africa AEROCLO-sA (Formenti et al., 2019), the ObseRvations of Aerosols Clouds and their interactions ORACLES (Redemann et al., 2020), and the Clouds and Aerosol Radiative Impacts and Forcing CLARIFY (Haywood et al., 2020) programs.

Beside a large direct forcing, there are also important regional cloud adjustments involving semidirect and indirect effects that lead to a regional ERF that differs substantially from the IRF (Fig. 2.5). The ERF is associated with regional climate adjustments that can have important implications and that we seek to better understand by distinguishing three important subregions:

i) Over the continental biomass-burning source regions of central and southern Africa, several climate studies indicate that the large surface-cooling induced by aerosol extinction tends, on average, to lead to more stable conditions associated with a decrease of precipitation and a anticyclonic anomaly over southern Africa (Sakaeda et al., 2011; Tosca et al., 2015; Hodnebrog et al., 2016; Mallet et al., 2020). It is also plausible that convective systems over central

Africa might feedback positively to the intense diabatic warming in the lower troposphere (Tummon et al., 2010; Heyblom et al., 2022). For a specific case study, Chaboureau et al. (2022) points out an aerosol-induced shift in the distribution of convective events, with a decrease of convection occurrences but a relative increase of intense deep convective events. This response is also associated with an intensification and a shift of the southern AEJ. Similarly to the previous dust-feedback discussion and considering only direct and semidirect effects, the aerosol-induced response of continental convection and regional climate is likely to result from the competitive effects of atmospheric diabatic warming vs surface cooling. For models where convection is inhibited, the decreased cloudiness translates in a positive SDE TOA SW radiative forcing, while in the LW, a compensating cooling might be obtained. The average LW signature of convective-cloud adjustment is, however, particularly uncertain, depending notably on convective cloud-height perturbation. These reasons are likely to explain differences in effective radiative forcing simulated for the central and southern African continental source region shown by different global models (Allen et al., 2019). Additionally, various aerosol indirect effects on convective systems might also be at play in continental source regions with potentially similar effects (e.g., cloud invigoration), as discussed in Subsection 2.2.2. There is clearly a lack of studies, both on the experimental and modeling sides, assessing the complex synergies between various aerosol effects operating at diverse scales for the central African convective region.

ii) Over the SEA, in the core of the outflow, many studies indicate that biomass-burning aerosols induce a mean negative TOA semidirect radiative forcing (Fig. 2.5) associated with an increase of the low-level cloud-water content and cloud fraction (Wilcox, 2010; Gordon et al., 2018; Mallet et al., 2020). The low-level cloud feedback mostly results from the diabatic heating produced by enhanced shortwave absorption in the biomass-burning aerosol layer. This heating is associated with an increase in above-cloud air buoyancy and a relative reduction in above-cloud subsidence (i.e., an upward circulation anomaly (Fig. 2.6) and associated dry-air intrusions. The low-level cloud increase might also be reinforced by an increase in marine boundary layer stability associated with SST cooling consecutive to both aerosol and low-cloud feedback, reducing incoming surface solar radiation. Over SEA, the negative SDE RF could potentially more than compensate for the positive IRF (Solmon et al., 2021; Chung et al., 2012; Che et al., 2020). Note that the picture is still uncertain, especially when and where the occurrence of mixing between aerosol and cloud layers increases, particularly in the stratocumulus-to-cumulus transition region. In such a situation, the semidirect effect could on the contrary significantly contribute to reduce cloudiness, while inducing a positive effective radiative forcing (Baró Pérez et al., 2023). Additionally for the outflow region, there is still a debate regarding the importance of biomass-burning aerosol indirect effects on low-level cloud feedback. Based on a LES study, (Lu et al., 2018) suggests that aerosol intrusions in the stratocumulus deck and associated indirect effects

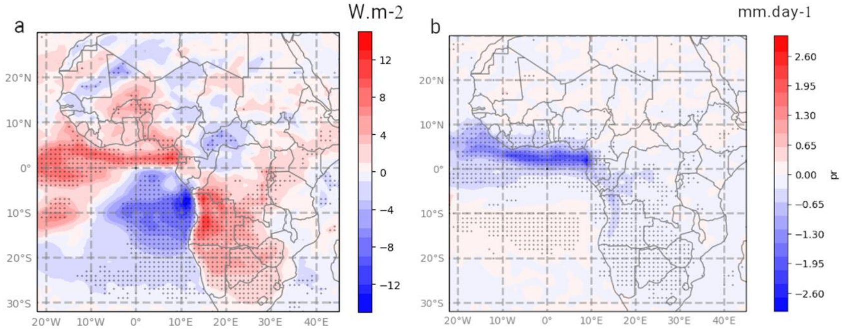

FIGURE 2.5 a) An example of simulated biomass-burning aerosol semidirect radiative forcing, JJAS 2003-2015. b) Simulated biomass-burning aerosol-induced precipitation anomaly, JJAS 2003-2015. Dots represent statistically significant forcing and anomalies. Adapted from Solmon et al. (2021).

could be of prime importance regarding aerosol ERF in the SEA. Other studies (Diamond et al., 2022; Gordon et al., 2018; Che et al., 2020) find that the above-cloud semidirect effect predominates the indirect effects. From a modeling point of view, difficulties arise from the fact that biomass-burning aerosols can influence marine boundary layer characteristics, cloud microphysics, and cloud macrophysics, simultaneously, in competing manners and at various scales. LES studies that employ a lot of detail in boundary layer dynamics, aerosol entrainment, and microphysical processes might not capture larger-scale environmental changes triggered by the regional forcing. Inversely, regional and global climate models may represent only crudely the interactions among the transported plume, boundary layer, and low clouds. Nevertheless, by enhancing low-cloud albedo and lifetime, biomass-burning indirect effects on the SEA stratocumulus deck are likely to act in synergy with the semidirect effect, i.e., enhancing above-cloud aerosol diabatic warming and inducing additional SST cooling.

iii) Over West Africa, some studies point out a significant SDE and ERF induced by southern biomass-burning aerosol (Fig. 2.5). This signal likely results from regional-scale circulation and cloud adjustments to aerosol radiative effects generated in the core biomass-burning outflow, in addition to the "local" effects of transported aerosol. Solmon et al. (2021) shows that biomass-burning aerosols might induce an anomalous meridional circulation with an ascending branch triggered by the large aerosol diabatic heating above the southern Sc deck (as illustrated in Fig. 2.6). Northward, there is a compensating descending branch, over the West African coastal region, which is also strengthened by the stabilizing effect of aerosol episodically transported over the Gulf of Guinea and the adjacent continental region. This subsiding anomaly is associated with a local decrease of convective activity translating into a decrease of precipitation rates over coastal southern West Africa from 10°N to 5°S (Fig. 2.5). Conceptually, this regional feedback exhibits similarity with the previously discussed EHP. Both the decrease in convective cloudiness and mid-level cloud liquid-

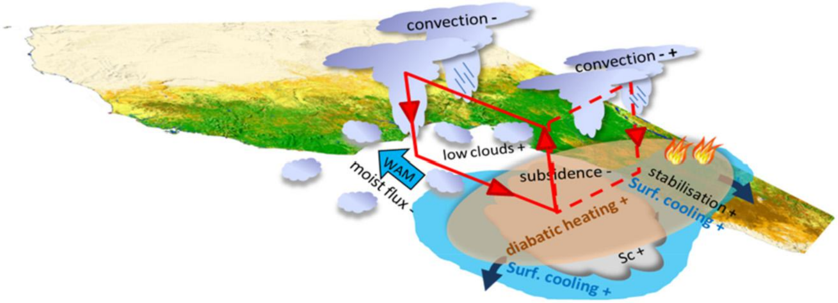

FIGURE 2.6 Schematic representation of the regional mean dynamical and precipitation feedback triggered by the southern biomass-burning aerosol outflow during WAM season.

water content results in a positive SW SDE RF over the Gulf of Guinea and coastal West Africa, and it is associated with dryer and warmer conditions. Radiatively, this positive TOA SW signal might be partly compensated by a decrease in TOA LW RF associated with convective-anvils reduction.

2.3.3.3 Importance of the regional SST feedback

Over sufficiently long time scales (seasonal to multiannual), the surface solar dimming resulting from direct, semidirect and indirect effects affect the SST over the SEA, which could affect the WAM response. Sakaeda et al. (2011), Solmon et al. (2021), indicate that aerosol could induce a regional SST cooling reaching up to −1 to −2 K. Over the Guinea gulf, the SST adjustment might contribute to enhance low level stability and cloudiness and strengthen the local decrease of precipitation already discussed. Over continental coastal regions, however, the aerosol-induced SST cooling could trigger a sea-breeze like feedback driven by a sharpening of meridional low-level thermal gradient between a colder ocean and the continent. Considered alone, this feedback leads to a slight northward shift of precipitation with a relative increase of continental precipitation in West African coastal regions and a decrease in the Gulf of Guinea. Thus, in the continental WAM domain, the mean effective precipitation response depends on the previously discussed rapid atmospheric circulation adjustment and an adjustment mediated by the SST cooling feedback. Overall, the effective change of precipitation associated with a southern-African biomass-burning aerosol perturbation might still be negative in the coastal WAM and Gulf of Guinea domain (e.g., Fig. 2.5). This signal is found to be quite robust in various regional-to-global climate modeling studies (Hirasawa et al., 2022; Shindell et al., 2023; Sakaeda et al., 2011, ...). But as argued in Solmon et al. (2021), the SST-mediated regional response is also likely to be delayed in time due to the ocean mixed-layer inertia and could become more significant (relative to the fast atmospheric adjustment) towards the end of the WAM season. Finally, beyond this regional connection, the SST mediated regional climate response is otherwise very important when analyzing global aerosol influences

(Section 2.3.4) on WAM and when discussing long-term climatic trends and projections.

2.3.4 Impact of regional and global anthropogenic aerosol sources on the WAM

In this section, we discuss more specifically the role of anthropogenic non-biomass-burning emissions. In southern West Africa, anthropogenic emissions are rapidly increasing as a result of demography and urban development (Liousse et al., 2014). High-level aerosol concentrations have been measured, inducing major air-quality and health-impact issues. Global emissions' inventories might still underestimate urban emissions in West Africa, and there is still a large uncertainty in the aerosol composition characterization. These local-to-regional sources naturally raise the question of possible regional climatic impacts, adding to dust and biomass-burning contributions, but, to date, there have been limited studies focusing on urban-emission impacts alone. For example, global studies often group urban and biomass-burning emissions for aerosol-impact assessments, despite the fact that they might have different properties, trends, and future evolutions. Based on mesoscale modeling Deroubaix et al. (2022), Taylor et al. (2019), Pante et al. (2020) argue that anthropogenic aerosol sources in west Africa induce a local stabilization associated with low-cloud cover enhancement and the inhibition of precipitation during the WAM. It is also suggested that, presently, the impact of urban emissions on coastal and regional concentrations and meteorology is dampened by a relatively high aerosol background resulting from the advection of biomass-burning particles emitted in southern and central Africa, as discussed earlier. Through competition for humidity, these particles would notably limit the indirect effect and the climatic impact of anthropogenic pollution from coastal megacities.

At a global scale, however, the WAM rainfall decadal variability has been connected to anthropogenic aerosols (mostly sulfate) and precursor trends in Europe and the USA, e.g. Monerie et al. (2023). This connection is mediated by changes in meridional SST gradients in the North Atlantic, as a result of large surface aerosol radiative-forcing variations, inducing shifts in the position of the Intertropical Convergence Zone. As an example, the Sahelian drying occurring from the 50s to early 80s, and the ensuing rainfall recovery since, have partly been attributed to the strong increase in, then decrease in, Northern Hemisphere sulfur-emission trends (Dong et al., 2014; Westervelt et al., 2018; Held et al., 2005). If global-scale aerosol variability effects are certainly a concern regarding the past and future evolution of the WAM, Shindell et al. (2023) and Wells et al. (2023) still emphasize the importance of the previously discussed regional mechanisms and the need to consider the prime role of regional emission trends in African climate-change analysis.

2.4 Regional aerosol trends and projections in Africa

2.4.1 Dust sources

Starting with dust aerosol, it should be emphasized that corresponding emissions are very much interactive with climate and land-use variability and should thus be considered as a climate–emission feedback (Thornhill et al., 2021) rather than a purely external forcing. At paleoclimatic timescales, this regional emission feedback (together with associated land-cover changes) is believed to contribute to the establishment of WAM regional climatic anomalies (through the previously discussed mechanisms), which are initially driven by global changes in SST (Mohtadi et al., 2016). There is, however, a part of dust-emission sources that could be directly associated with direct anthropogenic land-use disturbance. These "anthropogenic dust" sources could possibly explain, with large regional uncertainties, the historical increase in global dust concentration observed in proxies since 1850 (Kok et al., 2023). For the Sahel and Sahara, the anthropogenic dust contribution might, however, be less than for other source regions in the world and remains quite difficult to characterize in terms of specific climate impact (Chen et al., 2018).

In the most recent period (1980 to the present), observations suggest that North African dust activity has shown an important decadal variability, significantly correlated with the North Atlantic Oscillation activity (Xi, 2021) and other regional factors, such as the Saharan heat low activity (Lavaysse et al., 2015). After a peak corresponding to the early 80s drought, dust activity declined from 1986 to 1997 and stayed "relatively low" during most of the 2000s (Evan et al., 2016; Xi, 2021; Gupta et al., 2023). A significant increase in activity has, however, been suggested in the last decade (Xi, 2021). In terms of climate modeling, several studies have indicated that most model including online dust-cycle representations struggle to capture long-term trends and decadal variability in past dust activity (Evan et al., 2014; Kok et al., 2023). As for future projections, based on bias-corrected CMIP6 dust models exploring various climate scenarios, (Liu et al., 2024) emphasizes that the dust load is expected to increase significantly in the North African region. On the contrary, Evan et al. (2016) suggest a decrease of dust activity based on projected surface-wind analysis. Wang et al. (2015) shows that the significant anticorrelation between Sahel rainfall and dust activity observed in the historical period can be linked to the Saharan heat low activity influencing, in opposite directions, both Sahelian precipitation and surface winds over the major source regions. In this framework, a more intense monsoon would be associated to reduced dust emissions. The extent to which the associated dust–climatic effect would dampen or strengthen this relationship depends on how effective the EHP mechanism is in reality (Section 2.3.1). Reflecting these contrasting views, Thornhill et al. (2021) found that the average dust feedback calculated from a CMIP6 model ensemble was nearly zero, while pointig out a large intermodel variability and a poor representation of convection-driven emissions in GCMs.

2.4.2 Biomass burning and anthropogenic sources

For biomass burning, retrieving historical emissions is quite challenging, especially before the satellite era. Combining proxies and models, it is estimated that biomass-burning emissions in Southern-Hemisphere Africa increased from 1750 until 1950, after which emissions stabilized notably as an effect of the savannas conversion to agricultural land (van Marle et al., 2017). In recent decades, the satellite-based observation of the burned area over southern Africa shows a slightly negative trend on average, but with significant subregional variability (Chen et al., 2023). Moreover, Ramo et al. (2021) outline the potential importance of small fires underestimated by coarse-resolution sensors in total biomass-burning emissions. This could perhaps explain why, in contrast, recent AOD trend analysis based on ground and satellite observations, suggests a regional increase (0.1/decade) in southern Africa source regions over the 2000–2021 period (Gupta et al., 2023). For Northern Hemisphere African biomass burning, a more robust negative trend is pointed out. However, as mentioned earlier, there is also a significant increasing trend in non-biomass-burning anthropogenic carbonaceous aerosol emissions, notably in West Africa.

In the future, various emission scenarios are envisioned for instance through the Shared Socio Economic emission pathways framework: For Africa, regional biomass-burning emissions are generally decreasing, even in low mitigation scenarios. Other anthropogenic emissions are projected to decrease in active mitigation scenarios, but they can increase up to compensating biomass burning in low-mitigation scenarios (Wells et al., 2023). Based on a GCM analysis of the impact of regional vs global aerosol emissions on future West African climate, Shindell et al. (2023) argue that a reduction of regional aerosols co-emitted with greenhouse gas would promote enhanced WAM rainfall, consistent with mechanisms detailed earlier. Aerosol-emission control might thus be a key mitigation factor to counteract dryer boreal summer conditions otherwise projected in West Africa. Thus, the “climate penalty” of aerosol-pollution mitigation, pointed out for other part of the world, would not be at play for the specific WAM domain. Here again, uncertainties must be considered, notably linked to anthropogenic aerosol effective radiative properties and the indirect interactions with convective systems, which are not fully addressed in most GCM approaches.

2.5 Conclusion

Aerosol emitted in large quantities by African natural and anthropgenic sources can affect the WAM system through mechanisms operating at various scales, from radiation–cloud-microphysics interaction levels to regional-and-global climatic adjustments. Regionally-the major aerosol sources of dust and biomass burning are likely to perturb the energy gradients resulting in meridional shifts of the mean precipitation. In numbers of modeling studies, biomass-burning aerosols are shown to predominantly induce a negative precipitation feedback in the coastal region of the WAM domain and a southern shift of precipitation.

The picture is more contrasted for dust, depending mostly on the efficiency of the EHP mechanism conditioned by absorption/diffusion properties considered for the particles. Environmental factors, such as the presence and feedback of low clouds, the feedback of SST, and others, are also key ingredients in shaping the regional climate response. Precipitation variability is also affected by aerosols at finer temporal scales involving notably the response of convective systems to aerosol radiative and microphysical perturbations and to the modification of the regional environment in which convection develops. Case studies based on high-resolution convection-resolving modeling show that the intricacy of these effects and the ensuing convective cloud-scale adjustments prohibit us from assessing, with confidence, what are the implications of these interactions, e.g., on precipitation, at climatic time scales. However, these challenging questions are at the heart of recent and planned research projects aiming at providing better experimental constraints on aerosol–cloud interactions in African regions, and developing consistent modeling frameworks and analyses for strengthening result robustness.

As for future projections, one important challenge is to reduce uncertainties linked to dust (and other natural) emission feedback to climate and environmental changes. For instance, improving emission physics and parameterization, expanding relevant data bases through observations, and increasing climate-model resolution for representing key processes such as cold-pool induced emissions, are paths that are being actively explored. Finally, anthropogenic emissions resulting of the development of African megacities are becoming increasingly important. Assessing their impacts in more detail, and exploring the co-benefits of regional emission control in a changing climate, is also a key challenge.

References

Adebiyi, A., Kok, J., Murray, B., Ryder, C., Stuut, J., Kahn, R., Knippertz, P., Formenti, P., Mahowald, N., Pérez García-Pando, C., et al., 2023a. A review of coarse mineral dust in the Earth system. Aeolian Research 60, 100849.

Adebiyi, A.A., Akinsanola, A.A., Ajoku, O.F., 2023b. The misrepresentation of the southern African easterly jet in models and its implications for aerosol, clouds, and precipitation distributions. Journal of Climate 36, 7785–7809.

Ajoku, O., Norris, J.R., Miller, A.J., 2020. Observed monsoon precipitation suppression caused by anomalous interhemispheric aerosol transport. Climate Dynamics 54, 1077–1091.

Albrecht, B.A., 1989. Aerosols, cloud microphysics, and fractional cloudiness. Science 245, 1227–1230.

Allen, R.J., Amiri-Farahani, A., Lamarque, J.F., Smith, C., Shindell, D., Hassan, T., Chung, C.E., 2019. Observationally constrained aerosol–cloud semi-direct effects. npj Climate and Atmospheric Science 2. https://doi.org/10.1038/s41612-019-0073-9.

Balkanski, Y., Bonnet, R., Boucher, O., Checa-Garcia, R., Servonnat, J., 2021. Better representation of dust can improve climate models with too weak an African monsoon. Atmospheric Chemistry and Physics 21, 11423–11435. https://doi.org/10.5194/acp-21-11423-2021. https://acp.copernicus.org/articles/21/11423/2021/.

Bangalath, H.K., Raj, J., Stenchikov, G., 2023. Sensitivity of African easterly waves to dust forcing. Journal of Geophysical Research. Atmospheres 128, e2023JD038656. https://doi.org/10.1029/2023JD038656. https://agupubs.onlinelibrary.wiley.com/doi/abs/10.1029/2023JD038656.

Baró Pérez, A., Diamond, M.S., Bender, F.A.M., Devasthale, A., Schwarz, M., Savre, J., Tonttila, J., Kokkola, H., Lee, H., Painemal, D., Ekman, A.M.L., 2023. Comparing the simulated influence of biomass burning plumes on low-level clouds over the southeastern Atlantic under varying smoke conditions. EGUsphere 2023, 1–28. https://doi.org/10.5194/egusphere-2023-2070. https://egusphere.copernicus.org/preprints/2023/egusphere-2023-2070/.

Bellouin, N., Quaas, J., Gryspeerdt, E., Kinne, S., Stier, P., Watson-Parris, D., Boucher, O., Carslaw, K.S., Christensen, M., Daniau, A.L., et al., 2020. Bounding global aerosol radiative forcing of climate change. Reviews of Geophysics 58, e2019RG000660.

Bercos-Hickey, E., Nathan, T.R., Chen, S.H., 2017. Saharan dust and the African easterly jet–African easterly wave system: structure, location and energetics. Quarterly Journal of the Royal Meteorological Society 143, 2797–2808. https://doi.org/10.1002/qj.3128. https://rmets.onlinelibrary.wiley.com/doi/abs/10.1002/qj.3128.

Bercos-Hickey, E., Nathan, T.R., Chen, S.H., 2022. Effects of Saharan dust aerosols and West African precipitation on the energetics of African easterly waves. Journal of the Atmospheric Sciences 79, 1911–1926. https://doi.org/10.1175/JAS-D-21-0157.1. https://journals.ametsoc.org/view/journals/atsc/79/7/JAS-D-21-0157.1.xml.

Berry, G.J., Thorncroft, C.D., 2012. African easterly wave dynamics in a mesoscale numerical model: the upscale role of convection. Journal of the Atmospheric Sciences 69, 1267–1283. https://doi.org/10.1175/JAS-D-11-099.1. https://journals.ametsoc.org/view/journals/atsc/69/4/jas-d-11-099.1.xml.

Brown, H., Liu, X., Pokhrel, R., Murphy, S., Lu, Z., Saleh, R., Mielonen, T., Kokkola, H., Bergman, T., Myhre, G., Skeie, R.B., Watson-Paris, D., Stier, P., Johnson, B., Bellouin, N., Schulz, M., Vakkari, V., Beukes, J.P., van Zyl, P.G., Liu, S., Chand, D., 2021. Biomass burning aerosols in most climate models are too absorbing. Nature Communications 12, 277. https://doi.org/10.1038/s41467-020-20482-9.

Caniaux, G., Giordani, H., Redelsperger, J.L., Guichard, F., Key, E., Wade, M., 2011. Coupling between the Atlantic cold tongue and the West African monsoon in boreal spring and summer. Journal of Geophysical Research: Oceans 116. https://doi.org/10.1029/2010JC006570. https://agupubs.onlinelibrary.wiley.com/doi/abs/10.1029/2010JC006570.

Chaboureau, J.P., Labbouz, L., Flamant, C., Hodzic, A., 2022. Acceleration of the southern African easterly jet driven by the radiative effect of biomass burning aerosols and its impact on transport during aeroclo-sa. Atmospheric Chemistry and Physics 22, 8639–8658. https://doi.org/10.5194/acp-22-8639-2022. https://acp.copernicus.org/articles/22/8639/2022/.

Che, H., Stier, P., Gordon, H., Watson-Parris, D., Deaconu, L., 2020. The significant role of biomass burning aerosols in clouds and radiation in the south-eastern Atlantic Ocean. https://doi.org/10.5194/acp-2020-532.

Chen, S., Jiang, N., Huang, J., Xu, X., Zhang, H., Zang, Z., Huang, K., Xu, X., Wei, Y., Guan, X., Zhang, X., Luo, Y., Hu, Z., Feng, T., 2018. Quantifying contributions of natural and anthropogenic dust emission from different climatic regions. Atmospheric Environment 191, 94–104. https://doi.org/10.1016/j.atmosenv.2018.07.043. https://www.sciencedirect.com/science/article/pii/S1352231018304965.

Chen, Y., Hall, J., van Wees, D., Andela, N., Hantson, S., Giglio, L., van der Werf, G.R., Morton, D.C., Randerson, J.T., 2023. Multi-decadal trends and variability in burned area from the fifth version of the global fire emissions database (gfed5). Earth System Science Data 15, 5227–5259. https://doi.org/10.5194/essd-15-5227-2023. https://essd.copernicus.org/articles/15/5227/2023/.

Chung, C.E., Ramanathan, V., Decremer, D., 2012. Observationally constrained estimates of carbonaceous aerosol radiative forcing. Proceedings of the National Academy of Sciences 109, 11624–11629. https://doi.org/10.1073/pnas.1203707109.

Dajuma, A., Ogunjobi, K.O., Vogel, H., Knippertz, P., Silué, S., N'Datchoh, E.T., Yoboué, V., Vogel, B., 2020. Downward cloud venting of the central African biomass burning plume during the West Africa summer monsoon. Atmospheric Chemistry and Physics 20, 5373–5390. https://doi.org/10.5194/acp-20-5373-2020.

Dajuma, A., Silué, S., Ogunjobi, K.O., Vogel, H., N'Datchoh, E.T., Yoboué, V., Diedhiou, A., Vogel, B., 2021. Biomass Burning Effects on the Climate over Southern West Africa During the Summer Monsoon. Springer International Publishing, Cham, pp. 1515–1532.

Delbeke, L., Wang, C., Tulet, P., Denjean, C., Zouzoua, M., Maury, N., Deroubaix, A., 2023. The impact of aerosols on stratiform clouds over southern West Africa: a large-eddy-simulation study. Atmospheric Chemistry and Physics 23, 13329–13354. https://doi.org/10.5194/acp-23-13329-2023. https://acp.copernicus.org/articles/23/13329/2023/.

Deroubaix, A., Menut, L., Flamant, C., Knippertz, P., Fink, A.H., Batenburg, A., Brito, J., Denjean, C., Dione, C., Dupuy, R., Hahn, V., Kalthoff, N., Lohou, F., Schwarzenboeck, A., Siour, G., Tuccella, P., Voigt, C., 2022. Sensitivity of low-level clouds and precipitation to anthropogenic aerosol emission in southern West Africa: a dacciwa case study. Atmospheric Chemistry and Physics 22, 3251–3273. https://doi.org/10.5194/acp-22-3251-2022. https://acp.copernicus.org/articles/22/3251/2022/.

Di Biagio, C., Formenti, P., Balkanski, Y., Caponi, L., Cazaunau, M., Pangui, E., Journet, E., Nowak, S., Andreae, M.O., Kandler, K., Saeed, T., Piketh, S., Seibert, D., Williams, E., Doussin, J.F., 2019. Complex refractive indices and single-scattering albedo of global dust aerosols in the shortwave spectrum and relationship to size and iron content. Atmospheric Chemistry and Physics 19, 15503–15531. https://doi.org/10.5194/acp-19-15503-2019. https://acp.copernicus.org/articles/19/15503/2019/.

Diamond, M.S., Saide, P.E., Zuidema, P., Ackerman, A.S., Doherty, S.J., Fridlind, A.M., Gordon, H., Howes, C., Kazil, J., Yamaguchi, T., et al., 2022. Cloud adjustments from large-scale smoke–circulation interactions strongly modulate the southeastern Atlantic stratocumulus-to-cumulus transition. Atmospheric Chemistry and Physics 22, 12113–12151.

Diedhiou, A., Janicot, S., Viltard, A., de Felice, P., 1998. Evidence of two regimes of easterly waves over West Africa and the tropical Atlantic. Geophysical Research Letters 25, 2805–2808. https://doi.org/10.1029/98GL02152. https://agupubs.onlinelibrary.wiley.com/doi/abs/10.1029/98GL02152.

Dong, B., Sutton, R.T., Highwood, E., Wilcox, L., 2014. The impacts of European and Asian anthropogenic sulfur dioxide emissions on Sahel rainfall. Journal of Climate 27, 7000–7017.

Douville, H., Conil, S., Tyteca, S., Voldoire, A., 2006. Soil moisture memory and West African monsoon predictability: artefact or reality? Climate Dynamics 28, 723–742. https://doi.org/10.1007/s00382-006-0207-8. https://meteofrance.hal.science/meteo-00181733. The original publication is available at www.springerlink.com.

Eltahir, E.A.B., Gong, C., 1996. Dynamics of wet and dry years in West Africa. Journal of Climate 9, 1030–1042. https://doi.org/10.1175/1520-0442(1996)0092.0.CO;2. https://journals.ametsoc.org/view/journals/clim/9/5/1520-0442_1996_009_1030_dowady_2_0_co_2.xml.

Engelstaedter, S., Tegen, I., Washington, R., 2006. North African dust emissions and transport. Earth-Science Reviews 79, 73–100. https://doi.org/10.1016/j.earscirev.2006.06.004.

Evan, A.T., Flamant, C., Fiedler, S., Doherty, O., 2014. An analysis of aeolian dust in climate models. Geophysical Research Letters 41, 5996–6001. https://doi.org/10.1002/2014GL060545. https://agupubs.onlinelibrary.wiley.com/doi/abs/10.1002/2014GL060545.

Evan, A.T., Flamant, C., Gaetani, M., Guichard, F., 2016. The past, present and future of African dust. Nature 531, 493–495. https://doi.org/10.1038/nature17149.

Evan, A.T., Vimont, D.J., Heidinger, A.K., Kossin, J.P., Bennartz, R., 2009. The role of aerosols in the evolution of tropical North Atlantic Ocean temperature anomalies. Science 324, 778–781.

Fons, E., Runge, J., Neubauer, D., Lohmann, U., 2023. Stratocumulus adjustments to aerosol perturbations disentangled with a causal approach. npj Climate and Atmospheric Science 6, 130.

Formenti, P., D'Anna, B., Flamant, C., Mallet, M., Piketh, S.J., Schepanski, K., Waquet, F., Auriol, F., Brogniez, G., Burnet, F., Chaboureau, J.P., Chauvigné, A., Chazette, P., Denjean, C., Desboeufs, K., Doussin, J.F., Elguindi, N., Feuerstein, S., Gaetani, M., Giorio, C., Klopper, D., Mallet, M.D., Nabat, P., Monod, A., Solmon, F., Namwoonde, A., Chikwililwa, C., Mushi, R., Welton, E.J., Holben, B., 2019. The aerosols, radiation and clouds in southern Africa field campaign in Namibia: overview, illustrative observations, and way forward. Bulletin of the American Meteorological Society 100, 1277–1298. https://doi.org/10.1175/bams-d-17-0278.1.

Gibbons, M., Min, Q., Fan, J., 2018. Investigating the impacts of Saharan dust on tropical deep convection using spectral bin microphysics. Atmospheric Chemistry and Physics 18, 12161–12184. https://doi.org/10.5194/acp-18-12161-2018. https://acp.copernicus.org/articles/18/12161/2018/.

Ginoux, P., Prospero, J.M., Gill, T.E., Hsu, N.C., Zhao, M., 2012. Global-scale attribution of anthropogenic and natural dust sources and their emission rates based on modis deep blue aerosol products. Reviews of Geophysics 1985, 50.

Gordon, H., Field, P.R., Abel, S.J., Dalvi, M., Grosvenor, D.P., Hill, A.A., Johnson, B.T., Miltenberger, A.K., Yoshioka, M., Carslaw, K.S., 2018. Large simulated radiative effects of smoke in the South-East Atlantic. Atmospheric Chemistry and Physics 18, 15261–15289. https://doi.org/10.5194/acp-18-15261-2018.

Grogan, D.F., Thorncroft, C.D., 2019. The characteristics of African easterly waves coupled to Saharan mineral dust aerosols. Quarterly Journal of the Royal Meteorological Society 145, 1130–1146. https://doi.org/10.1002/qj.3483. https://rmets.onlinelibrary.wiley.com/doi/abs/10.1002/qj.3483.

Gupta, G., Venkat Ratnam, M., Madhavan, B., Jayaraman, A., 2023. Global trends in the aerosol optical, physical, and morphological properties obtained using multi-sensor measurements. Atmospheric Environment 295, 119569. https://doi.org/10.1016/j.atmosenv.2022.119569. https://www.sciencedirect.com/science/article/pii/S1352231022006343.

Haywood, J., Francis, P., Osborne, S., Glew, M., Loeb, N., Highwood, E., Tanré, D., Myhre, G., Formenti, P., Hirst, E., 2003. Radiative properties and direct radiative effect of Saharan dust measured by the c-130 aircraft during shade: 1. Solar spectrum. Journal of Geophysical Research. Atmospheres 108. https://doi.org/10.1029/2002JD002687. https://agupubs.onlinelibrary.wiley.com/doi/abs/10.1029/2002JD002687.

Haywood, J.M., Abel, S.J., Barrett, P.A., Bellouin, N., Blyth, A., Bower, K.N., Brooks, M., Carslaw, K., Che, H., Coe, H., Cotterell, M.I., Crawford, I., Cui, Z., Davies, N., Dingley, B., Field, P., Formenti, P., Gordon, H., de Graaf, M., Herbert, R., Johnson, B., Jones, A.C., Langridge, J.M., Malavelle, F., Partridge, D.G., Peers, F., Redemann, J., Stier, P., Szpek, K., Taylor, J.W., Watson-Parris, D., Wood, R., Wu, H., Zuidema, P., 2020. Overview: the cloud-aerosol-radiation interaction and forcing: Year-2017 (clarify-2017) measurement campaign. https://doi.org/10.5194/acp-2020-729.

Held, I.M., Delworth, T.L., Lu, J., Findell, K.L., Knutson, T.R., 2005. Simulation of Sahel drought in the 20th and 21st centuries. Proceedings of the National Academy of Sciences 102, 17891–17896. https://doi.org/10.1073/pnas.0509057102. https://www.pnas.org/doi/abs/10.1073/pnas.0509057102.

Heyblom, K.B., Singh, H.A., Rasch, P.J., DeRepentigny, P., 2022. Increased variability of biomass burning emissions in cmip6 amplifies hydrologic cycle in the cesm2 large ensemble. Geophysical Research Letters 49, e2021GL096868. https://doi.org/10.1029/2021GL096868. https://agupubs.onlinelibrary.wiley.com/doi/abs/10.1029/2021GL096868.

Hirasawa, H., Kushner, P.J., Sigmond, M., Fyfe, J., Deser, C., 2022. Evolving Sahel rainfall response to anthropogenic aerosols driven by shifting regional oceanic and emission influences. Journal of Climate 35, 3181–3193. https://doi.org/10.1175/JCLI-D-21-0795.1. https://journals.ametsoc.org/view/journals/clim/35/11/JCLI-D-21-0795.1.xml.

Hodnebrog, Ø., Myhre, G., Forster, P.M., Sillmann, J., Samset, B.H., 2016. Local biomass burning is a dominant cause of the observed precipitation reduction in southern Africa. Nature Communications 7. https://doi.org/10.1038/ncomms11236.

Hoose, C., Möhler, O., 2012. Heterogeneous ice nucleation on atmospheric aerosols: a review of results from laboratory experiments. Atmospheric Chemistry and Physics 12, 9817–9854. https://doi.org/10.5194/acp-12-9817-2012. https://acp.copernicus.org/articles/12/9817/2012/.

Hosseinpour, F., Wilcox, E.M., 2024. A new look into the impacts of dust radiative effects on the energetics of tropical easterly waves. Atmospheric Chemistry and Physics 24, 707–724. https://doi.org/10.5194/acp-24-707-2024. https://acp.copernicus.org/articles/24/707/2024/.

Huang, C.C., Chen, S.H., Lin, Y.C., Earl, K., Matsui, T., Lee, H.H., Tsai, I.C., Chen, J.P., Cheng, C.T., 2019. Impacts of dust–radiation versus dust–cloud interactions on the development of a modeled mesoscale convective system over North Africa. Monthly Weather Review 147, 3301–3326. https://doi.org/10.1175/MWR-D-18-0459.1. https://journals.ametsoc.org/view/journals/mwre/147/9/mwr-d-18-0459.1.xml.

Irvine, W.M., 1965. Light scattering by spherical particles: radiation pressure, asymmetry factor, and extinction cross section. JOSA 55, 16–21.

Jordan, A.K., Gnanadesikan, A., Zaitchik, B., 2018. Simulated dust aerosol impacts on western Sahelian rainfall: importance of ocean coupling. Journal of Climate 31, 9107–9124. https://doi.org/10.1175/JCLI-D-17-0819.1. https://journals.ametsoc.org/view/journals/clim/31/22/jcli-d-17-0819.1.xml.

Jury, M.R., Santiago, M.J., 2010. Composite analysis of dust impacts on African easterly waves in the moderate resolution imaging spectrometer era. Journal of Geophysical Research. Atmospheres 115. https://doi.org/10.1029/2009JD013612. https://agupubs.onlinelibrary.wiley.com/doi/abs/10.1029/2009JD013612.

Kärcher, B., DeMott, P.J., Jensen, E.J., Harrington, J.Y., 2022. Studies on the competition between homogeneous and heterogeneous ice nucleation in cirrus formation. Journal of Geophysical Research. Atmospheres 127, e2021JD035805. https://doi.org/10.1029/2021JD035805. https://agupubs.onlinelibrary.wiley.com/doi/abs/10.1029/2021JD035805.

Kaufman, Y.J., Tanré, D., Dubovik, O., Karnieli, A., Remer, L.A., 2001. Absorption of sunlight by dust as inferred from satellite and ground-based remote sensing. Geophysical Research Letters 28, 1479–1482. https://doi.org/10.1029/2000GL012647. https://agupubs.onlinelibrary.wiley.com/doi/abs/10.1029/2000GL012647.

Kniffka, A., Knippertz, P., Fink, A.H., 2019. The role of low-level clouds in the West African monsoon system. Atmospheric Chemistry and Physics 19, 1623–1647. https://doi.org/10.5194/acp-19-1623-2019. https://acp.copernicus.org/articles/19/1623/2019/.

Knippertz, P., Coe, H., Chiu, J.C., Evans, M.J., Fink, A.H., Kalthoff, N., Liousse, C., Mari, C., Allan, R.P., Brooks, B., Danour, S., Flamant, C., Jegede, O.O., Lohou, F., Marsham, J.H., 2015. The dacciwa project: dynamics–aerosol–chemistry–cloud interactions in West Africa. Bulletin of the American Meteorological Society 96, 1451–1460. https://doi.org/10.1175/BAMS-D-14-00108.1. https://journals.ametsoc.org/view/journals/bams/96/9/bams-d-14-00108.1.xml.

Knippertz, P., Todd, M.C., 2012. Mineral dust aerosols over the Sahara: meteorological controls on emission and transport and implications for modeling. Reviews of Geophysics 50. https://doi.org/10.1029/2011RG000362. https://agupubs.onlinelibrary.wiley.com/doi/abs/10.1029/2011RG000362.

Knopf, D.A., Alpert, P.A., 2023. Atmospheric ice nucleation. Nature Reviews Physics 5, 203–217. https://doi.org/10.1038/s42254-023-00570-7.

Kok, J.F., Storelvmo, T., Karydis, V.A., Adebiyi, A.A., Mahowald, N.M., Evan, A.T., He, C., Leung, D.M., 2023. Mineral dust aerosol impacts on global climate and climate change. Nature Reviews Earth & Environment 4, 71–86.

Köhler, H., 1936. The nucleus in and the growth of hygroscopic droplets. Transactions of the Faraday Society 32, 1152–1161. https://doi.org/10.1039/TF9363201152.

Lau, K.M., Kim, K.M., Sud, Y.C., Walker, G.K., 2009. A gcm study of the response of the atmospheric water cycle of West Africa and the Atlantic to Saharan dust radiative forcing. Annales Geophysicae 27, 4023–4037. https://doi.org/10.5194/angeo-27-4023-2009.

Lavaysse, C., Flamant, C., Evan, A.T., Janicot, S., Gaetani, M., 2015. Recent climatological trend of the Saharan Heat Low and its impact in West African climate. https://insu.hal.science/insu-01183132. P–3330–46, poster.

Liao, H., Seinfeld, J.H., 1998. Radiative forcing by mineral dust aerosols: sensitivity to key variables. Journal of Geophysical Research. Atmospheres 103, 31637–31645. https://

doi.org/10.1029/1998JD200036. https://agupubs.onlinelibrary.wiley.com/doi/abs/10.1029/1998JD200036.

Liousse, C., Assamoi, E., Criqui, P., Granier, C., Rosset, R., 2014. Explosive growth in African combustion emissions from 2005 to 2030. Environmental Research Letters 9, 035003. https://doi.org/10.1088/1748-9326/9/3/035003.

Liu, J., Wang, X., Wu, D., Wei, H., Li, Y., Ji, M., 2024. Historical footprints and future projections of global dust burden from bias-corrected cmip6 models. npj Climate and Atmospheric Science 7, 1. https://doi.org/10.1038/s41612-023-00550-9.

Liu, M., Westphal, D.L., Wang, S., Shimizu, A., Sugimoto, N., Zhou, J., Chen, Y., 2003. A high-resolution numerical study of the Asian dust storms of April 2001. Journal of Geophysical Research. Atmospheres 108.

Lohmann, U., Feichter, J., 2005. Global indirect aerosol effects: a review. Atmospheric Chemistry and Physics 5, 715–737. https://doi.org/10.5194/acp-5-715-2005. https://acp.copernicus.org/articles/5/715/2005/.

Lu, Z., Liu, X., Zhang, Z., Zhao, C., Meyer, K., Rajapakshe, C., Wu, C., Yang, Z., Penner, J.E., 2018. Biomass smoke from southern Africa can significantly enhance the brightness of stratocumulus over the southeastern Atlantic Ocean. Proceedings of the National Academy of Sciences 115, 2924–2929. https://doi.org/10.1073/pnas.1713703115.

Mallet, M., Nabat, P., Johnson, B., Michou, M., Haywood, J.M., Chen, C., Dubovik, O., 2021. Climate models generally underrepresent the warming by central Africa biomass-burning aerosols over the southeast Atlantic. Science Advances 7, eabg9998. https://doi.org/10.1126/sciadv.abg9998. https://www.science.org/doi/abs/10.1126/sciadv.abg9998.

Mallet, M., Solmon, F., Nabat, P., Elguindi, N., Waquet, F., Bouniol, D., Sayer, A.M., Meyer, K., Roehrig, R., Michou, M., Zuidema, P., Flamant, C., Redemann, J., Formenti, P., 2020. Direct and semi-direct radiative forcing of biomass burning aerosols over the southeast Atlantic (SEA) and its sensitivity to absorbing properties: a regional climate modeling study. Atmospheric Chemistry and Physics Discussions 2020, 1–39. https://doi.org/10.5194/acp-2020-317. https://acp.copernicus.org/preprints/acp-2020-317/.

Mari, C., Cailley, G., Corre, L., Saunois, M., Attié, J.L., Thouret, V., Stohl, A., 2008. Tracing biomass burning plumes from the Southern Hemisphere during the AMMA 2006 wet season experiment. https://doi.org/10.5194/acp-8-3951-2008. https://hal.science/hal-00330650, 2008. 7–12 September 2008.

van Marle, M.J.E., Kloster, S., Magi, B.I., Marlon, J.R., Daniau, A.L., Field, R.D., Arneth, A., Forrest, M., Hantson, S., Kehrwald, N.M., Knorr, W., Lasslop, G., Li, F., Mangeon, S., Yue, C., Kaiser, J.W., van der Werf, G.R., 2017. Historic global biomass burning emissions for cmip6 (bb4cmip) based on merging satellite observations with proxies and fire models (1750–2015). Geoscientific Model Development 10, 3329–3357. https://doi.org/10.5194/gmd-10-3329-2017. https://gmd.copernicus.org/articles/10/3329/2017/.

Martínez, I.R., Chaboureau, J.P., 2018. Precipitation and mesoscale convective systems: radiative impact of dust over northern Africa. Monthly Weather Review 146, 3011–3029. https://doi.org/10.1175/MWR-D-18-0103.1. https://journals.ametsoc.org/view/journals/mwre/146/9/mwr-d-18-0103.1.xml.

Menut, L., Flamant, C., Turquety, S., Deroubaix, A., Chazette, P., Meynadier, R., 2018. Impact of biomass burning on pollutant surface concentrations in megacities of the gulf of Guinea. Atmospheric Chemistry and Physics 18, 2687–2707. https://doi.org/10.5194/acp-18-2687-2018. https://acp.copernicus.org/articles/18/2687/2018/.

Miller, R.L., Knippertz, P., Pérez García-Pando, C., Perlwitz, J.P., Tegen, I., 2014. Impact of Dust Radiative Forcing upon Climate. Springer, Dordrecht, the Netherlands, pp. 327–357.

Miller, R.L., Tegen, I., 1998. Climate response to soil dust aerosols. Journal of Climate 11, 3247–3267. https://doi.org/10.1175/1520-0442(1998)011<3247:CRTSDA>2.0.CO;2.

Min, Q.L., Li, R., Li, B., Joseph, E., Morris, V., Hu, Y., Li, S.W., Wang, S. Impacts of mineral dust on ice clouds in tropical deep convection systems. Atmospheric Research 143, 64–72. https://doi.org/10.1016/j.atmosres.2014.01.026.

Mohtadi, M., Prange, M., Steinke, S., 2016. Palaeoclimatic insights into forcing and response of monsoon rainfall. Nature 533, 191–199. https://doi.org/10.1038/nature17450

.

Monerie, P.A., Dittus, A.J., Wilcox, L.J., Turner, A.G., 2023. Uncertainty in simulating twentieth century West African precipitation trends: the role of anthropogenic aerosol emissions. Earth's Future 11, e2022EF002995. https://doi.org/10.1029/2022EF002995. https://agupubs.onlinelibrary.wiley.com/doi/abs/10.1029/2022EF002995.

Paeth, H., Born, K., Girmes, R., Podzun, R., Jacob, D., 2009. Regional climate change in tropical and northern Africa due to greenhouse forcing and land use changes. Journal of Climate 22, 114–132. https://doi.org/10.1175/2008JCLI2390.1. https://journals.ametsoc.org/view/journals/clim/22/1/2008jcli2390.1.xml.

Pante, G., Knippertz, P., Fink, A.H., Kniffka, A., 2020. Increasing manmade air pollution likely to reduce rainfall in southern West Africa. https://doi.org/10.5194/acp-2020-463.

Pausata, F.S., Messori, G., Zhang, Q., 2016. Impacts of dust reduction on the northward expansion of the African monsoon during the green Sahara period. Earth and Planetary Science Letters 434, 298–307. https://doi.org/10.1016/j.epsl.2015.11.049. https://www.sciencedirect.com/science/article/pii/S0012821X15007530.

Petters, M.D., Kreidenweis, S.M., 2007. A single parameter representation of hygroscopic growth and cloud condensation nucleus activity. Atmospheric Chemistry and Physics 7, 1961–1971. https://doi.org/10.5194/acp-7-1961-2007. https://acp.copernicus.org/articles/7/1961/2007/.

Prospero, J.M., Ginoux, P., Torres, O., Nicholson, S.E., Gill, T.E., 2002. Environmental characterization of global sources of atmospheric soil dust identified with the nimbus 7 total ozone mapping spectrometer (toms) absorbing aerosol product. Reviews of Geophysics 40, 2-1–2-31. https://doi.org/10.1029/2000RG000095. https://agupubs.onlinelibrary.wiley.com/doi/abs/10.1029/2000RG000095.

Ramo, R., Roteta, E., Bistinas, I., van Wees, D., Bastarrika, A., Chuvieco, E., van der Werf, G.R., 2021. African burned area and fire carbon emissions are strongly impacted by small fires undetected by coarse resolution satellite data. Proceedings of the National Academy of Sciences 118, e2011160118. https://doi.org/10.1073/pnas.2011160118. https://www.pnas.org/doi/abs/10.1073/pnas.2011160118.

Redemann, J., Wood, R., Zuidema, P., Doherty, S.J., Luna, B., LeBlanc, S.E., Diamond, M.S., Shinozuka, Y., Chang, I.Y., Ueyama, R., Pfister, L., Ryoo, J.m., Dobracki, A.N., da Silva, A.M., Longo, K.M., Kacenelenbogen, M.S., Flynn, C.J., Pistone, K., Knox, N.M., Piketh, S.J., Haywood, J.M., Formenti, P., Mallet, M., Stier, P., Ackerman, A.S., Bauer, S.E., Fridlind, A.M., Carmichael, G.R., Saide, P.E., Ferrada, G.A., Howell, S.G., Freitag, S., Cairns, B., Holben, B.N., Knobelspiesse, K.D., Tanelli, S., L'Ecuyer, T.S., Dzambo, A.M., Sy, O.O., McFarquhar, G.M., Poellot, M.R., Gupta, S., O'Brien, J.R., Nenes, A., Kacarab, M.E., Wong, J.P.S., Small-Griswold, J.D., Thornhill, K.L., Noone, D., Podolske, J.R., Schmidt, K.S., Pilewskie, P., Chen, H., Cochrane, S.P., Sedlacek, A.J., Lang, T.J., Stith, E., Segal-Rozenhaimer, M., Ferrare, R.A., Burton, S.P., Hostetler, C.A., Diner, D.J., Platnick, S.E., Myers, J.S., Meyer, K.G., Spangenberg, D.A., Maring, H., Gao, L., 2020. An overview of the oracles (observations of aerosols above clouds and their interactions) project: aerosol-cloud-radiation interactions in the southeast Atlantic basin. https://doi.org/10.5194/acp-2020-449.

Russell, J.O.H., Aiyyer, A., Dylan White, J., 2020. African easterly wave dynamics in convection-permitting simulations: rotational stratiform instability as a conceptual model. Journal of Advances in Modeling Earth Systems 12, e2019MS001706. https://doi.org/10.1029/2019MS001706. https://agupubs.onlinelibrary.wiley.com/doi/abs/10.1029/2019MS001706.

Sakaeda, N., Wood, R., Rasch, P.J., 2011. Direct and semidirect aerosol effects of southern African biomass burning aerosol. Journal of Geophysical Research 116. https://doi.org/10.1029/2010jd015540.

Schepanski, K., Tegen, I., Laurent, B., Heinold, B., Macke, A., 2007. A new Saharan dust source activation frequency map derived from msg-seviri ir-channels. Geophysical Research Letters 34. https://doi.org/10.1029/2007GL030168. https://agupubs.onlinelibrary.wiley.com/doi/abs/10.1029/2007GL030168.

Schulz, M., Textor, C., Kinne, S., Balkanski, Y., Bauer, S., Berntsen, T., Berglen, T., Boucher, O., Dentener, F., Guibert, S., Isaksen, I.S.A., Iversen, T., Koch, D., Kirkevåg, A., Liu, X., Montanaro, V., Myhre, G., Penner, J.E., Pitari, G., Reddy, S., Seland, Ø., Stier, P., Takemura, T., 2006. Radiative forcing by aerosols as derived from the aerocom present-day and pre-industrial simulations. Atmospheric Chemistry and Physics 6, 5225–5246. https://doi.org/10.5194/acp-6-5225-2006. https://acp.copernicus.org/articles/6/5225/2006/.

Seigel, R.B., van den Heever, S.C., Saleeby, S.M., 2013. Mineral dust indirect effects and cloud radiative feedbacks of a simulated idealized nocturnal squall line. Atmospheric Chemistry and Physics 13, 4467–4485. https://doi.org/10.5194/acp-13-4467-2013. https://acp.copernicus.org/articles/13/4467/2013/.

Shindell, D., Parsons, L., Faluvegi, G., Hicks, K., Kuylenstierna, J., Heaps, C., 2023. The important role of African emissions reductions in projected local rainfall changes. npj Climate and Atmospheric Science 6, 47. https://doi.org/10.1038/s41612-023-00382-7.

Smith, C.J., Kramer, R.J., Myhre, G., Alterskjær, K., Collins, W., Sima, A., Boucher, O., Dufresne, J.L., Nabat, P., Michou, M., Yukimoto, S., Cole, J., Paynter, D., Shiogama, H., O'Connor, F.M., Robertson, E., Wiltshire, A., Andrews, T., Hannay, C., Miller, R., Nazarenko, L., Kirkevåg, A., Olivié, D., Fiedler, S., Lewinschal, A., Mackallah, C., Dix, M., Pincus, R., Forster, P.M., 2020. Effective radiative forcing and adjustments in cmip6 models. Atmospheric Chemistry and Physics 20, 9591–9618. https://doi.org/10.5194/acp-20-9591-2020. https://acp.copernicus.org/articles/20/9591/2020/.

Solmon, F., Elguindi, N., Mallet, M., 2012. Radiative and climatic effects of dust over West Africa, as simulated by a regional climate model. Climate Research 52, 97–113.

Solmon, F., Elguindi, N., Mallet, M., Flamant, C., Formenti, P., 2021. West African monsoon precipitation impacted by the south eastern Atlantic biomass burning aerosol outflow. npj Climate and Atmospheric Science 4, 54.

Solmon, F., Mallet, M., Elguindi, N., Giorgi, F., Zakey, A., Konaré, A., 2008. Dust aerosol impact on regional precipitation over Western Africa, mechanisms and sensitivity to absorption properties. Geophysical Research Letters 35. https://doi.org/10.1029/2008GL035900.

Takeishi, A., Wang, C., 2021. Radiative and microphysical responses of clouds to an anomalous increase in fire particles over the maritime continent in 2015. Atmospheric Chemistry & Physics Discussions.

Taylor, J.W., Haslett, S.L., Bower, K., Flynn, M., Crawford, I., Dorsey, J., Choularton, T., Connolly, P.J., Hahn, V., Voigt, C., Sauer, D., Dupuy, R., Brito, J., Schwarzenboeck, A., Bourriane, T., Denjean, C., Rosenberg, P., Flamant, C., Lee, J.D., Vaughan, A.R., Hill, P.G., Brooks, B., Catoire, V., Knippertz, P., Coe, H., 2019. Aerosol influences on low-level clouds in the West African monsoon. Atmospheric Chemistry and Physics 19, 8503–8522. https://doi.org/10.5194/acp-19-8503-2019.

Thornhill, G., Collins, W., Olivié, D., Skeie, R.B., Archibald, A., Bauer, S., Checa-Garcia, R., Fiedler, S., Folberth, G., Gjermundsen, A., Horowitz, L., Lamarque, J.F., Michou, M., Mulcahy, J., Nabat, P., Naik, V., O'Connor, F.M., Paulot, F., Schulz, M., Scott, C.E., Séférian, R., Smith, C., Takemura, T., Tilmes, S., Tsigaridis, K., Weber, J., 2021. Climate-driven chemistry and aerosol feedbacks in cmip6 Earth system models. Atmospheric Chemistry and Physics 21, 1105–1126. https://doi.org/10.5194/acp-21-1105-2021. https://acp.copernicus.org/articles/21/1105/2021/.

Tosca, M.G., Diner, D.J., Garay, M.J., Kalashnikova, O.V., 2015. Human-caused fires limit convection in tropical Africa: first temporal observations and attribution. Geophysical Research Letters 42, 6492–6501. https://doi.org/10.1002/2015GL065063. https://agupubs.onlinelibrary.wiley.com/doi/abs/10.1002/2015GL065063.

Tummon, F., Solmon, F., Liousse, C., Tadross, M., 2010. Simulation of the direct and semidirect aerosol effects on the southern Africa regional climate during the biomass burning season. Journal of Geophysical Research 115. https://doi.org/10.1029/2009jd013738.

Twomey, S., 1974. Pollution and the planetary albedo. Atmospheric Environment 1967 (8), 1251–1256. https://doi.org/10.1016/0004-6981(74)90004-3.

Wang, W., Evan, A.T., Flamant, C., Lavaysse, C., 2015. On the decadal scale correlation between African dust and Sahel rainfall: the role of Saharan heat low–forced winds. Science Advances 1, e1500646. https://doi.org/10.1126/sciadv.1500646. https://www.science.org/doi/abs/10.1126/sciadv.1500646.

Wells, C.D., Kasoar, M., Bellouin, N., Voulgarakis, A., 2023. Local and remote climate impacts of future African aerosol emissions. Atmospheric Chemistry and Physics 23, 3575–3593. https://doi.org/10.5194/acp-23-3575-2023. https://acp.copernicus.org/articles/23/3575/2023/.

Westervelt, D.M., Conley, A.J., Fiore, A.M., Lamarque, J.F., Shindell, D.T., Previdi, M., Mascioli, N.R., Faluvegi, G., Correa, G., Horowitz, L.W., 2018. Connecting regional aerosol emissions reductions to local and remote precipitation responses. Atmospheric Chemistry and Physics 18, 12461–12475.

Wilcox, E.M., 2010. Stratocumulus cloud thickening beneath layers of absorbing smoke aerosol. Atmospheric Chemistry and Physics 10, 11769–11777. https://doi.org/10.5194/acp-10-11769-2010.

Xi, X., 2021. Revisiting the recent dust trends and climate drivers using horizontal visibility and present weather observations. Journal of Geophysical Research. Atmospheres 126, e2021JD034687. https://doi.org/10.1029/2021JD034687. https://agupubs.onlinelibrary.wiley.com/doi/abs/10.1029/2021JD034687.

Yoshioka, M., Mahowald, N.M., Conley, A.J., Collins, W.D., Fillmore, D.W., Zender, C.S., Coleman, D.B., 2007. Impact of desert dust radiative forcing on Sahel precipitation: relative importance of dust compared to sea surface temperature variations, vegetation changes, and greenhouse gas warming. Journal of Climate 20, 1445–1467. https://doi.org/10.1175/JCLI4056.1. https://journals.ametsoc.org/view/journals/clim/20/8/jcli4056.1.xml.

Yuan, T., Song, H., Wood, R., Oreopoulos, L., Platnick, S., Wang, C., Yu, H., Meyer, K., Wilcox, E., 2023. Observational evidence of strong forcing from aerosol effect on low cloud coverage. Science Advances 9, eadh7716. https://doi.org/10.1126/sciadv.adh7716. https://www.science.org/doi/abs/10.1126/sciadv.adh7716.

Yue, X., Liao, H., Wang, H.J., Li, S.L., Tang, J.P., 2011. Role of sea surface temperature responses in simulation of the climatic effect of mineral dust aerosol. Atmospheric Chemistry and Physics 11, 6049–6062. https://doi.org/10.5194/acp-11-6049-2011. https://acp.copernicus.org/articles/11/6049/2011/.

Zakey, A., Solmon, F., Giorgi, F., 2006. Implementation and testing of a desert dust module in a regional climate model. Atmospheric Chemistry and Physics 6, 4687–4704.

Zang, L., Rosenfeld, D., Pan, Z., Mao, F., Zhu, Y., Lu, X., Gong, W., 2023. Observing aerosol primary convective invigoration and its meteorological feedback. Geophysical Research Letters 50, e2023GL104151. https://doi.org/10.1029/2023GL104151. https://agupubs.onlinelibrary.wiley.com/doi/abs/10.1029/2023GL104151.

Zender, C.S., Bian, H., Newman, D., 2003. Mineral dust entrainment and deposition (dead) model: description and 1990s dust climatology. Journal of Geophysical Research. Atmospheres 108.

Zhao, C., Liu, X., Ruby Leung, L., Hagos, S., 2011. Radiative impact of mineral dust on monsoon precipitation variability over West Africa. Atmospheric Chemistry and Physics 11, 1879–1893. https://doi.org/10.5194/acp-11-1879-2011. https://acp.copernicus.org/articles/11/1879/2011/.

Chapter 3

Impacts of dust aerosols on the climate of the tropical Atlantic

Farnaz Hosseinpour[a,b]
[a]*Desert Research Institute, Reno, NV, United States,* [b]*University of Nevada Reno, Reno, NV, United States*

3.1 Introduction

Aerosols play a crucial role in the environment and the Earth's system by affecting Earth's radiation budget through various mechanisms, including absorbing and scattering shortwave radiation and absorbing, scattering, and emitting longwave radiation (Dufresne et al., 2002; Mamun et al., 2021). Aerosols also exhibit indirect effects, serving as ice nuclei (IN) and cloud condensation nuclei (CCN) to create ice particles and cloud droplets (Twomey, 1977; Hoose and Möhler, 2012). The impacts of aerosols extend to health conditions through the deterioration of air quality (Querol et al., 2019), influence biogeochemical cycles by providing nutrients for plant growth (Yu et al., 2015), and modify the hydrological cycle by altering static stability, vertical motion, clouds, and convection (Myhre et al., 2017). Furthermore, aerosols affect atmospheric circulation by changing diabatic heating and transient changes in the wind shear and instability of the region (Hosseinpour and Wilcox, 2024). Each aerosol species possesses unique physical and chemical characteristics. The spatial and temporal variability of aerosol species and their quantities introduce significant uncertainty into the quantification of their impacts on the Earth system, affecting both observational and modeling studies (Samset, 2022). The aerosol direct and indirect effects represent the largest source of uncertainty in total anthropogenic radiative forcing, and, despite research efforts over the past decades, this uncertainty has not significantly diminished (Lohmann and Feichter, 2005; Forster et al., 2021). Therefore, improving our understanding of aerosol processes is essential for enhancing the accuracy of climate model predictions.

Two sources contribute to the origin of aerosols: primary and secondary. Primary aerosols are directly emitted into the atmosphere, including particles like mineral dust, sea salt, black carbon, and primary organic aerosols. Secondary aerosols form as a result of chemical reactions of gases in the atmosphere, leading to the creation of substances such as sulfate, nitrate, and secondary organic aerosols. Additionally, aerosols are categorized as natural (e.g., sea salt, most

Aerosols and Precipitation Over Africa. https://doi.org/10.1016/B978-0-44-314050-1.00008-6

mineral dust) or anthropogenic (e.g., most black carbon, sulfate, nitrate) based on whether they are formed by natural processes or human activities.

Among aerosols, Saharan dust plays a key role in the global climate and, in particular, North Africa and the Atlantic Ocean. Understanding the influence of Saharan dust on climate necessitates a comprehensive understanding of the mechanisms governing its emission, transport, and interactions with radiation, clouds, precipitation, and meteorological conditions. This chapter aims to present an overview of the influence of Saharan dust on the tropical Atlantic climate. Saharan dust aerosols have significant impacts on weather patterns, atmospheric stability, and hydrological cycles across the Atlantic region. This chapter is structured to first introduce the fundamental characteristics and sources of Saharan dust. Following this, we discuss how Saharan dust affects radiation through direct, semidirect, and indirect effects. The subsequent sections describe the specific climatic impacts of dust, including its effects on tropical cyclones, precipitation patterns, and cloud formation. The chapter concludes with a discussion of the challenges and future directions in dust–climate interaction research, emphasizing the need for enhanced observational capabilities and model accuracy.

3.2 General characteristics of dust aerosols

Covering over nine million km^2 across North Africa, the Sahara desert stands as the largest hot desert globally and serves as the primary source of mineral dust exported into the atmosphere, contributing approximately 50% of the total global dust (Kok et al., 2021). The Sahara's annual dust contribution averages around 1500 Tg per year (Ginoux et al., 2012). Further, dried lakes in arid and semiarid regions are significant dust sources, with Lake Chad being the main contributor in North Africa (Prospero et al., 2002). While agricultural and industrial activities in Africa can generate mineral dust, natural processes, especially wind erosion, account for over 90% of Saharan dust, wherein winds lift soil particles into the atmosphere, with the rate of dust emission heavily influenced by surface wind speeds. Dust radiative heating in the boundary layer can, in turn, modify wind speed, indicating a dust–wind feedback mechanism (Heinold et al., 2008). Other important factors in dust emission are vegetation phenology, soil type, and soil moisture (Shao, 2004; Xi and Sokolik, 2015; Kim et al., 2017). Lower soil moisture levels result in weaker cohesion between soil particles, favoring higher dust-emission rates (Huang and Hartemink, 2020).

Enhanced concentrations of Saharan dust in the atmosphere occur during the boreal summer months (June to August), coinciding with the peak of activity of the African Easterly Jet (AEJ) and African Easterly Waves (AEWs). These atmospheric phenomena facilitate the transport of dust over the tropical Atlantic Ocean within the Saharan Air Layer (SAL), characterized by a dust-laden, hot, and dry air mass extending from the surface to the middle troposphere (approximately 600 hPa) (Liu et al., 2008). Conversely, the lowest dust concentration is

18 June 2020, NOAA-20 VIIRS

18 June 2020, Aqua/MODIS

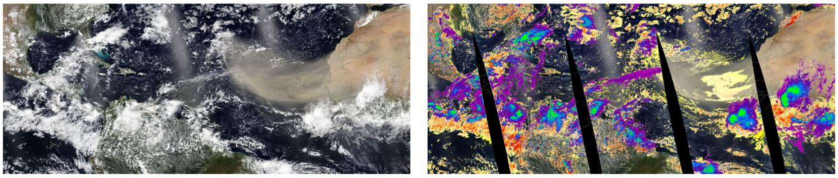

22 June 2020, NOAA-20 VIIRS

22 June 2020, Aqua/MODIS

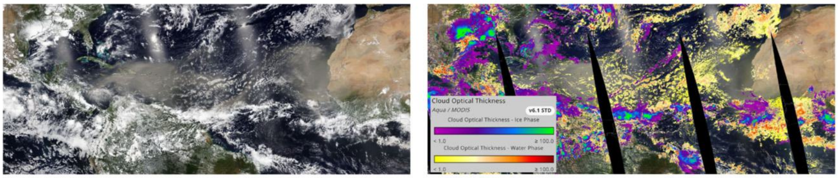

FIGURE 3.1 The *Godzilla* dust storm in June 2020 was one of the largest dust events ever recorded. Satellite imagery from NOAA-20 VIIRS visible band and Aqua/MODIS visible band and cloud optical thickness (COT) retrievals for two days are shown here. Note that the COT retrievals erroneously recognize thick layer of dust offshore of Northwestern Africa as low-level clouds. Images and data obtained from NASA Worldview website. https://worldview.earthdata.nasa.gov/.

observed during the boreal winter months (December to February), despite the continued presence of dust transport (Engelstaedter et al., 2006). The Amazon rainforest has notably benefited from the transport of Saharan dust because it leads to the deposition of nutrients, particularly phosphorus, from mineral dust (Mahowald et al., 2005; Yu et al., 2015). As a result of desert dust contributing approximately 95% of atmospheric iron globally (Mahowald et al., 2009), phytoplankton in various oceans, such as the Atlantic Ocean and the Caribbean Sea, benefit from Saharan dust as a vital nutrient source.

Moreover, dust events can lead to extreme weather conditions (Querol et al., 2019). Due to their considerable radiative effect, dust aerosols in the SAL strongly interact with weather and climate through their impacts on cloud processes (Weinzierl et al., 2017; Haarig et al., 2019), precipitation (Lau et al., 2009; Kim et al., 2010; Bercos-Hickey et al., 2020), and atmospheric circulation (Wilcox, 2010; Ming and Ramaswamy, 2011; Hosseinpour and Wilcox, 2014; Grogan et al., 2022; Hosseinpour and Wilcox, 2024). In June 2020, a record-breaking extreme dust storm, known as the "Godzilla" dust storm (Fig. 3.1), transported a significant amount of dust aerosols across the tropical Atlantic (Chang and Hosseinpour, 2023) that reached North America (Pu and Jin, 2021). Chang and Hosseinpour (2023) showed that the AEWs contributed to the significant dust transport across the tropical Atlantic Ocean and suggested that the semidirect effect of dust can play a crucial role during this extreme dust storm.

Saharan dust is not the only contributor to the aerosol radiative effect over Africa and the Atlantic Ocean. Biomass burning over the Sahel and Southern

Africa produces smoke aerosols that can be transported over the Atlantic Ocean and rise to 3–5 km in altitude impacting stratocumulus clouds via aerosol indirect effects (Redemann et al., 2021), among other effects. Due to the seasonal variability of precipitation in the Sahel and Southern Africa, the smoke emitted from biomass burning also varies significantly by season. Smoke emissions from the fire activity in the Sahel region peak during the boreal winter, where smoke particles are transported northward and mixed with Saharan dust aerosols (Haywood et al., 2008). Additionally, smoke emissions from Southern Africa reach their peak during boreal summer, with atmospheric circulations facilitating the transport of smoke over the southeast Atlantic (Cochrane et al., 2022). Previous studies have shown that smoke aerosols from Southern Africa contribute to less than 15% of total aerosols in the northeastern Atlantic and West Africa during the boreal summer (e.g., Matsuki et al., 2010). Hence, in boreal summer, smoke's contribution to aerosol transport across the North Atlantic is comparatively minor when compared to dust.

3.3 Dust direct radiative effect

Mineral dust stands out among various aerosols due to its significant shortwave (SW) or solar radiative effect, contributing to a quarter of total aerosol extinction (Ridley et al., 2016). Dust is highly effective in absorbing and scattering SW radiation, with absorption being particularly strong, leading to heating of the SAL and a reduction of SW incoming radiation and cooling at the surface (Tsikerdekis et al., 2019; Mamun et al., 2021). Further, dust aerosols play a significant role in the longwave (LW) or terrestrial radiation budget, contributing substantially to the total aerosol LW radiation effect (Dufresne et al., 2002). While dust does absorb, scatter, and emit LW radiation, its LW radiative effect tends to counteract its shortwave (SW) radiative effect, resulting in a net cooling effect in the atmosphere and warming at the surface. However, the LW effect is generally smaller than the SW effect (Meloni et al., 2018). The direct radiative effect of dust is influenced by several factors, including surface albedo, the presence of clouds below the dust layer, the height of the dust layer, and the size of dust particles. (Liao and Seinfeld, 1998).

Recent estimates suggest that the global mean dust radiative forcing is around $-0.2 \pm 0.5\ \mathrm{W\,m^{-2}}$, indicating an ongoing uncertainty regarding the strength and direction of the dust radiative effect on a global scale (Kok et al., 2023). This uncertainty has persisted over recent decades, as shown by modeling results (Boucher et al., 2013). The complexity of the dust emission and transport mechanisms, as well as its interactions with other environmental factors, contributes to this considerable uncertainty in the estimated radiative forcing (Kok et al., 2023). Despite this small value from global annual averages, the dust radiative effect is strong regionally (Saidou Chaibou et al., 2020; Soupiona et al., 2020). Over the Saharan dust sources in Northwest Africa, the radiative effect of dust can reach 35 $\mathrm{W\,m^{-2}}$ per unit Aerosol Optical Depth (AOD), and, over

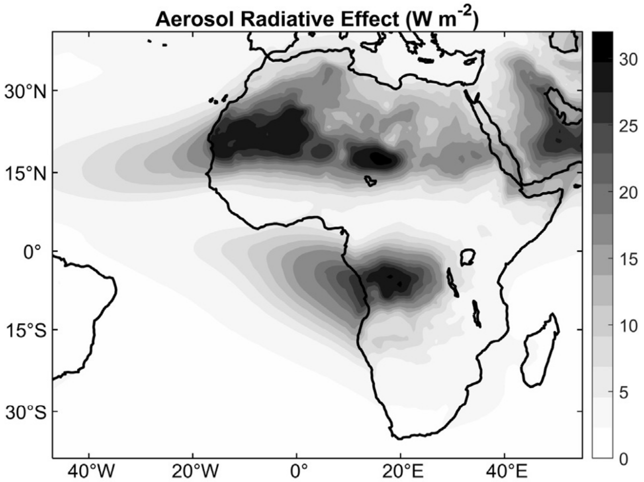

FIGURE 3.2 Long-term mean of aerosol radiative effect (W m^{-2}) in the atmosphere. The climatology is provided for June–August 2000–2021 using MERRA-2 reanalysis.

the adjacent Eastern tropical Atlantic Ocean, it can be as high as 20 W m^{-2} per unit AOD (Fig. 3.2) (Hosseinpour and Wilcox, 2024).

The enhanced diabatic heating induced by dust modifies the vertical profile of temperature in the troposphere, leading to changes in the static stability of the region (Hosseinpour and Wilcox, 2014). Some studies showed that SAL enhances the temperature and dryness of the middle troposphere, resulting in enhanced static stability (Chen et al., 2010; Bretl et al., 2015), while others suggest that SAL induces warming and drying in its lower layers and cooling and moistening in its upper layers, leading to reduced static stability (Jones et al., 2004; Ma et al., 2012). Tao et al. (2018) demonstrated that the southern side of the Saharan Air Layer (SAL) tends to experience enhanced static stability, while the northern side more frequently exhibits suppressed static stability. These dynamic alterations in the troposphere can significantly impact precipitation patterns, cyclogenesis, and the formation of large-scale waves.

3.4 Dust indirect effect

Aerosols, acting as both CCN and IN, contribute to the formation of a greater number of smaller cloud droplets while maintaining unchanged cloud water amounts and cloud cover. This effect is known as the first aerosol indirect effect or Twomey effect (Twomey, 1977), in which a cooling effect at the surface enhances cloud reflection or albedo. The second aerosol indirect effect, known as the "Albrecht effect" (Albrecht, 1989), describes how aerosol-induced smaller cloud droplets weaken the collision–coalescence process, leading to suppression of precipitation. This process enhances cloud cover and cloud lifetime.

The fluctuations in cloud water content and cloud cover reflect intricate aerosol–cloud–precipitation dynamics. Referred to as “cloud adjustments,” these alterations can yield either positive or negative cloud radiative effects, contingent upon the prevailing environmental conditions (Glassmeier et al., 2021; Erfani et al., 2022). Larger aerosols, typically exceeding 10 μm in size and existing at a concentration of 10^{-4} to 10^{-2} cm^{-3} can serve as giant Cloud Condensation Nuclei (GCCN). Although their concentration is notably lower than that of typical CCNs (by three–four orders of magnitude), ultrafine aerosols have a propensity to generate larger cloud droplets. This process broadens the cloud droplet-size distribution and enhances collision–coalescence efficiency, ultimately promoting an earlier onset of precipitation. While the GCCN impact on precipitation is substantial in polluted clouds, their impact on clean clouds is relatively minor (Feingold et al., 1999; Saleeby and Cotton, 2005; Van den Heever et al., 2006).

Aerosol impacts on deep convective clouds are not well understood due to the existence of both liquid and ice phases and the complexity of the dynamic processes involved. One hypothesis, known as “convection invigoration,” suggests that aerosols lead to the formation of a larger number of smaller cloud droplets, which initially suppress warm precipitation. Nevertheless, once formed, these droplets ascend via convective updrafts and freeze at higher altitudes. This freezing process releases latent heat of fusion, enhancing convective activity and ultimately resulting in more convective precipitation (Rosenfeld et al., 2008).

Aerosols can additionally decrease ice-particle size and fall speed, leading to an increase in cloud cover and cloud top height of deep convective systems (Fan et al., 2013). Several factors may determine the effectiveness of convection invigoration. For instance, weak wind shear (e.g., less than 5 m s^{-1} in the mid-troposphere) enhances the latent heat release in the clouds and facilitates convection invigoration (Lebo et al., 2012). Furthermore, when the cloud base is warmer than 15 °C, the liquid portion of the cloud is deeper, favoring the uplifting of cloud droplets and convection invigoration (Rosenfeld et al., 2014).

Another hypothesis for deep convective clouds, “condensational invigoration”, proposes that the invigoration results from the enhanced release of latent heat of condensation from the rising of polluted cloud droplets in the warm regions of clouds (Fan et al., 2007). While both theories of deep convective clouds are popular, recent observational and modeling studies suggest that the actual processes are more complex. For further insights into this subject, readers are directed to a recent review study by Varble et al. (2023).

Consisting of soluble organic and inorganic components in accumulation mode, smoke is considered a very efficient source of CCN to form cloud droplets in liquid and mixed-phase clouds (Hobbs and Radke, 1969; Martins et al., 2009; Holanda et al., 2020). While dust particles are insoluble and, on average, have a larger size than other aerosols, they can acquire coatings of soluble particles, such as nitrate and sulfate in the atmosphere. This coating enables them to act as

CCNs (Kumar et al., 2009), influencing cloud properties such as cloud albedo, cloud cover, cloud lifetime, and precipitation (Seigel et al., 2013).

Lidar measurements conducted over Barbados in the Caribbean (Haarig et al., 2019) confirm earlier research (Weinzierl et al., 2017) indicating that Saharan dust significantly contributes to CCN. Mineral dust is considered an effective source of IN to form ice particles in cirrus clouds or mixed-phase clouds through heterogeneous nucleation processes (Cziczo et al., 2004; Hoose et al., 2008; Hoose and Möhler, 2012) because dust particles have a crystal structure that facilitates freezing of water or deposition of vapor (Atkinson et al., 2013). With Saharan and Asian source regions each contributing approximately 40% to the total dust in the upper troposphere, mineral dust emerges as the primary source of cirrus cloud formation on a global scale (Froyd et al., 2022). Observations indicate that Saharan dust serves as the primary source of IN over the Eastern Atlantic (Price et al., 2018) and the Amazon basin (Prenni et al., 2009). Additionally, Saharan dust significantly influences deep convective clouds in the tropical Atlantic by acting as IN, which form a greater number of smaller ice particles. This effect leads to higher cloud tops that emit more longwave radiation (Gibbons et al., 2018; Hawker et al., 2021).

The microphysical impacts of Saharan dust vary depending on the type of cloud and environmental conditions. In shallow or layered clouds, Saharan dust can suppress precipitation by producing smaller cloud droplets that are less efficient in collision–coalescence (Rosenfeld et al., 2001; Min et al., 2009). However, in deep convective clouds, Saharan dust can enhance precipitation by increasing convection invigoration (Levin et al., 2005; Van den Heever et al., 2006; Zhang et al., 2021c). Dust particles can be coated by sea salt and serve as GCCN that promote collision–coalescence and, consequently, precipitation (Levin et al., 2005). The transport of Saharan dust aerosols over the Atlantic modifies convective storms by serving as CCN, IN, and GCCN, thereby notably intensifying updraft through the convection invigoration mechanism. This leads to greater masses of ice and liquid water, and, in some cases, even higher cloud-base precipitation (Van den Heever et al., 2006). There is no consensus on the definition of GCCN concerning aerosol size and concentration, and the efficiency of coating dust particles with soluble aerosols is uncertain. Nonetheless, super-coarse dust particles from the Sahara can act as GCCN near the source regions in Northern and Central Africa, the tropical Eastern Atlantic, the Mediterranean Sea, Southern Europe, and parts of Asia. If the definition of GCCN is extended to all coarse dust particles, Saharan dust aerosols act as GCCN in a larger area that includes all of the tropical Atlantic, Amazon basin, and Southeastern U.S., assuming that dust particles are coated with soluble aerosols (Adebiyi et al., 2023).

3.5 Dust semidirect effect

The aerosol semidirect effect, also known as the cloud burning effect, must be considered when aerosols exist within the cloud layer. Aerosols with significant solar radiation absorption capabilities create an anomalous vertical temperature gradient by heating the atmosphere and cooling the surface. This process suppresses the convection and reduces the cloud cover (Hansen et al., 1997; Ackerman et al., 2000; Koren et al., 2004), ultimately leading to a warming effect at the surface.

Another theory, known as a nonconventional aerosol semidirect effect, applies when aerosols are located above the clouds. In this scenario, the absorption of solar radiation by aerosols causes the warming and drying of the aerosol layer, which enhances low-level static stability (Koch and Del Genio, 2010; Sakaeda et al., 2011) and reduces the entrainment of free tropospheric dry air due to enhanced buoyancy (Johnson et al., 2004; Wilcox, 2010). As a result, the marine low cloud layer cools and moistens, leading to increased cloud cover and a cooling cloud radiative effect at the surface.

The nonconventional semidirect effect of Saharan dust on Africa has a cooling effect, where the SAL creates moisture convergence zones at the lower levels, increasing convective activities (Stephens et al., 2004), precipitation (Miller et al., 2004) and low-cloud cover (Perlwitz and Miller, 2010; Doherty and Evan, 2014; Chang and Hosseinpour, 2023). The magnitude of this effect varies depending on the underlying meteorological conditions and the intensity of the dust storms. A humid atmosphere is more likely to enhance convection and lead to a stronger semidirect effect (Stephens et al., 2004). In addition, the semidirect effect of dust causes a greater increase in cloud cover when radiative heating is significant in nonwinter seasons (Perlwitz and Miller, 2010). The conventional semidirect effect of Saharan dust on marine low clouds is also significant because dust resides at low levels more than 85% of the time in winter, leading to an enhanced positive radiative effect. Conversely, the nonconventional effect is significant in boreal summer because dust is above the marine low clouds more than 60% of the time (Amiri-Farahani et al., 2017).

3.6 Dust trends and variability

Variability of Saharan dust emission depends on the combination of factors that affect the dust emission rate and dust transport, including wind speed, precipitation, soil moisture, and vegetation cover (Werner et al., 2002; Marticorena et al., 2010; Bibi et al., 2020; Shi et al., 2021). Surface wind speed is a dominant factor in determining dust variability over the source regions where the emission of dust originates (Yuan et al., 2016; Zhou et al., 2023). Farther from the source regions, dust variability can be affected by surface air temperature, which affects static stability and the corresponding updraft (Zhou et al., 2023).

Saharan dust emissions increased over the 20th century partly due to vegetation change and enhanced land degradation from commercial farming in the Sahel (Mulitza et al., 2010). This increase in emissions is also influenced by large-scale climate oscillations, which play a role in dust variability. The interannual variability of Saharan dust transported over the Atlantic is notably influenced by the North Atlantic Oscillation (NAO), with a strong correlation between the two phenomena (Moulin et al., 1997; Chiapello and Moulin, 2002). The NAO Index, quantifying the pressure differential between the Icelandic Low and the Azores High (Hurrell, 1995), serves as a pivotal factor in this association. A positive NAO index indicates a stronger Icelandic Low and Azores High, leading to a northward shift of the North Atlantic westerly jet. This shift results in warmer and more humid conditions over the Eastern U.S. and Northern Europe, while leading to cooler and drier conditions over Southern Europe and Northern Africa. Conversely, a negative NAO index leads to the opposite effect, enhancing precipitation over North Africa, which in turn suppresses Saharan dust emission and transport (Moulin et al., 1997). On a decadal to millennial timescale, Saharan dust appears to be influenced by the Interhemispheric Contrast in Atlantic Sea Surface Temperature (SST) (ICAS). Enhanced SST in the North Atlantic leads to a positive ICAS anomaly, shifting the Intertropical Convergence Zone (ITCZ) northward and weakening surface winds over the Sahara, leading to a decrease in dust load (Yuan et al., 2020). Additionally, the El Niño Southern Oscillation (ENSO) is linked to dust variability through alteration in Walker-like lower-tropospheric circulations over North Africa (DeFlorio et al., 2016). Numerical simulations suggest that the lower Saharan dust load during the mid-Holocene (7000 to 5000 years ago) could weaken ENSO (Pausata et al., 2017) and the Atlantic Meridional Overturning Circulation (AMOC) (Zhang et al., 2021a).

In the 21st century, the Saharan dust variability shows a negative trend over the source regions (Fig. 3.3), potentially linked to an increase in soil moisture (Zhou et al., 2023). This trend is further linked to Atlantic teleconnections because Saharan dust demonstrates a negative correlation with the Atlantic Multidecadal Oscillation (AMO) (Shao et al., 2013), which represents decadal to multidecadal variability in SST characterized by a horseshoe shape in the Atlantic Ocean. The dust–AMO feedback involves a positive SST anomaly in the midlatitude North Atlantic, leading to reduced trade winds, decreased Saharan dust and low clouds over the Atlantic, and warming of the tropical North Atlantic (Yuan et al., 2016). Another mechanism involves positive feedback among SST, rainfall, and dust on multidecadal time scales. Warmer Atlantic SSTs lead to increased rainfall over the Sahel, resulting in a lower Saharan dust load. The reduced dust direct radiative effect further increases Atlantic SST (Foltz and McPhaden, 2008b; Wang et al., 2012). However, this feedback is not considered in climate models to predict the future of dust concentrations (Evan et al., 2016).

Climate models produce varying projections for future dust trends, with some foreseeing a significant increase in desert dust load due to climate-induced desertification (Woodward et al., 2005), while others indicate a marked decrease attributed to enhanced vegetation from elevated carbon dioxide fertilization (Mahowald et al., 2006), or suggest a more modest trend (Liao et al., 2009). Nevertheless, the influence of decadal-to-millennial oscillations emerges as a

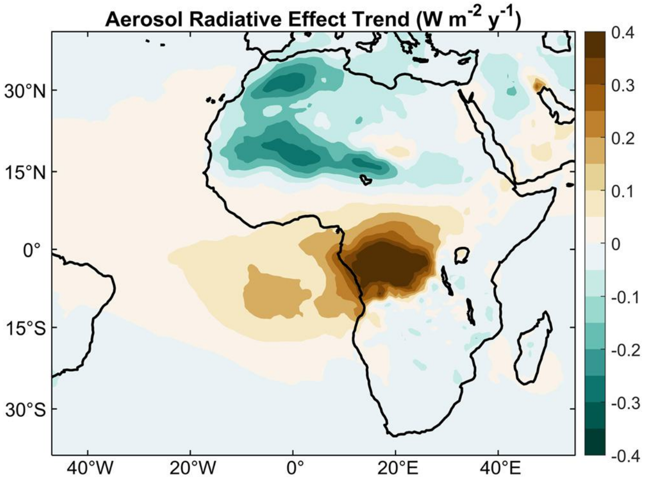

FIGURE 3.3 Long-term mean of aerosol radiative effect trends (W m^{-2} y^{-1}). The climatology is provided for June–August 2000–2021 using MERRA-2 reanalysis. High values prevail over Northern Africa as a result of dust, while Southern Africa experiences similar conditions due to smoke.

critical factor in shaping the future trajectory of Saharan dust, while the human-induced enhancement of interhemispheric contrast in the Atlantic SST over the next century may profoundly inhibit dust emission and transport, potentially reducing dust concentrations to levels lower than those observed during the mid-Holocene.

3.7 Dust impacts on precipitation

On a global scale, climate models exhibit a broad spectrum of simulated precipitation, partially attributed to their sensitivity to aerosols (Myhre et al., 2018). Previous studies suggested several mechanisms to explain the relationships between aerosol-induced atmospheric heating and precipitation. The first mechanism, referred to as “slow adjustment” or slow precipitation change, suggests that the surface cooling induced by atmospheric aerosols suppresses global annual mean precipitation. The second mechanism, known as “rapid adjustment”, proposes that the atmospheric heating caused by absorptive aerosols reduces condensation and, as a result, suppresses precipitation on a global scale (Bala et al., 2010; Myhre et al., 2017; Zhang et al., 2021b). The effectiveness of these mechanisms varies based on the quantity and composition of atmospheric aerosols (Sand et al., 2021; Samset, 2022), and regional impacts may diverge from the explanations for global annual means (Allen et al., 2019).

Saharan dust aerosols have a significant impact on Sahel precipitation and the West African monsoon (WAM) (Yoshioka et al., 2007; Strong et al., 2015). Solmon et al. (2012) identified a mechanism similar to “rapid adjustment” over much of the Sahel region. Moreover, the diurnal cycle plays a role in the dust-precipitation feedback: The direct radiative effect of dust causes enhanced stability during the day and decreases it at night, suppressing late-afternoon rainfall, while enhancing nighttime and early-morning rainfalls (e.g., Zhao et al., 2011).

Lau et al. (2006) proposed the "elevated heat pump" (EHP) hypothesis to explain the increase in Asian monsoon precipitation due to dust. Additionally, Lau et al. (2009) used a general circulation model with prescribed dust to study the EHP hypothesis regarding Saharan dust and the WAM. According to their findings, the significant heating of the SAL by dust induces the ascent of warm air, intensifying deep convection and precipitation over West Africa and the Eastern Atlantic Ocean. This upward motion, coupled with the subsidence, creates an east-west overturning circulation over the west tropical Atlantic Ocean. Recent studies (e.g., Bercos-Hickey et al., 2017; Sun and Zhao, 2020) further support this notion, although the impact of the EHP may be influenced by other factors. For instance, Jordan et al. (2018) investigated the effect of SST along with dust–precipitation dynamics in a global climate model. They demonstrated that, while EHP is valid over land, dust-induced SST cooling suppresses convection and subsequently reduces precipitation over the Eastern Atlantic Ocean.

Another mechanism highlights the significance of general circulation. Global climate model simulations have revealed that dust plays a role in shifting the ITCZ, consequently altering precipitation patterns across the tropical Atlantic (Evans et al., 2020). This shift arises from anomalous cross-equatorial energy transport generated by an anomalously warmer hemisphere, causing the ITCZ to shift toward the warmer hemisphere (Donohoe et al., 2013; Zhao and Suzuki, 2021). In response to the anomalous warming, the upper-level branch of the Hadley cell transports heat to the cooler hemisphere, while the lower-level branch of the Hadley cell transfers moisture to the warmer hemisphere, thus shifting the ITCZ precipitation toward the warmer hemisphere. The enhancement of the Saharan dust radiative effect in the Northern Hemisphere causes surface cooling and shifts the ITCZ toward the south (Evans et al., 2020). However, the shift induced by aerosols is also influenced by clouds via indirect effects (Zhao and Suzuki, 2021). The lack of consensus among various studies highlights the complexity of dust–precipitation interactions on a regional scale, which is not yet fully represented in models, with model results being sensitive to the resolutions and parameterizations of physical and aerosol properties (Strong et al., 2015; Jordan et al., 2018).

3.8 Dust impacts on tropical cyclones

The impact of dust on tropical cyclones (TCs) remains a subject of ongoing research, with divergent findings in the literature. Some studies suggest a weakening in TC strength, frequency, and duration in the presence of dust (Dunion and Velden, 2004; Lau and Kim, 2007; Strong et al., 2018; Reed et al., 2019; Luo and Han, 2021), while others indicate contrasting effects (Karyampudi and

Carlson, 1988; Karyampudi and Pierce, 2002; Braun, 2010; Bretl et al., 2015; Sun and Zhao, 2020; Pan et al., 2024). Extensive research on TCs has revealed that their formation is associated with conditions such as elevated SST in the tropical Atlantic, atmospheric static instability, high mid-tropospheric humidity, weak vertical shear, and robust AEWs (Bretl et al., 2015; Sun and Zhao, 2020).

Dust events are also linked to a decrease in hurricane frequency due to a reduction in SST (Lau and Kim, 2007; Strong et al., 2018). This occurs because Saharan dust absorbs solar radiation, leading to surface cooling and a subsequent decrease in the tropical North Atlantic SST. (Foltz and McPhaden, 2008a; Evan et al., 2009). Additionally, Saharan dust induces warming and drying of air in SAL, as well as cooling of low-level air over the tropical North Atlantic and beneath the SAL. This condition enhances static stability and vertical wind shear over this region which slows down the strengthening of TCs (Dunion and Velden, 2004; Reale et al., 2014).

Luo and Han (2021) showed that TCs with lower cloud tops are associated with the occurrence of SAL. They hypothesized that the heating in the SAL, resulting from solar radiation absorption, leads to dry air, weaker TCs, and consequently lower cloud-top heights. Statistical analysis has revealed a negative correlation between AOD and the frequency and intensity of Atlantic hurricanes. However, this correlation lacks a clear explanatory mechanism, suggesting that co-varying large-scale factors such as SST, wind shear, and climate indices may play a more significant role than AOD in influencing tropical cyclones (Xian et al., 2020).

Several studies have indicated that Saharan dust reduces TCs' intensity through microphysical effects. Numerical modeling has shown that Saharan dust particles act as CCN, inhibiting the formation of raindrops. This suppression of precipitation ultimately reduces the strength of TCs (Zhang et al., 2007; Rosenfeld et al., 2011). Dust acting as cloud CCN can also intensify convection in the periphery of TCs, resulting in near-surface cooling, decreased wind speeds, and ultimately weakening of the TCs (Khain et al., 2010; Rosenfeld et al., 2012).

The long-term correlation between low SST in the tropical North Atlantic and high dust concentrations may be coincidental, as there are instances where wind-driven reduction of latent heat, rather than SAL-driven cooling, was the primary factor in lowering SST (Foltz and McPhaden, 2008a). The favorable impact of dust on TC genesis is related to the dust-induced enhancement of the AEJ–AEWs system (Karyampudi and Carlson, 1988; Bretl et al., 2015; Hosseinpour and Wilcox, 2024). Dust in the SAL generates heating that intensifies convection at the southern edges of the SAL, creating a negative potential vorticity anomaly to the north of the AEJ and conversely to the south. The resulting reversal in the potential vorticity gradient promotes barotropic and baroclinic instability within the AEJ, enhancing the development of the AEWs (Karyampudi and Pierce, 2002; Hosseinpour and Wilcox, 2014).

Although SAL is located north of AEJ, it ultimately enhances the circulation related to the AEJ, which favors the positive vorticity and consequently the development of TCs on the southern flanks of the AEJ (Braun, 2010). Another mechanism for dust-induced TC enhancement was proposed by Sun and Zhao (2020) through the study of the region's large-scale climatology. Despite reducing lower tropospheric moisture due to dust, an increase in moisture could occur in the middle troposphere. Additionally, the lower tropospheric convection and vorticity are intensified by dust-induced heating in this region. These conditions are favorable for the formation and intensification of TCs. Recent cloud-resolving modeling studies have found that, while aerosols weaken TCs in their early stages, they intensify TCs as they mature (Lin et al., 2023; Pan et al., 2024). Some studies have indicated that the microphysical impacts of dust, such as acting as CCN, GCCN, or IN, can enhance convection and promote the development of TCs through aerosol indirect effects (Cotton et al., 2012). However, at a broader scale, the direct effect of dust exerts a greater influence on TCs (Tao et al., 2018; Pan et al., 2024), underscoring the need for further research to unravel the intricate mechanisms by which dust either facilitates or suppresses TC formation, strength, and frequency.

3.9 Dust impacts on wave activity

3.9.1 Dynamics of the AEJ–AEWs system

AEJ is a climatological feature of West Africa and the eastern tropical Atlantic Ocean, horizontally elongated westward from 20°E to 30°W, in which the AEJ core axis measures 600 hPa in boreal summer seasons (Hosseinpour and Wilcox, 2014). AEWs are synoptic-scale atmospheric disturbances with a wavelength ranging from 2000–4000 km (Dunn, 1940; Avila and Pasch, 1992), such that the horizontal axis of the waves is tilted at pressure levels close to the core of the AEJ (Reed et al., 1977).

Several studies have shown that the formation of the AEWs is associated with hydrodynamic instability in the AEJ (Pasch and Avila, 1994; Diaz and Aiyyer, 2013), especially contributing to the formation of TCs and hurricanes AEWs when the amplitude of the AEWs is maximized in boreal summers (Roundy and Frank, 2004). Another crucial factor influencing the growth of AEWs is the local diabatic heating over West Africa near the entrance of AEJ (Norquist et al., 1977; Russell et al., 2020), which aids in the development of vortices (Berry and Thorncroft, 2012). Moreover, the thermal structure of the AEWs is described as a cold core below the AEJ and a warm core above the AEJ, associated with convection (Jenkins and Cho, 1991; Russell et al., 2020), suggesting a coupling behavior between mesoscale convective systems and AEWs (Hsieh and Cook, 2007; Berry and Thorncroft, 2012).

Generally speaking, the kinetic energy of the atmosphere can be classified into two main components: the kinetic energy of the background mean flow, known as mean kinetic energy (MKE), and the kinetic energy of the transient flow, known as eddy kinetic energy (EKE) (Hoskins et al., 1983; Blackmon et al., 1984). The MKE is characterized by a barotropic and zonally elongated structure, whereas the EKE exhibits a baroclinic and meridionally elongated structure (Hoskins et al., 1983; Blackmon et al., 1984). Lorenz (1955) demonstrated the exchange of energy between eddies and zonal circulations through energy conversion terms known as eddy transformation functions. Subsequent studies have further explored the terms of the eddy energy budget, which redistributes energy from jet streams to transient eddies (Chang et al., 2002; Takahashi and Shirooka, 2014).

Both barotropic instability, linked to the horizontal gradient of the AEJ, and baroclinic instability, associated with the vertical shear of the jet, act as energy sources for the AEWs (Burpee, 1972; Pytharoulis and Thorncroft, 1999). AEWs generally initiate as baroclinic waves that intensify closer to the surface, propagating from east to west over the African continent, and transitioning into more barotropic waves downstream over the tropical Atlantic Ocean (Hall et al., 2006). In this process, either EKE, Eddy Available Potential Energy (EAPE), or both are transformed into MKE, especially when energy conversions of the zonal mean flow are dominated by convectively induced eddies (Hsieh and Cook, 2005, 2007).

Historically, unfiltered winds were employed to quantify AEWs by examining vorticity fields and identifying the point where the reversal of the vorticity gradient occurs (Carlson, 1969; Thorncroft and Hodges, 2001; Kiladis et al., 2006; Hopsch et al., 2007). The limitation of this technique lies in the potential overlap of the AEWs with other atmospheric features, necessitating careful examinations to distinguish between AEWs and local-scale circulations. As an alternative, the energetic framework suggested by Hosseinpour and Wilcox (2024) provides insights into the energetic behavior of the AEWs.

Their energetic analysis showed that, on average, the MKE (Fig. 3.4) peaks at ~12–18° N, collocated with the core of the AEJ, while the EKE (Fig. 3.5) and transient momentum fluxes (Fig. 3.6) are associated with AEWs, highlighting the significant contribution of two–six-day transient eddies of AEWs over the ocean. These patterns confirm that the formation of transient eddies occurs in the northern and southern tracks of the AEWs (Hosseinpour and Wilcox, 2014). These analyses revealed that, after propagating away from the West Coast of Africa, the majority of AEWs either develop further downstream or penetrate the higher latitudes above ~32°N toward the subtropics.

3.9.2 Relationships between dust radiative effects and the AEW's energetics

The AEJ–AEWs system modulates dust transport within the SAL across the Atlantic Ocean (Perry et al., 1997; Jones et al., 2003; Liu et al., 2008; Francis et al., 2022; Chang and Hosseinpour, 2023), and the SAL, in turn, intensifies AEJ and the AEWs through dust direct radiative effects (Bercos-Hickey et al.,

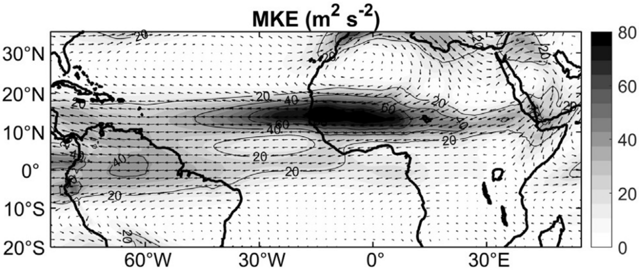

FIGURE 3.4 Long-term mean of 600-hPa MKE (m^2s^{-2}) shown by shades and wind speed (ms^{-1}) shown by vectors using MERRA-2 reanalysis for JJA, 2000–2021.

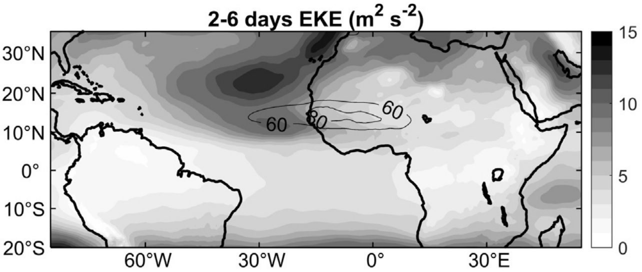

FIGURE 3.5 Long-term mean of 600-hPa two–six-day bandpass filtered EKE (m^2s^{-2}) shown by shades and 600-hPa MKE shown by contours using MERRA-2 reanalysis for JJA, 2000–2021.

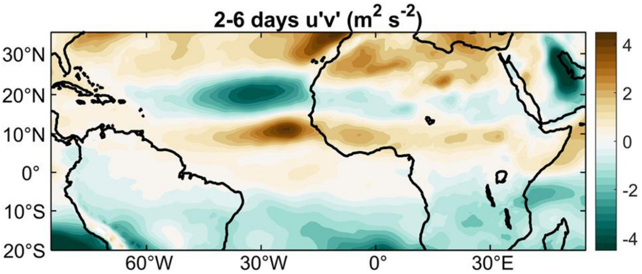

FIGURE 3.6 Long-term mean of 600 hPa 2-6-day filtered transient momentum fluxes, $\overline{u'v'}$ (m^2s^{-2}) using MERRA-2 reanalysis for JJA, 2000–2021.

2020; Grogan et al., 2022; Hosseinpour and Wilcox, 2024). Jones et al. (2004) found that dust precedes the occurrence of a maximum in 700-hPa geopotential height by about one–two days and suggested that dust may intensify the AEWs. Additionally, the dust transport model simulations suggested a possible role of dust radiative effects on the strengthening of the AEWs (Ma et al., 2012).

The direct radiative effect of dust influences the vertical temperature profile over West Africa and the Eastern Atlantic Ocean, exhibiting a dipole pattern, that modifies atmospheric diabatic heating and intensifies meridional temperature gradients. This consequently enhances baroclinic instability offshore, leading to amplification of the eddy activity of the AEWs (Hosseinpour and Wilcox, 2014, 2024).

Further analysis using 22 years of daily satellite observations and reanalysis data based on satellite assimilation, suggested that the downstream development of the AEWs peaks 2–4 days after the peak of dust radiative heating over the tropical Atlantic and that dust radiative effect can potentially trigger the development of zonal and meridional transient eddies across the northern and southern tracks of the AEWs. This confirms that Saharan dust aerosols not only are transported by the AEJ–AEWs system but also have the capability to modify the EKE of the baroclinic waves through diabatic heating (Hosseinpour and Wilcox, 2024).

3.10 Limitations of tools for dust–climate interaction research

While numerical modeling is a powerful tool for studying complex processes in climate systems, the accuracy of numerical simulations is dependent on the accuracy of physical and chemical parameterizations. These include cloud, aerosol, precipitation, radiation, convection, and boundary layer parameterizations, as well as their interactions, which are integrated into the models. Despite the notable advancements in these parameterizations, such as inclusion of prognostic aerosol microphysical schemes modern models, as well as enhancement in horizontal and vertical resolutions over the past decades, uncertainties persist in representing numerous complex mechanisms in models. This is due to the fact that most aerosol mechanisms remain unresolved in current global climate models, which typically operate at resolutions of 50–100 km. Hence, it is essential to enhance our comprehension of aerosol processes through theoretical approaches, observational studies, and process-based modeling, such as cloud-resolving models and large-eddy simulations. This will enable us to refine parameterizations in climate models and improve their accuracy.

Satellite measurements provide high-resolution global views of the Earth and atmosphere multiple times a day. Recent improvements in retrieval techniques have made it possible to produce aerosol datasets such as cloud or AOD, as well as the identification of various aerosol and cloud types at various vertical levels. However, satellite retrievals of aerosol and cloud properties are subject to numerous uncertainties. Minimizing these uncertainties is essential for obtaining more accurate observations that enhance our understanding of critical aerosol and cloud processes and improves numerical models. Recent satellites equipped with hyperspectral instruments, as well as instruments like the multi-angle polarimeter onboard the newly launched NASA Plankton, Aerosol, Cloud, ocean Ecosystem (PACE) satellite mission, represent the latest attempts to tackle these challenges.

Validating satellite observations and retrievals rely on ground-based and aircraft measurements, which are available over limited locations or nonexistent over remote oceanic regions, such as the Atlantic Ocean. Conducting observational field campaigns is a costly endeavor which necessitates coordination among multiple institutes from various countries. Over the past decades, several field campaigns have been undertaken, such as the 2003 Saharan Dust Experiment (SHADE), 2006 NASA African Monsoon Multidisciplinary Analyses (NAMMA), 2011–2012 Fennec Campaign, and 2015 AERosol Properties—Dust (AER-D) focusing on the Sahara and Eastern Atlantic regions. Nevertheless, to enhance our understanding of dust emission, transport, and its interactions with radiation, clouds, precipitation, and atmospheric dynamics, there is a need for research programs to be organized employing modern and improved instruments, ensuring more reliable measurements and addressing existing knowledge gaps.

3.11 Summary

The Sahara Desert is the world's main source of mineral dust emissions, and therefore Saharan dust aerosols play a crucial role in the climate dynamics of the tropical Atlantic Ocean. This chapter discussed the various aspects of Saharan dust, including its origins, transport mechanisms, radiative effects, and their influences on cloud microphysics and precipitation. Through direct, semidirect, and indirect effects, Saharan dust significantly modifies atmospheric conditions, such as stability, wind shear, and cloud properties. Moreover, dust aerosols exert significant influence on the AEJ–AEWs system and consequently tropical cyclones, modulating their energetics and dynamics and potentially altering their trajectories and intensities. The chapter not only discusses the profound impacts of Saharan dust on climate dynamics but also highlights the crucial necessity of advancements in observational techniques and numerical models to address the uncertainties inherent in investigating dust-induced changes in climate dynamics.

References

Ackerman, A.S., Toon, O.B., Stevens, D.E., Heymsfield, A.J., Ramanathan, V., Welton, E.J., 2000. Reduction of tropical cloudiness by soot. Science 288 (5468), 1042–1047. https://doi.org/10.1126/science.288.5468.1042.

Adebiyi, A., Kok, J.F., Murray, B.J., Ryder, C.L., Stuut, J.-B.W., Kahn, R.A., Knippertz, P., Formenti, P., Mahowald, N.M., Pérez García-Pando, C., Klose, M., Ansmann, A., Samset, B.H., Ito, A., Balkanski, Y., Di Biagio, C., Romanias, M.N., Huang, Y., Meng, J., 2023. A review of coarse mineral dust in the Earth system. Aeolian Research 60, 100849. https://doi.org/10.1016/j.aeolia.2022.100849.

Albrecht, B.A., 1989. Aerosols, cloud microphysics, and fractional cloudiness. Science 245 (4923), 1227–1230. https://doi.org/10.1126/science.245.4923.1227.

Allen, R.J., Amiri-Farahani, A., Lamarque, J.-F., Smith, C., Shindell, D., Hassan, T., Chung, C.E., 2019. Observationally constrained aerosol–cloud semi-direct effects. npj Climate and Atmospheric Science 2 (1), 1–12. https://doi.org/10.1038/s41612-019-0073-9.

Amiri-Farahani, A., Allen, R.J., Neubauer, D., Lohmann, U., 2017. Impact of Saharan dust on North Atlantic marine stratocumulus clouds: importance of the semidirect effect. Atmospheric Chemistry and Physics 17 (10), 6305–6322. https://doi.org/10.5194/acp-17-6305-2017.

Atkinson, J.D., Murray, B.J., Woodhouse, M.T., Whale, T.F., Baustian, K.J., Carslaw, K.S., Dobbie, S., O'Sullivan, D., Malkin, T.L., 2013. The importance of feldspar for ice nucleation by mineral dust in mixed-phase clouds. Nature 498 (7454), 7454. https://doi.org/10.1038/nature12278.

Avila, L.A., Pasch, R.J., 1992. Atlantic tropical systems of 1991. Monthly Weather Review 120 (11), 11. https://doi.org/10.1175/1520-0493(1992)120.

Bala, G., Caldeira, K., Nemani, R., 2010. Fast versus slow response in climate change: implications for the global hydrological cycle. Climate Dynamics 35 (2), 423–434. https://doi.org/10.1007/s00382-009-0583-y.

Bercos-Hickey, E., Nathan, T.R., Chen, S.H., 2017. Saharan dust and the African easterly jet-African easterly wave system: structure, location and energetics. Quarterly Journal of the Royal Meteorological Society 143, 2797–2808. https://doi.org/10.1002/qj.3128.

Bercos-Hickey, E., Nathan, T.R., Chen, S.-H., 2020. On the relationship between the African Easterly jet, Saharan mineral dust aerosols, and West African precipitation. Journal of Climate 33, 3533–3546. https://doi.org/10.1175/jcli-d-18-0661.1.

Berry, G.J., Thorncroft, C.D., 2012. African easterly wave dynamics in a mesoscale numerical model: the upscale role of convection. Journal of the Atmospheric Sciences 69, 1267–1283. https://doi.org/10.1175/JAS-D-11-099.1.

Bibi, M., Saad, M., Masmoudi, M., Laurent, B., Alfaro, S.C., 2020. Long-term (1980–2018) spatial and temporal variability of the atmospheric dust load and deposition fluxes along the North-African coast of the Mediterranean Sea. Atmospheric Research 234, 104689. https://doi.org/10.1016/j.atmosres.2019.104689.

Blackmon, M.L., Lee, Y.-H., Wallace, J.M., 1984. Horizontal structure of 500 mb height fluctuations with long, intermediate and short time scales. Journal of the Atmospheric Sciences 41 (6), 961–980. https://doi.org/10.1175/1520-0469(1984)041<0961:HSOMHF>2.0.CO;2.

Boucher, O., Randall, D., Artaxo, P., Bretherton, C., Feingold, G., Forster, P., Kerminen, V.-M., Kondo, Y., Liao, H., Lohmann, U., Rasch, P., Satheesh, S.K., Sherwood, S., Stevens, B., Zhang, X.Y., 2013. Clouds and aerosols. In: Climate Change 2013: The Physical Science Basis. Contribution of Working Group I to the Fifth Assessment Report of the Intergovernmental Panel on Climate Change. Cambridge University Press, pp. 571–657. https://pure.mpg.de/pubman/faces/ViewItemOverviewPage.jsp?itemId=item_2007900.

Braun, S.A., 2010. Reevaluating the role of the Saharan air layer in Atlantic tropical cyclogenesis and evolution. Monthly Weather Review 138 (6), 2007–2037. https://doi.org/10.1175/2009MWR3135.1.

Bretl, S., Reutter, P., Raible, C.C., Ferrachat, S., Poberaj, C.S., Revell, L.E., Lohmann, U., 2015. The influence of absorbed solar radiation by Saharan dust on hurricane genesis. Journal of Geophysical Research. Atmospheres 120 (5), 1902–1917. https://doi.org/10.1002/2014JD022441.

Burpee, R.W., 1972. The origin and structure of easterly waves in the lower troposphere of North Africa. Journal of the Atmospheric Sciences 29 (1), 77–90. https://doi.org/10.1175/1520-0469(1972)029<0077:TOASOE>2.0.CO;2.

Carlson, T.N., 1969. Synoptic histories of three African disturbances that developed into Atlantic hurricanes. Monthly Weather Review 97, 256–276. https://doi.org/10.1175/1520-0493(1969)097%3C0256:SHOTAD%3E2.3.CO;2.

Chang, C.H., Hosseinpour, F., 2023. Relationships between aerosols and marine cloud during the "Godzilla" dust storm: perspective of satellite and reanalysis products. Atmosphere 15 (1), 13. https://doi.org/10.3390/atmos15010013.

Chang, E.K.M., Lee, S., Swanson, K.L., 2002. Storm track dynamics. Journal of Climate 15, 2163–2183. https://doi.org/10.1175/1520-0442(2002)015.

Chen, S., Wang, S., Waylonis, M., 2010. Modification of Saharan air layer and environmental shear over the eastern Atlantic Ocean by dust-radiation effects. Journal of Geophysical Research. Atmospheres 115 (D21). https://doi.org/10.1029/2010JD014158.

Chiapello, I., Moulin, C., 2002. TOMS and METEOSAT satellite records of the variability of Saharan dust transport over the Atlantic during the last two decades (1979–1997). Geophysical Research Letters 29 (8), 17–1-17–4. https://doi.org/10.1029/2001GL013767.

Cochrane, S.P., Schmidt, K.S., Chen, H., Pilewskie, P., Kittelman, S., Redemann, J., LeBlanc, S., Pistone, K., Segal Rozenhaimer, M., Kacenelenbogen, M., Shinozuka, Y., Flynn, C., Ferrare, R., Burton, S., Hostetler, C., Mallet, M., Zuidema, P., 2022. Biomass burning aerosol heating rates from the ORACLES (ObseRvations of Aerosols above CLouds and their intEractionS) 2016 and 2017 experiments. Atmospheric Measurement Techniques 15, 61–77. https://doi.org/10.5194/amt-15-61-2022.

Cotton, W.R., Krall, G.M., Carrió, G.G., 2012. Potential indirect effects of aerosol on tropical cyclone intensity: convective fluxes and cold-pool activity. Tropical Cyclone Research and Review 1 (3), 293–306. https://doi.org/10.6057/2012TCRR03.05.

Cziczo, D., Murphy, D., Hudson, P., Thomson, D., 2004. Single particle measurements of the chemical composition of cirrus ice residue during CRYSTAL-FACE. Journal of Geophysical Research. Atmospheres 109 (D4). https://doi.org/10.1029/2003JD004032.

DeFlorio, M.J., Goodwin, I.D., Cayan, D.R., Miller, A.J., Ghan, S.J., Pierce, D.W., Russell, L.M., Singh, B., 2016. Interannual modulation of subtropical Atlantic boreal summer dust variability by ENSO. Climate Dynamics 46 (1), 585–599. https://doi.org/10.1007/s00382-015-2600-7.

Diaz, M., Aiyyer, A., 2013. The genesis of African easterly waves by upstream development. Journal of the Atmospheric Sciences 70, 3492–3512. https://doi.org/10.1175/JAS-D-12-0342.1.

Doherty, O.M., Evan, A.T., 2014. Identification of a new dust-stratocumulus indirect effect over the tropical North Atlantic. Geophysical Research Letters 41 (19), 6935–6942. https://doi.org/10.1002/2014GL060897.

Donohoe, A., Marshall, J., Ferreira, D., Mcgee, D., 2013. The relationship between ITCZ location and cross-equatorial atmospheric heat transport: from the seasonal cycle to the Last Glacial Maximum. Journal of Climate 26 (11), 3597–3618. https://doi.org/10.1175/JCLI-D-12-00467.1.

Dufresne, J.-L., Gautier, C., Ricchiazzi, P., Fouquart, Y., 2002. Longwave scattering effects of mineral aerosols. Journal of the Atmospheric Sciences 59 (12), 1959–1966. https://doi.org/10.1175/1520-0469(2002)059<1959:LSEOMA>2.0.CO;2.

Dunion, J.P., Velden, C.S., 2004. The impact of the Saharan air layer on Atlantic tropical cyclone activity. Bulletin of the American Meteorological Society 85 (3), 353–366. https://doi.org/10.1175/BAMS-85-3-353.

Dunn, G.E., 1940. Cyclogenesis in the tropical Atlantic. Bulletin of the American Meteorological Society 21, 215–229. https://doi.org/10.1175/1520-0477-21.6.215.

Engelstaedter, S., Tegen, I., Washington, R., 2006. North African dust emissions and transport. Earth-Science Reviews 79 (1–2), 73–100. https://doi.org/10.1016/j.earscirev.2006.06.004.

Erfani, E., Blossey, P., Wood, R., Mohrmann, J., Doherty, S.J., Wyant, M., O, K., 2022. Simulating aerosol lifecycle impacts on the subtropical stratocumulus-to-cumulus transition using large-eddy simulations. Journal of Geophysical Research. Atmospheres 127 (21), e2022JD037258. https://doi.org/10.1029/2022JD037258.

Evan, A.T., Flamant, C., Gaetani, M., Guichard, F., 2016. The past, present and future of African dust. Nature 531 (7595), 493–495. https://doi.org/10.1038/nature17149.

Evan, A.T., Vimont, D.J., Heidinger, A.K., Kossin, J.P., Bennartz, R., 2009. The role of aerosols in the evolution of tropical North Atlantic Ocean temperature anomalies. Science 324 (5928), 778–781. https://doi.org/10.1126/science.1167404.

Evans, S., Dawson, E., Ginoux, P., 2020. Linear relation between shifting ITCZ and dust hemispheric asymmetry. Geophysical Research Letters 47 (22), e2020GL090499. https://doi.org/10.1029/2020GL090499.

Fan, J., Leung, L.R., Rosenfeld, D., Chen, Q., Li, Z., Zhang, J., Yan, H., 2013. Microphysical effects determine macrophysical response for aerosol impacts on deep convective clouds. Proceedings of the National Academy of Sciences 110 (48), E4581–E4590. https://doi.org/10.1073/pnas.1316830110.

Fan, J., Zhang, R., Li, G., Tao, W.-K., 2007. Effects of aerosols and relative humidity on cumulus clouds. Journal of Geophysical Research. Atmospheres 112 (D14). https://doi.org/10.1029/2006JD008136.

Feingold, G., Cotton, W.R., Kreidenweis, S.M., Davis, J.T., 1999. The impact of giant cloud condensation nuclei on drizzle formation in stratocumulus: implications for cloud radiative properties. Journal of the Atmospheric Sciences 56 (24), 4100–4117. https://doi.org/10.1175/1520-0469(1999)056<4100:TIOGCC>2.0.CO;2.

Foltz, G.R., McPhaden, M.J., 2008a. Impact of Saharan dust on tropical North Atlantic SST. Journal of Climate 21 (19), 5048–5060. https://doi.org/10.1175/2008JCLI2232.1.

Foltz, G.R., McPhaden, M.J., 2008b. Trends in Saharan dust and tropical Atlantic climate during 1980–2006. Geophysical Research Letters 35 (20). https://doi.org/10.1029/2008GL035042.

Forster, P., Storelvmo, T., Armour, K., Collins, W., Dufresne, J.-L., Frame, D., Lunt, D., Mauritsen, T., Palmer, M., Watanabe, M., 2021. The Earth's energy budget, climate feedbacks, and climate sensitivity. In: Masson-Delmotte, V., Zhai, P., Pirani, A., Connors, S.L., Péan, C., Berger, S., Caud, N., Chen, Y., Goldfarb, L., Gomis, M.I., Huang, M., Leitzell, K., Lonnoy, E., Matthews, J.B.R., Maycock, T.K., Waterfield, T., Yelekçi, O., Yu, R., Zhou, B. (Eds.), Climate Change 2021: The Physical Science Basis. Contribution of Working Group I to the Sixth Assessment Report of the Intergovernmental Panel on Climate Change. Cambridge University Press.

Francis, D., Nelli, N., Fonseca, R., Weston, M., Flamant, C., Cherif, C., 2022. The dust load and radiative impact associated with the June 2020 historical Saharan dust storm. Atmospheric Environment 268, 118808. https://doi.org/10.1016/j.atmosenv.2021.118808.

Froyd, K.D., Yu, P., Schill, G.P., Brock, C.A., Kupc, A., Williamson, C.J., Jensen, E.J., Ray, E., Rosenlof, K.H., Bian, H., Darmenov, A.S., Colarco, P.R., Diskin, G.S., Bui, T., Murphy, D.M., 2022. Dominant role of mineral dust in cirrus cloud formation revealed by global-scale measurements. Nature Geoscience 15 (3), 177–183. https://doi.org/10.1038/s41561-022-00901-w.

Gibbons, M., Min, Q., Fan, J., 2018. Investigating the impacts of Saharan dust on tropical deep convection using spectral bin microphysics. Atmospheric Chemistry and Physics 18 (16), 12161–12184. https://doi.org/10.5194/acp-18-12161-2018.

Ginoux, P., Prospero, J.M., Gill, T.E., Hsu, N.C., Zhao, M., 2012. Global-scale attribution of anthropogenic and natural dust sources and their emission rates based on MODIS Deep Blue aerosol products. Reviews of Geophysics 50 (3). https://doi.org/10.1029/2012RG000388.

Glassmeier, F., Hoffmann, F., Johnson, J.S., Yamaguchi, T., Carslaw, K.S., Feingold, G., 2021. Aerosol-cloud-climate cooling overestimated by ship-track data. Science 371 (6528), 485–489. https://doi.org/10.1126/science.abd3980.

Grogan, D.F.P., Lu, C.-H., Wei, S.-W., Chen, S.-P., 2022. Investigating the impact of Saharan dust aerosols on analyses and forecasts of African easterly waves by constraining aerosol effects in radiance data assimilation. Atmospheric Chemistry and Physics 22, 2385–2398. https://doi.org/10.5194/acp-22-2385-2022.

Haarig, M., Walser, A., Ansmann, A., Dollner, M., Althausen, D., Sauer, D., Farrell, D., Weinzierl, B., 2019. Profiles of cloud condensation nuclei, dust mass concentration, and ice-nucleating-particle-relevant aerosol properties in the Saharan Air Layer over Barbados from polarization lidar and airborne in situ measurements. Atmospheric Chemistry and Physics 19 (22), 13773–13788. https://doi.org/10.5194/acp-19-13773-2019.

Hall, N.M., Kiladis, G.N., Thorncroft, C.D., 2006. Three-dimensional structure and dynamics of African easterly waves. Part II: Dynamical modes. Journal of the Atmospheric Sciences 63 (9), 2231–2245. https://doi.org/10.1175/JAS3742.1.

Hansen, J., Sato, M., Lacis, A., Ruedy, R., 1997. The missing climate forcing. Philosophical Transactions of the Royal Society of London. Series B, Biological Sciences 352 (1350), 231–240. https://doi.org/10.1098/rstb.1997.0018.

Hawker, R.E., Miltenberger, A.K., Wilkinson, J.M., Hill, A.A., Shipway, B.J., Cui, Z., Cotton, R.J., Carslaw, K.S., Field, P.R., Murray, B.J., 2021. The temperature dependence of ice-nucleating particle concentrations affects the radiative properties of tropical convective cloud systems. Atmospheric Chemistry and Physics 21 (7), 5439–5461. https://doi.org/10.5194/acp-21-5439-2021.

Haywood, J.M., Pelon, J., Formenti, P., Bharmal, N., Brooks, M., Capes, G., Chazette, P., Chou, C., Christopher, S., Coe, H., Cuesta, J., Derimian, Y., Desboeufs, K., Greed, G., Harrison, M., Heese, B., Highwood, E.J., Johnson, B., Mallet, M., Marticorena, B., Marsham, J., Milton, S., Myhre, G., Osborne, S.R., Parker, D.J., Rajot, J.-L., Schulz, M., Slingo, A., Tanre, D., Tulet, P., 2008. Overview of the dust and biomass-burning experiment and African monsoon multidisciplinary analysis special observing period-0. Journal of Geophysical Research. Atmospheres 113, D00C17. https://doi.org/10.1029/2008JD010077.

Heever, S.C. van den, Carrió, G.G., Cotton, W.R., DeMott, P.J., Prenni, A.J., 2006. Impacts of nucleating aerosol on Florida storms. Part I: Mesoscale simulations. Journal of the Atmospheric Sciences 63 (7), 1752–1775. https://doi.org/10.1175/JAS3713.1.

Heinold, B., Tegen, I., Schepanski, K., Hellmuth, O., 2008. Dust radiative feedback on Saharan boundary layer dynamics and dust mobilization. Geophysical Research Letters 35 (20). https://doi.org/10.1029/2008GL035319.

Hobbs, P.V., Radke, L.F., 1969. Cloud condensation nuclei from a simulated forest fire. Science 163 (3864), 279–280. https://doi.org/10.1126/science.163.3864.279.

Holanda, B.A., Pöhlker, M.L., Walter, D., Saturno, J., Sörgel, M., Ditas, J., Ditas, F., Schulz, C., Franco, M.A., Wang, Q., Donth, T., Artaxo, P., Barbosa, H.M.J., Borrmann, S., Braga, R., Brito, J., Cheng, Y., Dollner, M., Kaiser, J.W., et al., 2020. Influx of African biomass burning aerosol during the Amazonian dry season through layered transatlantic transport of black carbon-rich smoke. Atmospheric Chemistry and Physics 20 (8), 4757–4785. https://doi.org/10.5194/acp-20-4757-2020.

Hoose, C., Lohmann, U., Erdin, R., Tegen, I., 2008. The global influence of dust mineralogical composition on heterogeneous ice nucleation in mixed-phase clouds. Environmental Research Letters 3 (2), 025003. https://doi.org/10.1088/1748--9326/3/2/025003.

Hoose, C., Möhler, O., 2012. Heterogeneous ice nucleation on atmospheric aerosols: a review of results from laboratory experiments. Atmospheric Chemistry and Physics 12 (20), 9817–9854. https://doi.org/10.5194/acp-12-9817-2012.

Hopsch, S.B., Thorncroft, C.D., Hodge, K., Aiyyer, A., 2007. West African storm tracks and their relationship to Atlantic tropical cyclones. Journal of Climate 20, 2468–2483. https://doi.org/10.1175/JCLI4139.1.

Hoskins, B.J., James, I.N., White, G.H., 1983. The shape, propagation and mean-flow interaction of large-scale weather systems. Journal of the Atmospheric Sciences 40 (7), 7. https://doi.org/10.1175/1520-0469(1983)040.

Hosseinpour, F., Wilcox, E.M., 2024. A new look into the impacts of dust radiative forcing on the energetics of tropical easterly waves. EGUsphere 2023, 1–48. https://doi.org/10.5194/acp-24-707-2024.

Hosseinpour, F., Wilcox, E.M., 2014. Aerosol interactions with African/Atlantic climate dynamics. Environmental Research Letters 9 (075004), 075004. https://doi.org/10.1088/1748-9326/9/7/075004.

Hsieh, J.S., Cook, K.H., 2005. Generation of African easterly wave disturbances: relationship to the African easterly jet. Monthly Weather Review 133, 1311–1327. https://doi.org/10.1175/MWR2916.1.

Hsieh, J.S., Cook, K.H., 2007. A study of the energetics of African easterly waves using a regional climate model. Journal of the Atmospheric Sciences 64 (2), 2. https://doi.org/10.1175/JAS3851.1.

Huang, J., Hartemink, A.E., 2020. Soil and environmental issues in sandy soils. Earth-Science Reviews 208, 103295. https://doi.org/10.1016/j.earscirev.2020.103295.

Hurrell, J.W., 1995. Decadal trends in the North Atlantic oscillation: regional temperatures and precipitation. Science 269 (5224), 676–679. https://doi.org/10.1126/science.269.5224.676.

Jenkins, M.A., Cho, H.-R., 1991. An observational study of the first-order vorticity dynamics in a tropical easterly wave. Journal of the Atmospheric Sciences 48 (7), 965–975. https://doi.org/10.1175/1520-0469(1991)048<0965:AOSOTF>2.0.CO;2.

Johnson, B.T., Shine, K.P., Forster, P.M., 2004. The semi-direct aerosol effect: impact of absorbing aerosols on marine stratocumulus. Quarterly Journal of the Royal Meteorological Society 130 (599), 1407–1422. https://doi.org/10.1256/qj.03.61.

Jones, C., Mahowald, N., Luo, C., 2003. The role of easterly waves on African Desert dust transport. Journal of Climate 16, 3617–3628. https://doi.org/10.1175/1520-0442(2003)016.

Jones, C., Mahowald, N., Luo, C., 2004. Observational evidence of African Desert dust intensification of easterly waves. Geophysical Research Letters 31 (L17208). https://doi.org/10.1029/2004gl020107.

Jordan, A.K., Gnanadesikan, A., Zaitchik, B., 2018. Simulated dust aerosol impacts on western Sahelian rainfall: importance of ocean coupling. Journal of Climate 31 (22), 9107–9124. https://doi.org/10.1175/JCLI-D-17-0819.1.

Karyampudi, V.M., Carlson, T.N., 1988. Analysis and numerical simulations of the Saharan air layer and its effect on easterly wave disturbances. Journal of the Atmospheric Sciences 45 (21), 3102–3136. https://doi.org/10.1175/1520-0469(1988)045<3102:AANSOT>2.0.CO;2.

Karyampudi, V.M., Pierce, H.F., 2002. Synoptic-scale influence of the Saharan air layer on tropical cyclogenesis over the eastern Atlantic. Monthly Weather Review 130 (12), 3100–3128. https://doi.org/10.1175/1520-0493(2002)130%3C3100:SSIOTS%3E2.0.CO;2.

Khain, A., Lynn, B., Dudhia, J., 2010. Aerosol effects on intensity of landfalling hurricanes as seen from simulations with the WRF model with spectral bin microphysics. Journal of the Atmospheric Sciences 67 (2), 365–384. https://doi.org/10.1175/2009JAS3210.1.

Kiladis, G.N., Thorncroft, C.D., Hall, N.M.J., 2006. Three-dimensional structure and dynamics of African easterly waves part I: observations. Journal of the Atmospheric Sciences 63, 2212–2230. https://doi.org/10.1175/JAS3741.1.

Kim, D., Chin, M., Remer, L.A., Diehl, T., Bian, H., Yu, H., Brown, M.E., Stockwell, W.R., 2017. Role of surface wind and vegetation cover in multi-decadal variations of dust emission in the Sahara and Sahel. Atmospheric Environment 148, 282–296. https://doi.org/10.1016/j.atmosenv.2016.10.051.

Kim, K.M., Lau, W.K.M., Sud, Y.C., Walker, G.K., 2010. Influence of aerosol-radiative forcings on the diurnal and seasonal cycles of rainfall over West Africa and Eastern Atlantic Ocean using GCM simulations. Climate Dynamics 35, 115–126. https://doi.org/10.1007/s00382-010-0750-1.

Koch, D., Del Genio, A.D., 2010. Black carbon semi-direct effects on cloud cover: review and synthesis. Atmospheric Chemistry and Physics 10 (16), 7685–7696. https://doi.org/10.5194/acp-10-7685-2010.

Kok, J.F., Adebiyi, A.A., Albani, S., Balkanski, Y., Checa-Garcia, R., Chin, M., Colarco, P.R., Hamilton, D.S., Huang, Y., Ito, A., Klose, M., Li, L., Mahowald, N.M., Miller, R.L., Obiso, V., Pérez García-Pando, C., Rocha-Lima, A., Wan, J.S., 2021. Contribution of the world's main dust source regions to the global cycle of desert dust. Atmospheric Chemistry and Physics 21 (10), 8169–8193. https://doi.org/10.5194/acp-21-8169-2021.

Kok, J.F., Storelvmo, T., Karydis, V.A., Adebiyi, A.A., Mahowald, N.M., Evan, A.T., He, C., Leung, D.M., 2023. Mineral dust aerosol impacts on global climate and climate change. Nature Reviews Earth & Environment 4 (2), 2. https://doi.org/10.1038/s43017-022-00379-5.

Koren, I., Kaufman, Y.J., Remer, L.A., Martins, J.V., 2004. Measurement of the effect of Amazon smoke on inhibition of cloud formation. Science 303 (5662), 1342–1345. https://doi.org/10.1126/science.1089424.

Kumar, P., Nenes, A., Sokolik, I.N., 2009. Importance of adsorption for CCN activity and hygroscopic properties of mineral dust aerosol. Geophysical Research Letters 36 (24). https://doi.org/10.1029/2009GL040827.

Lau, K., Kim, K., 2007. Cooling of the Atlantic by Saharan dust. Geophysical Research Letters 34 (23). https://doi.org/10.1029/2007GL031538.

Lau, K.M., Kim, M.K., Kim, K.M., 2006. Asian summer monsoon anomalies induced by aerosol direct forcing: the role of the Tibetan Plateau. Climate Dynamics 26 (7), 855–864. https://doi.org/10.1007/s00382-006-0114-z.

Lau, K.M., Kim, K.M., Sud, Y.C., Walker, G.K., 2009. A GCM study of the response of the atmospheric water cycle of West Africa and the Atlantic to Saharan dust radiative forcing. Annals of Geophysics 27, 4023–4037. https://doi.org/10.5194/angeo-27-4023-2009.

Lebo, Z.J., Morrison, H., Seinfeld, J.H., 2012. Are simulated aerosol-induced effects on deep convective clouds strongly dependent on saturation adjustment? Atmospheric Chemistry and Physics 12 (20), 9941–9964. https://doi.org/10.5194/acp-12-9941-2012.

Levin, Z., Teller, A., Ganor, E., Yin, Y., 2005. On the interactions of mineral dust, sea-salt particles, and clouds: a measurement and modeling study from the Mediterranean Israeli Dust Experiment campaign. Journal of Geophysical Research. Atmospheres 110 (D20). https://doi.org/10.1029/2005JD005810.

Liao, H., Seinfeld, J.H., 1998. Radiative forcing by mineral dust aerosols: sensitivity to key variables. Journal of Geophysical Research. Atmospheres 103 (D24), 31637–31645. https://doi.org/10.1029/1998JD200036.

Liao, H., Zhang, Y., Chen, W.-T., Raes, F., Seinfeld, J.H., 2009. Effect of chemistry-aerosol-climate coupling on predictions of future climate and future levels of tropospheric ozone and aerosols. Journal of Geophysical Research. Atmospheres 114 (D10). https://doi.org/10.1029/2008JD010984.

Lin, Y., Wang, Y., Hsieh, J.-S., Jiang, J.H., Su, Q., Zhao, L., Lavallee, M., Zhang, R., 2023. Assessing the destructiveness of tropical cyclones induced by anthropogenic aerosols in an atmosphere–ocean coupled framework. Atmospheric Chemistry and Physics 23 (21), 13835–13852. https://doi.org/10.5194/acp-23-13835-2023.

Liu, D., Wang, Z., Liu, Z., Winker, D., Trepte, C., 2008. A height resolved global view of dust aerosols from the first year CALIPSO lidar measurements. Journal of Geophysical Research. Atmospheres 113 (D16214). https://doi.org/10.1029/2007JD009776.

Lohmann, U., Feichter, J., 2005. Global indirect aerosol effects: a review. Atmospheric Chemistry and Physics 5 (3), 715–737. https://doi.org/10.5194/acp-5-715-2005.

Lorenz, E.N., 1955. Available potential energy and the maintenance of the general circulation. Tellus 7, 157–167. https://doi.org/10.1111/j.2153-3490.1955.tb01148.x.

Luo, H., Han, Y., 2021. Impacts of the Saharan air layer on the physical properties of the Atlantic tropical cyclone cloud systems: 2003–2019. Atmospheric Chemistry and Physics 21 (19), 15171–15184. https://doi.org/10.5194/acp-21-15171-2021.

Ma, P.-L., Zhang, K., Shi, J.J., Matsui, T., Arking, A., 2012. Direct radiative effect of mineral dust on the development of African easterly waves in late summer, 2003–07. Journal of Applied Meteorology and Climatology 51 (12), 2090–2104. https://doi.org/10.1175/JAMC-D-11-0215.1.

Mahowald, N.M., Artaxo, P., Baker, A.R., Jickells, T.D., Okin, G.S., Randerson, J.T., Townsend, A.R., 2005. Impacts of biomass burning emissions and land use change on Amazonian atmospheric phosphorus cycling and deposition. Global Biogeochemical Cycles 19 (4). https://doi.org/10.1029/2005GB002541.

Mahowald, N.M., Engelstaedter, S., Luo, C., Sealy, A., Artaxo, P., Benitez-Nelson, C., Bonnet, S., Chen, Y., Chuang, P.Y., Cohen, D.D., Dulac, F., Herut, B., Johansen, A.M., Kubilay, N., Losno, R., Maenhaut, W., Paytan, A., Prospero, J.M., Shank, L.M., Siefert, R.L., 2009. Atmospheric iron deposition: global distribution, variability, and human perturbations. Annual Review of Marine Science 1 (1), 245–278. https://doi.org/10.1146/annurev.marine.010908.163727.

Mahowald, N.M., Muhs, D.R., Levis, S., Rasch, P.J., Yoshioka, M., Zender, C.S., Luo, C., 2006. Change in atmospheric mineral aerosols in response to climate: last glacial period, preindustrial, modern, and doubled carbon dioxide climates. Journal of Geophysical Research. Atmospheres 111 (D10). https://doi.org/10.1029/2005JD006653.

Mamun, A., Chen, Y., Liang, J., 2021. Radiative and cloud microphysical effects of the Saharan dust simulated by the WRF-Chem model. Journal of Atmospheric and Solar-Terrestrial Physics 219, 105646. https://doi.org/10.1016/j.jastp.2021.105646.

Marticorena, B., Chatenet, B., Rajot, J.L., Traoré, S., Coulibaly, M., Diallo, A., Koné, I., Maman, A., NDiaye, T., Zakou, A., 2010. Temporal variability of mineral dust concentrations over West Africa: analyses of a pluriannual monitoring from the AMMA Sahelian Dust Transect. Atmospheric Chemistry and Physics 10 (18), 8899–8915. https://doi.org/10.5194/acp-10-8899-2010.

Martins, J.A., Silva Dias, M.a.F., Gonçalves, F.L.T., 2009. Impact of biomass burning aerosols on precipitation in the Amazon: a modeling case study. Journal of Geophysical Research. Atmospheres 114 (D2). https://doi.org/10.1029/2007JD009587.

Matsuki, A., Quennehen, B., Schwarzenboeck, A., Crumeyrolle, S., Venzac, H., Laj, P., Gomes, L., 2010. Temporal and vertical variations of aerosol physical and chemical properties over West Africa: AMMA aircraft campaign in summer 2006. Atmospheric Chemistry and Physics 10, 8437–8451. https://doi.org/10.5194/acp-10-8437-2010.

Meloni, D., Sarra, A., Brogniez, G., Denjean, C., Silvestri, L., Iorio, T., Formenti, P., Gómez-Amo, J.L., Gröbner, J., Kouremeti, N., Liuzzi, G., Mallet, M., Pace, G., Sferlazzo, D.M., 2018. Determining the infrared radiative effects of Saharan dust: a radiative transfer modelling study based on vertically resolved measurements at Lampedusa. Atmospheric Chemistry and Physics 18, 4377–4401. https://doi.org/10.5194/acp-18-4377-2018.

Miller, R.L., Tegen, I., Perlwitz, J., 2004. Surface radiative forcing by soil dust aerosols and the hydrologic cycle. Journal of Geophysical Research. Atmospheres 109 (D4). https://doi.org/10.1029/2003JD004085.

Min, Q.-L., Li, R., Lin, B., Joseph, E., Wang, S., Hu, Y., Morris, V., Chang, F., 2009. Evidence of mineral dust altering cloud microphysics and precipitation. Atmospheric Chemistry and Physics 9 (9), 3223–3231. https://doi.org/10.5194/acp-9-3223-2009.

Ming, Y., Ramaswamy, V., 2011. A model investigation of aerosol-induced changes in tropical circulation. Journal of Climate 24 (19), 5125–5133. https://doi.org/10.1175/2011JCLI4108.1.

Moulin, C., Lambert, C.E., Dulac, F., Dayan, U., 1997. Control of atmospheric export of dust from North Africa by the North Atlantic oscillation. Nature 387 (6634), 691–694. https://doi.org/10.1038/42679.

Mulitza, S., Heslop, D., Pittauerova, D., Fischer, H.W., Meyer, I., Stuut, J.-B., Zabel, M., Mollenhauer, G., Collins, J.A., Kuhnert, H., Schulz, M., 2010. Increase in African dust flux at the onset of commercial agriculture in the Sahel region. Nature 466 (7303), 226–228. https://doi.org/10.1038/nature09213.

Myhre, G., Forster, P.M., Samset, B.H., Hodnebrog, Ø., Sillmann, J., Aalbergsjø, S.G., Andrews, T., Boucher, O., Faluvegi, G., Fläschner, D., Iversen, T., Kasoar, M., Kharin, V., Kirkevåg, A., Lamarque, J.-F., Olivié, D., Richardson, T.B., Shindell, D., Shine, K.P., et al., 2017. PDRMIP: a precipitation driver and response model intercomparison project—protocol and preliminary results. Bulletin of the American Meteorological Society 98 (6), 1185–1198. https://doi.org/10.1175/BAMS-D-16-0019.1.

Myhre, G., Kramer, R.J., Smith, C.J., Hodnebrog, Ø., Forster, P., Soden, B.J., Samset, B.H., Stjern, C.W., Andrews, T., Boucher, O., Faluvegi, G., Fläschner, D., Kasoar, M., Kirkevåg, A., Lamarque, J.-F., Olivié, D., Richardson, T., Shindell, D., Stier, P., et al., 2018. Quantifying the importance of rapid adjustments for global precipitation changes. Geophysical Research Letters 45 (20), 11399–11405. https://doi.org/10.1029/2018GL079474.

Norquist, D.C., Recker, E., Reed, R.J., 1977. The energetics of African wave disturbances as observed during the phase III of GATE. Monthly Weather Review 105, 334–342. https://doi.org/10.1175/1520-0493(1977)105.

Pan, B., Wang, Y., Lin, Y., Hsieh, J., Lavallee, M., Zhao, L., Zhang, R., 2024. Radiative and microphysical impacts of the Saharan dust on two concurrent tropical cyclones: Danielle and Earl (2010). Journal of Geophysical Research. Atmospheres 129 (2), e2023JD039245. https://doi.org/10.1029/2023JD039245.

Pasch, R.J., Avila, L.A., 1994. Atlantic tropical systems of 1992. Monthly Weather Review 122 (3), 3. https://doi.org/10.1175/1520-0493(1994)122.

Pausata, F.S.R., Zhang, Q., Muschitiello, F., Lu, Z., Chafik, L., Niedermeyer, E.M., Stager, J.C., Cobb, K.M., Liu, Z., 2017. Greening of the Sahara suppressed ENSO activity during the mid-Holocene. Nature Communications 8 (1), 16020. https://doi.org/10.1038/ncomms16020.

Perlwitz, J., Miller, R.L., 2010. Cloud cover increase with increasing aerosol absorptivity: a counterexample to the conventional semidirect aerosol effect. Journal of Geophysical Research. Atmospheres 115 (D8). https://doi.org/10.1029/2009JD012637.

Perry, K.D., Cahill, T.A., Eldred, R.A., Dutcher, D.D., Gill, T.E., 1997. Long-range transport of North African dust to the eastern United States. Journal of Geophysical Research. Atmospheres 102, 11,225–11,238. https://doi.org/10.1029/97JD00260.

Prenni, A.J., Petters, M.D., Kreidenweis, S.M., Heald, C.L., Martin, S.T., Artaxo, P., Garland, R.M., Wollny, A.G., Pöschl, U., 2009. Relative roles of biogenic emissions and Saharan dust as ice nuclei in the Amazon basin. Nature Geoscience 2 (6), 402–405. https://doi.org/10.1038/ngeo517.

Price, H.C., Baustian, K.J., McQuaid, J.B., Blyth, A., Bower, K.N., Choularton, T., Cotton, R.J., Cui, Z., Field, P.R., Gallagher, M., Hawker, R., Merrington, A., Miltenberger, A., Neely III, R.R., Parker, S.T., Rosenberg, P.D., Taylor, J.W., Trembath, J., Vergara-Temprado, J., et al., 2018. Atmospheric ice-nucleating particles in the dusty tropical Atlantic. Journal of Geophysical Research. Atmospheres 123 (4), 2175–2193. https://doi.org/10.1002/2017JD027560.

Prospero, J.M., Ginoux, P., Torres, O., Nicholson, S.E., Gill, T.E., 2002. Environmental characterization of global sources of atmospheric soil dust identified with the Nimbus 7 Total Ozone Mapping Spectrometer (TOMS) absorbing aerosol product. Reviews of Geophysics 40 (1), 2-1. https://doi.org/10.1029/2000RG000095.

Pu, B., Jin, Q., 2021. A record-breaking trans-Atlantic African dust plume associated with atmospheric circulation extremes in June 2020. Bulletin of the American Meteorological Society 102 (7), E1340–E1356. https://doi.org/10.1175/BAMS-D-21-0014.1.

Pytharoulis, I., Thorncroft, C., 1999. The low-level structure of African easterly waves in 1995. Monthly Weather Review 127 (10), 2266–2280. https://doi.org/10.1175/1520-0493(1999)127%3C2266:TLLSOA%3E2.0.CO;2.

Querol, X., Tobías, A., Pérez, N., Karanasiou, A., Amato, F., Stafoggia, M., Pérez García-Pando, C., Ginoux, P., Forastiere, F., Gumy, S., Mudu, P., Alastuey, A., 2019. Monitoring the impact of desert dust outbreaks for air quality for health studies. Environment International 130, 104867. https://doi.org/10.1016/j.envint.2019.05.061.

Redemann, J., Wood, R., Zuidema, P., Doherty, S.J., Luna, B., LeBlanc, S.E., Diamond, M.S., Shinozuka, Y., Chang, I.Y., Ueyama, R., Pfister, L., Ryoo, J.-M., Dobracki, A.N., da Silva, A.M., Longo, K.M., Kacenelenbogen, M.S., Flynn, C.J., Pistone, K., Knox, N.M., Piketh, S.J., Haywood, J.M., Formenti, P., Mallet, M., Stier, P., Ackerman, A.S., Bauer, S.E., Fridlind, A.M., Carmichael, G.R., Saide, P.E., Ferrada, G.A., Howell, S.G., Freitag, S., Cairns, B., Holben, B.N., Knobelspiesse, K.D., Tanelli, S., L'Ecuyer, T.S., Dzambo, A.M., Sy, O.O., McFarquhar, G.M., Poellot, M.R., Gupta, S., O'Brien, J.R., Nenes, A., Kacarab, M., Wong, J.P.S., Small-Griswold, J.D., Thornhill, K.L., Noone, D., Podolske, J.R., Schmidt, K.S., Pilewskie, P., Chen, H., Cochrane, S.P., Sedlacek, A.J., Lang, T.J., Stith, E., Segal-Rozenhaimer, M., Ferrare, R.A., Burton, S.P., Hostetler, C.A., Diner, D.J., Seidel, F.C., Platnick, S.E., Myers, J.S., Meyer, K.G., Spangenberg, D.A., Maring, H., Gao, L., 2021. An overview of the ORACLES (ObseRvations of Aerosols above CLouds and their intEractionS) project: aerosol–cloud–radiation interactions in the southeast Atlantic basin. Atmospheric Chemistry and Physics 21, 1507–1563. https://doi.org/10.5194/acp-21-1507-2021.

Reale, O., Lau, K., Da Silva, A., Matsui, T., 2014. Impact of assimilated and interactive aerosol on tropical cyclogenesis. Geophysical Research Letters 41 (9), 3282–3288. https://doi.org/10.1002/2014GL059918.

Reed, K.A., Bacmeister, J.T., Huff, J.J.A., Wu, X., Bates, S.C., Rosenbloom, N.A., 2019. Exploring the impact of dust on North Atlantic hurricanes in a high-resolution climate model. Geophysical Research Letters 46 (2), 1105–1112. https://doi.org/10.1029/2018GL080642.

Reed, R.J., Norquist, D.C., Recker, E.E., 1977. The structure and properties of African wave disturbances as observed during phase III of GATE. Monthly Weather Review 105 (3), 317–333. https://doi.org/10.1175/1520-0493(1977)105<0317:TSAPOA>2.0.CO;2.

Ridley, D.A., Heald, C.L., Kok, J.F., Zhao, C., 2016. An observationally constrained estimate of global dust aerosol optical depth. Atmospheric Chemistry and Physics 16 (23), 15097–15117. https://doi.org/10.5194/acp-16-15097-2016.

Rosenfeld, D., Andreae, M.O., Asmi, A., Chin, M., de Leeuw, G., Donovan, D.P., Kahn, R., Kinne, S., Kivekäs, N., Kulmala, M., Lau, W., Schmidt, K.S., Suni, T., Wagner, T., Wild, M., Quaas, J., 2014. Global observations of aerosol-cloud-precipitation-climate interactions. Reviews of Geophysics 52 (4), 750–808. https://doi.org/10.1002/2013RG000441.

Rosenfeld, D., Clavner, M., Nirel, R., 2011. Pollution and dust aerosols modulating tropical cyclones intensities. Atmospheric Research 102 (1), 66–76. https://doi.org/10.1016/j.atmosres.2011.06.006.

Rosenfeld, D., Lohmann, U., Raga, G.B., O'Dowd, C.D., Kulmala, M., Fuzzi, S., Reissell, A., Andreae, M.O., 2008. Flood or drought: how do aerosols affect precipitation? Science 321 (5894), 1309–1313. https://doi.org/10.1126/science.1160606.

Rosenfeld, D., Rudich, Y., Lahav, R., 2001. Desert dust suppressing precipitation: a possible desertification feedback loop. Proceedings of the National Academy of Sciences 98 (11), 5975–5980. https://doi.org/10.1073/pnas.101122798.

Rosenfeld, D., Woodley, W.L., Khain, A., Cotton, W.R., Carrió, G., Ginis, I., Golden, J.H., 2012. Aerosol effects on microstructure and intensity of tropical cyclones. Bulletin of the American Meteorological Society 93 (7), 987–1001. https://doi.org/10.1175/BAMS-D-11-00147.1.

Roundy, P.E., Frank, W.M., 2004. A climatology of waves in the equatorial region. Journal of the Atmospheric Sciences 61, 2105–2132. https://doi.org/10.1175/1520-0469(2004)061.

Russell, J.O., Aiyyer, A., Dylan White, J., 2020. African easterly wave dynamics in convection-permitting simulations: rotational stratiform instability as a conceptual model. Journal of Advances in Modeling Earth Systems 12 (1), 1. https://doi.org/10.1029/2019MS001706.

Saidou Chaibou, A.A., Ma, X., Sha, T., 2020. Dust radiative forcing and its impact on surface energy budget over West Africa. Scientific Reports 10 (1), 1. https://doi.org/10.1038/s41598-020-69223-4.

Sakaeda, N., Wood, R., Rasch, P.J., 2011. Direct and semidirect aerosol effects of southern African biomass burning aerosol. Journal of Geophysical Research. Atmospheres 116 (D12). https://doi.org/10.1029/2010JD015540.

Saleeby, S.M., Cotton, W.R., 2005. A large-droplet mode and prognostic number concentration of cloud droplets in the Colorado State University Regional Atmospheric Modeling System (RAMS). Part II: Sensitivity to a Colorado winter snowfall event. Journal of Applied Meteorology and Climatology 44 (12), 1912–1929. https://doi.org/10.1175/JAM2312.1.

Samset, B.H., 2022. Aerosol absorption has an underappreciated role in historical precipitation change. Communications Earth & Environment 3 (1), 1–8. https://doi.org/10.1038/s43247-022-00576-6.

Sand, M., Samset, B.H., Myhre, G., Gliß, J., Bauer, S.E., Bian, H., Chin, M., Checa-Garcia, R., Ginoux, P., Kipling, Z., Kirkevåg, A., Kokkola, H., Le Sager, P., Lund, M.T., Matsui, H., van Noije, T., Olivié, D.J.L., Remy, S., Schulz, M., et al., 2021. Aerosol absorption in global models from AeroCom phase III. Atmospheric Chemistry and Physics 21 (20), 15929–15947. https://doi.org/10.5194/acp-21-15929-2021.

Seigel, R.B., van den Heever, S.C., Saleeby, S.M., 2013. Mineral dust indirect effects and cloud radiative feedbacks of a simulated idealized nocturnal squall line. Atmospheric Chemistry and Physics 13 (8), 4467–4485. https://doi.org/10.5194/acp-13-4467-2013.

Shao, Y., 2004. Simplification of a dust emission scheme and comparison with data. Journal of Geophysical Research. Atmospheres 109 (D10). https://doi.org/10.1029/2003JD004372.

Shao, Y., Klose, M., Wyrwoll, K.-H., 2013. Recent global dust trend and connections to climate forcing. Journal of Geophysical Research. Atmospheres 118 (19), 11107–11118. https://doi.org/10.1002/jgrd.50836.

Shi, L., Zhang, J., Yao, F., Zhang, D., Guo, H., 2021. Drivers to dust emissions over dust belt from 1980 to 2018 and their variation in two global warming phases. Science of the Total Environment 767, 144860. https://doi.org/10.1016/j.scitotenv.2020.144860.

Solmon, F., Elguindi, N., Mallet, M., 2012. Radiative and climatic effects of dust over West Africa, as simulated by a regional climate model. Climate Research 52, 97–113. https://doi.org/10.3354/cr01039.

Soupiona, O., Papayannis, A., Kokkalis, P., Foskinis, R., Sánchez Hernández, G., Ortiz-Amezcua, P., Mylonaki, M., Papanikolaou, C.-A., Papagiannopoulos, N., Samaras, S., Groß, S., Mamouri, R.-E., Alados-Arboledas, L., Amodeo, A., Psiloglou, B., 2020. EARLINET observations of Saharan dust intrusions over the northern Mediterranean region (2014–2017): properties and impact on radiative forcing. Atmospheric Chemistry and Physics 20, 15147–15166. https://doi.org/10.5194/acp-20-15147-2020.

Stephens, G.L., Wood, N.B., Pakula, L.A., 2004. On the radiative effects of dust on tropical convection. Geophysical Research Letters 31 (23). https://doi.org/10.1029/2004GL021342.

Strong, J.D.O., Vecchi, G.A., Ginoux, P., 2015. The response of the tropical Atlantic and West African climate to Saharan dust in a fully coupled GCM. Journal of Climate 28 (18), 7071–7092. https://doi.org/10.1175/JCLI-D-14-00797.1.

Strong, J.D., Vecchi, G.A., Ginoux, P., 2018. The climatological effect of Saharan dust on global tropical cyclones in a fully coupled GCM. Journal of Geophysical Research. Atmospheres 123 (10), 5538–5559. https://doi.org/10.1029/2017JD027808.

Sun, Y., Zhao, C., 2020. Influence of Saharan dust on the large-scale meteorological environment for development of tropical cyclone over North Atlantic Ocean Basin. Journal of Geophysical Research. Atmospheres 125 (23), e2020JD033454. https://doi.org/10.1029/2020JD033454.

Takahashi, C., Shirooka, R., 2014. Storm track activity over the North Pacific associated with the Madden–Julian Oscillation under ENSO conditions during boreal winter. Journal of Geophysical Research. Atmospheres 119 (18), 10663–10683. https://doi.org/10.1002/2014JD021973.

Tao, Z., Braun, S.A., Shi, J.J., Chin, M., Kim, D., Matsui, T., Peters-Lidard, C.D., 2018. Microphysics and radiation effect of dust on Saharan air layer: an HS3 case study. Monthly Weather Review 146 (6), 1813–1835. https://doi.org/10.1175/MWR-D-17-0279.1.

Thorncroft, C.D., Hodges, K., 2001. African easterly wave variability and its relationship to Atlantic tropical cyclone activity. Journal of Climate 14, 116–1179. https://doi.org/10.1175/1520-0442(2001)014%3C1166:AEWVAI%3E2.0.CO;2.

Tsikerdekis, A., Zanis, P., Georgoulias, A.K., Alexandri, G., Katragkou, E., Karacostas, T., Solmon, F., 2019. Direct and semi-direct radiative effect of North African dust in present and future regional climate simulations. Climate Dynamics 53, 4311–4336. https://doi.org/10.1007/s00382-019-04788-z.

Twomey, S., 1977. The influence of pollution on the shortwave albedo of clouds. Journal of the Atmospheric Sciences 34 (7), 1149–1152. https://doi.org/10.1175/1520-0469(1977)034%3C1149:TIOPOT%3E2.0.CO;2.

Varble, A.C., Igel, A.L., Morrison, H., Grabowski, W.W., Lebo, Z.J., 2023. Opinion: a critical evaluation of the evidence for aerosol invigoration of deep convection. Atmospheric Chemistry and Physics 23 (21), 13791–13808. https://doi.org/10.5194/acp-23-13791-2023.

Wang, C., Dong, S., Evan, A.T., Foltz, G.R., Lee, S.-K., 2012. Multidecadal covariability of North Atlantic sea surface temperature, African dust, Sahel rainfall, and Atlantic hurricanes. Journal of Climate 25 (15), 5404–5415. https://doi.org/10.1175/JCLI-D-11-00413.1.

Weinzierl, B., Ansmann, A., Prospero, J.M., Althausen, D., Benker, N., Chouza, F., Dollner, M., Farrell, D., Fomba, W., Freudenthaler, V., 2017. The Saharan aerosol long-range transport and aerosol–cloud-interaction experiment: overview and selected highlights. Bulletin of the American Meteorological Society 98 (7), 1427–1451. https://doi.org/10.1175/BAMS-D-15-00142.1.

Werner, M., Tegen, I., Harrison, S.P., Kohfeld, K.E., Prentice, I.C., Balkanski, Y., Rodhe, H., Roelandt, C., 2002. Seasonal and interannual variability of the mineral dust cycle under present and glacial climate conditions. Journal of Geophysical Research. Atmospheres 107 (D24), 2–1-AAC 2-19. https://doi.org/10.1029/2002JD002365.

Wilcox, E.M., 2010. Stratocumulus cloud thickening beneath layers of absorbing smoke aerosol. Atmospheric Chemistry and Physics 10 (23), 11769–11777. https://doi.org/10.5194/acp-10-11769-2010.

Woodward, S., Roberts, D.L., Betts, R.A., 2005. A simulation of the effect of climate change-induced desertification on mineral dust aerosol. Geophysical Research Letters 32, L18810. https://doi.org/10.1029/2005GL023482.

Xi, X., Sokolik, I.N., 2015. Seasonal dynamics of threshold friction velocity and dust emission in Central Asia. Journal of Geophysical Research. Atmospheres 120 (4), 1536–1564. https://doi.org/10.1002/2014JD022471.

Xian, P., Klotzbach, P.J., Dunion, J.P., Janiga, M.A., Reid, J.S., Colarco, P.R., Kipling, Z., 2020. Revisiting the relationship between Atlantic dust and tropical cyclone activity using aerosol optical depth reanalyses: 2003–2018. Atmospheric Chemistry and Physics 20 (23), 15357–15378. https://doi.org/10.5194/acp-20-15357-2020.

Yoshioka, M., Mahowald, N.M., Conley, A.J., Collins, W.D., Fillmore, D.W., Zender, C.S., Coleman, D.B., 2007. Impact of desert dust radiative forcing on Sahel precipitation: relative importance of dust compared to sea surface temperature variations, vegetation changes, and greenhouse gas warming. Journal of Climate 20 (8), 1445–1467. https://doi.org/10.1175/JCLI4056.1.

Yu, H., Chin, M., Yuan, T., Bian, H., Remer, L.A., Prospero, J.M., Omar, A., Winker, D., Yang, Y., Zhang, Y., Zhang, Z., Zhao, C., 2015. The fertilizing role of African dust in the Amazon rainforest: a first multiyear assessment based on data from Cloud-Aerosol Lidar and Infrared Pathfinder Satellite Observations. Geophysical Research Letters 42 (6), 1984–1991. https://doi.org/10.1002/2015GL063040.

Yuan, T., Oreopoulos, L., Zelinka, M., Yu, H., Norris, J.R., Chin, M., Platnick, S., Meyer, K., 2016. Positive low cloud and dust feedbacks amplify tropical North Atlantic Multidecadal Oscillation. Geophysical Research Letters 43 (3), 1349–1356. https://doi.org/10.1002/2016GL067679.

Yuan, T., Yu, H., Chin, M., Remer, L.A., McGee, D., Evan, A., 2020. Anthropogenic decline of African dust: insights from the Holocene records and beyond. Geophysical Research Letters 47 (22), e2020GL089711. https://doi.org/10.1029/2020GL089711.

Zhang, H., McFarquhar, G.M., Saleeby, S.M., Cotton, W.R., 2007. Impacts of Saharan dust as CCN on the evolution of an idealized tropical cyclone. Geophysical Research Letters 34 (14). https://doi.org/10.1029/2007GL029876.

Zhang, M., Liu, Y., Zhang, J., Wen, Q., 2021a. AMOC and climate responses to dust reduction and greening of the Sahara during the mid-Holocene. Journal of Climate 34 (12), 4893–4912. https://doi.org/10.1175/JCLI-D-20-0628.1.

Zhang, S., Stier, P., Watson-Parris, D., 2021b. On the contribution of fast and slow responses to precipitation changes caused by aerosol perturbations. Atmospheric Chemistry and Physics 21 (13), 10179–10197. https://doi.org/10.5194/acp-21-10179-2021.

Zhang, Y., Yu, F., Luo, G., Fan, J., Liu, S., 2021c. Impacts of long-range-transported mineral dust on summertime convective cloud and precipitation: a case study over the Taiwan region. Atmospheric Chemistry and Physics 21 (23), 17433–17451. https://doi.org/10.5194/acp-21-17433-2021.

Zhao, C., Liu, X., Ruby Leung, L., Hagos, S., 2011. Radiative impact of mineral dust on monsoon precipitation variability over West Africa. Atmospheric Chemistry and Physics 11 (5), 1879–1893. https://doi.org/10.5194/acp-11-1879-2011.

Zhao, S., Suzuki, K., 2021. Exploring the impacts of aerosols on ITCZ position through altering different autoconversion schemes and cumulus parameterizations. Journal of Geophysical Research. Atmospheres 126 (14), e2021JD034803. https://doi.org/10.1029/2021JD034803.

Zhou, Y., Wu, T., Zhou, Y., Zhang, J., Zhang, F., Su, X., Jie, W., Zhao, H., Zhang, Y., Wang, J., 2023. Can global warming bring more dust? Climate Dynamics 61 (5), 2693–2715. https://doi.org/10.1007/s00382-023-06706-w.

Chapter 4

Precipitation distribution over Africa: observations and modeling

Thierry N. Taguela[a], **Akintomide A. Akinsanola**[a,b], **Vishal Bobde**[a], **Ibraheem Raji**[a], **Oluwafemi E. Adeyeri**[c], **and Adeyemi A. Adebiyi**[d]

[a]*Department of Earth and Environmental Sciences, University of Illinois Chicago, IL, United States,* [b]*Environmental Science Division, Argonne National Laboratory, Lemont, IL, United States,* [c]*Low-Carbon and Climate Impact Research Centre, School of Energy and Environment, City University of Hong Kong, Kowloon, Hong Kong Special Administrative Region,* [d]*Department of Life and Environmental Science, University of California Merced, Merced, CA, United States*

4.1 Introduction

Precipitation encompasses the diverse forms of water, such as rain, snow, sleet, and hail, which descend from the atmosphere to the Earth's surface due to water-vapor condensation. It constitutes a vital element of the hydrological cycle, serving as the principal mechanism for delivering freshwater to terrestrial ecosystems (Rast et al., 2014; Dey and Döös, 2019; Akinsanola et al., 2020; Adeyeri et al., 2024). In Africa, precipitation transcends a meteorological phenomenon and profoundly influences and shapes ecosystems, sustains terrestrial water resources, exerts considerable influence on socioeconomic activities (notably agriculture, water resources, hydroelectric power generation, etc.), and drives competition between human and natural ecosystems for scarce freshwater resources (Nicholson, 2018; Adeyeri et al., 2024). Despite its immense importance in Africa, precipitation distribution over the continent exhibits high spatial and seasonal variability, as reported by previous studies (Sultan and Janicot, 2000; Williams and Funk, 2011; Nicholson, 2013; Ongoma and Chen, 2016; Akinsanola and Zhou, 2018; Akinsanola et al., 2020, 2021; Mba et al., 2022). For instance, West Africa is dominated primarily by the West African Monsoon (WAM), and its maximum precipitation delivery during the summer months of June–September (JJAS) accounts for over 70% of its total annual precipitation, with coastal areas (e.g., the Guinea coast) receiving more precipitation than inland areas (e.g., the Sahel) (Sultan and Janicot, 2000; Nicholson, 2013; Akinsanola and Zhou, 2018; Akinsanola et al., 2020). Eastern Africa experiences a bimodal precipitation regime, with long-term rains typically occurring

Aerosols and Precipitation Over Africa. https://doi.org/10.1016/B978-0-44-314050-1.00009-8

from March to May and short rains from October to December. The precipitation over this region is strongly influenced by the Indian Ocean's sea surface temperature variability patterns (Williams and Funk, 2011), moisture transport from the Indian Ocean (Adeyeri et al., 2024), and topography (Ongoma and Chen, 2016; Akinsanola et al., 2021), with highlands like the Ethiopian Plateau receiving significant precipitation year-round, and lowlands such as Somalia experiencing drier conditions. On the other hand, central Africa also experiences a bimodal precipitation regime, but the long (short) rains typically occur from September to November (March to May). Within this region, the Congo basin experiences high and relatively evenly distributed precipitation, while the northern and southern margins of the basin exhibit more seasonal variation (Mba et al., 2022). For southern Africa, most precipitation occurs during the Southern Hemisphere summer months (i.e., October–March), with a gradient from the wetter eastern regions to the drier western areas (Cook, 2001). These pronounced spatial and seasonal characteristics of the continent's precipitation exert a noteworthy influence across various socioeconomic sectors.

Many parts of Africa have been identified as some of the areas most vulnerable to precipitation variability worldwide. This is due to overreliance on precipitation for agriculture, water resources, mining activities, and hydroelectric power. The continent also has low adaptive capacity, mainly due to a lack of infrastructure and a large proportion of the population being below the poverty line (Krishnamurthy et al., 2014; Akinsanola and Zhou, 2019a). For instance, in sub-Saharan Africa, most people depend on smallholder farming for subsistence (International Water Management Institute [IWMI], 2014). Therefore, sufficient precipitation during planting seasons is critical for some crops, while too much rain can lead to flooding, disruption of agricultural activities, and displacement of communities (Funk et al., 2015; Maidment et al., 2015; Onyutha, 2018; Le Coz and van de Giesen, 2020). Beyond agriculture, precipitation is also essential for hydroelectric power generation, a critical energy source for numerous African nations (Hamududu and Killingtveit, 2012). Reduced precipitation is associated with diminished reservoir levels, leading to reduced hydropower generation and adversely affecting electricity production and economic vitality (Chang'a et al., 2020). Furthermore, mining operations, particularly those requiring significant water usage, such as dust suppression and machinery cooling in mineral processing, can face challenges during low precipitation or drought (Hilson, 2009). Precipitation patterns also play a crucial role in shaping water-resource management, particularly in regions where erratic precipitation necessitates substantial investment in rainwater-storage infrastructure. Given the critical role of precipitation in sustaining livelihoods and economic development across Africa, an improved understanding of precipitation variability at regional-to-subregional scales across various temporal dimensions becomes imperative. Such insight is indispensable for facilitating precise policymaking and strategic management initiatives, particularly those addressing imminent hydrometeorological threats.

Accurate measurements of precipitation in Africa have posed a significant challenge (Adeyewa and Nakamura, 2003; Camberlin et al., 2019), partly because of the limited availability of ground-based observations (Washington et al., 2013) and the continent's complex topographic features (e.g., mountain ranges and vast deserts). In particular, observational datasets obtained in situ are frequently constrained and inconsistently dispersed in Africa. Station data may harbor uncertainties and biases in areas with scanty or substandard local observations, necessitating rigorous homogenization procedures (Akinsanola and Ogunjobi, 2017; Adeyeri et al., 2022a). Therefore, overcoming these challenges requires innovative approaches and advancements in techniques to improve our understanding of African precipitation patterns. Climate modeling is a promising tool for effectively tackling these challenges. Over time, significant advancement has been made through numerous modeling efforts. For example, the African Monsoon Multidisciplinary Analysis (AMMA; Redelsperger et al., 2006), the Coordinated Regional Climate Downscaling Experiment (CORDEX; Giorgi and Gutowski, 2015), the West African Monsoon Modeling and Evaluation (WAMME; Redelsperger et al., 2006), and the Coupled Model Intercomparison Project (CMIP; Taylor et al., 2012) have been initiated to understand the region's climate. Despite these advances, the models still have limited ability to accurately reproduce precipitation distribution over the continent. For instance, most models operate at coarse spatial resolutions that may not adequately resolve small-scale features critical for precipitation distribution over Africa, such as convective storms and topographical effects (Patricola and Cook, 2009; Demissie and Sime, 2021). In addition, in many models, precipitation biases have been attributed to inaccurate representation of the complex atmospheric dynamics that govern precipitation patterns over Africa—such as the West African Monsoon circulation and its interaction with other regional climate systems (Cook and Vizy, 2006; Roehrig et al., 2013; Tamoffo et al., 2023), and the African Easterly Jet components over Central Africa (Tamoffo et al., 2019; Taguela et al., 2022; Kuete et al., 2022; Adebiyi et al., 2023)—and the inability of the models to correctly resolve important biophysical features such as solar radiation, vegetation, and cloud features (Wild et al., 2005; Adeyeri et al., 2022b). However, despite these limitations, CMIP, which has been very popular and extensively used over the continent, has played a crucial role in enhancing our comprehension of global climate change through the coordination and comparison of simulations generated by numerous climate models worldwide. Furthermore, CMIP aids in assessing uncertainties in future climate projections and serves as a cornerstone for international climate assessments and policy formulation (Iturbide et al., 2020).

The latest version of the CMIP (CMIP6; Eyring et al., 2016) dataset includes updates to existing parameterizations, new physical processes, and a higher resolution than the previous version. In addition, while earlier versions primarily used Representative Concentration Pathways (RCPs) for their scenario framework, CMIP6 has adopted Shared Socioeconomic Pathways (SSPs), which integrate both greenhouse gas emissions and socioeconomic factors. Obtaining precise assessments of CMIP6 GCM precipitation across Africa is imperative because confidence in climate model predictions is established by the ability of these models to accurately replicate observed climate patterns (Randall et al., 2007). Previous studies have focused on subregional evaluations of CMIP6, examining the models' ability to reproduce historical precipitation patterns across the continent. For instance, Faye and Akinsanola (2021) evaluated the performance of CMIP6 GCMs in simulating extreme precipitation in West Africa, while Ngoma et al. (2021) and Akinsanola et al. (2021) assessed the models' ability to represent mean and extreme precipitation in East Africa. However, it is crucial to comprehensively understand how well these models capture the entire spectrum of precipitation characteristics, including the mean, extremes, variability, and onset and cessation dates across all African reference subregions as defined in the latest Intergovernmental Panel on Climate Change (IPCC) Special Report (Masson-Delmotte et al., 2021).

This chapter aims to assess present-day precipitation characteristics over Africa and across its subregions. We assess the spatial distribution of not only the mean precipitation but also extremes, variability, and onset and cessation dates using multiple gridded observations. These gridded observations are then used to validate CMIP6 simulations.

4.2 Study area, data, and methods

4.2.1 Study area

Africa is a vast continent with diverse topography encompassing plateaus, mountains, deserts, and plains. Due to its size and vastly diverse climatic conditions, it is necessary to identify and study subregions separately. As per the Köppen–Geiger climate classification, most of Africa is either tropical (between 15°N and 15°S) or arid, with parts of southern Africa experiencing temperate climate (Beck et al., 2018). For this study, the IPCC-AR6 reference subregions are used, which are: Northern Africa (NAF, including parts of the Mediterranean); Sahara (SAH); Western-Africa (WAF); Central-Africa (CAF); North Eastern-Africa (NEAF); South Eastern-Africa (SEAF); East Southern-Africa (ESAF); West Southern-Africa (WSAF); and Madagascar (MDG) (Iturbide et al., 2020). The Sahara is primarily arid, with vast dunes and rocky plateaus, and the driest area has an annual precipitation of less than 25 mm (Liebmann et al., 2012). WAF and CAF have very dense rainforests with yearly precipitation reaching up to 3,000 mm. However, these regions experience distinct annual precipitation patterns and seasonal variations (Onyutha, 2018). NEAF and SEAF are known as the Horn of Africa, characterized by mountains uplifted by the Great Rift Valley. This region experiences an average annual precipitation of approximately 800 mm. However, due to variations associated with local topography, the lowland areas can receive as little as 300 mm of precipitation per year. In comparison, the highland regions can experience precipitation levels as high as 1200 mm annually (Fenta et al., 2017). Additionally, southern Africa is segmented into three distinct areas owing to complex topography and varied climatic conditions, with mean annual precipitation ranging from a few hundred mm to 2000 mm from west to east (Siebert, 2014; Lim Kam Sian et al., 2021). This significant variation necessitates a subregional approach for adequate climate studies.

4.2.2 Data and methods

We use simulated precipitation from 19 CMIP6 models (Eyring et al., 2016). The names of the models used, along with their institutions and spatial resolution, are summarized in Table 4.1. For each model, we use the historical simulation's first realization ('r1i1p1f1'). Earlier studies (e.g., Herold et al., 2017 and Odoulami and Akinsanola, 2017) have identified uncertainties and inconsistencies among different observation products due to variations in data sources and processing algorithms. To this end, we use numerous observations to assess model outputs. The observations used here are (1) the Climate Hazards group Infrared Precipitation with Stations (CHIRPS; Funk et al., 2015) at 0.05° grid spacing; (2) Global Precipitation Climatology Center full data daily V2018 (GPCC_FDD) at 1° spatial resolution (Ziese et al., 2018); (3) unified gauge-based analysis of global daily precipitation (CPC) at 0.5° resolution (Xie et al., 2010); and (4) NOAA NCEP CPC FEWS African precipitation climatology from the famine early warning system (ARC2) available at 0.1° grid resolution (ftp.cpc.ncep.noaa.gov/fews/AFR_CLIM/ARC2/). Furthermore, with increasing usage of reanalysis precipitation over the continent, especially in regions with less observational data, we incorporate two reanalysis datasets in our analysis, namely ERA5, a fifth-generation reanalysis developed by the European Centre for Medium-Range Weather Forecasts, with a grid resolution of $0.25° \times 0.25°$ (Hersbach et al., 2020); and MERRA2, provided by the National Aeronautics and Space Administration in the United States (US), with a grid resolution of $0.5° \times 0.625°$ (Gelaro et al., 2017).

The model simulations, gridded observations, and reanalysis data have different spatial and temporal resolutions. To ensure consistency and facilitate comparison across all datasets, we remap all data onto a spatial grid of $2.81° \times 2.81°$ using first-order conservative remapping, with the lowest model resolution serving as the basis (Faye and Akinsanola, 2021). Furthermore, all analyses presented herein are carried out over the period 1985–2014 with a focus on the annual and summer months from May to September (November to March) for the Northern (Southern) Hemisphere, aggregated across the African continent. Aside from the mean precipitation, we assess the spatial characteristics of precipitation extremes over the continent by considering two precipitation indices defined by the Expert Team on Climate Change Detection and Indices (ETCCDI; Zhang et al., 2011): consecutive dry days (CDD) and five-consecutive-day maximum (Rx5day). CDD is defined as the maximum number of consecutive days with daily precipitation less than 1 mm and is often used as a meteorological drought or dryness indicator, while Rx5day is defined as the maximum amount of precipitation recorded over a consecutive period of five days within a given time frame and is frequently used as an extreme precipitation index in flood risk assessments (Zhang et al., 2011; Seneviratne et al., 2012; Pokam et al., 2018; Akinsanola et al., 2023). The indices are first calculated for individual models on a common grid and then averaged to form the models' ensemble mean (EnsMean). We further assess the right tail of the precipitation distribution (i.e., 99th percentile minus 90th percentile precipitation), which is a measure of very heavy precipitation (Akinsanola et al., 2024). In addition, the standard deviation is used to assess the variability of precipitation over Africa (Eq. (4.1)):

$$\sigma = \sqrt{\frac{1}{n}\sum_{i=1}^{n}(x_i - \overline{x})^2}, \tag{4.1}$$

where "σ" is the standard deviation, "n" is the number of points, and "x" is either observation or model. Finally, we further compute the onset and cessation dates following Bombardi et al. (2019), whose method uses only precipitation data to calculate the timing of the rainy (or dry) season at the local scale (e.g., station or grid point). The daily accumulation of precipitation anomalies (S) initiated from the dry season is used to detect the onset and cessation dates. Depending on the climatology of a specific region, S defines a threshold for the onset and cessation dates, considering the persistence of precipitation prior to these dates. S is calculated using Eq. (4.2):

$$S = \sum_{i-t_0}(P_i - \overline{P}), \tag{4.2}$$

where P_i is the daily precipitation rate on day "i", "$\overline{P}$" is the long-term mean annual precipitation rate in mm/day, and "t_0" is the starting date for the calculations. Two inflection points are identified along the curve S, corresponding to the onset and cessation period, described as the minimum and maximum accumulated precipitation anomalies for each grid point (see Fig. 4.1).

Similar to Akinsanola et al. (2021), we evaluate the ability of the CMIP6 models to accurately capture the observed precipitation characteristics using a suite of statistical metrics presented in Eqs. (4.3)–(4.5). Specifically, we assess the percentage bias, root mean square error (RMSE), and pattern correlation coefficient (PCC). The results are presented graphically using portrait diagrams, which provide a compact overview of model performance relative to each other in all subregions under consideration (Sillmann et al., 2013; Akinsanola et al., 2020).

$$\%BIAS = \frac{\sum_{i=1}^{n}(M_i - O_i)}{\sum_{i=1}^{n} O_i} \times 100 \tag{4.3}$$

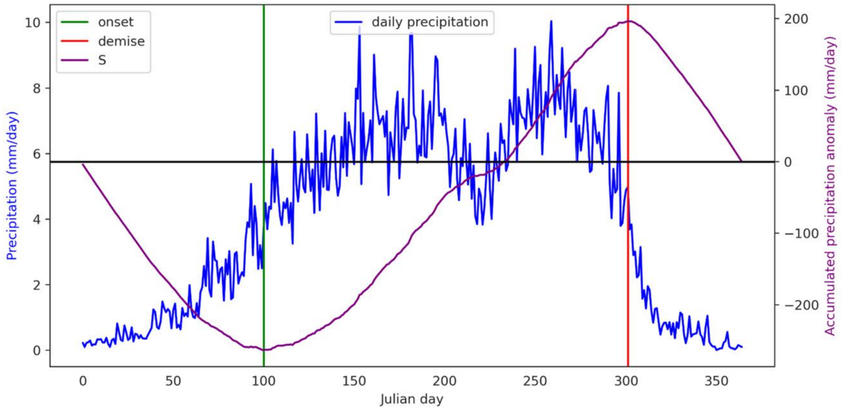

FIGURE 4.1 Illustration of the detection of the onset (vertical green line) and cessation (vertical red line) dates of the rainy season at a random grid point (7.5°N and 5°E) obtained using accumulated precipitation anomalies (*S*) from the climatological (1985–2014) mean of all observations (GPCC, CPC, ARC2, and CHIRPS) used in this study.

$$RMSE = \sqrt{\frac{1}{n}\sum_{i=1}^{n}(M_i - O_i)^2} \tag{4.4}$$

$$PCC(M, O) = \frac{cov\,(M, O)}{\sqrt{Var\,(M) \times Var\,(O)}}, \tag{4.5}$$

where “M” and “O” are the mean of the model and reference datasets, respectively, “cov” denotes covariance, “Var” is variance, and “*n*” represents the total number of points.

4.3 Results and discussion

4.3.1 Precipitation climatology: seasonal and interannual variabilities

The annual precipitation cycle across African subregions can vary significantly due to the continent’s diverse and complex geography, including the presence of mountain ranges and the influence of neighboring oceans. This section analyzes the mean annual cycles for observations, reanalyses, and the CMIP6 EnsMean across the nine African subregions (Fig. 4.2). Across all the observations, precipitation peaks occur in August in Western Africa (WAF), with values reaching up to 6 mm/day, while, in the Sahara (SAH), the maximum precipitation remains below 1 mm/day in the same month. However, obvious differences exist among the observed peak intensity estimates. Previous studies have shown that this peak in WAF is associated with the West African Monsoon (WAM), which transports moisture from the Atlantic Ocean, orchestrated by southwesterlies within the lower troposphere (Sylla et al., 2009; Akinsanola and Zhou, 2019b;

TABLE 4.1 CMIP6 model names, institution, horizontal resolution, and reference.

Model name	Institution	Resolution (°lon x °lat)	Reference
ACCESS-CM2	Commonwealth Scientific and Industrial Research Organisation, Australia	1.88 × 1.25	Dix et al. (2019)
ACCESS-ESM1-5	Commonwealth Scientific and Industrial Research Organisation, Australia	1.88 × 1.24	Ziehn et al. (2019)
CanESM5	Canadian Earth System Model	2.81 × 2.81	Swart et al. (2019)
CESM2-WACCM	National Center for Atmospheric Research (NCAR), USA	1.25 × 0.94	Danabasoglu (2019)
CMCC-CM2-SR5	Euro-Mediterranean Centre on Climate Change coupled climate model, Italy	1.25 × 0.94	Lovato and Peano (2020)
CMCC-ESM2	Euro-Mediterranean Centre on Climate Change coupled climate model, Italy	1.25 × 0.94	Lovato et al. (2021)
EC-Earth3-CC	EC-EARTH consortium	0.70 × 0.70	EC-Earth (2021)
EC-Earth3	EC-EARTH consortium	0.70 × 0.70	EC-Earth (2019a)
EC-Earth3-Veg	EC-EARTH consortium	0.70 × 0.70	EC-Earth (2019b)
EC-Earth3-Veg-LR	EC-EARTH consortium	1.13 × 1.13	EC-Earth (2020)
INM-CM4-8	Institute of Numerical Mathematics of the Russian Academy of Sciences, Russia	2.00 × 1.50	Volodin et al. (2019a)
INM-CM5-0	Institute of Numerical Mathematics of the Russian Academy of Sciences, Russia	2.00 × 1.50	Volodin et al. (2019b)
IPSL-CM6A-LR	Institute Pierre-Simon Laplace (IPSL)	2.50 × 1.26	Boucher et al. (2018)
MIROC6	Japanese Modeling Community	1.41 × 1.41	Tatebe and Watanabe (2018)
MPI-ESM1-2-HR	Max Planck Institute	0.94 × 0.94	Jungclaus et al. (2019)
MPI-ESM1-2-LR	Max Planck Institute	1.88 × 1.88	Wieners et al. (2019)
MRI-ESM2-0	Meteorological Research Institute (MRI)	1.13 × 1.13	Yukimoto et al. (2019)

continued on next page

TABLE 4.1 (*continued*)

Model name	Institution	Resolution (∘lon x ∘lat)	Reference
NESM3	Nanjing University of Information Science and Technology, Nanjing, China	1.88 × 1.88	Cao and Wang (2019)
TaiESM1	Research Center for Environmental Changes, Academia Sinica, Nankang, Taipei, Taiwan	0.94 × 1.25	Lee et al. (2020)

Adeyeri et al., 2024), and is associated with variability in sea-surface temperature (SST) (Monerie et al., 2019). Over Central Africa (CAF), two rainy seasons are evident in the observations, which occur in March–May and September–November, separated by a dry season in June–August. The second rainy season is much stronger than the first, with a difference of more than 1 mm/day between the two peaks. This double-peaked structure over CAF is associated with the latitudinal migration of the Inter Tropical Convergence Zone (ITCZ) that sweeps through this and adjacent equatorial regions twice a year (Dezfuli and Nicholson, 2013; Mba et al., 2022). However, observations do not always agree on the precipitation magnitude since CPC underestimates other observations year-round. This highlights observational uncertainty over CAF due to insufficiently well-sampled ground stations, as indicated by Washington et al. (2013) and James et al. (2018). In East Africa, observations in the northern and southern portions exhibit contrasts. The rainy season occurs from May to September in North Eastern-Africa (NEAF), whereas this period corresponds to the dry season in South Eastern-Africa (SEAF). This contrasts with previous studies (Yang et al., 2015; Gamoyo et al., 2015), which depict a typical bimodal annual precipitation cycle over East Africa by considering Northern and Southern East Africa as a single subregion. Variation in SST significantly influences precipitation patterns in East Africa. For instance, alterations in the SST of the Indian Ocean (Tierney et al., 2013; Yang et al., 2015) and Pacific Ocean (Lyon, 2014) impact the atmospheric circulation that modulates precipitation over East Africa. Over southern Africa, our results demonstrate that observations in all subregions (East Southern-Africa, ESAF; West Southern-Africa, WSAF; and Madagascar, MDG) align consistently. Specifically, the rainy season occurs during the Southern Hemisphere summer months due to the southward position of the ITCZ, while the remainder of the year is characterized by dry conditions (Daron et al., 2019). In addition, changes in the intensity and position of atmospheric pressure systems like the Angola Low (Munday and Washington, 2017; Crétat et al., 2019), the Kalahari Low (Taljaard, 1986), and the Botswana

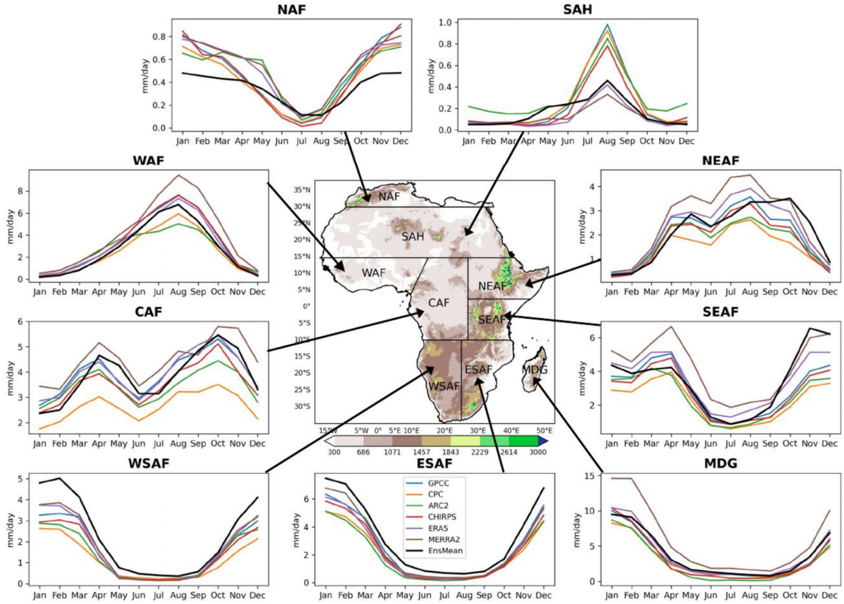

FIGURE 4.2 Mean annual cycle of precipitation (1985–2014) across the nine African subregions from observations (GPCC, CPC, ARC2, and CHIRPS), reanalyses (ERA5 and MERRA2), and the CMIP6 EnsMean. The subregions include Northern Africa (NAF), Sahara (SAH), Western-Africa (WAF), Central-Africa (CAF), North Eastern-Africa (NEAF), South Eastern-Africa (SEAF), East Southern-Africa (ESAF), West Southern-Africa (WSAF), and Madagascar (MDG). The shading in the spatial plot represents the topography or surface elevation (m).

High (Driver and Reason, 2017) influence the variability of precipitation across southern Africa. Moreover this, other dynamic and thermodynamic features like the African Easterly Jet and moisture transport are crucial in the distribution of precipitation in Africa (Adeyeri et al., 2024).

The CMIP6 EnsMean demonstrates good performance in capturing the annual cycle of precipitation across all subregions (Fig. 4.2). However, there are notable discrepancies between observations and the EnsMean total amount of rainy season precipitation. Although EnsMean is found in the spread of observations in CAF and NEAF, it underestimates the rainy season intensity precipitation in SAH and NAF by approximately 0.5 mm/day and 0.2 mm/day, respectively. Conversely, in southern Africa subregions (WSAF and ESAF), EnsMean overestimates the intensity (∼1 mm/day) in WSAF and ESAF.

Regarding the spatial distribution of precipitation across Africa, the observed annual mean (Fig. 4.3a) reveals maximum values of around 7 mm/day in CAF. Notably, the Congo Basin rainforest in CAF profoundly impacts the intensity and distribution of precipitation through its dense structure, facilitating the accumulation and interception of precipitation (Adeyeri et al., 2024). In addition, the Congo rainforest favors atmospheric convection by interacting with the land and

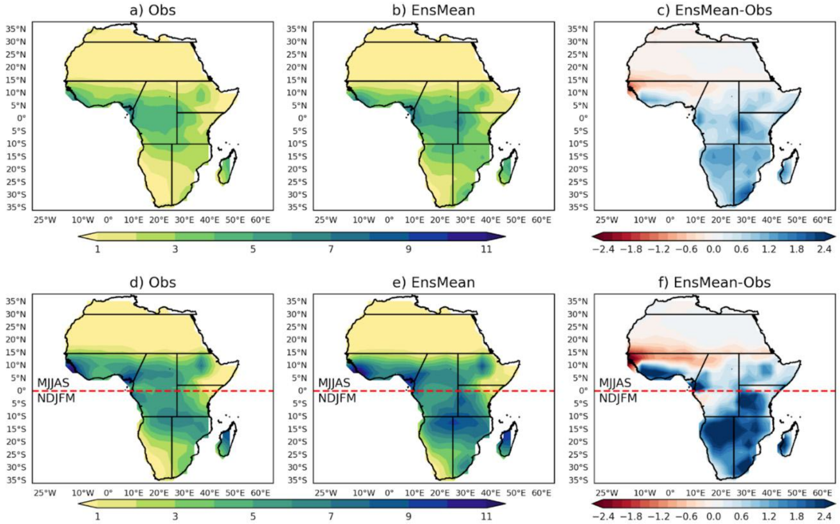

FIGURE 4.3 Spatial distribution of the mean (1985–2014) annual (a, b, and c) and summer (d, e, and f) precipitation (mm/day) over Africa from the (a, d) mean of all observations, (b, e) CMIP6 EnsMean, and (c, f) bias of CMIP6 EnsMean with respect to the mean of all observations. The dashed red line is the equator, which divides the continent between the Northern and Southern Hemispheres. Summer refers to May to September (November to March) in the Northern Hemisphere (Southern Hemisphere).

atmosphere, thereby significantly shaping the climate of the region (Washington et al., 2013). Summer mean precipitation in both hemispheres is higher than the annual mean and reaches up to 9 mm/day in some regions. In the Northern Hemisphere (Fig. 4.3d), maximum precipitation values are observed over WAF, CAF, and the western portion of NEAF during the summer months. Conversely, during the Southern Hemisphere summer months (Fig. 4.3d), maximum precipitation occurs in the southern part of CAF, the northern areas of both WSAF and ESAF, and in NEAF. All are associated with the migration of the ITCZ (Nicholson, 2018; Daron et al., 2019). EnsMean generally overestimates both the annual (Fig. 4.3b) and summer (Fig. 4.3e) mean precipitation, with the overestimation being more pronounced during the summer (Fig. 4.3e). Consistent with Fig. 4.2, EnsMean (Fig. 4.3c, f) generally exhibits a wet bias over sub-Saharan regions, while a dry bias is evident in the northern part of WAF, over SAH, and over NAF. The magnitude of the bias is generally higher and more pronounced during the summertime (Fig. 4.3f). Additionally, the wet (dry) bias exceeds 2 mm/day (−2 mm/day) over WSAF (northern part of WAF) (Fig. 4.3f).

The ability of the individual CMIP6 models to realistically represent annual mean precipitation is further assessed using multiple descriptive statistics: percentage bias, root mean square error, and the pattern correlation coefficient. Portrait diagrams are computed relative to the mean of all observations (Fig. 4.4). The utility of these metrics for assessing precipitation distribution

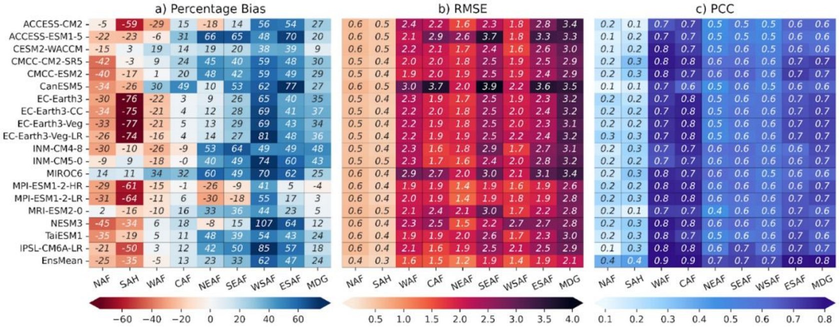

FIGURE 4.4 Portrait diagrams showing the (a) percentage bias, (b) root mean square error, and (c) pattern correlation coefficient between the mean of all observations and individual models over the nine subregions of Africa.

has been demonstrated in previous studies (e.g., Sillmann et al., 2013; Akinsanola et al., 2020; Taguela et al., 2020). Our results show that most models exhibit negative biases (depicted in red in Fig. 4.4a) over NAF and SAH, with values as large as −75% in SAH for models such as EC-Earth3 and EC-Earth3-Veg. Conversely, most models demonstrate positive biases (depicted in blue in Fig. 4.4a and consistent with Fig. 4.3) in the sub-Saharan regions, with WSAF exhibiting the highest percentage biases, ranging from +38% to +107% across all models. To complement the discussion on biases, Fig. 4.4b presents the root mean square error (RMSE), a valuable metric that is less influenced by spatially compensating errors (Akinsanola et al., 2021). NAF and SAH exhibit the lowest RMSE values, ranging between 0.4 and 0.6 across all models. Conversely, MDG displays the highest RMSE values, ranging from 2.8 to 3.4. Furthermore, most models across all regions except NAF and SAH exhibit pattern correlation-coefficient values greater than 0.6. In NAF and SAH, the values range from 0.1 to 0.4. Overall, regardless of the statistical metric employed, EnsMean consistently demonstrates superior performance compared to most individual models across all regions. This finding aligns with previous studies conducted in South Africa (Lim Kam Sian et al., 2021), North Africa (Babaousmail et al., 2021), West Africa (Ajibola et al., 2020; Faye and Akinsanola, 2021), and East Africa (Akinsanola et al., 2021; Ayugi et al., 2021).

Fig. 4.5 shows the spatial distribution of the standard deviations of annual and summer precipitation, a measure of precipitation variability. The mean of all observations (Fig. 4.5a and d) generally shows higher standard deviations in the sub-Saharan regions, an indication of significant variability in annual precipitation. This pattern is particularly pronounced over WAF, CAF, and the northern part of ESAF (Fig. 4.5a). During the summer, the spatial pattern remains similar in both hemispheres but with lower values (Fig. 4.5d). This suggests that summer precipitation variability is less pronounced than annual variability. Although the overall distribution is relatively well-captured by EnsMean (Fig. 4.5b and 4.5e), including regions of low and high standard-deviation values, limita-

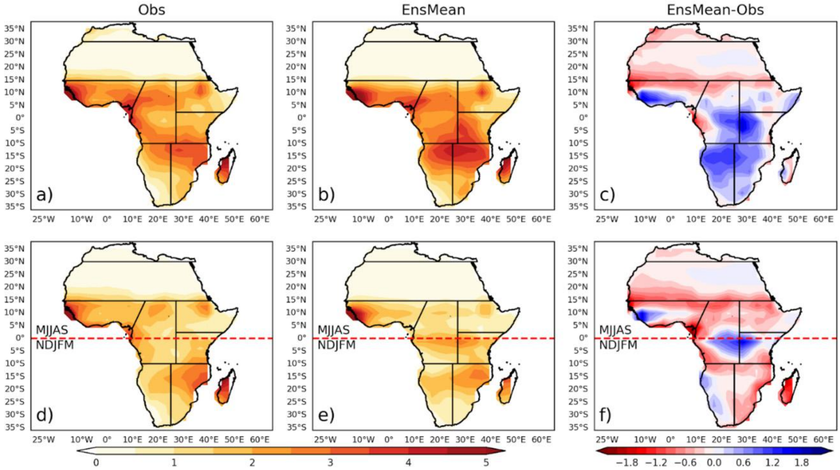

FIGURE 4.5 Spatial distribution of mean annual (a, b, and c) and summer (d, e, and f) precipitation standard deviation (1985–2014) across Africa from the (a, d) mean of all observations (GPCC, CPC, ARC2, and CHIRPS), (b, e) CMIP6 EnsMean, and (c, f) bias of CMIP6 EnsMean with respect to the mean of all observations. The dashed red line is the equator, which divides the continent between the Northern and Southern Hemispheres. Summer refers to May to September (November to March) in the Northern Hemisphere (Southern Hemisphere).

tions in reproducing the magnitude of the observed variability are evident across Africa. In general, relative to the observations, EnsMean underestimates the annual standard deviation of precipitation over North Africa while overestimating it in sub-Saharan regions (Fig. 4.5c). Notably, WAF exhibits a pattern of positive bias in the southern areas and negative bias in the northern regions (Fig. 4.5c). The summer precipitation variability is mostly underestimated by EnsMean across most subregions excluding eastern CAF and western SEAF, which show a positive bias (Fig. 4.5f). Overall, it is difficult for EnsMean to accurately reproduce both annual and summer precipitation variability over Africa.

4.3.2 Spatial distribution of precipitation characteristics: onset and cessation dates

The timing of the rainy season onset and cessation is critical for understanding Africa's climate dynamics and informing agricultural practices. Fig. 4.6 presents the climatological mean dates of onset and cessation. It is important to note that blank areas around the equator (Figs. 4.6a, d) arise because the method employed in obtaining the onset and cessation dates is difficult to use in regions with a pronounced bimodal precipitation regime, such as CAF (Bombardi et al., 2019). Nevertheless, in agreement with Oguntunde et al. (2014), Dunning et al. (2016), and Bombardi et al. (2019), the mean of all observations (Fig. 4.6a, d) shows that the onset (cessation) dates are generally earlier (later) in the year in the Northern Hemisphere, and the opposite in the Southern Hemisphere. This is

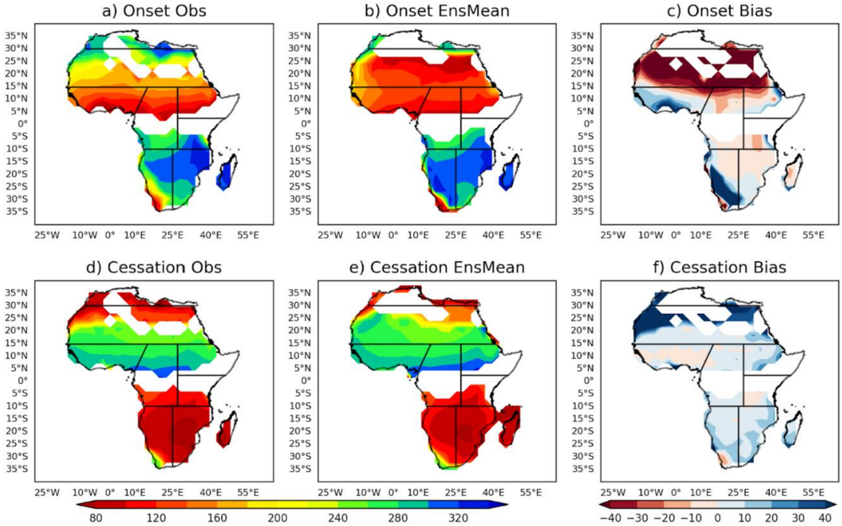

FIGURE 4.6 Spatial distribution of the mean (1985–2014) rainy season onset (a, b) and cessation (d, e) dates from the (a, d) mean of all observations, (b, e) CMIP6 EnsMean, and (c, f) bias of CMIP6 EnsMean with respect to the mean of all observations. Unit: Julian day.

consistent with the timing/active period of the known physical drivers of African seasonal precipitation, namely the ITCZ and the monsoon systems. The patterns of onset and cessation are consistent with previous studies (e.g., Mugalavai et al., 2008; Liebmann et al., 2012; Oguntunde et al., 2014; Ngetich et al., 2014). Around the equator, onset and cessation progress in a zonal manner (Oguntunde et al., 2014; Fitzpatrick et al., 2015; Kumi et al., 2020), with the Guinea coast experiencing its onset earlier than the Sahel. Conversely, over southern Africa, the onset simultaneously spreads southeast and northwest (Tadross et al., 2005). EnsMean generally captures the spatial distribution of onset and cessation dates over Africa, albeit with a noticeable bias (Fig. 4.6c). For instance, over the Sahara region, the simulated onsets are delayed by more than 30 days compared to observations. Conversely, in the southern portion of the West African Sahel (WSAF), the model simulates onsets more than 30 days earlier than observed. However, cessation dates are simulated relatively well (Fig. 4.6e), with low biases (Fig. 4.6f) in most subregions except the Sahara, where the simulated cessation dates are more than 20–30 days later.

4.3.3 Climatology of some extreme precipitation indices

In recent years, Africa has experienced a significant increase in extreme precipitation events, raising concerns about their frequency and impact on communities throughout the continent (IPCC Special Report; Masson-Delmotte et al., 2021). We analyze extreme climate indices, including the right tail (99th percentile minus 90th percentile), consecutive dry days (CDD), and five-consecutive-day maximum precipitation (Rx5day). The observations reveal a concentration of intense CDD (>7 days) over southern Africa in general, and the northern parts of WAF, CAF, and NEAF (Fig. 4.7a). We mask out the CDD values over NAF and SAH using a threshold of < 0.3 mm/day mean precipitation of EnsMean, considering that the region is predominantly dry and exhibits very high values that spatially suppress the signals from other subregions. Other areas exhibit fewer dry days (< 4 days), with the central part of CAF exhibiting the lowest CDD (≤ 2 days). If EnsMean is compared to observations, the bias in CDD (Fig. 4.6c) is positive over WAF, NEAF, SEAF, and the central area of CAF, whereas negative biases are evident over WSAF and ESAF. The highest positive bias is found in the northeastern part of NEAF, while the highest negative bias is located south of WSAF. The observational mean spatial distributions of Rx5day and the right tail indices exhibit similar spatial patterns but differ in magnitude (Figs. 4.7d & 4.7g). CAF and MDG typically experience higher values, while SAH and NAF experience lower values. EnsMean reasonably captures the spatial distribution of both indices but struggles to reproduce their magnitude. For instance, it generally underestimates both indices across the 15°N to 15°S latitude band, with values reaching −50 days for Rx5day and −12 mm/day for the right tail. While this underestimation is prevalent in central, northeastern, southeastern, and western Africa, some variations exist. EnsMean overestimates Rx5day (> 20 mm/day), with minimal bias for the right tail, in some portions of West Africa, particularly away from the Guinea coast. Additionally, for both indices, southern Africa displays minimal positive bias except for Madagascar, which experiences underestimation similar to central Africa.

4.4 Summary, socioeconomic implications, and conclusion

The African continent's reliance on precipitation for agriculture, water resources, mining, and hydroelectric power generation makes it vulnerable to spatial and temporal variability of precipitation. This chapter examines the distribution of precipitation across Africa. Observed precipitation patterns reveal distinct characteristics for each subregion: West Africa receives its highest precipitation during the summer monsoon (June–September); central Africa receives precipitation year-round, with a rainy (dry) period occurring from May to September in North (South) Eastern Africa; and precipitation in southern Africa occurs mostly during the Southern Hemisphere summer. The maximum mean annual precipitation is over CAF, with the Congo Basin rainforest facilitating the accumulation and interception of precipitation. Furthermore, onset (cessation) dates are generally earlier (later) in the year in the Northern Hemisphere, and the opposite in the Southern Hemisphere. In addition, high concentration of CDD is generally evident over southern Africa, whereas CAF, NEAF, and SEAF exhibit high wet extremes (Rx5day and right tail). These results suggest critical implications for socioeconomic sectors, necessitating targeted strategies to address potential impacts. For instance, regions with high CDD combined

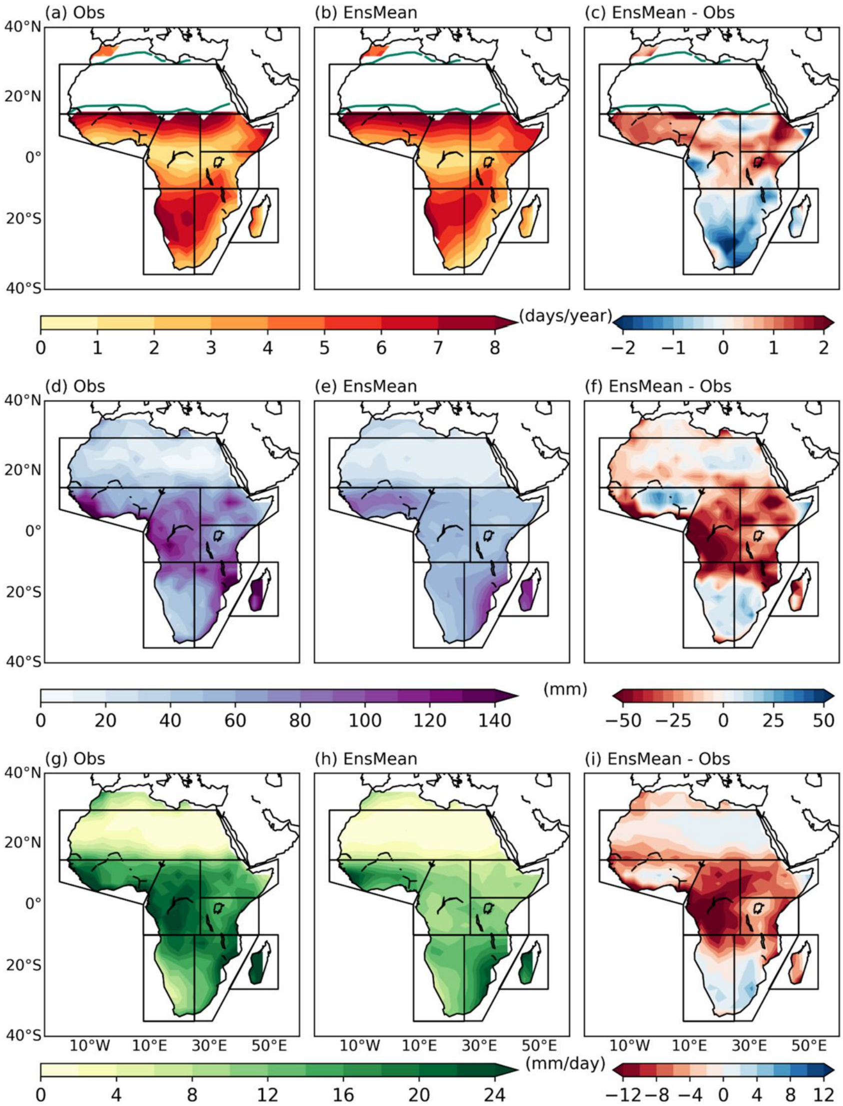

FIGURE 4.7 Spatial distribution of mean (1985–2014) consecutive dry days (CDD; a–c), five-consecutive-day maximum precipitation (RX5day; d–f), and extreme right tail (99th percentile minus 90th percentile; d–f) from the mean of all observations (a, d, g), CMIP6 EnsMean (b, e, h), and bias of CMIP6 EnsMean with respect to the mean of all observations (c, f, i). CDD values over NAF and SAH are masked out using a threshold of < 0.3 mm/day mean precipitation of EnsMean (green contour line), considering that the region is predominantly dry and exhibits very high values that spatially suppress the signals from other subregions.

with a late rainy season onset are likely to experience prolonged drought conditions associated with reduced agricultural productivity, leading to food insecurity, exacerbating poverty, and triggering unsustainable migration patterns (Descheemaeker et al., 2016). Prolonged droughts can exacerbate respiratory ailments and other type of diseases, imposing additional burdens on healthcare systems and hindering socioeconomic development (Alamgir et al., 2009). Additionally, intense CDD and drought can trigger thermal discomfort that will adversely affect people's well-being, leading to various heat-related illnesses such as heat stroke, heart attack, and lung disease (Adeyeri et al., 2023). To address these problems, for example, those associated with agricultural productivity, implementing programs that monitor soil moisture, precipitation patterns, an early warning system for weather forecasts/droughts is important. This would make possible proactive measures like planting drought-resistant crops or delaying planting altogether. Regarding drought-related diseases, special attention should be paid to vulnerable populations such as children, the elderly, and individuals with preexisting health conditions, as they may be more susceptible to the health impacts of droughts. Additionally, healthcare infrastructure should be strengthened in drought-prone areas to ensure timely medical assistance, including the provision of sufficient medical supplies, trained healthcare professionals, and emergency-response systems.

Although it can be highly beneficial to hydroelectric power generation and water resources, excessive precipitation, characterized by low CDD, high mean precipitation, and wet extremes (Rx5day and right tail), as evident over central and East Africa, can lead to flooding and soil erosion, disrupting agricultural activities and reducing crop yields (Dinku et al., 2018; Nicholson, 2013). These can also affect infrastructure and urban development since heavy precipitation can damage roads, bridges, and buildings, further disrupting transportation networks and increasing maintenance costs (Tanessong et al., 2021; Iroume et al., 2022). Stagnant water from prolonged precipitation can create breeding grounds for mosquitoes and other vectors, increasing the risk of vector-borne diseases such as malaria and dengue fever, as well as waterborne illnesses like cholera (Mbouna et al., 2022). To address these challenges, effective adaptation and mitigation measures are required to help design strong subregional policies. These include upgraded drainage systems, flood walls and levees in high-risk areas, improved urban planning to manage rainwater runoff, sustainable water management strategies, diversified livelihood options, early warning systems, and investment in resilient infrastructure in general (Masson-Delmotte et al., 2021).

Given Africa's limited ground-based observations and complex topography, climate modeling is essential for understanding precipitation patterns and for making projections. In this chapter, the ability of CMIP6 models to reproduce observed precipitation characteristics over Africa is evaluated. Our findings reveal that the CMIP6 models can generally reproduce Africa's precipitation characteristics, albeit with noticeable biases. For instance, the models underestimate (overestimate) precipitation in northern (sub-Saharan) Africa. Furthermore, the models struggle to reproduce observed precipitation variability since they underestimate the standard deviation across the continent. While the models can capture the spatial patterns of the rainy season onset and cessation, they show biases in timing, exhibiting later and earlier onsets over the Sahara and southern Africa, respectively. In addition, CMIP6 models exhibit limitations in simulating extreme precipitation events such as high consecutive dry days (CDD) in the Sahara and extreme precipitation (RX5day and right tail) across central, northeastern, southeastern, and parts of western Africa. The findings herein underscore the need for continuous refinement and evaluation of climate models to enhance their accuracy in simulating regional precipitation, thereby facilitating effective climate adaptation and mitigation strategies for sustainable development.

Data availability

All datasets used in this study are publicly and freely available. CMIP6 data are publicly available through the Earth System Grid Federation at https://esgf.llnl.gov/. The ERA5 data are available from the ECMWF Copernicus Climate Change Service: https://doi.org/10.24381/cds.adbb2d47, while MERRA2 data are available on the National Aeronautics and Space Administration (NASA) website at https://disc.gsfc.nasa.gov/. The Global Precipitation Climatology Centre (GPCC) dataset was retrieved from https://psl.noaa.gov/data/gridded/data.gpcc.html. The Climate Hazards Group InfraRed Precipitation with Station data (CHIRPS) products are available at https://www.chc.ucsb.edu/data/. The CPC Global Unified Gauge-Based Analysis of Daily Precipitation (CPC-Unified) was retrieved from https://psl.noaa.gov/data/gridded/data.cpc.globalprecip.html. The African Rainfall Climatology (ARC) dataset is available at https://iridl.ldeo.columbia.edu/SOURCES/.NOAA/.NCEP/.CPC/.FEWS/.Africa/.DAILY/.ARC2/.daily/index.html?Set-Language=en. The derived data generated for the study are available from the corresponding author upon reasonable request.

Code availability

All analyses and figures were computed and drawn using Python packages (e.g., matplotlib: https://matplotlib.org/stable/). The codes used for the analysis in this study are available upon request from the corresponding author.

Acknowledgments

We acknowledge the World Climate Research Programme's Working Group on Coupled Modeling, which is responsible for CMIP, and we thank the climate modeling groups (models listed in Table 4.1) for producing and making available their model outputs. We are also grateful to the institutions that provided observational and reanalysis data used in this chapter.

References

Adebiyi, A.A., Akinsanola, A.A., Ajoku, O.F., 2023. The misrepresentation of the Southern African easterly jet in models and its implications for aerosol, clouds, and precipitation distributions. Journal of Climate 36 (22), 7785–7809. https://doi.org/10.1175/jcli-d-23-0083.1.

Adeyeri, O.E., et al., 2022a. Homogenising meteorological variables: impact on trends and associated climate indices. Journal of Hydrology 607, 127585. https://doi.org/10.1016/j.jhydrol.2022.127585.

Adeyeri, O.E., Zhou, W., Wang, X., et al., 2022b. The trend and spatial spread of multisectoral climate extremes in CMIP6 models. Scientific Reports 12, 21000. https://doi.org/10.1038/s41598-022-25265-4.

Adeyeri, O.E., Zhou, W., et al., 2023. Land use and land cover dynamics: implications for thermal stress and energy demands. Renewable & Sustainable Energy Reviews 179. https://doi.org/10.1016/j.rser.2023.113274.

Adeyeri, O.E., et al., 2024. Minimizing uncertainties in climate projections and water budget reveals the vulnerability of freshwater to climate change. One Earth 10. https://doi.org/10.1016/j.oneear.2023.12.013.

Adeyewa, Z.D., Nakamura, K., 2003. Validation of TRMM radar rainfall data over major climatic regions in Africa. Journal of Applied Meteorology 42 (2), 331–347. https://doi.org/10.1175/1520-0450(2003)042<0331:votrrd>2.0.co;2.

Ajibola, F.O., Zhou, B., Tchalim Gnitou, G., Onyejuruwa, A., 2020. Evaluation of the performance of CMIP6 HighResMIP on West African precipitation. Atmosphere 11 (10), 1053. https://doi.org/10.3390/atmos11101053.

Akinsanola, A.A., Ogunjobi, K.O., 2017. Recent homogeneity analysis and long-term spatio-temporal rainfall trends in Nigeria. Theoretical and Applied Climatology 128, 275–289. https://doi.org/10.1007/s00704-015-1701-x.

Akinsanola, A.A., Zhou, W., 2018. Ensemble-based CMIP5 simulations of West African summer monsoon rainfall: current climate and future changes. Theoretical and Applied Climatology 136 (3–4), 1021–1031. https://doi.org/10.1007/s00704-018-2516-3.

Akinsanola, A.A., Zhou, W., 2019a. Projections of West African summer monsoon rainfall extremes from two CORDEX models. Climate Dynamics 52, 2017–2028. https://doi.org/10.1007/s00382-018-4238-8.

Akinsanola, A.A., Zhou, W., 2019b. Dynamic and thermodynamic factors controlling increasing summer monsoon rainfall over the West African Sahel. Climate Dynamics 52, 4501–4514. https://doi.org/10.1007/s00382-018-4394-x.

Akinsanola, A.A., Zhou, W., Zhou, T., Keenlyside, N., 2020. Amplification of synoptic to annual variability of West African summer monsoon rainfall under global warming. npj Climate and Atmospheric Science 3 (1). https://doi.org/10.1038/s41612-020-0125-1.

Akinsanola, A.A., Ongoma, V., Kooperman, G.J., 2021. Evaluation of CMIP6 models in simulating the statistics of extreme precipitation over Eastern Africa. Atmospheric Research 254, 105509. https://doi.org/10.1016/j.atmosres.2021.105509.

Akinsanola, A.A., Kooperman, G.J., Hannah, W.M., Reed, K.A., Pendergrass, A.G., Wei-Ching, H., 2023. Evaluation of present-day extreme precipitation over the United States: an inter-comparison of convection and dynamic permitting configurations of E3SMv1. Environmental Research: Climate 3 (1), 011002. https://doi.org/10.1088/2752-5295/ad0f9e.

Akinsanola, A.A., Jung, C., Wang, J., et al., 2024. Evaluation of precipitation across the contiguous United States, Alaska, and Puerto Rico in multi-decadal convection-permitting simulations. Scientific Reports 14, 1238. https://doi.org/10.1038/s41598-024-51714-3.

Alamgir, F., Nahar, P., Collins, A.E., Ray-Bennett, N.S., Bhuiya, A., 2009. Climate change and food security: health risks and vulnerabilities of the poor in Bangladesh. The International Journal of Climate Change: Impacts and Responses 1 (4), 37–54. https://doi.org/10.18848/1835-7156/cgp/v01i04/37283.

Ayugi, B., Dike, V., Ngoma, H., Babaousmail, H., Mumo, R., Ongoma, V., 2021. Future changes in precipitation extremes over East Africa based on CMIP6 models. Water 13 (17), 2358. https://doi.org/10.3390/w13172358.

Babaousmail, H., Hou, R., Ayugi, B., Ojara, M., Ngoma, H., Karim, R., et al., 2021. Evaluation of the performance of CMIP6 models in reproducing rainfall patterns over North Africa. Atmosphere 12 (4), 475. https://doi.org/10.3390/atmos12040475.

Beck, H.E., Zimmermann, N.E., McVicar, T.R., Vergopolan, N., Berg, A., Wood, E.F., 2018. Present and future Köppen–Geiger climate classification maps at 1-km resolution. Scientific Data 5, 180214. https://doi.org/10.1038/sdata.2018.214.

Bombardi, R.J., Kinter, J.L., Frauenfeld, O.W., 2019. A global gridded dataset of the characteristics of the rainy and dry seasons. Bulletin of the American Meteorological Society 100 (7), 1315–1328. https://doi.org/10.1175/bams-d-18-0177.1.

Boucher, Olivier, Denvil, Sébastien, Levavasseur, Guillaume, Cozic, Anne, Caubel, Arnaud, Foujols, Marie-Alice, Meurdesoif, Yann, Cadule, Patricia, Devilliers, Marion, Ghattas, Josefine, Lebas, Nicolas, Lurton, Thibaut, Mellul, Lidia, Musat, Ionela, Mignot, Juliette, Cheruy, Frédérique, 2018. IPSL IPSL-CM6A-LR model output prepared for CMIP6 CMIP historical. Earth System Grid Federation. https://doi.org/10.22033/ESGF/CMIP6.5195.

Camberlin, P., Barraud, G., Bigot, S., Dewitte, O., Makanzu Imwangana, F., Maki Mateso, J., et al., 2019. Evaluation of remotely sensed rainfall products over Central Africa. Quarterly Journal of the Royal Meteorological Society 145 (722), 2115–2138. https://doi.org/10.1002/qj.3547.

Cao, Jian, Wang, Bin, 2019. NUIST NESMv3 model output prepared for CMIP6 CMIP historical. Earth System Grid Federation. https://doi.org/10.22033/ESGF/CMIP6.8769.

Chang'a, L., Kijazi, A., Mafuru, K., Nying'uro, P., Ssemujju, M., Deus, B., Kondowe, A., Yonah, I., Ngwali, M., Kisama, S., Aimable, G., Sebaziga, J., Mukamana, B., 2020. Understanding the evolution and socio-economic impacts of the extreme rainfall events in March–May 2017 to 2020 in East Africa. Atmospheric and Climate Sciences 10, 553–572. https://doi.org/10.4236/acs.2020.104029.

Cook, K.H., 2001. A Southern Hemisphere wave response to ENSO with implications for Southern Africa precipitation. Journal of the Atmospheric Sciences 58 (15), 2146–2162. https://doi.org/10.1175/1520-0469(2001)058<2146:ashwrt>2.0.co;2.

Cook, K.H., Vizy, E.K., 2006. Coupled model simulations of the West African monsoon system: twentieth- and twenty-first-century simulations. Journal of Climate 19 (15), 3681–3703. https://doi.org/10.1175/jcli3814.1.

Crétat, J., Pohl, B., Dieppois, B., et al., 2019. The Angola low: relationship with southern African rainfall and ENSO. Climate Dynamics 52, 1783–1803. https://doi.org/10.1007/s00382-018-4222-3.

Danabasoglu, Gokhan, 2019. NCAR CESM2-WACCM model output prepared for CMIP6 CMIP historical. Earth System Grid Federation. https://doi.org/10.22033/ESGF/CMIP6.10071.

Daron, J., Burgin, L., Janes, T., Jones, R.G., Jack, C., 2019. Climate process chains: examples from southern Africa. International Journal of Climatology 39 (12), 4784–4797. https://doi.org/10.1002/joc.6106.

Demissie, T.A., Sime, C.H., 2021. Assessment of the performance of CORDEX regional climate models in simulating rainfall and air temperature over southwest Ethiopia. Heliyon 7 (8), e07791. https://doi.org/10.1016/j.heliyon.2021.e07791.

Descheemaeker, K., Oosting, S.J., Homann-Kee Tui, S., Masikati, P., Falconnier, G.N., Giller, K.E., 2016. Climate change adaptation and mitigation in smallholder crop–livestock systems in sub-Saharan Africa: a call for integrated impact assessments. Regional Environmental Change 16 (8), 2331–2343. https://doi.org/10.1007/s10113-016-0957-8.

Dey, D., Döös, K., 2019. The coupled ocean–atmosphere hydrologic cycle. Tellus. Series A, Dynamic Meteorology and Oceanography 71 (1), 1650413. https://doi.org/10.1080/16000870.2019.1650413.

Dezfuli, A.K., Nicholson, S.E., 2013. The relationship of rainfall variability in western equatorial Africa to the tropical oceans and atmospheric circulation. Part II: The boreal autumn. Journal of Climate 26, 66–84. https://doi.org/10.1175/JCLI-D-11-00686.1.

Dinku, T., Thomson, M.C., Cousin, R., del Corral, J., Ceccato, P., Hansen, J., Connor, S.J., 2018. Enhancing national climate services (ENACTS) for development in Africa. Climate and Development 10 (7), 664–672. https://doi.org/10.1080/17565529.2017.1405784.

Dix, Martin, Bi, Daohua, Dobrohotoff, Peter, Fiedler, Russell, Harman, Ian, Law, Rachel, Mackallah, Chloe, Marsland, Simon, O'Farrell, Siobhan, Rashid, Harun, Srbinovsky, Jhan, Sullivan, Arnold, Trenham, Claire, Vohralik, Peter, Watterson, Ian, Williams, Gareth, Woodhouse, Matthew, Bodman, Roger, Dias, Fabio Boeira, Domingues, Catia M., Hannah, Nicholas, Heerdegen, Aidan, Savita, Abhishek, Wales, Scott, Allen, Chris, Druken, Kelsey, Evans, Ben, Richards, Clare, Ridzwan, Syazwan Mohamed, Roberts, Dale, Smillie, Jon, Snow, Kate, Ward, Marshall, Yang, Rui, 2019. CSIRO-ARCCSS ACCESS-CM2 model output prepared for CMIP6 CMIP historical. Earth System Grid Federation. https://doi.org/10.22033/ESGF/CMIP6.4271.

Driver, P., Reason, C.J.C., 2017. Variability in the Botswana High and its relationships with rainfall and temperature characteristics over southern Africa. International Journal of Climatology 37 (S1), 570–581. https://doi.org/10.1002/joc.5022.

Dunning, C.M., Black, E.C.L., Allan, R.P., 2016. The onset and cessation of seasonal rainfall over Africa. Journal of Geophysical Research. Atmospheres 121, 11,405–11,424. https://doi.org/10.1002/2016JD025428.

EC-Earth Consortium (EC-Earth), 2019a. EC-Earth-Consortium EC-Earth3 model output prepared for CMIP6 CMIP historical. Earth System Grid Federation. https://doi.org/10.22033/ESGF/CMIP6.4700.

EC-Earth Consortium (EC-Earth), 2019b. EC-Earth-Consortium EC-Earth3-Veg model output prepared for CMIP6 CMIP historical. Earth System Grid Federation. https://doi.org/10.22033/ESGF/CMIP6.4706.

EC-Earth Consortium (EC-Earth), 2020. EC-Earth-Consortium EC-Earth3-Veg-LR model output prepared for CMIP6 CMIP historical. Earth System Grid Federation. https://doi.org/10.22033/ESGF/CMIP6.4707.

EC-Earth Consortium (EC-Earth), 2021. EC-Earth-Consortium EC-Earth-3-CC model output prepared for CMIP6 CMIP historical. Earth System Grid Federation. https://doi.org/10.22033/ESGF/CMIP6.4702.

Eyring, V., Bony, S., Meehl, G.A., Senior, G.A., Stevens, B., Stouffer, R.J., Taylor, K.E., 2016. Overview of the Coupled Model Intercomparison Project Phase 6 (CMIP6) experimental design and organization. Geoscientific Model Development 9, 1937–1958. https://doi.org/10.5194/gmd-9-1937-2016.

Faye, A., Akinsanola, A.A., 2021. Evaluation of extreme precipitation indices over West Africa in CMIP6 models. Climate Dynamics 58 (3–4), 925–939. https://doi.org/10.1007/s00382-021-05942-2.

Fenta, A.A., Yasuda, H., Shimizu, K., Haregeweyn, N., Kawai, T., Sultan, D., Ebabu, K., Belay, A.S., 2017. Spatial distribution and temporal trends of rainfall and erosivity in the Eastern Africa region. Hydrological Processes 31 (25), 4555–4567. https://doi.org/10.1002/hyp.11378.

Fitzpatrick, R.G.J., Bain, C.L., Knippertz, P., Marsham, J.H., Parker, D.J., 2015. The West African monsoon onset: a concise comparison of definitions. Journal of Climate 28 (22), 8673–8694. https://doi.org/10.1175/jcli-d-15-0265.1.

Funk, C., Peterson, P., Landsfeld, M., Pedreros, D., Verdin, J., Shukla, S., et al., 2015. The climate hazards infrared precipitation with stations—a new environmental record for monitoring extremes. Scientific Data 2 (1). https://doi.org/10.1038/sdata.2015.66.

Gamoyo, M., Reason, C., Obura, D., 2015. Rainfall variability over the East African coast. Theoretical and Applied Climatology 120, 311–322. https://doi.org/10.1007/s00704-014-1171-6.

Gelaro, R., McCarty, W., Suárez, M.J., Todling, R., Molod, A., Takacs, L., et al., 2017. The Modern-Era Retrospective Analysis for Research and Applications, Version 2 (MERRA-2). Journal of Climate 30 (14), 5419–5454. https://doi.org/10.1175/jcli-d-16-0758.1.

Giorgi, F., Gutowski, W.J., 2015. Regional dynamical downscaling and the CORDEX initiative. Annual Review of Environment and Resources 40 (1), 467–490. https://doi.org/10.1146/annurev-environ-102014-021217.

Hamududu, B., Killingtveit, A., 2012. Assessing climate change impacts on global hydropower. Energies 5 (2), 305–322. https://doi.org/10.3390/en5020305.

Herold, N., Behrangi, A., Alexander, L.V., 2017. Large uncertainties in observed daily precipitation extremes over land. Journal of Geophysical Research. Atmospheres 122 (2), 668–681. https://doi.org/10.1002/2016jd025842.

Hersbach, H., Bell, B., Berrisford, P., Hirahara, S., Horányi, A., Muñoz-Sabater, J., et al., 2020. The ERA5 global reanalysis. Quarterly Journal of the Royal Meteorological Society 146 (730), 1999–2049. https://doi.org/10.1002/qj.3803.

Hilson, G., 2009. Small-scale mining, poverty and economic development in sub-Saharan Africa: an overview. Resources Policy 34 (1–2), 1–5. https://doi.org/10.1016/j.resourpol.2008.12.001.

International Water Management Institute: IWMI, 2014. East Africa. http://eastafrica.iwmi.cgiar.org/. (Accessed 1 February 2014).

Iroume, J.Y.-A., Onguéné, R., Djanna Koffi, F., Colmet-Daage, A., Stieglitz, T., Essoh Sone, W., et al., 2022. The 21st August 2020 flood in Douala (Cameroon): a major urban flood investigated with 2D HEC-RAS modeling. Water 14 (11), 1768. https://doi.org/10.3390/w14111768.

Iturbide, M., Gutiérrez, J.M., Alves, L.M., Bedia, J., Cerezo-Mota, R., Cimadevilla, E., Cofiño, A.S., Di Luca, A., Faria, S.H., Gorodetskaya, I.V., Hauser, M., Herrera, S., Hennessy, K., Hewitt, H.T., Jones, R.G., Krakovska, S., Manzanas, R., Martínez-Castro, D., Narisma, G.T., et al., 2020. An update of IPCC climate reference regions for subcontinental analysis of climate model data: definition and aggregated datasets. Earth System Science Data 12 (4), 2959–2970. https://doi.org/10.5194/essd-12-2959-2020.

James, R., Washington, R., Abiodun, B., Kay, G., Mutemi, J., Pokam, W., Hart, N., Artan, G., Senior, C., 2018. Evaluating climate models with an African lens. Bulletin of the American Meteorological Society 99 (2), 313–336. https://doi.org/10.1175/BAMS-D-16-0090.1.

Jungclaus, J., Bittner, M., Wieners, K.-H., Wachsmann, F., Schupfner, M., Legutke, S., Giorgetta, M., Reick, C., Gayler, V., Haak, H., de Vrese, P., Raddatz, T., Esch, M., Mauritsen, T., von Storch, J.-S., Behrens, J., Brovkin, V., Claussen, M., Crueger, T., Fast, I., Fiedler, S., Hagemann, S., Hohenegger, C., Jahns, T., Kloster, S., Kinne, S., Lasslop, G., Kornblueh, L., Marotzke, J., Matei, D., Meraner, K., Mikolajewicz, U., Modali, K., Müller, W., Nabel, J., Notz, D., Peters, K., Pincus, R., Pohlmann, H., Pongratz, J., Rast, S., Schmidt, H., Schnur, R., Schulzweida, U., Six, K., Stevens, B., Voigt, A., Roeckner, E., 2019. MPI-M MPI-ESM1.2-HR model output prepared for CMIP6 CMIP. Earth System Grid Federation. Available at: https://doi.org/10.22033/ESGF/CMIP6.6594.

Krishnamurthy, P., Lewis, K., Choularton, R., 2014. A methodological framework for rapidly assessing the impacts of climate risk on national-level food security through a vulnerability index. Global Environmental Change 25, 121–132. https://doi.org/10.1016/j.gloenvcha.2013.11.004.

Kuete, G., Mba, W.P., James, R., Dyer, E., Annor, T., Washington, R., 2022. How do coupled models represent the African Easterly Jets and their associated dynamics over Central Africa during the September–November rainy season? Climate Dynamics 60 (9–10), 2907–2929. https://doi.org/10.1007/s00382-022-06467-y.

Kumi, N., Abiodun, B.J., Adefisan, E.A., 2020. Performance evaluation of a Subseasonal to Seasonal model in predicting rainfall onset over West Africa. Earth and Space Science 7, e2019EA000928-T. https://doi.org/10.1029/2019EA000928.

Le Coz, C., van de Giesen, N., 2020. Comparison of rainfall products over sub-Saharan Africa. Journal of Hydrometeorology 21 (4), 553–596. https://doi.org/10.1175/jhm-d-18-0256.1.

Lee, W.-L., Wang, Y.-C., Shiu, C.-J., Tsai, I., Tu, C.-Y., Lan, Y.-Y., et al., 2020. Taiwan Earth System Model: description and evaluation of mean. Geoscientific Model Development 13, 3887–3904. https://doi.org/10.5194/gmd-2019-377.

Liebmann, B., Bladé, I., Kiladis, G.N., Carvalho, L.M.V., Senay, G.B., Allured, D., Leroux, S., Funk, C., 2012. Seasonality of African precipitation from 1996 to 2009. Journal of Climate 25 (12), 4304–4322. https://doi.org/10.1175/jcli-d-11-00157.1.

Lim Kam Sian, K.T.C., Wang, J., Ayugi, B.O., Nooni, I.K., Ongoma, V., 2021. Multi-decadal variability and future changes in precipitation over Southern Africa. Atmosphere 12 (6), 742. https://doi.org/10.3390/atmos12060742.

Lovato, Tomas, Peano, Daniele, 2020. CMCC CMCC-CM2-SR5 model output prepared for CMIP6 CMIP historical. Earth System Grid Federation. https://doi.org/10.22033/ESGF/CMIP6.3825.

Lovato, Tomas, Peano, Daniele, Butenschön, Momme, 2021. CMCC CMCC-ESM2 model output prepared for CMIP6 CMIP historical. Earth System Grid Federation. https://doi.org/10.22033/ESGF/CMIP6.13195.

Lyon, B., 2014. Seasonal drought in the greater horn of Africa and its recent increase during the March–May long rains. Journal of Climate 27, 7953–7975. https://doi.org/10.1175/JCLI-D-13-00459.1.

Maidment, R.I., Allan, R.P., Black, E., 2015. Recent observed and simulated changes in precipitation over Africa. Geophysical Research Letters 42 (19), 8155–8164. https://doi.org/10.1002/2015gl065765.

Masson-Delmotte, V., Zhai, P., Pirani, A., Connors, S.L., Péan, C., Berger, S., Caud, N., Chen, Y., Goldfarb, L., Gomis, M.I., et al., 2021. Climate change 2021: The physical science basis. Contribution of working group I to the sixth assessment report of the intergovernmental panel on climate change. IPCC, Geneva, Switzerland.

Mba, W.P., Vondou, D.A., Kamsu-Tamo, P.H., 2022. Central African climate. Congo Basin Hydrology, Climate, and Biogeochemistry, 13–23. https://doi.org/10.1002/9781119657002.ch2.

Mbouna, A.D., Tamoffo, A.T., Asare, E.O., Lenouo, A., Tchawoua, C., 2022. Malaria metrics distribution under global warming: assessment of the VECTRI malaria model over Cameroon. International Journal of Biometeorology 67 (1), 93–105. https://doi.org/10.1007/s00484-022-02388-x.

Monerie, P-A., Robson, J., Dong, B., et al., 2019. Effect of the Atlantic multidecadal variability on the global monsoon. Geophysical Research Letters 46. https://doi.org/10.1029/2018GL080903.

Mugalavai, E.M., Kipkorir, E.C., Raes, D., Rao, M.S., 2008. Analysis of rainfall onset, cessation and length of growing season for western Kenya. Agricultural and Forest Meteorology 148 (6–7), 1123–1135. https://doi.org/10.1016/j.agrformet.2008.02.013.

Munday, C., Washington, R., 2017. Circulation controls on southern African precipitation in coupled models: the role of the Angola low. Journal of Geophysical Research. Atmospheres 122, 861–877. https://doi.org/10.1002/2016JD025736.

Ngetich, K., Mucheru-Muna, M., Mugwe, J., Shisanya, C., Diels, J., Mugendi, D., 2014. Length of growing season, rainfall temporal distribution, onset and cessation dates in the Kenyan highlands. Agricultural and Forest Meteorology 188, 24–32. https://doi.org/10.1016/j.agrformet.2013.12.011.

Ngoma, H., Wen, W., Ayugi, B., Babaousmail, H., Karim, R., Ongoma, V., 2021. Evaluation of precipitation simulations in CMIP6 models over Uganda. International Journal of Climatology 41 (9), 4743–4768. https://doi.org/10.1002/joc.7098.

Nicholson, S.E., 2013. The West African Sahel: a review of recent studies on the rainfall regime and its interannual variability. ISRN Meteorology 2013, 1–32. https://doi.org/10.1155/2013/453521.

Nicholson, S.E., 2018. The ITCZ and the seasonal cycle over equatorial Africa. Bulletin of the American Meteorological Society 99 (2), 337–348. https://doi.org/10.1175/bams-d-16-0287.1.

Odoulami, R.C., Akinsanola, A.A., 2017. Recent assessment of West African summer monsoon daily rainfall trends. Weather 73 (9), 283–287. https://doi.org/10.1002/wea.2965.

Oguntunde, P.G., Lischeid, G., Abiodun, B.J., Dietrich, O., 2014. Analysis of spatial and temporal patterns in onset, cessation, and length of growing season in Nigeria. Agricultural and Forest Meteorology 194, 77–87. https://doi.org/10.1016/j.agrformet.2014.03.017.

Ongoma, V., Chen, H., 2016. Temporal and spatial variability of temperature and precipitation over East Africa from 1951 to 2010. Meteorology and Atmospheric Physics 129 (2), 131–144. https://doi.org/10.1007/s00703-016-0462-0.

Onyutha, C., 2018. Trends and variability in African long-term precipitation. Stochastic Environmental Research and Risk Assessment 32, 2721–2739. https://doi.org/10.1007/s00477-018-1587-0.

Patricola, C.M., Cook, K.H., 2009. Northern African climate at the end of the twenty-first century: an integrated application of regional and global climate models. Climate Dynamics 35 (1), 193–212. https://doi.org/10.1007/s00382-009-0623-7.

Pokam, M.W., Longandjo, G.N., Moufouma-Okia, W., Bell, J.P., James, R., Vondou, D.A., Haensler, A., Fotso-Nguemo, T.C., Guenang, G.M., Tchotchou, A.L.D., Kamsu-Tamo, P.H., Takong, R.R., Nikulin, G., Lennard, C.J., Dosio, A., 2018. Consequences of 1.5°C and 2°C global warming levels for temperature and precipitation changes over Central Africa. Environmental Research Letters 13, 1–12. https://doi.org/10.1088/1748-9326/aab048.

Randall, D.A., Wood, R.A., Bony, S., Colman, R., Fichefet, T., Fyfe, J., Kattsov, V., Pitman, A., Shukla, J., Srinivasan, J., et al., 2007. Climate models and their evaluation. In: Solomon, S., Qin, D., Manning, M., Chen, Z., Marquis, M., Averyt, K.B., Tignor, M., Miller, H.L. (Eds.), Climate Change 2007: The Physical Science Basis. Contribution of Working Group i to the Fourth Assessment Report of the Intergovernmental Panel on Climate Change. Cambridge University Press, Cambridge.

Rast, M., Johannessen, J., Mauser, W., 2014. Review of understanding of Earth's hydrological cycle: observations, theory and modelling. Surveys in Geophysics 35 (3), 491–513. https://doi.org/10.1007/s10712-014-9279-x.

Redelsperger, J.L., Thorncroft, C.D., Diedhiou, A., Lebel, T., Parker, D.J., Polcher, J., 2006. African monsoon multidisciplinary analysis: an international research project and field campaign. Bulletin of the American Meteorological Society 87 (12), 1739–1746. https://doi.org/10.1175/bams-87-12-1739.

Roehrig, R., Bouniol, D., Guichard, F., Hourdin, F., Redelsperger, J.L., 2013. The present and future of the West African monsoon: a process-oriented assessment of CMIP5 simulations along the AMMA transect. Journal of Climate 26 (17), 6471–6505. https://doi.org/10.1175/jcli-d-12-00505.1.

Seneviratne, S.I., et al., 2012. Changes in climate extremes and their impacts on the natural physical environment. In: Managing the Risks of Extreme Events and Disasters to Advance Climate Change Adaptation, A Special Report of Working Groups I and II of the Intergovernmental Panel on Climate Change (IPCC), Rep. Cambridge Univ. Press, Cambridge, UK, and New York, pp. 109–230.

Siebert, A., 2014. Hydroclimate extremes in Africa: variability, observations and modeled projections. Geography Compass 8 (6), 351–367. https://doi.org/10.1111/gec3.12136.

Sillmann, J., Kharin, V.V., Zhang, X., Zwiers, F.W., Bronaugh, D., 2013. Climate extremes indices in the CMIP5 multimodel ensemble: Part 1. Model evaluation in the present climate. Journal of Geophysical Research. Atmospheres 118 (4), 1716–1733. https://doi.org/10.1002/jgrd.50203.

Sultan, B., Janicot, S., 2000. Abrupt shift of the ITCZ over West Africa and intra-seasonal variability. Geophysical Research Letters 27 (20), 3353–3356. https://doi.org/10.1029/1999gl011285.

Swart, Neil Cameron, Cole, Jason N.S., Kharin, Viatcheslav V., Lazare, Mike, Scinocca, John F., Gillett, Nathan P., Anstey, James, Arora, Vivek, Christian, James R., Jiao, Yanjun, Lee, Warren G., Majaess, Fouad, Saenko, Oleg A., Seiler, Christian, Seinen, Clint, Shao, Andrew, Solheim, Larry, von Salzen, Knut, Yang, Duo, Winter, Barbara, Sigmond, Michael, 2019. CCCma CanESM5 model output prepared for CMIP6 CMIP historical. Earth System Grid Federation. https://doi.org/10.22033/ESGF/CMIP6.3610.

Sylla, M.B., Coppola, E., Mariotti, L., Giorgi, F., Ruti, P.M., Dell'Aquila, A., Bi, X., 2009. Multiyear simulation of the African climate using a regional climate model (RegCM3) with the high resolution ERA-interim reanalysis. Climate Dynamics 35 (1), 231–247. https://doi.org/10.1007/s00382-009-0613-9.

Tadross, M.A., Hewitson, B.C., Usman, M.T., 2005. The interannual variability of the onset of the maize growing season over South Africa and Zimbabwe. Journal of Climate 18 (16), 3356–3372. https://doi.org/10.1175/jcli3423.1.

Taguela, T.N., Vondou, D.A., Moufouma-Okia, W., Fotso-Nguemo, T.C., Pokam, W.M., Tanessong, R.S., Yepdo, Z.D., Haensler, A., Longandjo, G.N., Bell, J.P., Takong, R.R., Djiotang Tchotchou, L.A., 2020. CORDEX Multi-RCM Hindcast over Central Africa: evaluation within observational uncertainty. Journal of Geophysical Research. Atmospheres 125 (5), e2019JD031607. https://doi.org/10.1029/2019JD031607.

Taguela, T.N., Pokam, W.M., Washington, R., 2022. Rainfall in uncoupled and coupled versions of the Met Office Unified Model over Central Africa: Investigation of processes during the September–November rainy season. International Journal of Climatology 42 (12), 6311–6331. https://doi.org/10.1002/joc.7591.

Taljaard, J.J., 1986. Change of rainfall distribution and circulation patterns over Southern Africa in summer. Journal of Climatology 6, 579–592. https://doi.org/10.1002/joc.3370060602.

Tamoffo, A.T., Moufouma-Okia, W., Dosio, A., James, R., Pokam, W.M., Vondou, D.A., et al., 2019. Process-oriented assessment of RCA4 regional climate model projections over the Congo Basin under 1.5°C and 2°C global warming levels: influence of regional moisture fluxes. Climate Dynamics 53 (3–4), 1911–1935. https://doi.org/10.1007/s00382-019-04751-y.

Tamoffo, A.T., Akinsanola, A.A., Weber, T., 2023. Understanding the diversity of the West African monsoon system change projected by CORDEX-CORE regional climate models. Climate Dynamics 61 (5–6), 2395–2419. https://doi.org/10.1007/s00382-023-06690-1.

Tanessong, R.S., Mbienda, A.J.K., Guenang, G.M., Kaissassou, S., Djiotang, L.A.T., Vondou, D.A., et al., 2021. Sensitivity of rainfall to cumulus parameterization schemes from a WRF model over the city of Douala in Cameroon. Journal of Extreme Events 08. https://doi.org/10.1142/s2345737621500214.

Tatebe, H., Watanabe, M., 2018. MIROC MIROC6 model output prepared for CMIP6 CMIP historical. Earth System Grid Federation. https://doi.org/10.22033/ESGF/CMIP6.5603.

Taylor, K.E., Stouffer, R.J., Meehl, G.A., 2012. An overview of CMIP5 and the experiment design. Bulletin of the American Meteorological Society 93 (4), 485–498. https://doi.org/10.1175/bams-d-11-00094.1.

Tierney, J.E., Smerdon, J.E., Anchukaitis, K.J., Seager, R., 2013. Multidecadal variability in East African hydroclimate controlled by the Indian Ocean. Nature 493, 389–392. https://doi.org/10.1038/nature11785.

Volodin, Evgeny, Mortikov, Evgeny, Gritsun, Andrey, Lykossov, Vasily, Galin, Vener, Diansky, Nikolay, Gusev, Anatoly, Kostrykin, Sergey, Iakovlev, Nikolay, Shestakova, Anna, Emelina, Svetlana, 2019a. INM INM-CM4-8 model output prepared for CMIP6 CMIP historical. Earth System Grid Federation. https://doi.org/10.22033/ESGF/CMIP6.5069.

Volodin, Evgeny, Mortikov, Evgeny, Gritsun, Andrey, Lykossov, Vasily, Galin, Vener, Diansky, Nikolay, Gusev, Anatoly, Kostrykin, Sergey, Iakovlev, Nikolay, Shestakova, Anna, Emelina, Svetlana, 2019b. INM INM-CM5-0 model output prepared for CMIP6 CMIP historical. Version. Earth System Grid Federation. https://doi.org/10.22033/ESGF/CMIP6.5070.

Washington, R., James, R., Pearce, H., Pokam, W.M., Moufouma-Okia, W., 2013. Congo Basin rainfall climatology: can we believe the climate models? Philosophical Transactions of the Royal Society. Series B, Biological Sciences 368 (1625), 20120296. https://doi.org/10.1098/rstb.2012.0296.

Wieners, Karl-Hermann, Giorgetta, Marco, Jungclaus, Johann, Reick, Christian, Esch, Monika, Bittner, Matthias, Legutke, Stephanie, Schupfner, Martin, Wachsmann, Fabian, Gayler, Veronika, Haak, Helmuth, de Vrese, Philipp, Raddatz, Thomas, Mauritsen, Thorsten, von Storch, Jin-Song, Behrens, Jörg, Brovkin, Victor, Claussen, Martin, Crueger, Traute, Fast, Irina, Fiedler, Stephanie, Hagemann, Stefan, Hohenegger, Cathy, Jahns, Thomas, Kloster, Silvia, Kinne, Stefan, Lasslop, Gitta, Kornblueh, Luis, Marotzke, Jochem, Matei, Daniela, Meraner, Katharina, Mikolajewicz, Uwe, Modali, Kameswarrao, Müller, Wolfgang, Nabel, Julia, Notz, Dirk, Peters-von Gehlen, Karsten, Pincus, Robert, Pohlmann, Holger, Pongratz, Julia, Rast, Sebastian, Schmidt, Hauke, Schnur, Reiner, Schulzweida, Uwe, Six, Katharina, Stevens, Bjorn, Voigt, Aiko, Roeckner, Erich, 2019. MPI-M MPIESM1.2-LR model output prepared for CMIP6. Earth System Grid Federation. https://doi.org/10.22033/ESGF/CMIP6.742.

Wild, M., Gilgen, H., Roesch, A., Ohmura, A., Long, C.N., Dutton, E.G., et al., 2005. From dimming to brightening: decadal changes in solar radiation at Earth's surface. Science 308 (5723), 847–850. https://doi.org/10.1126/science.1103215.

Williams, A.P., Funk, C., 2011. A westward extension of the warm pool leads to a westward extension of the Walker circulation, drying eastern Africa. Climate Dynamics 37 (11–12), 2417–2435. https://doi.org/10.1007/s00382-010-0984-y.

Xie, P., Chen, M., Shi, W., 2010. CPC Unified gauge-based analysis of global daily precipitation. In: 24th Conf. on Hydrology. Atlanta, GA. Amer. Meteor. Soc. 2.3A. Available online at: https://ams.confex.com/ams/90annual/webprogram/Paper163676.html.

Yang, W., Seager, R., Cane, M.A., Lyon, B., 2015. The annual cycle of East African precipitation. Journal of Climate 28 (6), 2385–2404. https://doi.org/10.1175/jcli-d-14-00484.1.

Yukimoto, S., Kawai, H., Koshiro, T., Oshima, N., Yoshida, K., Urakawa, S., Tsujino, H., Deushi, M., Tanaka, T., Hosaka, M., Yabu, S., Yoshimura, H., Shindo, E., Mizuta, R., Obata, A., Adachi, Y., Ishii, M., 2019. The Meteorological Research Institute Earth System Model version 2.0, MRI-ESM2.0: description and basic evaluation of the physical component. Journal of the Meteorological Society of Japan 97, 931–965. https://doi.org/10.2151/jmsj.2019-051.

Zhang, X., Alexander, L., Hegerl, G.C., Jones, P., Tank, A.K., Peterson, T.C., Trewin, B., Zwiers, F.W., 2011. Indices for monitoring changes in extremes based on daily temperature and precipitation data. Wiley Interdisciplinary Reviews: Climate Change 2, 851–870. https://doi.org/10.1002/wcc.147.

Ziehn, Tilo, Chamberlain, Matthew, Lenton, Andrew, Law, Rachel, Bodman, Roger, Dix, Martin, Wang, Yingping, Dobrohotoff, Peter, Srbinovsky, Jhan, Stevens, Lauren, Vohralik, Peter, Mackallah, Chloe, Sullivan, Arnold, O'Farrell, Siobhan, Druken, Kelsey, 2019. CSIRO ACCESS-ESM1. 5 model output prepared for CMIP6 CMIP historical. Earth System Grid Federation. https://doi.org/10.22033/ESGF/CMIP6.4272.

Ziese, M., Rauthe-Schöch, A., Becker, A., Finger, P., Meyer-Christoffer, A., Schneider, U., 2018. GPCC full data daily version.2018 at 1.0°: daily land-surface precipitation from rain-gauges built on GTS-based and historic data. https://doi.org/10.5676/DWD_GPCC/FD_D_V2018_100.

Chapter 5

Recent trends of clouds over Africa

Osinachi F. Ajoku[a,b], **Mumin Abdulahi**[b], **and Oye Ideki**[b]
[a]*Department of Earth, Environment and Equity, Howard University, Washington D.C., United States,* [b]*Department of Interdisciplinary Studies, Howard University, Washington D.C., United States*

5.1 Introduction

Clouds are a critical component of Earth's short-term weather system and long-term climate system. The balance between the absorbed incident solar radiation and concomitantly emitted longwave terrestrial radiation binds the cloud and Earth's energy balance. They play an important role in modulating local and global radiative fluxes, atmospheric circulation, and the hydrological cycle (IPCC, 2014; Probst et al., 2012; Stephens et al., 1990). Clouds are composed of liquid and/or ice-water droplets, dependent on vertical structure and local thermodynamics. Fig. 5.1 displays satellite images of cloud coverage over Africa for various months representative of the various seasons. Throughout continental Africa, clouds are a key feature of annual and semiannual weather extremes, including over monsoon regions in West, East and Central Africa. Compared to the rest of the world, not nearly enough attention has been paid to Africa for a better understanding of its climate and how it may change in the future. Africa is the only continent to traverse both hemispheres and contain subtropical high-pressure systems in each. The intertropical convergence zone (ITCZ), which is a band of low pressure circling the Earth creating a visible band of clouds, modulates in position throughout the continent, while equatorial regions (mainly central Africa) experience its influence semiannually. As the ITCZ migrates meridionally throughout the year, large-scale convective clouds are associated with its position.

The West African Monsoon (WAM) season involves large meridional temperature gradients between the equatorial Atlantic and Saharan regions and contributes much-needed moisture to southern West Africa. The WAM is accompanied with large-scale convective clouds that envelop large portions of southern West Africa (SWA). Of all the regions in Africa, SWA is by far the most studied region for clouds and climate change. Key characteristics of the WAM are hard to quantify mainly due to the limitations and uncertainties of

Aerosols and Precipitation Over Africa. https://doi.org/10.1016/B978-0-44-314050-1.00010-4

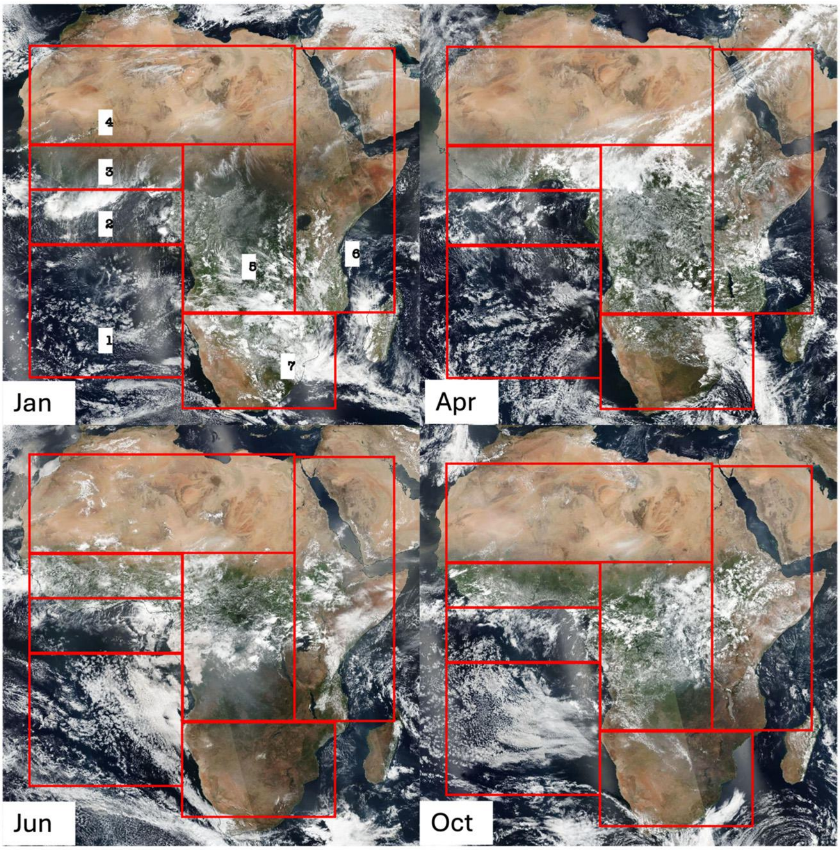

FIGURE 5.1 Satellite images retrieved from NASA's Worldview of true-color corrected reflectance during 2017. Each panel reflects cloud cover for a different season. Red rectangles within each panel reflect different regions used in this study. Each region is labeled 1–7 for (1) southeast Atlantic (SeATL), (2) equatorial Atlantic (EA), (3) West Africa (WA), (4) North Africa (NA), (5) central Africa (CA), (6) East Africa (EA), and (7) South Africa (SA) respectively. The NA region encompasses 15°N to 30°N and 15°W to 30°E, WA covers 5°N to 15°N and 15°W to 12°E, EA covers 30°E to 50°E and 30°N to 15°S, SA covers 12°E to 35°E and 15°S to 35°S, CA covers 15°N to 15°S and 12°E to 30°E, EqATL covers 5°N to 5°S and 15°W to 12°E, and lastly SeATL covers 5°S to 35°S and 15°W to 12°E.

climate models to accurately simulate convection and low-level clouds (Christensen et al., 2013). In addition to higher-level cumulus convective clouds, SWA is frequently covered with low-level stratus clouds (Schrage and Fink, 2012). Obtaining a better understanding of cloud properties in this region can be difficult because satellite products used to study its features often disagree with each other (Tompkins and Adebiyi, 2012). Van der Linden et al. (2015) used CloudSat and CALIPSO cross sections of cloud frequency to determine that Meteosat Second Generation (MSG) and Terra Multiangle Imaging Spectroradiometer satellite products underestimate and overestimate, respectively, lower-level cloud coverage over SWA. Further north, towards the Sahel region, low-level clouds have been shown to persist frequently during the WAM (Danso et al., 2020), thus altering shortwave radiative fluxes.

East Africa is characterized by having both a long (March to May) and short (September to October) wet season, both of which are highly variable due to the complex terrain. Such complexities in East Africa lead to regional differences in cloud coverage throughout the seasons, and, thus, regionally averaged analysis may fall short of capturing noticeable changes in cloud characteristics (Ntale et al., 2003). The greatest cloud coverage over most of East Africa occurs during the wet seasons. According to Didier (2015), the most dominant cloud types in this region are mid-level altostratus (November) and high-level Cirrus (April). It is important to note that middle and higher-level clouds can be difficult to detect during periods of high cloud coverage (Lau and Crane, 1997). East Africa spans over 40° of latitude, including both tropical and subtropical zones, thus all cloud types occur throughout the region all year-round.

Central Africa is home to the Congo rainforest, a region heavily affected by land–atmosphere interactions. Evaporation of liquid droplets aloft from the top of forest canopies act as a source of moisture for the local hydrological cycle (Burnett et al., 2020). To a higher degree, the ITCZ and deep convection associated with its position is the primary source of tropical rainfall (Houze, 2004). Due to the zone's migration, precipitation activity and convective maxima occur during the spring and autumn months (Nikulin et al., 2012). Shallow and deep convective processes are most prevalent over Central Africa and have been shown to influence other cloud properties such as cloud-top height and the cloud-area fraction (Chakraborty et al., 2020).

North and South Africa are in midlatitudinal regions, receiving noticeably less precipitation relative to East, West, and central Africa. North Africa's climate is characterized as dry all year-round, besides the summer season, where monsoon rains bring scarce amounts of moisture into the region. Thus, the presence of clouds over North Africa serves to modulate local radiation budgets. The Sahara provides an ample source of dust aerosols to potentially modulate cloud production. Gu et al. (2012) used offline simulations to reveal that increased dust loading enhances aerosol direct and semidirect effects over North Africa, potentially reflecting more incoming radiation and trapping more longwave infrared radiation. The rainy season in southern Africa and thus maximum cloud coverage occurs during austral summer (December–February). Cloud types dominating the rainy season over South Africa are cirrus, cumulus, and stratocumulus clouds (Ntwali et al., 2017).

Atlantic Ocean cloud coverage is predominantly controlled by low-level clouds, while higher-level clouds occur more frequently near the equator because of ITCZ migration. Due to varying sea-surface temperatures (SSTs), cloud structures are usually analyzed separately in tropical and subtropical regions. A semipermanent stratocumulus cloud deck located in the subtropical, southeastern Atlantic has a global impact on Earth's radiation budget. This cloud deck is maintained by relatively cool sea-surface temperatures below and large-scale subsidence aloft (Wood, 2012). Equatorward of 5°S, compact stratiform cloud decks consisting of light drizzle become the dominant cloud type and are maintained at the surface by consistent ocean upwelling, which brings cooler temperatures to the surface from below (Eastman et al., 2011; Eastman and Warren, 2014; Wood, 2012). Maximum cloud coverage over this region occurs from June to October, and its vertical cloud structure is modulated by a zonal, overturning circulation (Cook and Vizy, 2016, 2019; Neupane, 2016; Moron et al., 2023).

This chapter reviews cloud properties over continental Africa and the adjacent Atlantic Ocean on seasonal timescales for the most recent 20 years of available data (2003–2022) using a gridded observation-based product. This timescale is sufficient to capture any signatures associated with recent increases in global atmospheric temperatures. Data is analyzed for each season throughout all levels of the atmosphere instead of only where maxima occur to capture changes in less-studied cloud types. This chapter evaluates recent changes in cloud coverage, temperature, and moisture content. In the next section, the observational data and techniques used for analysis are described.

5.2 Methods

5.2.1 Data sources

The primary dataset used in this study is derived from the Clouds and the Earth's Radiant Energy System (CERES) project. CERES provides global observations of Earth's radiation budget and cloud-distribution measurements from NASA's Terra and Aqua satellites. Monthly averaged, global gridded data was acquired from NASA's Langley Research Center (LARC) SYN1deg product. This data comprises hourly CERES and geostationary satellite top-of-atmosphere fluxes, MODIS/VIIRS cloud and aerosol properties, and Fu–Liou radiative transfer atmospheric profile and surface fluxes consistent with observed top-of-atmosphere fluxes (Doelling et al., 2013, 2016). Monthly averaged cloud area, temperature, liquid-water path (LWP), ice-water path (IWP), cloud-top temperature, and cloud-top pressure was obtained at $1^\circ \times 1^\circ$ horizontal resolution at all available cloud levels (low, mid-low, mid-high, high, and total) for the most recent 20 years at the time this study was conducted (2003–2022). With CERES data products, low clouds represent pressure levels from the surface to 750mb, mid-low clouds range from 750mb to 500mb, mid-high clouds range from 500mb to 300mb, and high clouds span from 300mb to the tropopause.

5.2.2 Regional analysis

Our study area comprises continental Africa and the adjacent Atlantic Ocean, spanning from 15°W to 50°E in longitude to 30°N to 35°S in latitude. A total of

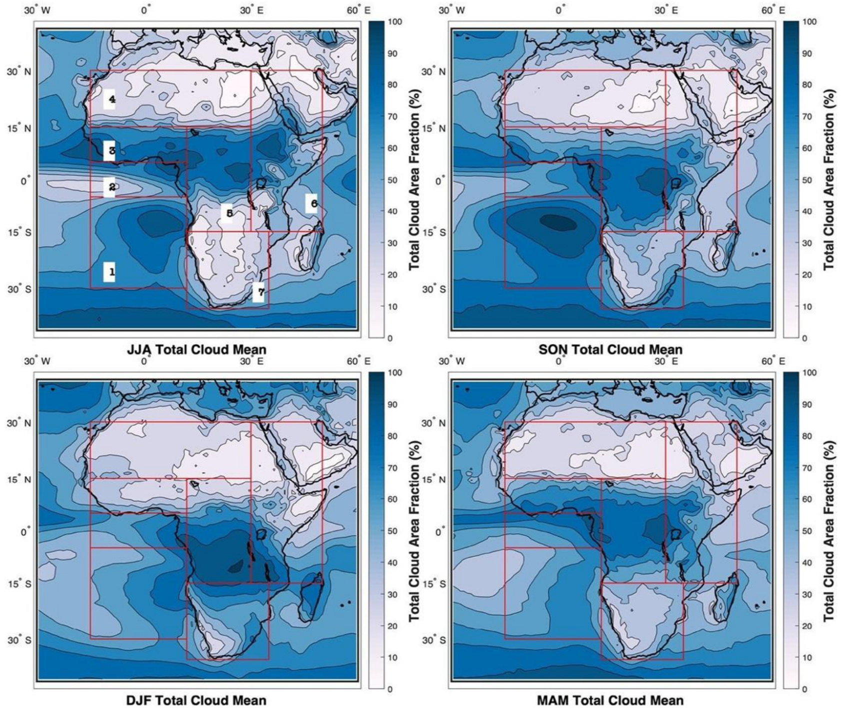

FIGURE 5.2 Seasonally averaged total cloud area fraction over Africa. Red boxes represent areas used for regional analysis. All data is averaged between the years 2003–2022. Rectangular boxed regions reflect the same areas as in Fig. 5.1.

seven (7) regions were created for further cloud-property analysis (Fig. 5.2). These regions comprise North Africa (NA), West Africa (WA), East Africa (EA), South Africa (SA), central Africa (CA), equatorial (EqATL), and south-east Atlantic Ocean (SeATL) basins. Due to the large spatial extent and complex regional differences in geography and local climates, breaking our study area down into distinct regions is an efficient way to conduct such an analysis. To explore the changes in cloud properties, seasonal averages are created for each study region, and trends are calculated using the least squares method (Wilks, 2011). The p-values from these trends are obtained through the slope of the regression for determining levels of significance. Data is analyzed as seasonal averages; thus, summer months encompass June to August (JJA), September to November (SON) for autumn months, December to February (DJF) for winter months, and March to May (MAM) for spring months.

5.3 Results

The outcome of the various analyses conducted on cloud physical properties, their seasonal influence, and spatial characteristics along regional lines are presented in this section. The result concerning cloud areas is presented first.

5.3.1 Spatial distributions and trends of cloud areas

A breakdown of the 20-year averaged total cloud-area fractions for each season is shown in Fig. 5.2. Over the SeATL (region 1), the presence of a semipermanent stratocumulus deck is clearly visible through boreal summer (JJA), peaking in boreal autumn (SON) and slightly visible during boreal winter (DJF). Clouds are present during boreal spring (MAM) but are not well-structured as in other seasons. Coverage over WA (region 3) is highly variable and achieves a maximum during the local monsoon season (JJA). NA (region 4) exhibits the lowest cloud area fraction average as indicative of a predominantly desert landscape. Both CA and EA (regions 5 and 6) exhibit meridional variations in coverage associated with ITCZ migration. The largest, northern (southern) extent of cloud coverage occurs during the JJA (DJF) within each region. SA achieves its largest cloud fraction during DJF, coinciding with the local rainy season. Fig. 5.3 shows a time series of seasonal, box-averaged cloud area fraction over each study region for all pressure levels. The total cloud area fraction for the SeATL region ranges between ~60–72%, with low-level clouds accounting for ~90% of total clouds throughout JJA and SON months (Fig. 5.3g). SON months have the largest cloud-fraction amounts, ranging ~70–83%. DJF and MAM months have lesser coverage amounts ranging ~58–63% and 51–60%, respectively. Low-level clouds comprise most of the coverage, although to a lesser extent compared for JJA and SON months (75–80%). Cloud fraction areas show an overall increasing trend for JJA, SON, and MAM months. Fig. 5.4 reveals spatial distributions of total cloud cover trends significant at 95%. Increasing trends in total cloud cover over the SeATL region are focused over its eastern portion near the South African coastline (0.5–1.5% year^{-1}).

Coverage conditions within the EqATL (Fig. 5.3f) are like SeATL since low-level clouds comprise the bulk of total cloud cover (~65–80%). Total cloud cover over the EqATL peaks during JJA and SON (~70–77%), coinciding with the northward migration of the ITCZ. Annual changes in total cloud coverage over EA (Fig. 5.3c) varies less, relative to other regions for all seasons, ranging between 35–47%. Low-level clouds in EA represent most of the total coverage and show signs of slight decreases. Spatial distribution of these trends reveals decreases in some areas ranging from 0.2–1.1% year^{-1} (Fig. 5.4). Over NA, as illustrated in Fig. 5.3b, total cloud coverage ranges between 25–48%, with the highest amounts occurring during the JJA months (~40–48%). High-level and mid high-level clouds represent most cloud types in NA. Noticeable increases in coverage are seen in the JJA, MAM, and, to a lesser degree, SON months ranging 0.2–0.8% year^{-1} (Fig. 5.4). Furthermore, CA exhibits consistent cloud cov-

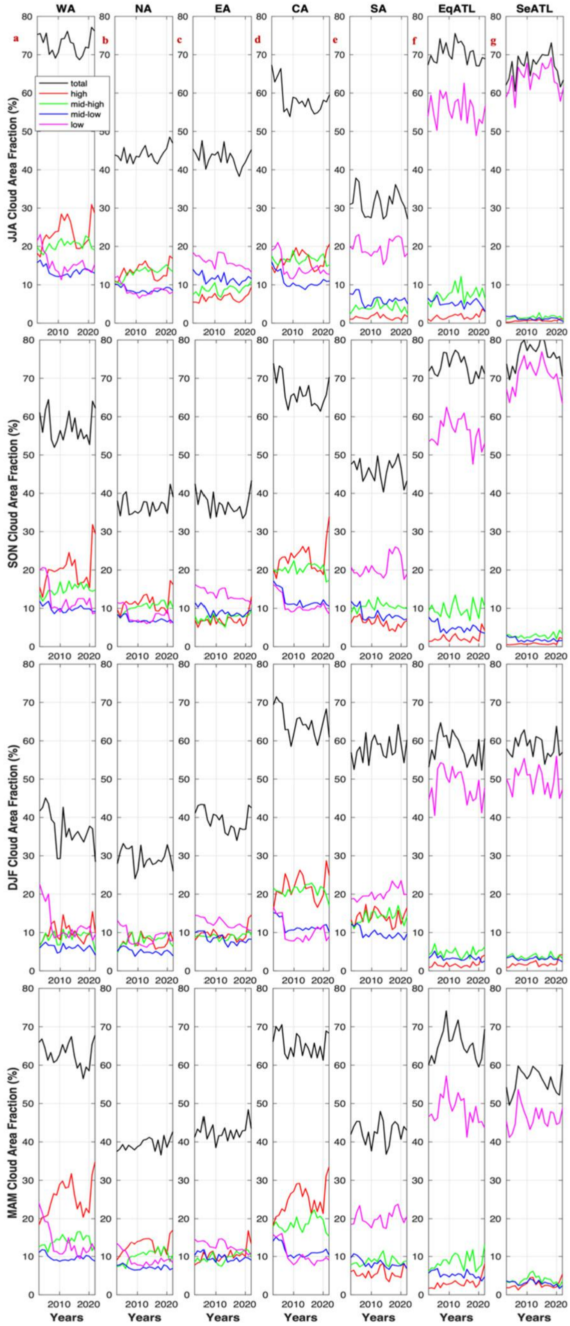

FIGURE 5.3 Time series of seasonal cloud area averaged over each study region for all cloud types. Black lines reflect total clouds, red lines for high-level clouds, green for middle-high level clouds, blue for middle low-level clouds and magenta for lower-level clouds.

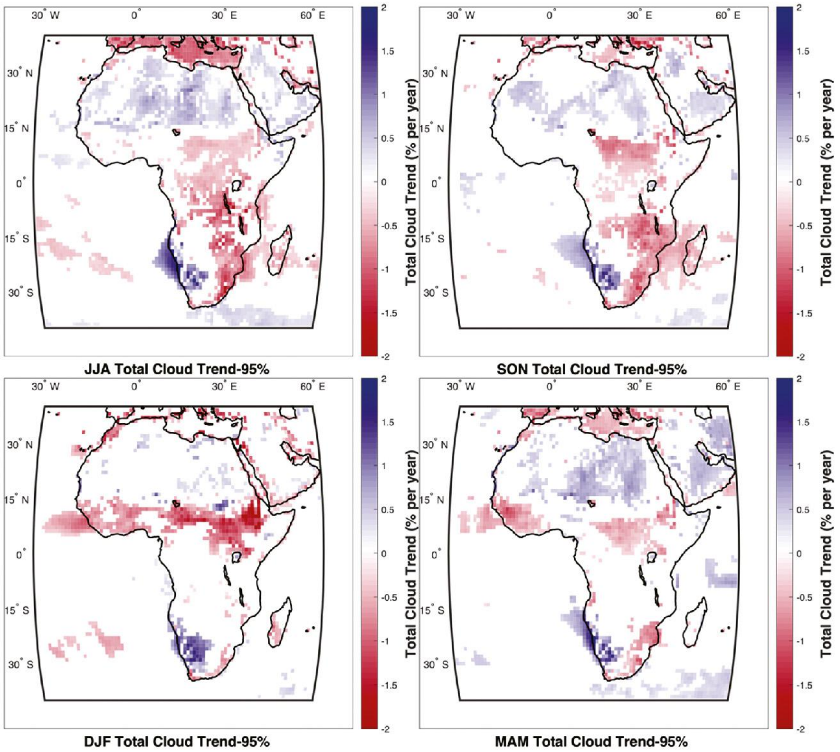

FIGURE 5.4 Seasonal trends in total cloud cover over Africa. Only changes significant at the 95% are shown.

erage throughout the year, with noticeable differences over its northern (Fig. 5.2, JJA) and southern (Fig. 5.2, DJF) counterparts. JJA total cloud over CA ranges $\sim$55–65% with contributions from all cloud types with nearly similar values. High and mid-high cloud types make up most of the total cloud coverage during SON (61–73%), DJF (59–72%), and MAM (61–73%) months. Decreasing cloud trends occur during all seasons over the northern section of CA but are more pronounced for JJA and SON months (Fig. 5.4). Overall trends within CA range -0.2–-1.0% year^{-1}. Of all regions, WA (Fig. 5.3a) exhibits the largest divergence of total cloud averages, with the lowest and highest values occurring in DJF (29–43%) and JJA (66–79%) months, respectively. High and mid-high cloud types dominate each season besides DJF months, where low contribute the most during 7 out of the 20 years studied. Decreasing cloud trends ranging ~ -0.3 to -0.7% year^{-1} are found during MAM and, more noticeably, DJF months. It is worth noting that slight, positive trends are found in the northern edge of the WA box. SA experiences large contrasts in total cloud coverage for JJA and DJF months (Fig. 5.2), reflecting local dry and wet seasons, respectively. Higher cloud amounts persist when the ITCZ makes its southerly

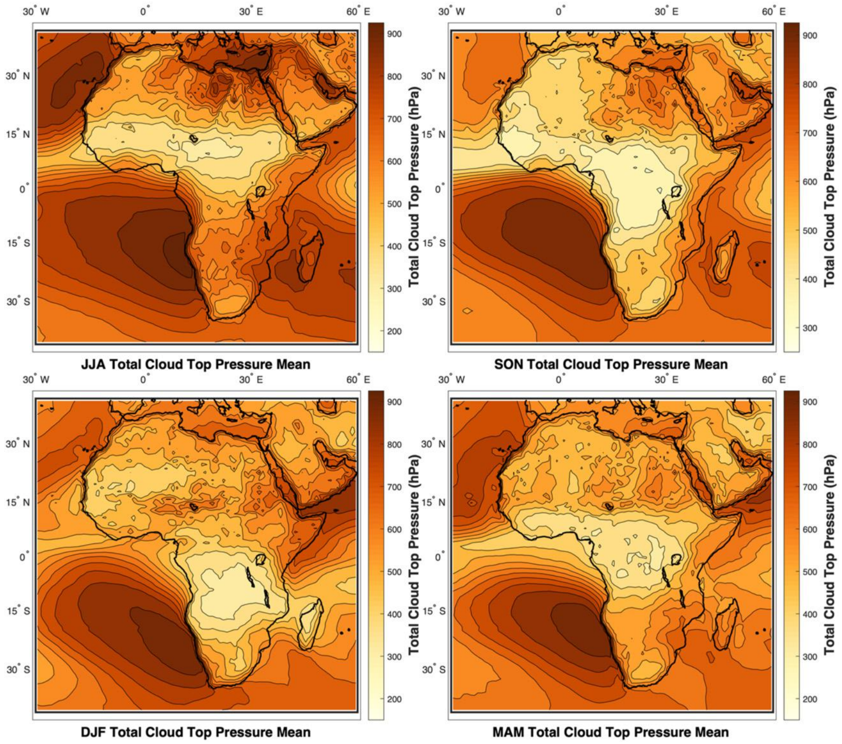

FIGURE 5.5 Same as Fig. 5.2 but for cloud-top temperatures.

migration during SON (40–53%) and DJF (54–62%) months. Lower values are found during MAM (35–48%) and JJA months as the local dry season develops (Fig. 5.3e). Regardless of the season, low-level clouds contribute to most of the total cloud coverage. Trend analysis over SA reveals a dipole signature between the western and eastern portions of the region. Positive total cloud cover trends up to ~1.2% year^{-1} can be seen along the western coastline of SA. Negative trends up to ~−1.3% per year are seen along the eastern cape, including portions of Zimbabwe and Mozambique.

5.3.2 Spatial distributions and trends of cloud pressure and temperature

Seasonally averaged cloud-top pressure (Fig. 5.5) over Africa reflects both cloud distribution and local thermodynamics. The largest pressure values, exceeding 850 hPa, occur in subtropical zones due to strong lower tropospheric stability from subsidence circulation. In addition to the semipermanent stratocumulus deck over the SeATL, some were observed on the west coast of NA during the MAM and JJA months. The lowest values, nearing ~250 hPa, are found in re-

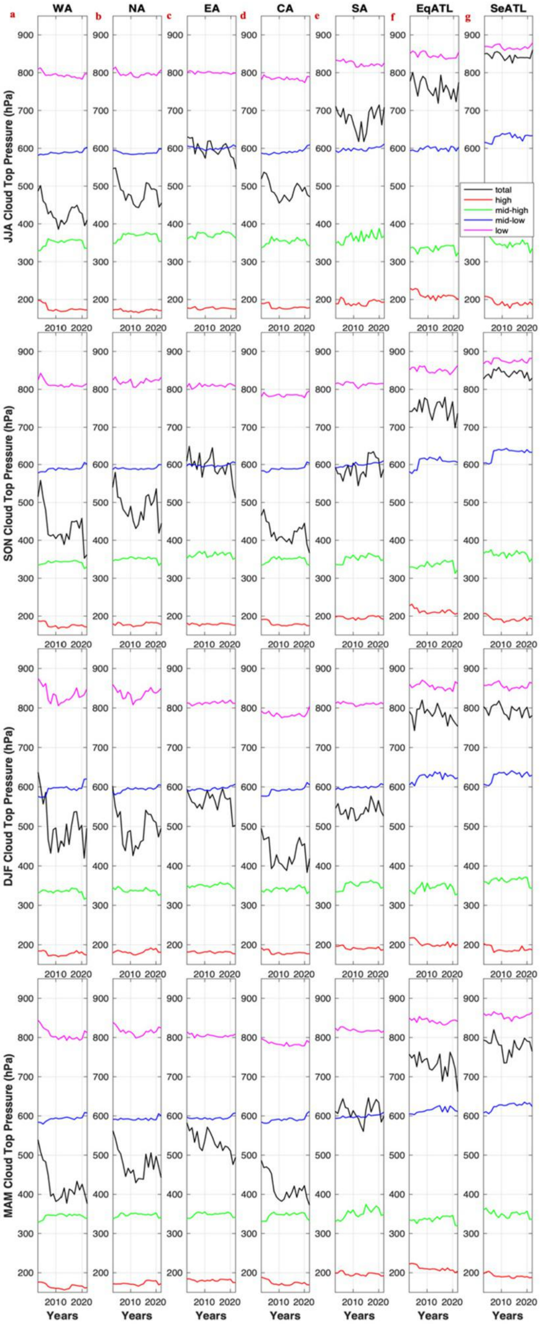

FIGURE 5.6 Same as Fig. 5.3 but for cloud-top pressure.

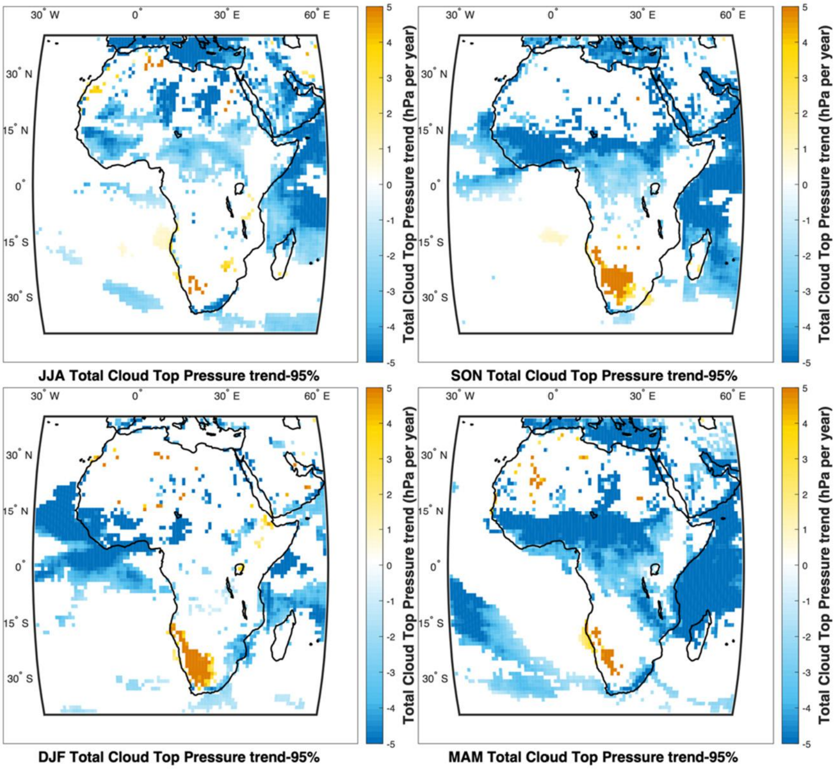

FIGURE 5.7 Same as Fig. 5.4 but for cloud-top pressure.

gions of deep convection, primarily over WA and CA. Fig. 5.6 highlights annual changes in cloud-top pressure for each region during all seasons. Increases (decreases) in pressure mean that the cloud top is higher (lower) in altitude and further away from (closer to) the surface. The result further reveals a decreasing trend in cloud pressure over WA in all the four seasons considered in the study. Similarly, the EqATL exhibits the same characteristics in DJF and MAM.

Moreover, the following regions in NA during JJA and EA during MAM and SA are the only region that shows overall increases in cloud top pressure, particularly in SON and DJF months. Spatial distributions of cloud top pressure trends (Fig. 5.7) portray where changes are the most significant (95% confidence). WA and the northern section of CA exhibit decreasing pressure trends for all seasons, with values starting around -1.2 hPa year^{-1} and often exceeding -5 hPa year^{-1}. EA experienced decreasing trends during both rainy seasons, mostly during MAM months (long rain). The increasing trends found over SA commonly exceed 5 hPa year^{-1} and are focused primarily on the central and western portions of the region.

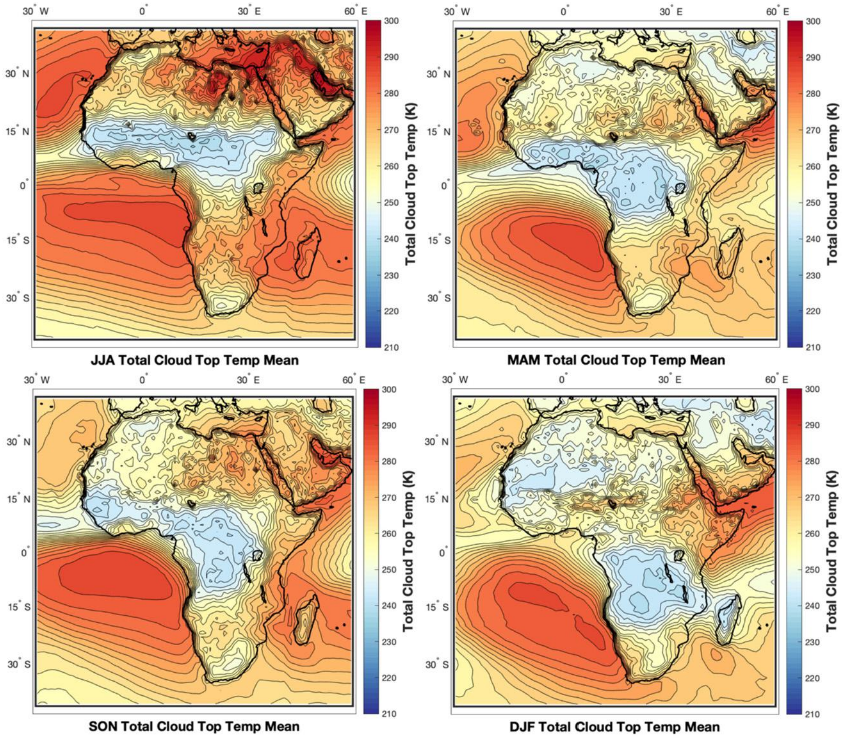

JJA Total Cloud Top Temp Mean

MAM Total Cloud Top Temp Mean

SON Total Cloud Top Temp Mean

DJF Total Cloud Top Temp Mean

FIGURE 5.8 Same as Fig. 5.2 but for cloud-top temperatures.

Cloud-top temperatures and pressures are both retrieved through satellite measurements of infrared radiation from a cloudy scene. Fig. 5.8 displays seasonally averaged cloud top temperatures. As expected, the lowest temperatures ($\sim$240 K) are confined to areas of deep convection over WA and CA, thus containing the largest cloud coverage areas. The highest temperatures ($>$ 290 K) occur over NA during JJA and SeATL during JJA and SON months. Figs. 5.9 and 5.10 display annual changes in cloud-top temperatures and seasonally averaged temperature trends, respectively. Many regions reveal a decreasing trend in temperature values. Most of these decreases occur in WA, CA, and SeATL, and, to a lesser extent, EqATL. Decreases over WA occur over all seasons but are most pronounced during SON and MAM months. The anomalous trend dipole in the cloud area over SA persists towards changes in temperatures as well. Temperature trends have increased up to $\sim$0.8 K year^{-1} on the western side and decreased up to around ~-0.4 K year^{-1} on the eastern side. Such increases are most noticeable during SON and DJF months.

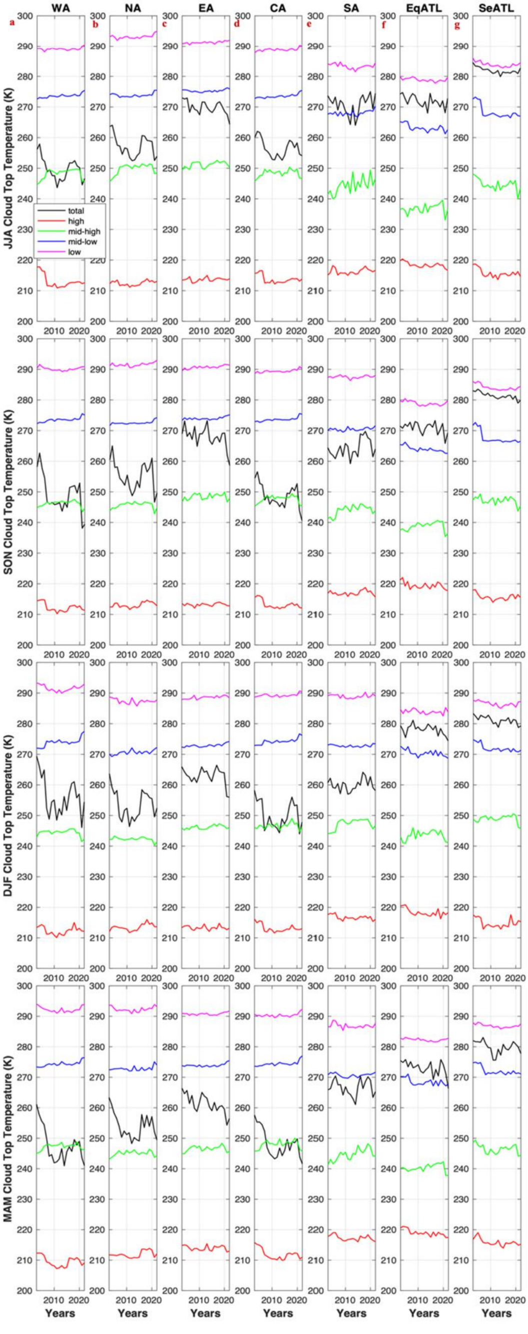

FIGURE 5.9 Same as Fig. 5.3 but for cloud-top temperatures.

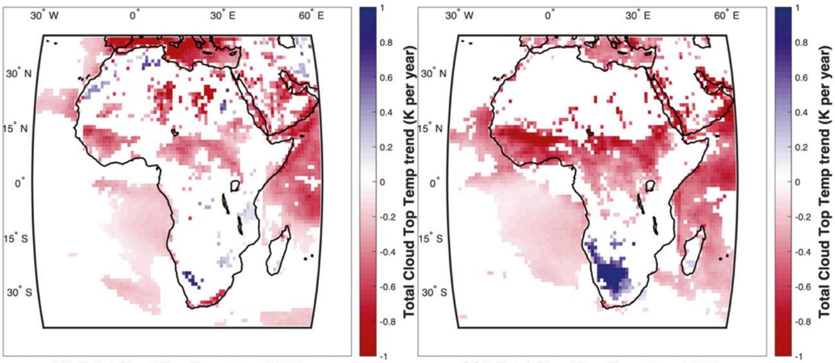

JJA Total Cloud Top Temp trend-95% **SON Total Cloud Top Temp trend-95%**

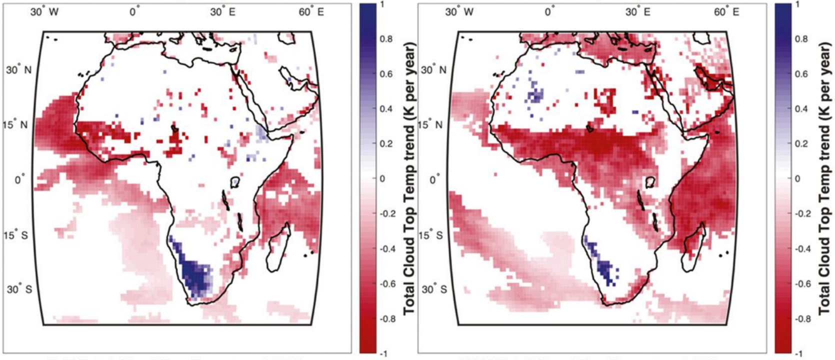

DJF Total Cloud Top Temp trend-95% **MAM Total Cloud Top Temp trend-95%**

FIGURE 5.10 Same as Fig. 5.4 but for cloud-top temperatures.

5.3.3 Spatial distributions and trends of cloud liquid- and ice-water path

LWP accounts for moisture in liquid-phase clouds, usually occurring at warmer temperatures (> 273.15 K). The largest LWP occurs over the SeATL and SA regions (Fig. 5.11). Values exceeding 115 $\mathrm{g\,m^{-2}}$ occur at the center of the semipermanent stratocumulus deck, with the largest values appearing in JJA and SON months. Larger LWP values over the SA region are confined to the South African coastline, where values commonly exceed 120 $\mathrm{g\,m^{-2}}$. In particular, LWP reaches a maximum along the eastern cape, where sea-surface temperatures are much warmer due to the Agulhas current transporting water from the equator. Areas where values exceed this threshold grow as the local wet season progresses (SON and DJF months). Seasonal LWP trends show an overall significant increase (Fig. 5.12) across all regions. The largest changes occur where low-level clouds dominate (EqATL, SeATL, South Africa coastline). These increases range between ~1 to 4.5 $\mathrm{g\,m^{-2}\,year^{-1}}$.

The spatial distribution of seasonally averaged IWP over Africa is shown in Fig. 5.13. This zonal band of deep convection near the equator meanders across

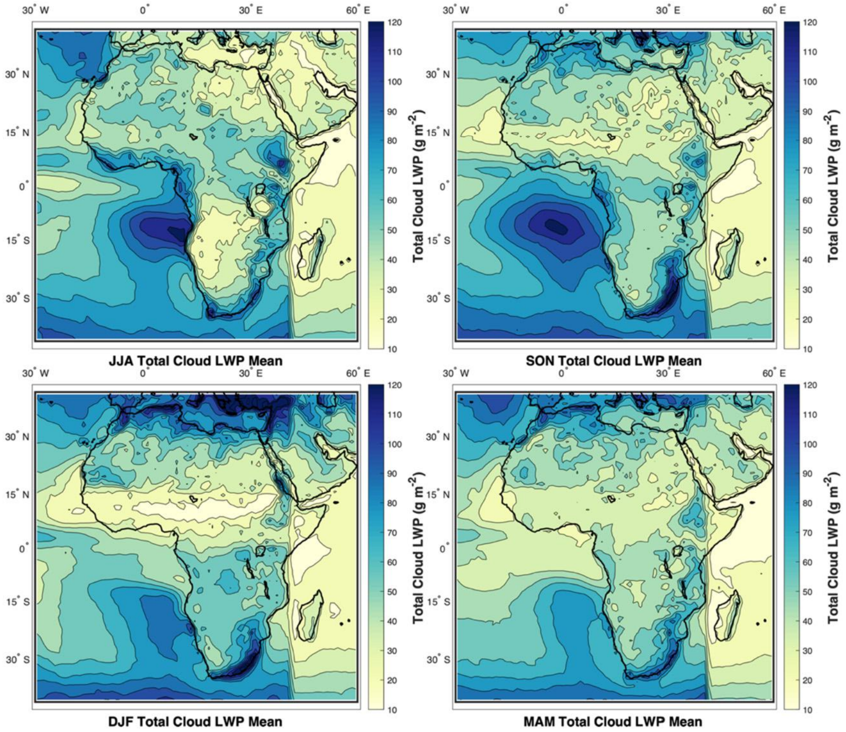

FIGURE 5.11 Same as Fig. 5.2 but for the liquid-water path.

hemispheres annually and covers each study region. Locations with IWP values below ~200 $\mathrm{g\,m^{-2}}$ fall outside of deep convective regions but still experience the presence of ice clouds. Equivalent to LWP, IWP displays positive trends throughout most of the study regions (Fig. 5.14). Significant decreases in IWP are seen over the SeATL (~1 to 3 $\mathrm{g\,m^{-2}\,yr^{-1}}$) during JJA and SON, EA during JJA (up to -5 $\mathrm{g\,m^{-2}\,yr^{-1}}$), and SA during JJA (up to -7 $\mathrm{g\,m^{-2}\,yr^{-1}}$). Increasing trends are visible over WA for MAM, JJA, and SON. The largest positive trends over WA and NA (exceeding 10 $\mathrm{g\,m^{-2}\,yr^{-1}}$) occur in JJA months alongside peak WAM activity. Portions of CA exhibit positive trends in all seasons (up to 6 $\mathrm{g\,m^{-2}\,yr^{-1}}$). Positive trends over SA (up to 10 $\mathrm{g\,m^{-2}\,yr^{-1}}$) for DJF are similar in magnitude to changes seen in WA. Smaller, positive trends are also found over SA for MAM months.

5.4 Discussion and conclusions

Spatial and time series analysis of cloud properties over Africa was done using CERES 1° global gridded, monthly averaged data for 2003–2022. Data is presented for seasonal averages and their associated trends. Analysis of satellite

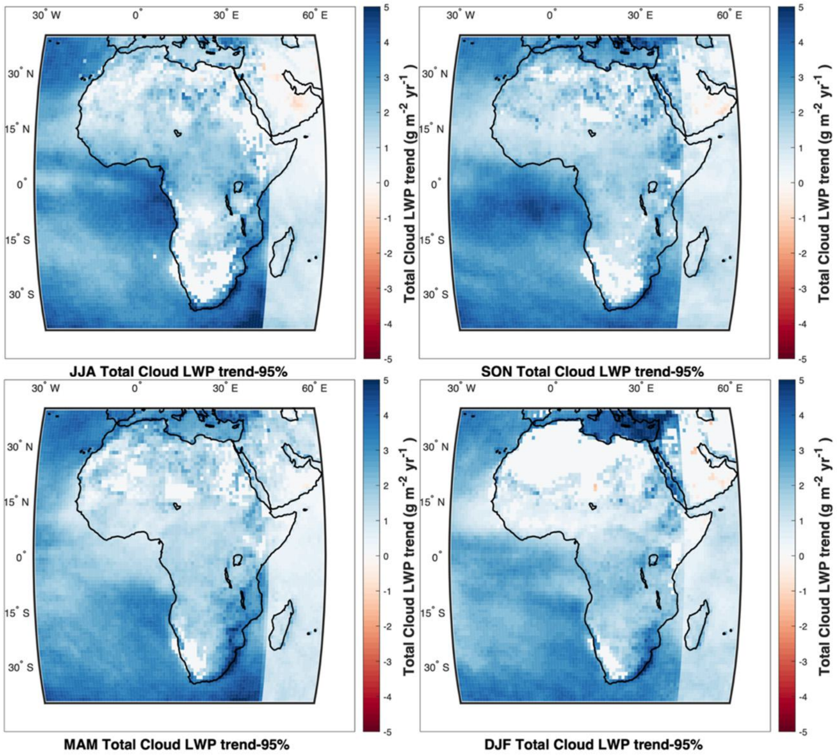
JJA Total Cloud LWP trend-95%

SON Total Cloud LWP trend-95%

MAM Total Cloud LWP trend-95%

DJF Total Cloud LWP trend-95%

FIGURE 5.12 Same as Fig. 5.4 but for the liquid-water path.

observations over Africa was broken down into seven (7) subregions, encompassing a wide range of various geography and climate classifications. This study does not account for mechanisms causing changes in cloud properties and characteristics or how changes in cloud properties impact local and regional climate.

The SeATL stratocumulus deck region is one of the most studied cloud systems due to its global impacts on Earth's radiation budget as well as local aerosol–cloud interactions (Pennypacker et al., 2020; Abel et al., 2020; Adebiyi et al., 2015; Ajoku et al., 2021). The cloud-top radiative cooling associated with such low-level capped clouds influences turbulence within marine boundary layers (Zheng et al., 2018). The increasing cloud cover trend that we find in portions of SeATL may be a signal of global temperature increases. Without stable, long-term observations of cloud cover and sea-surface temperatures over the ocean, modeling studies have been used to attribute potential low-level cloud increases to positive changes in sea-surface temperatures (Zhou et al., 2016). Previous research has compared various cloud products and identified uncertainties in observation retrievals from each (Stubenrauch et al., 2013).

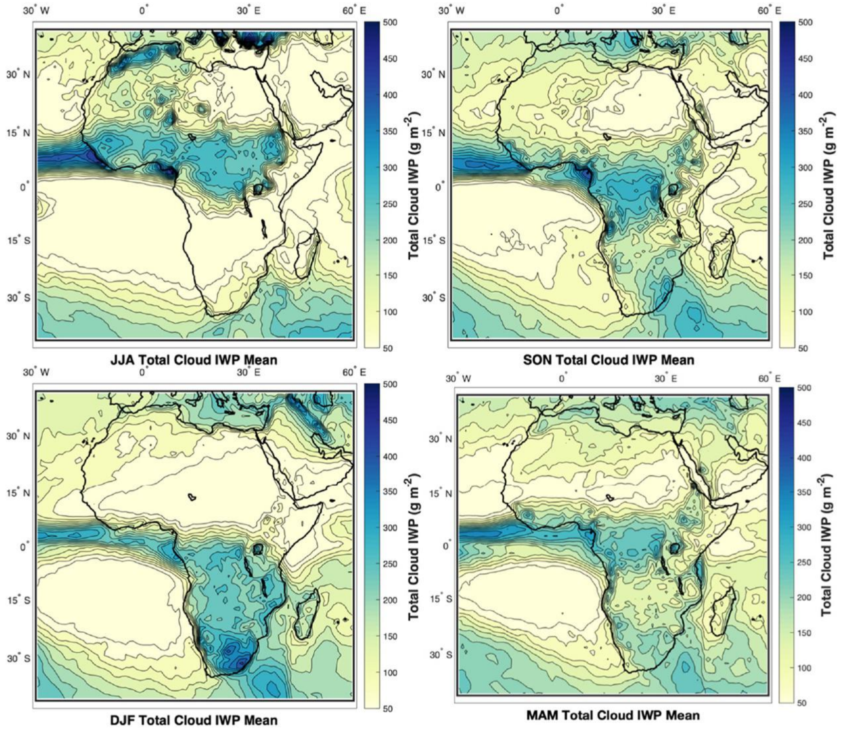

FIGURE 5.13 Same as Fig. 5.2 but for the ice-water path.

The anomalous dipole trend in total cloud cover over SA persists through all seasons. Negative trends are focused along the coastline of the eastern Cape. The period of this study overlaps with recent drought conditions occurring over the country of South Africa (Chikoore and Jury, 2021; Archer et al., 2022). Mahlalela et al. (2020) studied precipitation trends over the eastern cape of SA and found decreases across all seasons, with a maximum occurring during SON months. Our results compare well when looking at total cloud cover trends, with a maximum occurring through SON months. Cloud-top pressure and temperature trends for SON over SA reveal positive increases associated with increased subsidence and anticyclonic circulation aloft. Also, in this region, a decreasing IWP trend only exacerbates drier conditions during the local dry season. Over the western cape, increased cloud-cover trends during the rainy season (DJF) have occurred with decreasing precipitation trends (Lakhraj-Govender and Grab, 2019).

Decreasing cloud cover trends persist over CA for all seasons and are consistent with previous studies that find similar decreases for global tropical cloud cover (Dim et al., 2011; Warren et al., 2007). These decreases are associated with decreases in total cloud-top temperatures and pressure indicating that cloud

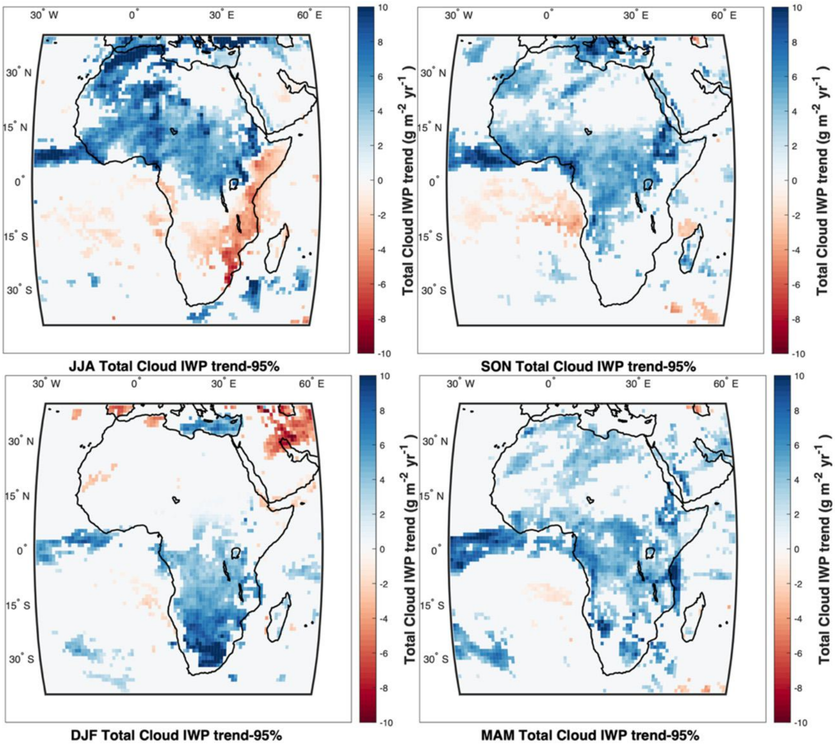

FIGURE 5.14 Same as Fig. 5.4 but for the ice-water path.

tops over tropical Africa reach higher altitudes. The Sahel borders both WA and NA regions. Increases in JJA total cloud cover and IWP along this transition zone agree well with recent recovery of Sahelian precipitation (Biasutti, 2019; Vischel et al., 2019; Akinsanola and Zhou, 2019). Tropical Africa extends into the EA region where decreasing cloud trends agree with the well-studied long-term standing drought conditions (Nicholson, 2016, 2017; Gebrechorkos et al., 2019; Wainwright et al., 2019).

Climate change over Africa is not as well-studied as other parts of the modern world. Looking toward the future, Africa needs to develop and maintain sustainable development goals such as using renewable energy sources like panels as a part of United Nations 2030 agenda (Adenle, 2020). Toward this goal, a better understanding of cloud properties is needed to accurately assess the dispersal of such renewable technology. In addition to satellite data availability, more ground-based (lidar) measurements are needed to validate satellite retrievals over rural, isolated locations throughout Africa.

Data availability

NASA's CERES data used to complete the research presented in this study can be found here: https://ceres.larc.nasa.gov/data/. See Doelling et al. (2013, 2016).

Funding

This work was supported by the Department of Energy [grant number DE-SC0022931].

References

Abel, S.J., Barrett, P.A., Zuidema, P., Zhang, J., Christensen, M., Peers, F., Taylor, J.W., Crawford, I., Bower, K.N., Flynn, M., 2020. Open cells exhibit weaker entrainment of free-tropospheric biomass burning aerosol into the south-east Atlantic boundary layer. Atmospheric Chemistry and Physics 20 (7), 4059–4084.

Adebiyi, A.A., Zuidema, P., Abel, S.J., 2015. The convolution of dynamics and moisture with the presence of shortwave absorbing aerosols over the southeast Atlantic. Journal of Climate 28, 1997–2024. https://doi.org/10.1175/JCLID-14-00352.1.

Adenle, A.A., 2020. Assessment of solar energy technologies in Africa-opportunities and challenges in meeting the 2030 agenda and sustainable development goals. Energy Policy 137, 111180.

Ajoku, O.F., Miller, A.J., Norris, J.R., 2021. Impacts of aerosols produced by biomass burning on the stratocumulus-to-cumulus transition in the equatorial Atlantic. Atmospheric Science Letters 22 (4), e1025.

Akinsanola, A.A., Zhou, W., 2019. Dynamic and thermodynamic factors controlling increasing summer monsoon rainfall over the West African Sahel. Climate Dynamics 52, 4501–4514. https://doi.org/10.1007/s00382-018-4394-x.

Archer, E., Du Toit, J., Engelbrecht, C., Hoffman, M.T., Landman, W., Malherbe, J., Stern, M., 2022. The 2015-19 multi year drought in the Eastern Cape, South Africa: it's evolution and impacts on agriculture. Journal of Arid Environments 196, 104630.

Biasutti, M., 2019. Rainfall trends in the African Sahel: characteristics, processes, and causes. Wiley Interdisciplinary Reviews: Climate Change 10 (4), e591.

Burnett, M.W., Quetin, G.R., Konings, A.G., 2020. Data-driven estimates of evapotranspiration and its controls in the Congo Basin. Hydrology and Earth System Sciences 24 (8), 4189–4211.

Chakraborty, S., Jiang, J.H., Su, H., Fu, R., 2020. Deep convective evolution from shallow clouds over the Amazon and Congo rainforests. Journal of Geophysical Research. Atmospheres 125 (1), e2019JD030962.

Chikoore, H., Jury, M.R., 2021. South African drought, deconstructed. Weather and Climate Extremes 33, 100334.

Christensen, J.H., Kumar, K.K., Aldrian, E., An, S.I., Cavalcanti, I.F.A., de Castro, M., Dong, W., Goswami, A., Hall, A., Kanyanga, J.K., Kitoh, A., 2013. Climate Change 2013: The Physical Scientific Basis. Contribution of Working Group I to the Fifth Assessment Report of the Intergovernmental Panel on Climate Change.

Cook, K.H., Vizy, E.K., 2016. The Congo Basin Walker circulation: dynamics and connections to precipitation. Climate Dynamics 47, 697–717.

Cook, K.H., Vizy, E.K., 2019. Contemporary climate change of the African monsoon systems. Current Climate Change Reports 5, 145–159.

Danso, D.K., Anquetin, S., Diedhiou, A., Kouadio, K., Kobea, A.T., 2020. Daytime low-level clouds in West Africa–occurrence, associated drivers, and shortwave radiation attenuation. Earth System Dynamics 11 (4), 1133–1152.

Didier, N., 2015. Comparison of spatial and temporal cloud coverage derived from CloudSat, CERES, ISCCP and their relationship with precipitation over Africa. American Journal of Remote Sensing 3 (2), 17–28.

Dim, J.R., Murakami, H., Nakajima, T.Y., Nordell, B., Heidinger, A.K., Takamura, T., 2011. The recent state of the climate: driving components of cloud-type variability. Journal of Geophysical Research. Atmospheres 116 (D11).

Doelling, D.R., Loeb, N.G., Keyes, D.F., Nordeen, M.L., Morstad, D., Nguyen, C., Wielicki, B.A., Young, D.F., Sun, M., 2013. Geostationary enhanced temporal Interpolation for CERES flux products. Journal of Atmospheric and Oceanic Technology 30 (6), 1072–1090. https://doi.org/10.1175/JTECH-D-12-00136.1.

Doelling, D.R., Sun, M., Nguyen, L.T., Nordeen, M.L., Haney, C.O., Keyes, D.F., Mlynczak, P.E., 2016. Advances in geostationary-derived longwave fluxes for the CERES Synoptic (SYN1deg) product. Journal of Atmospheric and Oceanic Technology 33 (3), 503–521. https://doi.org/10.1175/JTECH-D-15-0147.1.

Eastman, R., Warren, S.G., Hahn, C.J., 2011. Variations in cloud cover and cloud types over the ocean from surface observations, 1954–2008. Journal of Climate 24 (22), 5914–5934.

Eastman, R., Warren, S.G., 2014. Diurnal cycles of cumulus, cumulonimbus, stratus, stratocumulus, and fog from surface observations over land and ocean. Journal of Climate 27 (6), 2386–2404.

Gebrechorkos, S.H., Hülsmann, S., Bernhofer, C., 2019. Long-term trends in rainfall and temperature using high-resolution climate datasets in East Africa. Scientific Reports 9 (1), 11376.

Gu, Y., Liou, K.N., Jiang, J.H., Su, H., Liu, X., 2012. Dust aerosol impact on North Africa climate: a GCM investigation of aerosol-cloud-radiation interactions using A-Train satellite data. Atmospheric Chemistry and Physics 12 (4), 1667–1679.

Houze Jr, R.A., 2004. Mesoscale convective systems. Reviews of Geophysics 42 (4).

IPCC, 2014. In: Stocker, T.F., Qin, D., Plattner, G.K., Tignor, M., Allen, S.K., Boschung, J., Nauels, A., Xia, Y., Bex, V., Midgley, P.M. (Eds.), Climate Change 2013 – The Physical Science Basis. Cambridge University Press, Cambridge, UK and New York, NY. https://doi.org/10.1017/cbo9781107415324.

Lakhraj-Govender, R., Grab, S.W., 2019. Rainfall and river flow trends for the Western Cape Province, South Africa. South African Journal of Science 115 (9–10), 1–6.

Lau, N.C., Crane, M.W., 1997. Comparing satellite and surface observations of cloud patterns in synoptic-scale circulation systems. Monthly Weather Review 125 (12), 3172–3189.

Mahlalela, P.T., Blamey, R.C., Hart, N.C.G., Reason, C.J.C., 2020. Drought in the Eastern Cape region of South Africa and trends in rainfall characteristics. Climate Dynamics 55, 2743–2759.

Moron, V., Camberlin, P., Aellig, R., Champagne, O., Fink, A.H., Knippertz, P., Philippon, N., 2023. Diurnal to interannual variability of low-level cloud cover over western equatorial Africa in May–October. International Journal of Climatology 43 (13), 6038–6064.

Neupane, N., 2016. The Congo basin zonal overturning circulation. Advances in Atmospheric Sciences 33, 767–782.

Nicholson, S.E., 2016. An analysis of recent rainfall conditions in eastern Africa. International Journal of Climatology 36 (1), 526–532.

Nicholson, S.E., 2017. Climate and climatic variability of rainfall over eastern Africa. Reviews of Geophysics 55 (3), 590–635.

Nikulin, G., Jones, C., Giorgi, F., Asrar, G., Büchner, M., Cerezo-Mota, R., Christensen, O.B., Déqué, M., Fernandez, J., Hänsler, A., van Meijgaard, E., 2012. Precipitation climatology in an ensemble of CORDEX-Africa regional climate simulations. Journal of Climate 25 (18), 6057–6078.

Ntale, H.K., Gan, T.Y., Mwale, D., 2003. Prediction of East African Seasonal rainfall using simplex canonical correlation analysis. Journal of Climate 16, 2105–2112. https://doi.org/10.1175/1520-0442(2003)016<2105:POEASR>2.0.CO;2.

Ntwali, D., Mugisha, E., Vuguziga, F., Kakpa, D., 2017. Liquid and ice water content in clouds and their variability with temperature in Africa based on ERA-Interim, JRA-55, MERRA and ISCCP. Meteorology and Atmospheric Physics 129 (1), 17–34.

Pennypacker, S., Diamond, M., Wood, R., 2020. Ultra-clean and smoky marine boundary layers frequently occur in the same season over the southeast Atlantic. Atmospheric Chemistry and Physics 20 (4), 2341–2351.

Probst, P., Rizzi, R., Tosi, E., Lucarini, V., Maestri, T., 2012. Total cloud cover from satellite observations and climate models. Atmospheric Research 107, 161–170.

Schrage, J.M., Fink, A.H., 2012. Nocturnal continental low-level stratus over tropical West Africa: observations and possible mechanisms controlling its onset. Monthly Weather Review 140 (6), 1794–1809.

Stephens, G.L., Tsay, S.C., Stackhouse Jr, P.W., Flatau, P.J., 1990. The relevance of the microphysical and radiative properties of cirrus clouds to climate and climatic feedback. Journal of the Atmospheric Sciences 47 (14), 1742–1754.

Stubenrauch, C.J., Rossow, W.B., Kinne, S., Ackerman, S., Cesana, G., Chepfer, H., Di Girolamo, L., Getzewich, B., Guignard, A., Heidinger, A., Maddux, B.C., 2013. Assessment of global cloud datasets from satellites: project and database initiated by the GEWEX radiation panel. Bulletin of the American Meteorological Society 94 (7), 1031–1049.

Tompkins, A.M., Adebiyi, A.A., 2012. Using CloudSat cloud retrievals to differentiate satellite-derived rainfall products over West Africa. Journal of Hydrometeorology 13 (6), 1810–1816.

van der Linden, R., Fink, A.H., Redl, R., 2015. Satellite-based climatology of low-level continental clouds in southern West Africa during the summer monsoon season. Journal of Geophysical Research. Atmospheres 120, 1186–1201. https://doi.org/10.1002/2014JD022614.

Vischel, T., Panthou, G., Peyrillé, P., Roehrig, R., Quantin, G., Lebel, T., Wilcox, C., Beucher, F., Budiarti, M., 2019. Precipitation extremes in the West African Sahel: recent evolution and physical mechanisms. In: Tropical Extremes. Elsevier, pp. 95–138.

Wainwright, C.M., Marsham, J.H., Keane, R.J., Rowell, D.P., Finney, D.L., Black, E., Allan, R.P., 2019. 'Eastern African Paradox' rainfall decline due to shorter not less intense long rains. npj Climate and Atmospheric Science 2 (1), 34.

Warren, S.G., Eastman, R.M., Hahn, C.J., 2007. A survey of changes in cloud cover and cloud types over land from surface observations, 1971–96. Journal of Climate 20 (4), 717–738.

Wilks, D.S., 2011. Statistical Methods in the Atmospheric Sciences, vol. 100. Academic Press.

Wood, R., 2012. Stratocumulus clouds. Monthly Weather Review 140 (8), 2373–2423.

Zheng, Y., Rosenfeld, D., Li, Z., 2018. The relationships between cloud top radiative cooling rates, surface latent heat fluxes, and cloud-base heights in marine stratocumulus. Journal of Geophysical Research. Atmospheres 123 (20), 11–678.

Zhou, C., Zelinka, M.D., Klein, S.A., 2016. Impact of decadal cloud variations on the Earth's energy budget. Nature Geoscience 9 (12), 871–874.

Chapter 6

Future changes in precipitation distributions over Africa

Paul-Arthur Monerie[a], Hamida Ngoma Nadoya[b], Izidine Pinto[c], Alain T. Tamoffo[d], and Koffi Worou[e]

[a]*National Centre for Atmospheric Science, Reading, United Kingdom,* [b]*Department of Earth Sciences, University of Connecticut, Storrs, CT, United States,* [c]*Royal Netherlands Meteorological Institute (KNMI), De Bilt, the Netherlands,* [d]*Climate Service Center Germany (GERICS), Helmholtz-Zentrum Hereon, Hamburg, Germany,* [e]*Swedish Centre for Impacts of Climate Extremes (CLIMES), Uppsala University, Uppsala, Sweden*

6.1 Introduction

The African continent is home to approximately 1.4 billion people, constituting around 18% of the world's population. Africa exhibits a diverse range of climates, from the second largest rainforest in the Congo basin in central Africa to the arid Sahara and Kalahari deserts in northern and southern Africa, respectively. Precipitation is particularly high along the equator, with seasonal and spatial changes associated with the development of monsoon precipitations across Africa. Monsoon dynamics and seasonality are influenced by large-scale temperature gradients and the resulting cross-equatorial energy imbalance (Schneider et al., 2014; Biasutti et al., 2018). However, variations in topography, distance from the equator, and specific regional and local features (e.g., the Saharan Heat Low; the Angola Low) contribute to notable differences between monsoon regions. For instance, the equatorial East Africa and West African Guinea Coast have a bimodal structure of the annual rainfall cycle (i.e., two rainy seasons per year), which changes to a unimodal pattern moving away from the equator. In addition, the Sahelian region in West Africa also follows a unimodal (i.e., only one rainy season) annual cycle (Worou et al., 2020; Palmer et al., 2023).

Monsoon precipitation is crucial for African societies, contributing approximately 80% of the annual total precipitation within a short period (Liebmann et al., 2012; Worou et al., 2020) over most of the monsoon domains (~50% over regions of East Africa and South Africa). Variations in precipitation are associated with strong societal impacts. Unusually low rainfall led to a large and prolonged drought over the Sahel in the 1970s–1990s, leading to population migration, water scarcity, and famine (Giannini et al., 2003; Rodríguez-Fonseca

Aerosols and Precipitation Over Africa. https://doi.org/10.1016/B978-0-44-314050-1.00011-6

et al., 2015), to around 450,000 deaths in Ethiopia and Sudan in the period 1984–1985 and around 100,000 deaths in Mozambique in 1981 (Gebremeskel Haile et al., 2019). More recently, the City of Cape Town in South Africa experienced a major water crisis in 2018, known as Day Zero, attributed to the effect of exceptionally low rainfall. Additionally, southern Sudan faced severe flooding in 2023 due to heavy rainfall.

Changes in rainfall levels and variability pose challenges for African communities. As African nations strive to expand agriculture, enhance freshwater supply and sanitation, and increase hydropower generation, understanding the impacts of a warming climate becomes crucial for their livelihood and development. In this chapter, we describe the projected changes in precipitation throughout the 21st century based on current knowledge and the latest generations of the Coupled Model Intercomparison Project (CMIP) climate models (Eyring et al., 2016). We specifically address changes in both seasonal mean precipitation and extreme precipitation events, with a dedicated focus on various regions of the African continent to consider their regional specificities: West Africa, East Africa, Central Africa, and Southern Africa. The text also provides a brief description of the role played by future changes in cloud cover and aerosol on precipitation variability over Africa. We describe the feedback between aerosol loading, cloud cover and precipitation, and document potential effects of future changes in aerosol loading on precipitation across Africa. We then describe the potential future changes in cloud cover and aerosol and what this implies for future changes in precipitation. The final section is a discussion of important prospects for improving of our understanding of future changes in precipitation.

6.2 Data and method

We assess the effect of climate change on precipitation using historical simulations and SSP5-8.5 projections (see Table 6.2). The historical simulations are forced with observed and natural anthropogenic forcings from 1850 to 2014 (Eyring et al., 2016). The SSP5-8.5 projections are forced using a high-emissions scenario following a forcing of 8.5 Wm^{-2} by the end of the 21st century (O'Neill et al., 2016). The SSP5-8.5 emission scenario is widely used in the literature and makes possible comparison with published studies. The effect of climate change is defined as the difference between the period 2060–2099 under the SSP5-8.5 emissions scenario and the period 1960–1999 under the historical emissions scenario, showing the change over a 40-year period, and with a century interval. We utilized monthly means and a single ensemble member (the first available ensemble member, e.g., r1i1p1) for each model. We show the effect of climate change on precipitation and near-surface wind speed. All data were interpolated to a common horizontal resolution of 2.5° using a bilinear interpolation. All models in this chapter have been part of the Coupled Model Intercomparison Project Phase 6 (CMIP6; Eyring et al., 2016).

We present the multi-model mean changes in precipitation and near-surface zonal and meridional wind speed (i.e., the average across all models), along with the uncertainty in the effect of climate change, defined as the standard deviation computed across all models for the change in precipitation. The climatology, representing the average over the period 1960–1999 under the historical emissions scenario, is provided to facilitate understanding of the shift in precipitation change. We highlight the robustness of the precipitation change, defined as when at least 75% of the models agree on the sign of change in precipitation as the multi-model mean.

6.3 Precipitation across Africa: climatology and future changes

6.3.1 West Africa

6.3.1.1 Precipitation over West Africa

Precipitation in West Africa exhibits heterogeneity, with high amounts along the coast and the Gulf of Guinea contrasting with lower amounts in the Sahel (Worou et al., 2020). The region's topography affects the pattern of precipitation, with a large maximum near the Fouta Djalon (Guinea) and the Cameroon mountains. A gradual decrease in precipitation occurs from the Gulf of Guinea towards the Sahara Desert (Fig. 6.1a; contours). Positioned between the Guinean coast and the Sahara, the Sahel serves as a transitional semiarid zone. Changes in precipitation amounts are associated with changes in vegetation cover, with a tropical rainforest along the coast, near the Gulf of Guinea, a Savannah in the Sahel, and semiarid vegetation in the northern Sahel (Bamba et al., 2015).

The monsoon precipitation in West Africa follows an annual cycle associated with the movement of the Intertropical Convergence Zone (ITCZ). The cycle is bimodal over the coast (between 5 and 10°N), with the rainy seasons extending from April to the end of June and from August or September to November (Dunning et al., 2016). The two rainy seasons are separated by the so-called "little dry season" (Adejuwon and Odekunle, 2006; Fink et al., 2017), which coincides with the development of the Atlantic cold tongue, due to an intensified coastal upwelling. It is noteworthy that the bimodal structure of the rainfall over coastal West Africa can be less pronounced over some decades (Worou et al., 2020). The cycle is unimodal elsewhere (Liebmann et al., 2012; Dunning et al., 2016), with the onset of the rainy season starting in mid-May (14 May, ±9.5 days) over the Sudano–Sahelian zone and in early June (24 June, ±8 days) over the Sahel, north of 10°N (Sultan and Janicot, 2003).

Variations in precipitation are linked to atmospheric circulation and moisture transport, influenced by Sea Surface Temperature (SST) changes. Changes in North Atlantic SST (Martin and Thorncroft, 2014; Monerie et al., 2019; Mohino et al., 2024) Tropical Atlantic SST (Okumura and Xie, 2004; Worou et al., 2020, 2022; Thiam et al., 2024; Wane et al., 2024) in the Pacific Decadal Variability (PDV) (e.g., Villamayor and Mohino, 2015), Indian Ocean (Dyer et al., 2017a), and Mediterranean Sea (Rowell, 2003; Park et al., 2016; Worou et al., 2020), strongly affect West African precipitation on synoptic to multidecadal timescales. Based on the aforementioned relationship between SST and monsoon precipitation, we hypothesize that the future change in SST may affect the patterns of precipitation change.

6.3.1.2 *Future changes in precipitation over West Africa*

CMIP6 model projections indicate a potential increase in precipitation across a large portion of the Sahel, stretching from eastern Mali to Sudan, by the end of the 21st century (Monerie et al., 2021, 2012, 2013, 2016a, 2020b; Biasutti, 2013; Roehrig et al., 2013; James et al., 2015; Diallo et al., 2016; Akinsanola and Zhou, 2018; Almazroui et al., 2020; Dosio et al., 2021) (Fig. 6.1a). Conversely, precipitation is projected to decrease over the western Sahel (Senegal and western Mali) (Biasutti, 2013; Roehrig et al., 2013; James et al., 2015; Diallo et al., 2016; Akinsanola and Zhou, 2018; Almazroui et al., 2020; Monerie et al., 2020b,a) (Fig. 6.1a).

The thermodynamic effect of climate change, namely, the increase in global low-level specific humidity allows an increase in precipitation globally (Chadwick et al., 2016). Consequently, global warming is linked to heightened moisture flux, increased moisture convergence, and amplified precipitation over the central Sahel. Climate change is also associated with a shift in atmospheric circulation, with the monsoon circulation shifting northwards over the central Sahel and West Africa, enhancing moisture transport and precipitation over the Sahel (Monerie et al., 2020b) (Fig. 6.1a). Faster warming of the Sahara Desert compared to the Guinea Coast would also come into play, resulting in an intensified northward surface pressure gradient, thereby strengthening moisture transport (Tamoffo et al., 2023a). Over the western Sahel, the decrease in precipitation is associated with a southward shift of the monsoon circulation, enhanced atmospheric subsidence, and reduced deep convection (Monerie et al., 2012). The zonal contrast in precipitation change in the Sahel is thus associated with two distinct responses to climate change. Rising temperatures in the Northern Hemisphere (including North Africa) shift the monsoon circulation northward, increasing precipitation, while rising SSTs globally are associated with a stabilization of the atmospheric column in the tropics (Ma et al., 2018) and a decrease in precipitation over the western Sahel (Gaetani et al., 2017; Hill et al., 2017; Monerie et al., 2021). Monerie et al. (2021) demonstrated that these two aforementioned responses to climate change could explain both the pattern and timescale of precipitation change. Note that the mean precipitation changes are nonrobust over most of the Guinea Coast region (Fig. 6.1a).

Climate change will also affect the characteristics of precipitation distribution over West Africa. The number of rainy days, a key factor associated with seasonal mean precipitation change (Biasutti, 2019), is projected to increase over the central Sahel and to decrease over the western Sahel and the Guinea coast (Dosio et al., 2021). Similarly, there is an anticipated rise in the intensity of extreme rainfall events over the central Sahel and Guinea coast, contrasted by a decrease over the western Sahel (Diallo et al., 2016). Changes in consecutive dry days are consistent with changes in the number of rainy days. Models project an increase in consecutive dry days in the western Sahel and a decrease in consecutive dry days in the central Sahel (Diallo et al., 2016). Over the Guinea coast, the consecutive wet days are projected to decrease (Worou, 2023). However, it's crucial to note that these results are resolution-dependent: Regional climate models (CORDEX-Coordinated Regional Climate Downscaling Experiment) exhibit contrasting responses compared to CMIP5 and CMIP6 climate models (Dosio et al., 2021). For instance, the number of rainy days over the central Sahel is projected to decrease within the CORDEX ensemble (Akinsanola and Zhou, 2019; Dosio et al., 2021), while the CMIP5 and CMIP6 climate models project an increase. Climate change is also altering the timing of the annual monsoon cycle. The onset of the monsoon is significantly delayed over the western Sahel, leading to a reduction in the length of the rainy season (Kumi and Abiodun, 2018; Dunning et al., 2018). Similarly, the onset of the monsoon is delayed over the central Sahel (Monerie et al., 2016a; Dunning et al., 2018).

Changes in precipitation remain uncertain, as evidenced by the substantial inter-model spread in precipitation change (Fig. 6.1b). Near-term (2020–2040) projections are strongly impacted by internal climate variability (Monerie et al., 2017), with an expected out-of-phase behavior among different ensemble members of the same climate model (Hawkins and Sutton, 2011). The uncertainty in longer-term projections (e.g., 2080–2100) mainly arises from differences between climate models in simulating the effect of the externally forced responses on atmospheric circulation (Monerie et al., 2020b). Recent studies emphasize the significance of sea surface temperature (SST) changes in understanding the uncertainty associated with future changes in precipitation over West Africa. Future changes in the North Atlantic, Mediterranean, Pacific equatorial, and interhemispheric SST gradients play a role in shaping the future evolution of the West African precipitation (Park et al., 2015, 2016; Monerie et al., 2023a; Guilbert et al., 2024). Moreover, the literature suggests that the uncertainty in future changes in North Atlantic SST, and hence West African precipitation, stems from the uncertainty in simulating future changes in the Atlantic Meridional Overturning Circulation (Bellomo et al., 2021).

In addition to changes in SST, climate model biases and parameterization (Yan et al., 2018) are important sources of uncertainty for climate projections. However, Monerie et al. (2016b) showed that the link between precipitation biases and changes in precipitation is not clear. Differences between emission scenarios also result in differences in projections of precipitation change. Importantly, the choice of scenario does not affect the pattern of precipitation change but rather modulates the intensity of change (e.g., Almazroui et al., 2020).

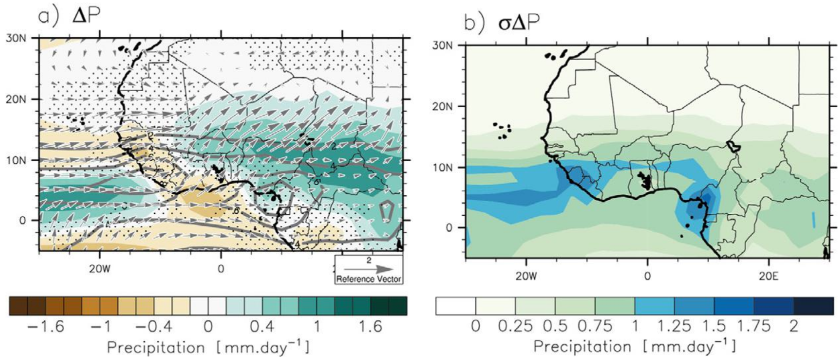

FIGURE 6.1 (a) Effect of climate change on precipitation (multi-model mean) [mm d^{-1}] and (b) uncertainty (ensemble spread) of the effect of climate change on precipitation [mm d^{-1}], in AMJJASO (April–October). The effect of climate change is defined as the difference between the period 2060–2099 [SSP5-8.5] and the period 1960–1999 [historical emission scenario]. Arrows indicate the future change in near-surface wind speed. The contours show the climatology (precipitation average over the period 1960–1999 in AMJJASON). Stippling indicates that the multi-model mean precipitation change is not robust (i.e., not reproduced by at least 75% of the models).

6.3.2 East Africa

6.3.2.1 *Precipitation over East Africa*

Eastern Africa includes Burundi, Djibouti, Eritrea, Ethiopia, Kenya, Rwanda, Somalia, South Sudan, Tanzania, and Uganda. Eastern African countries are highly vulnerable to climate variability and change, experiencing frequent severe droughts (Nicholson, 2017) and floods (Li et al., 2016). Precipitation climatology is heterogeneous. The annual precipitation cycle exhibits a bimodal pattern near the equator between Tanzania, South Sudan, and Ethiopia and a unimodal pattern northwards and southwards. The bimodal cycle is marked by the long rains from March to May, while the short rains last from October to December. Northern Ethiopia, Northern Uganda, and Southern Sudan receive most of their precipitation from July to September (Camberlin, 2018).

The annual precipitation cycle is partly related to the migration of the ITCZ over East Africa (Gamoyo et al., 2015). The movement of the ITCZ is characterized by a seasonal reversal in wind direction from northerlies during December–February to southerlies during July–August. The northward progression of the ITCZ leads to the development of the long rains, while its southward movement contributes to the occurrence of the short rains. However, the ITCZ's migration alone cannot fully explain the variability in East African precipitation. Precipitation variability is underpinned by several factors, including heterogeneous topography, with the Ethiopian and East African highlands contrasting with the coastal plains (Lyon, 2014), lakes, the Congo air mass, and the influence of tropical circulation. Topography affects the low-level atmospheric circulation (Kinuthia, 1992). In the highlands and the Turkana Channel, the flow is concentrated into strong, low-level currents (King et al., 2021; Munday et al., 2023). Additionally, SST variability affects East African precipitation, with, for example, changes in the Indian Ocean (Pohl and Camberlin, 2011; Tierney et al., 2013; Yang et al., 2015) and Pacific Ocean (Lyon, 2014) SSTs driving atmospheric circulation and, subsequently, precipitation. The July–September precipitation over northern Ethiopia, northern Uganda, and South Sudan is attributed to moisture influx from the Congo basin (Camberlin, 2018).

6.3.2.2 Future changes in precipitation over East Africa

Climate change is associated with a future increase in precipitation over most of East Africa, affecting both the long and short rains (Ongoma et al., 2018; Osima et al., 2018; Gebrechorkos et al., 2019; Cook et al., 2020a; Choi et al., 2023) (Fig. 6.2a and Fig. 6.2c). However, we note that the future change in precipitation is not in line with the recently observed trend, with observation showing a decrease in the long rains and the climate models projecting an increase in precipitation over the region (Wainwright et al., 2019). Changes in precipitation are more pronounced for the short rains (Fig. 6.2c) compared to the long rains (Fig. 6.2a). The changes are heterogeneous for the short rains, with precipitation projected to increase over Kenya, Uganda, and Rwanda, but decrease over Tanzania (Fig. 6.2c). The overall increase in East African precipitation is related to both the thermodynamic effects of climate change and the strengthening and shifting of atmospheric circulation (Rowell and Chadwick, 2018).

Predictions of changes in East African precipitation feature a high level of uncertainty, with models showing a wide range of responses (Rowell and Chadwick, 2018) (see the large spread in Figs. 6.2b and 6.2d). The uncertainty in precipitation change is due to differences between models in simulating changes in atmospheric circulation, especially shifts in circulation patterns (Rowell and Chadwick, 2018). Additionally, uncertainty is closely linked to the response of both the increase in SST and the pattern of SST warming, with the direct impact of CO_2 contributing less to uncertainty in precipitation change (Rowell and Chadwick, 2018). The future change in East African precipitation is sensitive to the future change in South Indian SST (Rowell and Chadwick, 2018) and eliminating the models that do not realistically simulate the interannual sensitivity of the South Indian Ocean SST to clouds generates a large reduction in the intermodel spread in March–April–May precipitation change (Rowell, 2019).

In addition to changes in seasonal mean precipitation, climate models indicate significant changes in the distribution of precipitation. The change in precipitation is contrasted during the long rains, with an increase over Kenya, Uganda, and Rwanda, but a decrease over Tanzania (Fig. 6.2b). This aligns with the enhancement in the number of rainy days (> 1 mm d^{-1}) over the northern part of East Africa, with a reduction at its southern margin (Ongoma et al., 2018). The change in the number of rainy days is projected to intensify over time, with a more pronounced effect towards the end of the 21st century compared to the middle of the century (Ongoma et al., 2018). Climate models also

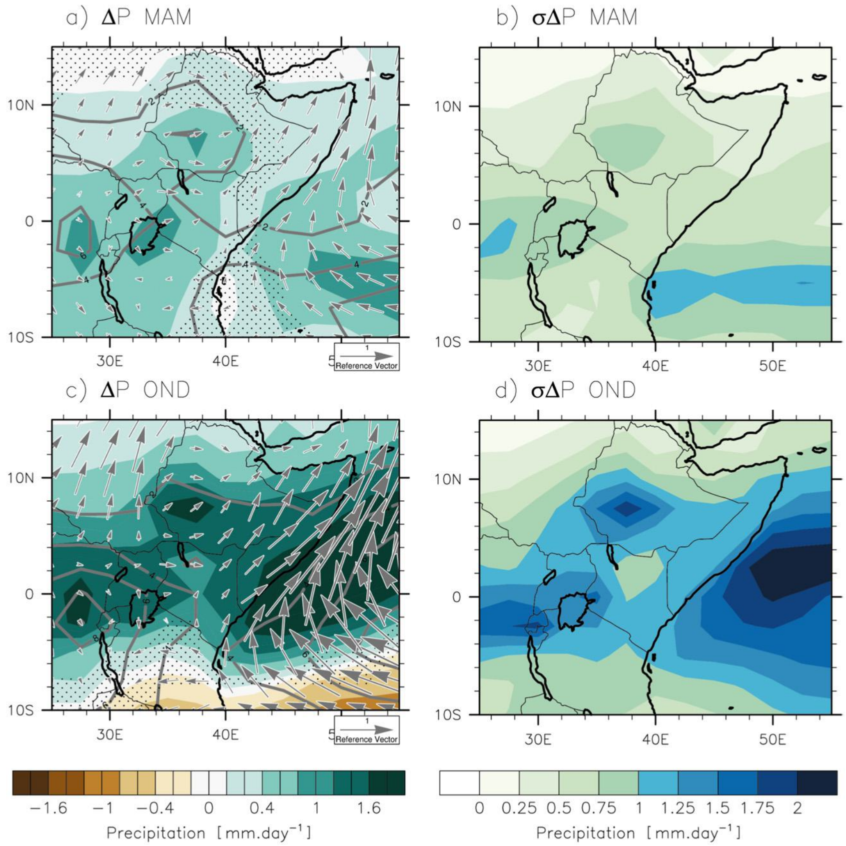

FIGURE 6.2 (a) Effect of climate change on precipitation (multi-model mean) [mm d^{-1}] and (b) uncertainty (ensemble spread) of the effect of climate change on precipitation [mm d^{-1}], in MAM (March–May). (C) and (d) as in (a) and (b) for the change in precipitation in OND (October–December). The effect of climate change is defined as the difference between the period 2060–2099 [SSP5-8.5] and the period 1960–1999 [historical emission scenario]. Arrows indicate the future change in near-surface zonal and meridional wind speed. The contours show the climatology (precipitation average over the period 1960–1999 in MAM and OND). Stippling indicates that the multi-model mean precipitation change is not robust (i.e., not reproduced by at least 75% of the models).

project an increase in rainfall intensity towards the end of the 21st century (Ongoma et al., 2018), with an increase in intense and extreme events, as defined by rainfall events exceeding 10 mm d^{-1}, 20 mm d^{-1}, the 95th and 99th percentiles (Nikulin et al., 2018; Ogega et al., 2020; Ayugi et al., 2021; Li et al., 2021). The shift toward a wetter climate is associated with a decrease in the number of consecutive dry days (Ayugi et al., 2021) and has substantial implications for agricultural yields. Furthermore, precipitation is projected to increase over the northern edge of East Africa (Ethiopia, Sudan) (Gebrechorkos et al., 2019; Choi et al., 2023). This suggests a potential rise in the number of extreme events (Choi et al., 2023), leading to an increased risk of flooding. Conversely, drought frequency, duration, and intensity are projected to increase in Sudan, South Sudan, Somalia, and Tanzania (Haile et al., 2020; Spinoni et al., 2021).

The increased precipitation in January–February, during the dry season, alters the shape of the seasonal cycle. A high-resolution convection-permitting model shows that a warmer climate may lead to a delay in the onset of the short rains, while the onset of the long rains is projected to occur earlier (Wainwright et al., 2021). CMIP5 climate models also show that long rains are projected to start and end earlier, and short rains are projected to start and end later, with no significant change in the length of the rainy season (Dunning et al., 2018). However, Gudoshava et al. (2020) indicate that the short rains are projected to last longer.

6.3.3 Central Africa

6.3.3.1 Precipitation over Central Africa

Central Africa is home to the second largest river basin, the Congo Basin, and tropical forests, playing a crucial role in maintaining the planet's biodiversity and sequestration of carbon. The meridional migration of the ITCZ and the surface conditions influence the processes that generate precipitation over central Africa (e.g., Dezfuli and Nicholson, 2013; Longandjo and Rouault, 2024). The seasonal cycle of precipitation in central Africa is often described as bimodal only. However, studies (e.g., Herrmann and Mohr, 2011; Knoben et al., 2019) have shown that a narrow band (2°–3° wide) located along the equator is characterized by a bimodal seasonal cycle. In the rest of the Congo Basin, there is only one rainy season, with one or two peaks within a single rainy season (Cook and Vizy, 2022). The characteristics of the precipitation seasonal cycle differ between the Northern and Southern Hemispheres. Precipitation is heavy from March to November in the Northern Hemisphere and from October to May in the Southern Hemisphere.

The Congo rainforest fosters the development of atmospheric convection through land-atmosphere feedback and thus plays an important role in the region's climate system (Washington et al., 2013). This influence extends to processes such as soil-moisture recycling (Dyer et al., 2017b; Sorí et al., 2017). Trends in the meridional location of the continental thermal lows and convergence of the circulation of the thermal lows and cross-equatorial flow from the winter hemisphere modulate precipitation variability over the Congo Basin (Cook et al., 2020b). In MAM (March–May) and SON (September–November), a south-easterly flow brings moisture from the southern Indian Ocean (Cook et al., 2020b), while the Atlantic Ocean also serves as a source of moisture for central African precipitation (Cook and Vizy, 2019), although its significance is lower compared to the Indian Ocean. African easterly jets and tropical easterly jets (Farnsworth et al., 2011; Nicholson and Dezfuli, 2013) also influence precipitation. Additionally, topography, such as the highlands of Cameroon and the Rift Valley, influences precipitation patterns by favoring convection through mesoscale development (e.g., Janiga and Thorncroft, 2014).

Variability in Congo Basin precipitation is associated with several factors, such as the phases of the Madden–Julian Oscillation (Laing et al., 2011) and the Atlantic Multidecadal Variability (a decadal mode of variability in North Atlantic SST) (Diem et al., 2014), for example.

It is worth noting that the climate of Central Africa remains poorly understood due to a lack of observational data (Washington et al., 2013). Furthermore, uncertainties persist regarding the drivers of precipitation variability over the region (Cook and Vizy, 2022; Kenfack et al., 2023).

6.3.3.2 *Future changes in precipitation over Central Africa*

Global warming is associated with an increase in precipitation over Central Africa during the wet season (Aloysius et al., 2016; Tamoffo et al., 2023b) (Fig. 6.3a). The future increase in precipitation is associated with both the thermodynamic and dynamic effects of climate change (Tamoffo et al., 2023b), through both an increase in global mean near-surface specific humidity and a change in atmospheric circulation. The projected decrease in precipitation during the dry season (December–February) is linked to increased moisture divergence driven by dynamic effects, specifically changes in circulation. Overall, precipitation is projected to increase during the peak of the wet season, attributed to both dynamic and thermodynamic effects. However, the thermodynamic effect explains a larger proportion of the precipitation increases than the dynamic effect (Tamoffo et al., 2023b).

Climate models show a low consensus on precipitation change over central Africa (Aloysius et al., 2016; Mba et al., 2018). For instance, Fig. 6.3b shows that the ensemble spread in precipitation change can exceed the effect of climate change, defined as the ensemble mean in precipitation change (Fig. 6.3a), calculated across models.

Fotso-Nguemo et al. (2018) and Fotso-Nguemo et al. (2019) demonstrated that the 95th and 99th percentile of rainfall events is projected to increase over southern Chad, northern Cameroon, northern Zambia, and the Great Lakes, based on an ensemble of 20 CMIP5 (Taylor et al., 2012) ocean–atmosphere coupled general circulation models. They suggested that this surge in extreme precipitation events was associated with an increase in moisture convergence, intensifying over the Congo rainforest (Fotso-Nguemo et al., 2018). In addition to extreme events, Fotso-Kamga et al. (2023) illustrated a future increase in precipitation variability, with an overall increase in precipitation intensity and extreme events along with longer dry spells and a decrease in the number of rainy days. These conclusions hold across models and are consistent with 15 regional climate models, showing robustness across models. Similarly, Mboka et al. (2021) predict similar changes in Cameroon using a regional climate model. They highlight a decrease in the number of rainy days and an increase in precip-

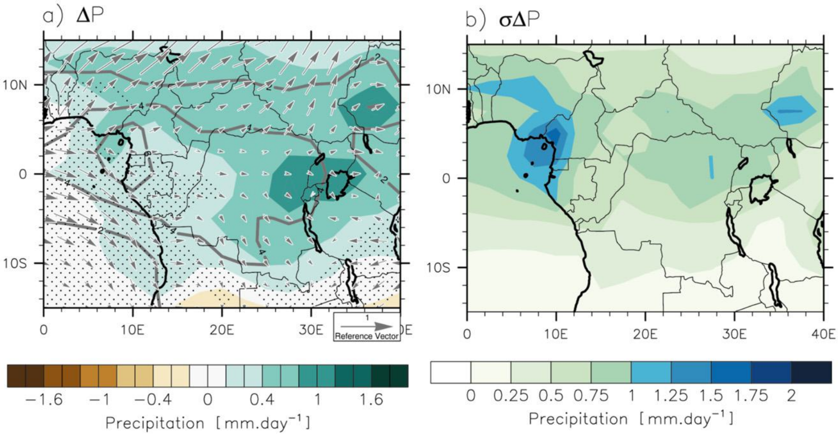

FIGURE 6.3 (a) Effect of climate change on precipitation (multi-model mean) [mm d^{-1}] and (b) Uncertainty (ensemble spread) of the effect of climate change on precipitation [mm d^{-1}], using annual mean. The effect of climate change is defined as the difference between the period 2060–2099 [SSP5-8.5] and the period 1960–1999 [historical emission scenario]. Arrows indicate the future change in near-surface zonal and meridional wind speed. The contours show the climatology (precipitation average over the period 1960–1999). Stippling indicates that the multi-model mean precipitation change is not robust (i.e., not reproduced by at least 75% of the models).

itation intensity and the length of dry spells in the 21st century, consistent with Tamoffo et al. (2023b).

6.3.4 Southern Africa

6.3.4.1 Precipitation over Southern Africa

Southern Africa is a semiarid to arid region that receives most of its precipitation during austral summer (December–January–February–March), except for southwestern South Africa, where precipitation is highest in winter (June–August) (Dieppois et al., 2016). Southern African precipitation is associated with the migration of the ITCZ (Daron et al., 2019) and interactions between the midlatitude and tropical weather systems. These interactions involve variations in the strength and location of the Angola Low (Munday and Washington, 2017; Crétat et al., 2019; Pascale et al., 2019), the Kalahari Low (Taljaard, 1986), the Botswana High (Driver and Reason, 2017), the wind circulation over the Mozambique Channel (Barimalala et al., 2020), and the Tropical Temperate Troughs (Macron et al., 2013). All these features affect wind convergence that transports moisture from the tropical Atlantic and the tropical and southern Indian Oceans.

Southern African precipitation is impacted by changes in SSTs, including El-Nino (La-Nina) events associated with below (above) normal precipitation. Changes in Indian Ocean SST further contribute to Southern African precipitation. Thus, Southern African precipitation varies on several time scales. On interannual timescales, its precipitation is strongly linked to the El Nino Southern Oscillation (ENSO) (e.g., Crétat et al., 2012; Dieppois et al., 2015; Gore et al., 2020; among others). Overland, the variations in the strength and location of the Angola Low modulate the interannual variability of the Southern African precipitation (Munday and Washington, 2017; Crétat et al., 2019; Pascale et al., 2019). On longer time scales (multiannual to decadal), Southern African precipitation variability is strongly modulated by the decadal variability modes, such as the Pacific Decadal Oscillation and the Interdecadal Pacific Oscillation (Dieppois et al., 2016). The decadal variability of Indian Ocean SST also affects Southern African precipitation, including the Subtropical Indian Ocean Dipole (SIOD; Behera and Yamagata, 2001). In addition to SST, changes in atmospheric circulation, such as the Southern Annular Mode and changes in the Hadley circulation, also impact precipitation variability (Malherbe et al., 2014, 2016).

6.3.4.2 Future changes in precipitation over Southern Africa

The externally forced response to anthropogenic activity is associated with a spatially contrasting change in precipitation (Fig. 6.4a). The summer precipitation decreases over Namibia, Angola, Botswana, Lesotho, Mozambique, and western South Africa. Projections show that precipitation may increase towards the end of the 21st century over eastern South Africa, Malawi, and parts of Zambia, following a strengthening of the South Indian Convergence Zone (SICZ) and low-level wind over the Mozambique Channel (Fig. 6.4a). Consistency in these projections has been demonstrated across multiple generations of climate models (Shongwe et al., 2009; Pinto et al., 2016; Pohl et al., 2017; Lazenby et al., 2018; Spinoni et al., 2019).

Changes in precipitation are uncertain and model-dependent, showing poor agreement between models in simulating precipitation changes, particularly during the core of the wet season in the Austral summer (Laprise et al., 2013; Pohl et al., 2017; Munday and Washington, 2019; Almazroui et al., 2020; Dosio et al., 2021; Wu et al., 2024). This uncertainty is illustrated in Fig. 6.4b, where the ensemble spread of inter-model precipitation change is large relative to the multi-model mean (Fig. 6.4a). The uncertainty in simulating the effect of global warming on southern African precipitation is partly related to uncertainties in simulating the changes in SST. For example, differences between climate models in simulating changes in the interhemispheric temperature contrast partly explain differences between models in simulating shifts in the atmospheric circulation over southern Africa (Munday and Washington, 2019). As for the other monsoon domains, uncertainty in precipitation change is also tied to the differences between models in simulating shifts of atmospheric circulation (Lazenby et al., 2018).

While there is a high level of uncertainty regarding changes in seasonal mean precipitation, studies have indicated greater agreement between models when assessing future changes in high-impact weather events (e.g., Pohl et al., 2017;

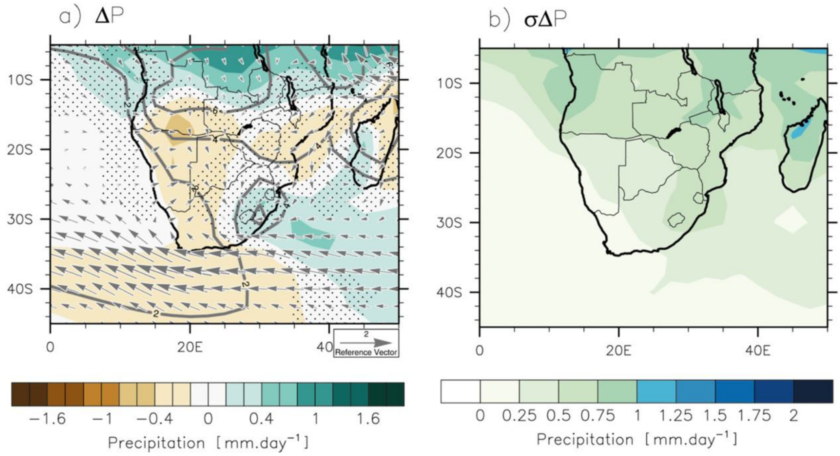

FIGURE 6.4 (a) Effect of climate change on precipitation (multi-model mean) [mm d^{-1}] and (b) uncertainty (ensemble spread) of the effect of climate change on precipitation [mm d^{-1}], in ONDFJM (October-March). The effect of climate change is defined as the difference between the period 2060–2099 [SSP5-8.5] and the period 1960–1999 [historical emission scenario]. Arrows indicate the future change in near-surface zonal and meridional wind speed. The contours show the climatology (precipitation average over the period 1960–1999 in ONDJFM). Stippling indicates that the multi-model mean precipitation change is not robust (i.e., not reproduced by at least 75% of the models).

Ukkola et al., 2020). Specifically, the effect of global warming is more pronounced for changes in the frequency of dry and wet days than seasonal means (Dosio et al., 2019). The increased risk of drought is particularly notable in southern Africa, where climate models consistently project a robust increase in potential evapotranspiration that exceeds the increase in precipitation, leading to an increase in aridity (Hoegh Guldberg et al., 2018; Ukkola et al., 2020). This trend aligns with recent increases in aridity over southern Africa (Bonfils et al., 2020), heightening the likelihood of a new Day Zero drought (Pascale et al., 2020), and multiyear droughts (Zhao and Dai, 2017, 2022; Seneviratne et al., 2021). Unprecedented extreme droughts are projected to occur at a global warming level of 2 °C (Spinoni et al., 2021). Increased aridity is also foreseen in future increases in consecutive dry days (Pinto et al., 2016; Déqué et al., 2017; Maúre et al., 2018) and dry spells (Abiodun et al., 2017).

Projections indicate a potential decrease in the number of rainy days in the future (Abiodun et al., 2017; Pohl et al., 2017), along with a heightened contribution of extreme precipitation events (the 99% percentile precipitation events) to total precipitation (Pohl et al., 2017), potentially leading to an increase in precipitation daily variability. The change in heavy precipitation exhibits spatial contrast, aligning with changes in seasonal mean precipitation: decreasing in western parts and increasing in eastern and northern parts of southern Africa (Pinto et al., 2016; Li et al., 2021; Seneviratne et al., 2021).

Simulations indicate that the timing of the monsoon season could be affected by global warming. Climate models project a delay in the onset and cessation dates of the monsoon season over Zambia, Malawi, Northern Mozambique, and Zimbabwe (Shongwe et al., 2009; Déqué et al., 2017), suggesting a temporal shift in the monsoon season. Conversely, over most of South Africa, Botswana, southern Mozambique and Zimbabwe, and Lesotho and Eswatini, climate models project a delayed onset and earlier cessation, suggesting a shortening of the monsoon season (Dunning et al., 2018).

6.4 Cloud–aerosol-precipitation feedback

6.4.1 Brief description of the feedback between aerosol loading, cloud cover, and precipitation

Cloud variability and patterns are linked to atmospheric circulation and orography (Dommo et al., 2018), exerting strong effects that lead to precipitation and modulate incoming solar and outgoing longwave radiation, surface temperature, and the Earth's atmospheric general circulation (Danso et al., 2019). Interactions between aerosols and clouds are notable, where aerosols act as cloud condensation nuclei and ice nuclei, inducing changes in cloud droplets, particle number, and size (e.g., Knippertz et al., 2015; Deetz et al., 2018; Huang et al., 2019). Aerosols subsequently influence cloud lifetime and cloud albedo, causing an impact on radiation. Moreover, aerosols can directly perturb the heat budget by scattering shortwave radiation back into space, thereby, locally altering surface shortwave radiation (Hui et al., 2008; Collins et al., 2017; Kok et al., 2023). Black carbon (BC) aerosols absorb solar radiation and can affect the hydrological cycle through changes in the atmospheric and surface-energy budgets (Hodnebrog et al., 2016).

Anthropogenic emissions play a significant role in climate alteration by influencing sea surface temperatures, land temperature, and atmospheric adjustments (Hirasawa et al., 2022). Various pollutants, such as SO_2 and black carbon, associated with anthropogenic aerosols, have demonstrated impacts on both the amount and variability of precipitation (Wang et al., 2009, 2019; Ackerley et al., 2011; Bollasina et al., 2011; Hwang et al., 2013; Polson et al., 2014; Komkoua Mbienda et al., 2017; Giannini and Kaplan, 2019; Saha and Ghosh, 2019; Herman et al., 2020; Marvel et al., 2020; Westervelt et al., 2020; Ayantika et al., 2021; Sherman et al., 2021).

Changes in dust levels have also been found to be linked to changes in precipitation (Evan et al., 2016). Dust, by influencing incoming solar radiation and affecting monsoon dynamics, has a notable impact on monsoon systems (Bercos-Hickey et al., 2022; Bangalath et al., 2023). However, dust emissions are interconnected with variations in wind strength, precipitation amount, and soil conditions (Harrison et al., 2001; Kim et al., 2017; Zhao et al., 2022). Dust aerosols can inhibit precipitation by increasing the number of cloud condensation nuclei (Hui et al., 2008; Zhao et al., 2011) and impact monsoon dynamics by cooling the Sahara and reducing the meridional gradient of moist static energy (Konare et al., 2008). Dust loading primarily originates from the Sahara Desert (Zhao et al., 2022) and mainly affects the West African monsoon. However, it is noteworthy that mineral dust can also impact the climate in southern Africa (e.g., Bryant et al., 2007).

Biomass burning strongly influences the climate of the African continent (Cachier and Ducret, 1991; Abel et al., 2005; Ichoku et al., 2016; Menut et al., 2018). According to Hodnebrog et al. (2016), biomass burning is the main contributor to the recent drying trend in southern Africa. Furthermore, African biomass burning is transported across the Atlantic Ocean impacting the climate in the Amazon rainforest (Holanda et al., 2023).

6.4.2 Future change in aerosols and its role in African precipitation

Aerosol forcing and cloud–radiation interactions contribute significantly to the uncertainty in general circulation models (Soden and Held, 2006; Boucher et al., 2013; Dolinar et al., 2015). Differences in model formulations, including their representations of aerosol–cloud interactions and aerosol-radiation interactions, as well as variations in anthropogenic aerosol radiative forcing, could introduce uncertainty in the effects of anthropogenic factors (Wilcox et al., 2013, 2015; Myhre et al., 2014). Consequently, the impact of aerosols on monsoon precipitation is model-dependent (e.g., Monerie et al., 2022). This has significant implications for simulating events with societal consequences, such as the prolonged drought that affected the Sahel region in the 1970s and 1980s (Monerie et al., 2023b). In addition, model differences in simulating dust concentration and pattern also serve as a source of uncertainty in simulating climate (Zhao et al., 2022) and monsoon dynamics (Bercos-Hickey et al., 2017). Additionally, there is evidence of model biases in the simulation of biomass-burning aerosols (Brown et al., 2021) and their impacts on climate (e.g., Mallet et al., 2021).

Tang et al. (2019) and Sawadogo et al. (2021) demonstrated that cloud cover is expected to decrease over southern Africa by the end of the 21st century, based on various general circulation models and regional climate models. This reduction aligns with a projected decrease in precipitation by the end of the 21st century. In addition, Sawadogo et al. (2021) showed that, by the end of the 21st century, cloud cover may decrease over northern Africa, while an increase in cloud cover is expected over central Africa and parts of East Africa for the medium-term horizon (2041–2060).

The loading of anthropogenic aerosols varies depending on the emissions scenario (Lund et al., 2019). This variability may result in uncertain changes in precipitation and cloud cover over Africa (Lin et al., 2018; Wells et al., 2023). For instance, Wells et al. (2023) show that uncertainty in the future changes in biomass burning and SO_2 emissions could significantly impact the climate of Africa. The rise in non-biomass burning emissions, such as organic carbon and black carbon, is linked to a reduction in net downwards surface shortwave radiation over Africa, resulting in cooling along the equator and a spatially contrasting shift in precipitation. A decrease in biomass burning emissions is associated with an increase in net downwards surface shortwave radiation over central and southern Africa (Wells et al., 2023). This leads to an increase in temperature but only a moderate change in precipitation (Wells et al., 2023). The Regional Aerosol Model Intercomparison Project (RAMIP; Wilcox et al., 2022) provides insight into the effects of various pathways in anthropogenic aerosol emissions. Wilcox et al. (2022) evaluated the impact of significant variations in future anthropogenic aerosol changes over Africa, Asia, and Europe using three general circulation models. The study demonstrates that the uncertainty in the future evolution of anthropogenic aerosols has a significant effect on the future precipitation changes over Africa. However, it is important to note that changes in precipitation are model-dependent, with one model simulating an increase in precipitation over northern Africa, while another model simulates a decrease in precipitation over the same region (Wilcox et al., 2022). These changes are attributed to a strong shift in anthropogenic aerosols across Africa (Wilcox et al., 2022).

The uncertainty surrounding changes in mineral dust is due to model dependence, as noted by Kok et al. (2023). Mousavi et al. (2023) found a projected decrease in dust loadings over northern Africa and the Middle East by the end of the 21st century, using general circulation models. Similarly, Evan et al. (2016) showed a future decrease in mineral dust aerosol optical depth in Cape Verde. However, Woodward et al. (2005) demonstrated that atmospheric dust load is projected to increase globally by 2100. Additionally, Ji et al. (2018) used regional climate models to demonstrate a future increase in dust loading. The impact of the change in mineral dust emission on African precipitation remains unclear. However, future changes in dust loading may have a strong impact on global temperature and precipitation. For instance, Ji et al. (2018) conducted simulations using a regional climate model to examine the impact of changes in dust emissions under a high-emissions scenario (RCP8.5). They found that an increase in mineral dust loading can lead to a reduction in warming. The impact of the dust also affects future precipitation patterns, with an increase in precipitation over the northern part of West Africa (5–20%) and a decrease over the southern part (5–20%).

6.5 Summary

We provide a summary of findings from numerous authors, detailed in Section 6.3. Our focus encompasses changes in seasonal mean precipitation, the number of precipitation events, high-impact extreme weather events (including extreme precipitation events and drought changes), and changes in the onset and end dates of the monsoon, all of which have strong societal impacts. The summarized results can be found in Table 6.1.

List of models used in this chapter is given in Table 6.2.

TABLE 6.1 Summary of the predicted future changes in monsoon precipitation across Africa for the end of the 21st century.

	Seasonal mean precipitation	Number of rainy events	Extreme precipitation events	Changes in onset / cessation dates
West Africa	Decrease in precipitation over Senegal/West Mali Increase in precipitation over eastern Mali, Chad, Niger, Sudan No strong changes over the coast (from Guinea to Nigeria)	*General circulation models*: Increase in the number of rainy days in the central and eastern Sahel. Decrease in the number of rainy days in the western Sahel Decrease in the number of rainy events over the Guinea coast *Regional circulation models*: Decrease in the number of rainy days over a large part of West Africa	Increase in the intensity of the extreme rainy events over the Guinea coast, the central and eastern Sahel, and a decrease over the western Sahel	Delay of the onset and shortening of the rainy season over the Sahel, except in the central region Delay of the onset dates over the Guinea coast, delay in the cessation dates over the western Guinea coast, and shortening of the rainy season over the westernmost and eastern regions of the Guinea coast
East Africa	Increase in precipitation over most of East Africa for both the long rains and short rains. Decrease in precipitation over Tanzania during the short rains.	Increase in the number of rainy days over most of East Africa; decrease over the southern East Africa	Increase in rainfall intensity and strong and extreme events Increase in drought frequency	Delayed onset of the short rains The onset of the long rains is projected to occur earlier

continued on next page

TABLE 6.1 (*continued*)

	Seasonal mean precipitation	Number of rainy events	Extreme precipitation events	Changes in onset / cessation dates
Central Africa	Increase in precipitation in summer Decrease in precipitation during the dry season	Decrease in the number of rainy days (increase in precipitation intensity)	Increase in intensity of the extreme precipitation events over southern Chad, northern Cameroon, northern Zambia, and the Great Lakes	No clear/mentioned changes in onset and cessation dates of the monsoon
Southern Africa	Decrease in precipitation over Namibia, Angola, Botswana, Lesotho, and western South Africa. Precipitation increases over eastern South Africa, Malawi, and Mozambique	Decrease in the number of rainy days	Contrasted changes in heavy and extreme precipitation that follow the change in seasonal mean precipitation Particularly strong increase in drought risk	Delay in the onset and cessation dates of the monsoon season over Zambia, Malawi, northern, Mozambique, and Zimbabwe. Delayed onset and earlier cessation over most of South Africa, Botswana, southern Mozambique, and Zimbabwe, Lesotho and Eswatini, indicating a shortening of the monsoon season.

6.6 Future prospects

Future changes in precipitation, including seasonal means, extreme events, and frequency of precipitation events, remain uncertain across Africa (e.g., Seneviratne et al., 2021). Reducing uncertainty about future precipitation changes is essential to inform decision-makers about the impacts of climate change and

TABLE 6.2 List of models used in this chapter.

Model	Institution	Resolution	Reference
ACCESS-CM2	Australian Community Climate and Earth System Model. Australia.	144 x 192	Ziehn et al. (2020)
ACCESS-ESM1-5	Australian Community Climate and Earth System Model. Australia.	145 x 192	Ziehn et al. (2020)
AWI-CM-1-1-MR	Alfred Wegener Institute, Germany	192 x 384	Semmler et al. (2020)
BCC-CSM2-MR	Beijing Climate Center, China.	160 x 320	Shi et al. (2020)
BCC-ESM1	Beijing Climate Center, China.	64 x 128	Shi et al. (2020)
CAMS-CMS1-0	Chinese Academy of Meteorological Sciences, China.	160 x 320	Rong et al. (2021)
CanESM5	Canadian Centre for Climate Modelling and Analysis, Canada.	64 x 128	Swart et al. (2019)
CAS-ESM2-0	Chinese Academy of Sciences, China	128 x 256	Dong et al. (2021)
CIESM	Tsinghua University, China.	192 x 288	Lin et al. (2020)
CMCC-CM2-SR5	Fondazione Centro Euro-Mediterraneo sui Cambiamenti Climatici, Italy	192 x 288	Cherchi et al. (2019)
CMCC-ESM2	Fondazione Centro Euro-Mediterraneo sui Cambiamenti Climatici, Italy	192 x 288	Lovato et al. (2022)
CNRM-CM6	Centre National de Recherches Météorologiques/Centre Européen de Recherche et de Formation Avancée en Calcul Scientifique. France	128 x 256	Voldoire et al. (2019)
CNRM-CM6-1-HR	Centre National de Recherches Météorologiques/Centre Européen de Recherche et de Formation Avancée en Calcul Scientifique. France	360 x 720	Voldoire et al. (2019)

continued on next page

TABLE 6.2 (*continued*)

Model	Institution	Resolution	Reference
CNRM-ESM2-1	Centre National de Recherches Météorologiques/Centre Européen de Recherche et de Formation Avancée en Calcul Scientifique. France	128 x 256	Séférian et al. (2019)
EC-EARTH3	EC-Earth-Consortium.	256 x 512	Wyser et al. (2020)
EC-EARTH3-VEG	EC-Earth-Consortium.	256 x 512	Wyser et al. (2020)
E3SM-1-1	E3SM-Project	180 x 360	Golaz et al. (2019)
FGOALS-F3-L	Chinese Academy of Sciences. China.	180 x 288	Li et al. (2020)
FGOALS-G3	Chinese Academy of Sciences, China.	180 x 288	Li et al. (2020)
FIO-ESM2-0	First Institute of Oceanography, China.	192 x 288	Li et al. (2019)
GFDL-CM4	Geophysical Fluid Dynamics Laboratory/NOAA, USA	180 x 288	Held et al. (2019)
GFDL-ESM4	Geophysical Fluid Dynamics Laboratory/NOAA, USA	180 x 288	Dunne et al. (2020)
GISS-E2-1-G	Goddard Institute for Space Studies, USA.	90 x 144	Kelley et al. (2020)
GISS-E2-1-H	Goddard Institute for Space Studies. USA.	90 x 144	Kelley et al. (2020)
HADGEM3-GC31-LL	Met Office Hadley Centre. UK.	144 x 192	Kuhlbrodt et al. (2018)
HADGEM-GC31-MM	Met Office Hadley Centre, UK.		Kuhlbrodt et al. (2018)
INM-CM4-8	Institute for Numerical Mathematics, Russia	120 x 180	Volodin et al. (2018)
INM-CM5-0	Institute for Numerical Mathematics, Russia	120 x 180	Volodin et al. (2017)
IITM-ESM	Centre for Climate Change Research, Indian Institute of Tropical Meteorology, India	94 x 192	Swapna et al. (2018)
IPSL-CM6-A-LR	Institut Pierre Simon Laplace, France.	144 x 143	Boucher et al. (2020)

TABLE 6.2 (*continued*)

Model	Institution	Resolution	Reference
KACE-1-0-G	National Institute of Meteorological Sciences, Korea Meteorological Administration, Korea	144 x 192	Lee et al. (2020)
MCM-UA	University of Arizona, USA	96 x 80	Delworth et al. (2002)
MIROC6	Japan Agency for Marine-Earth Science and Technology, Japan	128 x 256	Tatebe et al. (2019)
MPI-ESM1-2-LR	Max Planck Institute Earth System, Germany	96 x 192	Mauritsen et al. (2019)
MRI-ESM2-0	Meteorological Research Institute, Japan	160 x 320	Yukimoto et al. (2019)
MPI-ESM1-2-HR	Deutsches Klimarechenzentrum, Germany	192 x 384	Müller et al. (2018)
NESM3	Nanjing University of Information Science and Technology, China	96 x 192	Cao et al. (2018)
NORESM2-MM	NorESM Climate modeling Consortium, Norway.	192 x 288	Seland et al. (2020)
UKESM-1-0-LL	Met Office Hadley Centre, UK.	192 x 144	Mulcahy et al. (2020)

facilitate the development of African countries. Here, we identify some key directions for improving our understanding of the changes ahead.

6.6.1 Biases and model horizontal and vertical resolution

Climate models exhibit systematic biases, undermining confidence in climate projections. For instance, precipitation is normally underestimated over West Africa, with a monsoon system that lacks sufficient northward shift in summer (Monerie et al., 2020b) and overestimated over Southern Africa (Munday and Washington, 2018). We propose that enhancing the representation of monsoon dynamics and thus precipitation in climate models can boost confidence in climate projections.

One issue with the CMIP6 atmosphere–ocean general circulation models is their horizontal and vertical resolution, which necessitates the parameterization of precipitation. This limitation prevents models from reliably simulating fine-scale and mesoscale processes (Dosio et al., 2021). Numerous efforts have been undertaken to improve the horizontal and vertical resolution of the climate models. One approach to improve simulations is to dynamically downscale the projections of general circulation models by means of regional climate models (e.g., the CORDEX projects; Giorgi and Gutowski, 2015; Tamoffo et al., 2019b,a, 2024; Akinsanola et al., 2020). This results in a finer horizontal grid of 50 km (CORDEX) and 25 km (CORDEX-CORE—Coordinated Output of Regional Evaluations; Giorgi et al., 2021). Authors have reported improvements in the simulation of precipitation characteristics (e.g., Gibba et al., 2019; Akinsanola and Zhou, 2019). However, biases remain (Olusegun et al., 2022) and improvements are not homogeneous across key seasonal climate features (Gnitou et al., 2021). Furthermore, dynamical downscaling could lead to increased uncertainty due to inconsistencies between general and regional circulation models (Saini et al., 2015). The validity of this argument is reinforced by a recent study conducted by Tamoffo et al. (2024), which demonstrated that dynamically downscaling a general circulation model through a coupled regional climate model, while accounting for consistency between the physics of the regional and general circulation models, significantly adds value over Central Africa.

A limitation of CORDEX and CORDEX-CORE is that the climate models still need to parameterize sub-grid scale processes, including convection. This challenge has spurred the development of convective permitting simulations, such as, for instance, the recent development of the “CP4-Africa” simulations (Stratton et al., 2018; Kendon et al., 2019), conducted with a 4.5-km grid spacing. The results have shown an improvement in the representation of West African monthly and hourly precipitation features compared to 25 km simulations and when compared to observations (Berthou et al., 2019; Kendon et al., 2019). Notable differences exist between projections from general circulation models and convection-permitting models. For instance, convection-permitting climate models simulate a future increase in the length of dry spells over central Africa, a feature not apparent at coarser resolutions (Stratton et al., 2018). However, due to the high computational cost of convective-permitting simulations, large ensembles cannot be simulated, leading to strong limitations in quantifying the impact of climate change on African monsoon precipitation.

Another limitation is the availability of observations to assess the ability of the models to simulate precipitation across Africa. An example is the number of rain gauges, which has significantly decreased over the Congo Basin since the 1980s (Washington et al., 2013).

6.6.2 Identifying sources of precipitation changes uncertainty

Monerie et al. (2016b) demonstrated that there are no simple relationships between model biases and projections: model improvements have not led to a reduction in the intermodel spread in precipitation change. Another way to reduce uncertainty is therefore to identify sources of uncertainty in precipitation changes such as model differences, internal climate variability, and differences in emissions scenarios (Hawkins and Sutton, 2011). While there are a moderate number of studies pointing to sources of uncertainty in African monsoon precipitation changes, focusing on model differences (e.g., Park et al., 2015; Lazenby et al., 2018; Rowell and Chadwick, 2018; Monerie et al., 2020b, 2023a; Bellomo et al., 2021; Guilbert et al., 2024) and internal climate variability (e.g., Monerie et al., 2017), further analysis in this direction could contribute to understanding future changes in precipitation by providing future plausible trajectories of precipitation change (e.g., Monerie et al., 2023a). Such studies can inform impact studies. Additionally, such analyses may help reduce uncertainty in future precipitation change by identifying drivers of uncertainty, whose future changes could be constrained using an observational or emergent constraint framework (Chen et al., 2022).

Data availability statement

CMIP6 GCM output is available from public repositories, including https://esgf-index1.ceda.ac.uk/search/cmip6-ceda/.

Acknowledgments

We acknowledge the World Climate Research Programme, which, through its Working Group on Coupled Modelling, coordinated and promoted CMIP6. We thank the climate modeling groups for producing and making available their model output, the Earth System Grid Federation (ESGF) for archiving the data and providing access, and the multiple funding agencies who support CMIP6 and ESGF.

References

Abel, S.J., Highwood, E.J., Haywood, J.M., Stringer, M.A., 2005. The direct radiative effect of biomass burning aerosols over southern Africa. Atmos. Chem. Phys. 5, 1999–2018. https://doi.org/10.5194/acp-5-1999-2005.

Abiodun, B.J., Adegoke, J., Abatan, A.A., et al., 2017. Potential impacts of climate change on extreme precipitation over four African coastal cities. Clim. Change 143, 399–413. https://doi.org/10.1007/s10584-017-2001-5.

Ackerley, D., Booth, B.B.B., Knight, S.H.E., et al., 2011. Sensitivity of twentieth-century Sahel rainfall to sulfate aerosol and CO2 forcing. J. Climate 24, 4999–5014. https://doi.org/10.1175/JCLI-D-11-00019.1.

Adejuwon, J.O., Odekunle, T.O., 2006. Variability and the severity of the “Little Dry Season” in Southwestern Nigeria. J. Climate 19, 483–493. https://doi.org/10.1175/JCLI3642.1.

Akinsanola, A.A., Zhou, W., 2018. Ensemble-based CMIP5 simulations of West African summer monsoon rainfall: current climate and future changes. Theor. Appl. Climatol. https://doi.org/10.1007/s00704-018-2516-3.

Akinsanola, A.A., Zhou, W., 2019. Projection of West African summer monsoon rainfall in dynamically downscaled CMIP5 models. Clim. Dyn. 53, 81–95. https://doi.org/10.1007/s00382-018-4568-6.

Akinsanola, A.A., Zhou, W., Zhou, T., Keenlyside, N., 2020. Amplification of synoptic to annual variability of West African summer monsoon rainfall under global warming. npj Clim. Atmos. Sci. 3 (21). https://doi.org/10.1038/s41612-020-0125-1.

Almazroui, M., Saeed, F., Saeed, S., et al., 2020. Projected change in temperature and precipitation over Africa from CMIP6. Earth Syst. Environ. https://doi.org/10.1007/s41748-020-00161-x.

Aloysius, N.R., Sheffield, J., Saiers, J.E., et al., 2016. Evaluation of historical and future simulations of precipitation and temperature in central Africa from CMIP5 climate models. J. Geophys. Res., Atmos. 121, 130–152. https://doi.org/10.1002/2015JD023656.

Ayantika, D.C., Krishnan, R., Singh, M., et al., 2021. Understanding the combined effects of global warming and anthropogenic aerosol forcing on the South Asian monsoon. Clim. Dyn. https://doi.org/10.1007/s00382-020-05551-5.

Ayugi, B., Dike, V., Ngoma, H., et al., 2021. Future changes in precipitation extremes over East Africa based on CMIP6 models. Water 13.

Bamba, A., Dieppois, B., Konaré, A., et al., 2015. Changes in vegetation and rainfall over West Africa during the last three decades (1981-2010). Atmos. Clim. Sci. 5, 367–379.

Bangalath, H.K., Raj, J., Stenchikov, G., 2023. Sensitivity of African easterly waves to dust forcing. J. Geophys. Res., Atmos. 128, e2023JD038656. https://doi.org/10.1029/2023JD038656.

Barimalala, R., Blamey, R.C., Desbiolles, F., Reason, C.J.C., 2020. Variability in the Mozambique Channel trough and impacts on Southeast African rainfall. J. Climate 33, 749–765. https://doi.org/10.1175/JCLI-D-19-0267.1.

Behera, S.K., Yamagata, T., 2001. Subtropical SST dipole events in the southern Indian Ocean. Geophys. Res. Lett. 28, 327–330. https://doi.org/10.1029/2000GL011451.

Bellomo, K., Angeloni, M., Corti, S., von Hardenberg, J., 2021. Future climate change shaped by inter-model differences in Atlantic meridional overturning circulation response. Nat. Commun. 12, 3659. https://doi.org/10.1038/s41467-021-24015-w.

Bercos-Hickey, E., Nathan, T.R., Chen, S-H., 2022. Effects of Saharan dust aerosols and West African precipitation on the energetics of African easterly waves. J. Atmos. Sci. 79, 1911–1926. https://doi.org/10.1175/JAS-D-21-0157.1.

Bercos-Hickey, E., Nathan, T.R., Chen, S-H., 2017. Saharan dust and the African easterly jet–African easterly wave system: structure, location and energetics. Q. J. R. Meteorol. Soc. 143, 2797–2808. https://doi.org/10.1002/qj.3128.

Berthou, S., Rowell, D.P., Kendon, E.J., et al., 2019. Improved climatological precipitation characteristics over West Africa at convection-permitting scales. Clim. Dyn. 53, 1991–2011. https://doi.org/10.1007/s00382-019-04759-4.

Biasutti, M., 2013. Forced Sahel rainfall trends in the CMIP5 archive. J. Geophys. Res., Atmos. 118, 1613–1623. https://doi.org/10.1002/jgrd.50206.

Biasutti, M., 2019. Rainfall trends in the African Sahel: characteristics, processes, and causes. WIREs Clim. Chang. 10, e591. https://doi.org/10.1002/wcc.591.

Biasutti, M., Voigt, A., Boos, W.R., et al., 2018. Global energetics and local physics as drivers of past, present and future monsoons. Nat. Geosci. 11, 392–400. https://doi.org/10.1038/s41561-018-0137-1.

Bollasina, M.A., Ming, Y., Ramaswamy, V., 2011. Anthropogenic aerosols and the weakening of the South Asian summer monsoon. Science (80-) 334 (334), 502–505. https://doi.org/10.1126/science.1204994.

Bonfils, C.J.W., Santer, B.D., Fyfe, J.C., et al., 2020. Human influence on joint changes in temperature, rainfall and continental aridity. Nat. Clim. Change 10, 726–731. https://doi.org/10.1038/s41558-020-0821-1.

Boucher, O., Randall, D., Artaxo, P., et al., 2013. Climate change 2013: the physical science basis. Contribution of Working Group I to the Fifth Assessment Report of the Intergovernmental Panel on Climate Change. In: Tignor, M., Allen, S.K., Boschung, J., Nauels, A., Xia, Y., Bex, V., Midgley, P.M. (Eds.). Cambridge Univ Press, Cambridge, UK.

Boucher, O., Servonnat, J., Albright, A.L., et al., 2020. Presentation and evaluation of the IPSL-CM6A-LR climate model. J. Adv. Model. Earth Syst. 12, e2019MS002010. https://doi.org/10.1029/2019MS002010.

Brown, H., Liu, X., Pokhrel, R., et al., 2021. Biomass burning aerosols in most climate models are too absorbing. Nat. Commun. 12, 277. https://doi.org/10.1038/s41467-020-20482-9.

Bryant, R.G., Bigg, G.R., Mahowald, N.M., et al., 2007. Dust emission response to climate in southern Africa. J. Geophys. Res., Atmos. 112. https://doi.org/10.1029/2005JD007025.

Cachier, H., Ducret, J., 1991. Influence of biomass burning on equatorial African rains. Nature 352, 228–230. https://doi.org/10.1038/352228a0.

Camberlin, P., 2018. Climate of Eastern Africa.

Cao, J., Wang, B., Yang, Y-M., et al., 2018. The NUIST Earth System Model~(NESM) version 3: description and preliminary evaluation. Geosci. Model Dev. 11, 2975–2993. https://doi.org/10.5194/gmd-11-2975-2018.

Chadwick, R., Good, P., Willett, K., 2016. A simple moisture advection model of specific humidity change over land in response to SST warming. J. Climate 29, 7613–7632. https://doi.org/10.1175/JCLI-D-16-0241.1.

Chen, Z., Zhou, T., Chen, X., et al., 2022. Observationally constrained projection of Afro-Asian monsoon precipitation. Nat. Commun. 13, 2552. https://doi.org/10.1038/s41467-022-30106-z.

Cherchi, A., Fogli, P.G., Lovato, T., et al., 2019. Global mean climate and main patterns of variability in the CMCC-CM2 coupled model. J. Adv. Model. Earth Syst. 11, 185–209. https://doi.org/10.1029/2018MS001369.

Choi, Y-W., Campbell, D.J., Eltahir, E.A.B., 2023. Near-term regional climate change in East Africa. Clim. Dyn. 61, 961–978. https://doi.org/10.1007/s00382-022-06591-9.

Collins, W.J., Lamarque, J-F., Schulz, M., et al., 2017. AerChemMIP: quantifying the effects of chemistry and aerosols in CMIP6. Geosci. Model Dev. 10, 585–607. https://doi.org/10.5194/gmd-10-585-2017.

Cook, K.H., Fitzpatrick, R.G.J., Liu, W., Vizy, E.K., 2020a. Seasonal asymmetry of equatorial East African rainfall projections: understanding differences between the response of the long rains and the short rains to increased greenhouse gases. Clim. Dyn. 55, 1759–1777. https://doi.org/10.1007/s00382-020-05350-y.

Cook, K.H., Liu, Y., Vizy, E.K., 2020b. Congo Basin drying associated with poleward shifts of the African thermal lows. Clim. Dyn. 54, 863–883. https://doi.org/10.1007/s00382-019-05033-3.

Cook, K.H., Vizy, E.K., 2019. Contemporary climate change of the African monsoon systems. Curr. Clim. Change Rep. 5, 145–159. https://doi.org/10.1007/s40641-019-00130-1.

Cook, K.H., Vizy, E.K., 2022. Hydrodynamics of regional and seasonal variations in Congo Basin precipitation. Clim. Dyn. 59, 1775–1797. https://doi.org/10.1007/s00382-021-06066-3.

Crétat, J., Pohl, B., Dieppois, B., et al., 2019. The Angola Low: relationship with southern African rainfall and ENSO. Clim. Dyn. 52, 1783–1803. https://doi.org/10.1007/s00382-018-4222-3.

Crétat, J., Richard, Y., Pohl, B., et al., 2012. Recurrent daily rainfall patterns over South Africa and associated dynamics during the core of the austral summer. Int. J. Climatol. 32, 261–273. https://doi.org/10.1002/joc.2266.

Danso, D.K., Anquetin, S., Diedhiou, A., et al., 2019. Spatio-temporal variability of cloud cover types in West Africa with satellite-based and reanalysis data. Q. J. R. Meteorol. Soc. 145, 3715–3731. https://doi.org/10.1002/qj.3651.

Daron, J., Burgin, L., Janes, T., et al., 2019. Climate process chains: examples from southern Africa. Int. J. Climatol. 39, 4784–4797. https://doi.org/10.1002/joc.6106.

Deetz, K., Vogel, H., Knippertz, P., et al., 2018. Numerical simulations of aerosol radiative effects and their impact on clouds and atmospheric dynamics over southern West Africa. Atmos. Chem. Phys. 18, 9767–9788. https://doi.org/10.5194/acp-18-9767-2018.

Delworth, T., Stouffer, R., Dixon, K., et al., 2002. Review of simulations of climate variability and change with the GFDL R30 coupled climate model. Clim. Dyn. 19, 555–574. https://doi.org/10.1007/s00382-002-0249-5.

Déqué, M., Calmanti, S., Christensen, O.B., et al., 2017. A multi-model climate response over tropical Africa at +2 °C. Clim. Serv. 7, 87–95. https://doi.org/10.1016/j.cliser.2016.06.002.

Dezfuli, A.K., Nicholson, S.E., 2013. The relationship of rainfall variability in Western Equatorial Africa to the tropical oceans and atmospheric circulation. Part II: The boreal autumn. J. Climate 26, 66–84. https://doi.org/10.1175/JCLI-D-11-00686.1.

Diallo, I., Giorgi, F., Deme, A., et al., 2016. Projected changes of summer monsoon extremes and hydroclimatic regimes over West Africa for the twenty-first century. Clim. Dyn. 47, 3931–3954. https://doi.org/10.1007/s00382-016-3052-4.

Diem, J.E., Ryan, S.J., Hartter, J., Palace, M.W., 2014. Satellite-based rainfall data reveal a recent drying trend in central equatorial Africa. Clim. Change 126, 263–272. https://doi.org/10.1007/s10584-014-1217-x.

Dieppois, B., Pohl, B., Rouault, M., et al., 2016. Interannual to interdecadal variability of winter and summer southern African rainfall, and their teleconnections. J. Geophys. Res., Atmos. 121, 6215–6239. https://doi.org/10.1002/2015JD024576.

Dieppois, B., Rouault, M., New, M., 2015. The impact of ENSO on Southern African rainfall in CMIP5 ocean atmosphere coupled climate models. Clim. Dyn. 45, 2425–2442. https://doi.org/10.1007/s00382-015-2480-x.

Dolinar, E.K., Dong, X., Xi, B., et al., 2015. Evaluation of CMIP5 simulated clouds and TOA radiation budgets using NASA satellite observations. Clim. Dyn. 44, 2229–2247. https://doi.org/10.1007/s00382-014-2158-9.

Dommo, A., Philippon, N., Vondou, D.A., et al., 2018. The June–September low cloud cover in Western Central Africa: mean spatial distribution and diurnal evolution, and associated atmospheric dynamics. J. Climate 31, 9585–9603. https://doi.org/10.1175/JCLI-D-17-0082.1.

Dong, X., Jin, J., Liu, H., et al., 2021. CAS-ESM2.0 model datasets for the CMIP6 Ocean Model Intercomparison Project Phase 1 (OMIP1). Adv. Atmos. Sci. 38, 307–316. https://doi.org/10.1007/s00376-020-0150-3.

Dosio, A., Jones, R.G., Jack, C., et al., 2019. What can we know about future precipitation in Africa? Robustness, significance and added value of projections from a large ensemble of regional climate models. Clim. Dyn. 53, 5833–5858. https://doi.org/10.1007/s00382-019-04900-3.

Dosio, A., Jury, M.W., Almazroui, M., et al., 2021. Projected future daily characteristics of African precipitation based on global (CMIP5, CMIP6) and regional (CORDEX, CORDEX-CORE) climate models. Clim. Dyn. 57, 3135–3158. https://doi.org/10.1007/s00382-021-05859-w.

Driver, P., Reason, C.J.C., 2017. Variability in the Botswana High and its relationships with rainfall and temperature characteristics over southern Africa. Int. J. Climatol. 37, 570–581. https://doi.org/10.1002/joc.5022.

Dunne, J.P., Horowitz, L.W., Adcroft, A.J., et al., 2020. The GFDL Earth System Model Version 4.1 (GFDL-ESM 4.1): overall coupled model description and simulation characteristics. J. Adv. Model. Earth Syst. 12, e2019MS002015. https://doi.org/10.1029/2019MS002015.

Dunning, C.M., Black, E., Allan, R.P., 2018. Later wet seasons with more intense rainfall over Africa under future climate change. J. Climate 31, 9719–9738. https://doi.org/10.1175/JCLI-D-18-0102.1.

Dunning, C.M., Black, E.C.L., Allan, R.P., 2016. The onset and cessation of seasonal rainfall over Africa. J. Geophys. Res., Atmos. 121 (11), 405–411. https://doi.org/10.1002/2016JD025428. 424.

Dyer, E.L.E., Jones, D.B.A., Li, R., et al., 2017a. Sahel precipitation and regional teleconnections with the Indian Ocean. J. Geophys. Res., Atmos. 122, 5654–5676. https://doi.org/10.1002/2016JD026014.

Dyer, E.L.E., Jones, D.B.A., Nusbaumer, J., et al., 2017b. Congo Basin precipitation: Assessing seasonality, regional interactions, and sources of moisture. J. Geophys. Res., Atmos. 122, 6882–6898. https://doi.org/10.1002/2016JD026240.

Evan, A.T., Flamant, C., Gaetani, M., Guichard, F., 2016. The past, present and future of African dust. Nature 531, 493–495. https://doi.org/10.1038/nature17149.

Eyring, V., Bony, S., Meehl, G.A., et al., 2016. Overview of the Coupled Model Intercomparison Project Phase 6 (CMIP6) experimental design and organization. Geosci. Model Dev. 9, 1937–1958. https://doi.org/10.5194/gmd-9-1937-2016.

Farnsworth, A., White, E., Williams, C.J.R., et al., 2011. Understanding the large scale driving mechanisms of rainfall variability over Central Africa BT – African climate and climate change: physical, social and political perspectives. In: Williams, C.J.R., Kniveton, D.R. (Eds.). Springer, Netherlands, Dordrecht, pp. 101–122.

Fink, A.H., Engel, T., Ermert, V., et al., 2017. Mean climate and seasonal cycle. In: Meteorology of Tropical West Africa, pp. 1–39.

Fotso-Kamga, G., Fotso-Nguemo, T.C., Diallo, I., et al., 2023. Projected changes in extreme precipitation and temperature events over Central Africa from COSMO-CLM simulations under the global warming level of 1.5 °C and above. Int. J. Climatol. 43, 6330–6351. https://doi.org/10.1002/joc.8208.

Fotso-Nguemo, T.C., Chamani, R., Yepdo, Z.D., et al., 2018. Projected trends of extreme rainfall events from CMIP5 models over Central Africa. Atmos. Sci. Lett. 19:e803. https://doi.org/10.1002/asl.803.

Fotso-Nguemo, T.C., Diallo, I., Diakhaté, M., et al., 2019. Projected changes in the seasonal cycle of extreme rainfall events from CORDEX simulations over Central Africa. Clim. Change 155, 339–357. https://doi.org/10.1007/s10584-019-02492-9.

Gaetani, M., Flamant, C., Bastin, S., et al., 2017. West African monsoon dynamics and precipitation: the competition between global SST warming and CO2 increase in CMIP5 idealized simulations. Clim. Dyn. 48, 1353–1373. https://doi.org/10.1007/s00382-016-3146-z.

Gamoyo, M., Reason, C., Obura, D., 2015. Rainfall variability over the East African coast. Theor. Appl. Climatol. 120, 311–322. https://doi.org/10.1007/s00704-014-1171-6.

Gebrechorkos, S.H., Bernhofer, C., Hülsmann, S., 2019. Impacts of projected change in climate on water balance in basins of East Africa. Sci. Total Environ. 682, 160–170. https://doi.org/10.1016/j.scitotenv.2019.05.053.

Gebremeskel Haile, G., Tang, Q., Sun, S., et al., 2019. Droughts in East Africa: causes, impacts and resilience. Earth-Sci. Rev. 193, 146–161. https://doi.org/10.1016/j.earscirev.2019.04.015.

Giannini, A., Kaplan, A., 2019. The role of aerosols and greenhouse gases in Sahel drought and recovery. Clim. Change 152, 449–466. https://doi.org/10.1007/s10584-018-2341-9.

Giannini, A., Saravanan, R., Chang, P., 2003. Oceanic forcing of Sahel rainfall on interannual to interdecadal time scales. Science (80-) 302, 1027–1030. https://doi.org/10.1126/science.1089357.

Gibba, P., Sylla, M.B., Okogbue, E.C., et al., 2019. State-of-the-art climate modeling of extreme precipitation over Africa: analysis of CORDEX added-value over CMIP5. Theor. Appl. Climatol. 137, 1041–1057. https://doi.org/10.1007/s00704-018-2650-y.

Giorgi, F., Coppola, E., Teichmann, C., Jacob, D., 2021. Editorial for the CORDEX-CORE experiment I Special Issue. Clim. Dyn. 57, 1265–1268. https://doi.org/10.1007/s00382-021-05902-w.

Giorgi, F., Gutowski, W.J., 2015. Regional dynamical downscaling and the CORDEX initiative. Annu. Rev. Environ. Resour. 40, 467–490. https://doi.org/10.1146/annurev-environ-102014-021217.

Gnitou, G.T., Tan, G., Niu, R., Nooni, I.K., 2021. Assessing past climate biases and the added value of CORDEX-CORE precipitation simulations over Africa. Remote Sens. 13.

Golaz, J-C., Caldwell, P.M., Van Roekel, L.P., et al., 2019. The DOE E3SM coupled model version 1: overview and evaluation at standard resolution. J. Adv. Model. Earth Syst. 11, 2089–2129. https://doi.org/10.1029/2018MS001603.

Gore, M., Abiodun, B.J., Kucharski, F., 2020. Understanding the influence of ENSO patterns on drought over southern Africa using SPEEDY. Clim. Dyn. 54, 307–327. https://doi.org/10.1007/s00382-019-05002-w.

Gudoshava, M., Misiani, H.O., Segele, Z.T., et al., 2020. Projected effects of 1.5 °C and 2 °C global warming levels on the intra-seasonal rainfall characteristics over the Greater Horn of Africa. Environ. Res. Lett. 15, 34037. https://doi.org/10.1088/1748-9326/ab6b33.

Guilbert, M., Terray, P., Mignot, J., et al., 2024. Interhemispheric temperature gradient and equatorial Pacific SSTs drive Sahel monsoon uncertainties under global warming. J. Climate 37, 1033–1052. https://doi.org/10.1175/JCLI-D-23-0162.1.

Haile, G.G., Tang, Q., Hosseini-Moghari, S-M., et al., 2020. Projected impacts of climate change on drought patterns over East Africa. Earth's Future 8, e2020EF001502. https://doi.org/10.1029/2020EF001502.

Harrison, S.P., Kohfeld, K.E., Roelandt, C., Claquin, T., 2001. The role of dust in climate changes today, at the last glacial maximum and in the future. Earth-Sci. Rev. 54, 43–80. https://doi.org/10.1016/S0012-8252(01)00041-1.

Hawkins, E., Sutton, R., 2011. The potential to narrow uncertainty in projections of regional precipitation change. Clim. Dyn. 37, 407–418. https://doi.org/10.1007/s00382-010-0810-6.

Held, I.M., Guo, H., Adcroft, A., et al., 2019. Structure and performance of GFDL's CM4.0 climate model. J. Adv. Model. Earth Syst. 11, 3691–3727. https://doi.org/10.1029/2019MS001829.

Herman, R.J., Giannini, A., Biasutti, M., Kushnir, Y., 2020. The effects of anthropogenic and volcanic aerosols and greenhouse gases on twentieth century Sahel precipitation. Sci. Rep. 10, 12203. https://doi.org/10.1038/s41598-020-68356-w.

Herrmann, S.M., Mohr, K.I., 2011. A continental-scale classification of rainfall seasonality regimes in Africa based on gridded precipitation and land surface temperature products. J. Appl. Meteorol. Climatol. 50, 2504–2513. https://doi.org/10.1175/JAMC-D-11-024.1.

Hill, S.A., Ming, Y., Held, I.M., Zhao, M., 2017. A moist static energy budget-based analysis of the Sahel rainfall response to uniform oceanic warming. J. Climate 30, 5637–5660. https://doi.org/10.1175/JCLI-D-16-0785.1.

Hirasawa, H., Kushner, P.J., Sigmond, M., et al., 2022. Evolving Sahel rainfall response to anthropogenic aerosols driven by shifting regional oceanic and emission influences. J. Climate 35, 3181–3193. https://doi.org/10.1175/JCLI-D-21-0795.1.

Hodnebrog, Ø., Myhre, G., Forster, P.M., et al., 2016. Local biomass burning is a dominant cause of the observed precipitation reduction in southern Africa. Nat. Commun. 7, 11236. https://doi.org/10.1038/ncomms11236.

Hoegh Guldberg, O., Jacob, D., Taylor, M., et al., 2018. Impacts of 1.5°C global warming on natural and human systems.

Holanda, B.A., Franco, M.A., Walter, D., et al., 2023. African biomass burning affects aerosol cycling over the Amazon. Commun. Earth Environ. 4, 154. https://doi.org/10.1038/s43247-023-00795-5.

Huang, H., Gu, Y., Xue, Y., et al., 2019. Assessing aerosol indirect effect on clouds and regional climate of East/South Asia and West Africa using NCEP GFS. Clim. Dyn. 52, 5759–5774. https://doi.org/10.1007/s00382-018-4476-9.

Hui, W.J., Cook, B.I., Ravi, S., et al., 2008. Dust-rainfall feedbacks in the West African Sahel. Water Resour. Res. 44. https://doi.org/10.1029/2008WR006885.

Hwang, Y-T., Frierson, D.M.W., Kang, S.M., 2013. Anthropogenic sulfate aerosol and the southward shift of tropical precipitation in the late 20th century. Geophys. Res. Lett. 40, 2845–2850. https://doi.org/10.1002/grl.50502.

Ichoku, C., Ellison, L.T., Willmot, K.E., et al., 2016. Biomass burning, land-cover change, and the hydrological cycle in Northern sub-Saharan Africa. Environ. Res. Lett. 11, 95005. https://doi.org/10.1088/1748-9326/11/9/095005.

James, R., Washington, R., Jones, R., 2015. Process-based assessment of an ensemble of climate projections for West Africa. J. Geophys. Res., Atmos. 120, 1221–1238. https://doi.org/10.1002/2014JD022513.

Janiga, M.A., Thorncroft, C.D., 2014. Convection over Tropical Africa and the East Atlantic during the West African Monsoon: regional and diurnal variability. J. Climate 27, 4159–4188. https://doi.org/10.1175/JCLI-D-13-00449.1.

Ji, Z., Wang, G., Yu, M., Pal, J.S., 2018. Potential climate effect of mineral aerosols over West Africa: Part II – contribution of dust and land cover to future climate change. Clim. Dyn. 50, 2335–2353. https://doi.org/10.1007/s00382-015-2792-x.

Kelley, M., Schmidt, G.A., Nazarenko, L.S., et al., 2020. GISS-E2.1: configurations and climatology. J. Adv. Model. Earth Syst. 12, e2019MS002025. https://doi.org/10.1029/2019MS002025.

Kendon, E.J., Stratton, R.A., Tucker, S., et al., 2019. Enhanced future changes in wet and dry extremes over Africa at convection-permitting scale. Nat. Commun. 10, 1794. https://doi.org/10.1038/s41467-019-09776-9.

Kenfack, K., Tamoffo, A.T., Djiotang Tchotchou, L.A., Vondou, D.A., 2023. Assessment of uncertainties in reanalysis datasets in reproducing thermodynamic mechanisms in the moisture budget's provision in the Congo Basin. Theor. Appl. Climatol. 154, 613–626. https://doi.org/10.1007/s00704-023-04576-0.

Kim, D., Chin, M., Remer, L.A., et al., 2017. Role of surface wind and vegetation cover in multidecadal variations of dust emission in the Sahara and Sahel. Atmos. Environ. 148, 282–296. https://doi.org/10.1016/j.atmosenv.2016.10.051.

King, J.A., Engelstaedter, S., Washington, R., Munday, C., 2021. Variability of the Turkana low-level jet in reanalysis and models: implications for rainfall. J. Geophys. Res., Atmos. 126, e2020JD034154. https://doi.org/10.1029/2020JD034154.

Kinuthia, J.H., 1992. Horizontal and vertical structure of the lake Turkana jet. J. Appl. Meteorol. Climatol. 31, 1248–1274. https://doi.org/10.1175/1520-0450(1992)031<1248:HAVSOT>2.0.CO;2.

Knippertz, P., Coe, H., Chiu, J.C., et al., 2015. The DACCIWA project: dynamics–aerosol–chemistry–cloud interactions in West Africa. Bull. Am. Meteorol. Soc. 96, 1451–1460. https://doi.org/10.1175/BAMS-D-14-00108.1.

Knoben, W.J.M., Woods, R.A., Freer, J.E., 2019. Global bimodal precipitation seasonality: a systematic overview. Int. J. Climatol. 39, 558–567. https://doi.org/10.1002/joc.5786.

Kok, J.F., Storelvmo, T., Karydis, V.A., et al., 2023. Mineral dust aerosol impacts on global climate and climate change. Nat. Rev. Earth. Environ. 4, 71–86. https://doi.org/10.1038/s43017-022-00379-5.

Komkoua Mbienda, A.J., Tchawoua, C., Vondou, D.A., et al., 2017. Impact of anthropogenic aerosols on climate variability over Central Africa by using a regional climate model. Int. J. Climatol. 37, 249–267. https://doi.org/10.1002/joc.4701.

Konare, A., Zakey, A.S., Solmon, F., et al., 2008. A regional climate modeling study of the effect of desert dust on the West African monsoon. J. Geophys. Res., Atmos. 113. https://doi.org/10.1029/2007JD009322.

Kuhlbrodt, T., Jones, C.G., Sellar, A., et al., 2018. The low-resolution version of HadGEM3 GC3.1: development and evaluation for global climate. J. Adv. Model. Earth Syst. 10, 2865–2888. https://doi.org/10.1029/2018MS001370.

Kumi, N., Abiodun, B.J., 2018. Potential impacts of 1.5 °C and 2 °C global warming on rainfall onset, cessation and length of rainy season in West Africa. Environ. Res. Lett. 13, 55009. https://doi.org/10.1088/1748-9326/aab89e.

Laing, A.G., Carbone, R.E., Levizzani, V., 2011. Cycles and propagation of deep convection over Equatorial Africa. Mon. Weather Rev. 139, 2832–2853. https://doi.org/10.1175/2011MWR3500.1.

Laprise, R., Hernández-Díaz, L., Tete, K., et al., 2013. Climate projections over CORDEX Africa domain using the fifth-generation Canadian Regional Climate Model (CRCM5). Clim. Dyn. 41, 3219–3246. https://doi.org/10.1007/s00382-012-1651-2.

Lazenby, M.J., Todd, M.C., Chadwick, R., Wang, Y., 2018. Future precipitation projections over Central and Southern Africa and the adjacent Indian Ocean: what causes the changes and the uncertainty? J. Climate 31, 4807–4826. https://doi.org/10.1175/JCLI-D-17-0311.1.

Lee, J., Kim, J., Sun, M-A., et al., 2020. Evaluation of the Korea Meteorological Administration Advanced Community Earth-System model (K-ACE). Asia-Pacific J. Atmos. Sci. 56, 381–395. https://doi.org/10.1007/s13143-019-00144-7.

Li, C., Chai, Y., Yang, L., Li, H., 2016. Spatio-temporal distribution of flood disasters and analysis of influencing factors in Africa. Nat. Hazards 82, 721–731. https://doi.org/10.1007/s11069-016-2181-8.

Li, J., Bao, Q., Liu, Y., et al., 2019. Evaluation of FAMIL2 in simulating the climatology and seasonal-to-interannual variability of tropical cyclone characteristics. J. Adv. Model. Earth Syst. 11, 1117–1136. https://doi.org/10.1029/2018MS001506.

Li, J., Huo, R., Chen, H., et al., 2021. Comparative assessment and future prediction using CMIP6 and CMIP5 for annual precipitation and extreme precipitation simulation. Front. Earth Sci. 9.

Li, L., Yu, Y., Tang, Y., et al., 2020. The Flexible Global Ocean-Atmosphere-Land System Model Grid-Point Version 3 (FGOALS-g3): description and evaluation. J. Adv. Model. Earth Syst. 12, e2019MS002012. https://doi.org/10.1029/2019MS002012.

Liebmann, B., Bladé, I., Kiladis, G.N., et al., 2012. Seasonality of African precipitation from 1996 to 2009. J. Climate 25, 4304–4322. https://doi.org/10.1175/JCLI-D-11-00157.1.

Lin, L., Gettelman, A., Fu, Q., Xu, Y., 2018. Simulated differences in 21st century aridity due to different scenarios of greenhouse gases and aerosols. Clim. Change 146, 407–422. https://doi.org/10.1007/s10584-016-1615-3.

Lin, Y., Huang, X., Liang, Y., et al., 2020. Community Integrated Earth System Model (CIESM): description and evaluation. J. Adv. Model. Earth Syst. 12, e2019MS002036. https://doi.org/10.1029/2019MS002036.

Longandjo, G.-N.T., Rouault, M., 2024. Revisiting the seasonal cycle of rainfall over Central Africa. J. Climate 37, 1015–1032. https://doi.org/10.1175/JCLI-D-23-0281.1.

Lovato, T., Peano, D., Butenschön, M., et al., 2022. CMIP6 simulations with the CMCC Earth System Model (CMCC-ESM2). J. Adv. Model. Earth Syst. 14, e2021MS002814. https://doi.org/10.1029/2021MS002814.

Lund, M.T., Myhre, G., Samset, B.H., 2019. Anthropogenic aerosol forcing under the shared socioeconomic pathways. Atmos. Chem. Phys. 19, 13827–13839. https://doi.org/10.5194/acp-19-13827-2019.

Lyon, B., 2014. Seasonal drought in the Greater Horn of Africa and its recent increase during the March–May long rains. J. Climate 27, 7953–7975. https://doi.org/10.1175/JCLI-D-13-00459.1.

Ma, J., Chadwick, R., Seo, K-H., et al., 2018. Responses of the tropical atmospheric circulation to climate change and connection to the hydrological cycle. Annu. Rev. Earth Planet. Sci. 46, 549–580. https://doi.org/10.1146/annurev-earth-082517-010102.

Macron, C., Pohl, B., Richard, Y., Bessafi, M., 2013. How do tropical temperate troughs form and develop over Southern Africa? J. Climate 27, 1633–1647. https://doi.org/10.1175/JCLI-D-13-00175.1.

Malherbe, J., Dieppois, B., Maluleke, P., et al., 2016. South African droughts and decadal variability. Nat. Hazards 80, 657–681. https://doi.org/10.1007/s11069-015-1989-y.

Malherbe, J., Landman, W.A., Engelbrecht, F.A., 2014. The bi-decadal rainfall cycle, southern annular mode and tropical cyclones over the Limpopo River Basin, Southern Africa. Clim. Dyn. 42, 3121–3138. https://doi.org/10.1007/s00382-013-2027-y.

Mallet, M., Nabat, P., Johnson, B., et al., 2021. Climate models generally underrepresent the warming by Central Africa biomass-burning aerosols over the Southeast Atlantic. Sci. Adv. 7:eabg9998. https://doi.org/10.1126/sciadv.abg9998.

Martin, E.R., Thorncroft, C.D., 2014. The impact of the AMO on the West African monsoon annual cycle. Q. J. R. Meteorol. Soc. 140, 31–46. https://doi.org/10.1002/qj.2107.

Marvel, K., Biasutti, M., Bonfils, C., 2020. Fingerprints of external forcing agents on Sahel rainfall: aerosols, greenhouse gases, and model-observation discrepancies. Environ. Res. Lett. 15, 084023.

Maúre, G., Pinto, I., Ndebele-Murisa, M., et al., 2018. The southern African climate under 1.5 °C and 2 °C of global warming as simulated by CORDEX regional climate models. Environ. Res. Lett. 13, 65002. https://doi.org/10.1088/1748-9326/aab190.

Mauritsen, T., Bader, J., Becker, T., et al., 2019. Developments in the MPI-M Earth System Model version 1.2 (MPI-ESM1.2) and its response to increasing CO2. J. Adv. Model. Earth Syst. 11, 998–1038. https://doi.org/10.1029/2018MS001400.

Mba, W.P., Longandjo, G.-N.T., Moufouma-Okia, W., et al., 2018. Consequences of 1.5 °C and 2 °C global warming levels for temperature and precipitation changes over Central Africa. Environ. Res. Lett. 13, 55011. https://doi.org/10.1088/1748-9326/aab048.

Mboka, J.-J.M., Kouna, S.B., Chouto, S., et al., 2021. Simulated impact of global warming on extreme rainfall events over Cameroon during the 21st century. Weather 76, 347–353. https://doi.org/10.1002/wea.3867.

Menut, L., Flamant, C., Turquety, S., et al., 2018. Impact of biomass burning on pollutant surface concentrations in megacities of the Gulf of Guinea. Atmos. Chem. Phys. 18, 2687–2707. https://doi.org/10.5194/acp-18-2687-2018.

Mohino, E., Monerie, P-A., Mignot, J., et al., 2024. Impact of Atlantic multidecadal variability on rainfall intensity distribution and timing of the West African monsoon. Earth Syst. Dyn. 15, 15–40. https://doi.org/10.5194/esd-15-15-2024.

Monerie, P-A., Biasutti, M., Mignot, J., et al., 2023a. Storylines of Sahel precipitation change: roles of the North Atlantic and Euro-Mediterranean temperature. J. Geophys. Res., Atmos. 128, e2023JD038712. https://doi.org/10.1029/2023JD038712.

Monerie, P-A., Biasutti, M., Roucou, P., 2016a. On the projected increase of Sahel rainfall during the late rainy season. Int. J. Climatol. https://doi.org/10.1002/joc.4638.

Monerie, P-A., Dittus, A.J., Wilcox, L.J., Turner, A.G., 2023b. Uncertainty in simulating twentieth century West African precipitation trends: the role of anthropogenic aerosol emissions. Earth's Future 11, e2022EF002995. https://doi.org/10.1029/2022EF002995.

Monerie, P-A., Fontaine, B., Roucou, P., 2012. Expected future changes in the African monsoon between 2030 and 2070 using some CMIP3 and CMIP5 models under a medium-low RCP scenario. J. Geophys. Res., Atmos. 117. https://doi.org/10.1029/2012JD017510.

Monerie, P-A., Pohl, B., Gaetani, M., 2021. The fast response of Sahel precipitation to climate change allows effective mitigation action. npj Clim. Atmos. Sci. 4 (24). https://doi.org/10.1038/s41612-021-00179-6.

Monerie, P-A., Robson, J., Dong, B., et al., 2019. Effect of the Atlantic multidecadal variability on the global monsoon. Geophys. Res. Lett. 46. https://doi.org/10.1029/2018GL080903.

Monerie, P-A., Roucou, P., Fontaine, B., 2013. Mid-century effects of climate change on African monsoon dynamics using the A1B emission scenario. Int. J. Climatol. 33. https://doi.org/10.1002/joc.3476.

Monerie, P-A., Sanchez-Gomez, E., Boé, J., 2016b. On the range of future Sahel precipitation projections and the selection of a sub-sample of CMIP5 models for impact studies. Clim. Dyn. https://doi.org/10.1007/s00382-016-3236-y.

Monerie, P-A., Sanchez-Gomez, E., Gaetani, M., et al., 2020a. Future evolution of the Sahel precipitation zonal contrast in CESM1. Clim. Dyn. https://doi.org/10.1007/s00382-020-05417-w.

Monerie, P-A., Sanchez-Gomez, E., Pohl, B., et al., 2017. Impact of internal variability on projections of Sahel precipitation change. Environ. Res. Lett. 12. https://doi.org/10.1088/1748-9326/aa8cda.

Monerie, P-A., Wainwright, C.M., Sidibe, M., Akinsanola, A.A., 2020b. Model uncertainties in climate change impacts on Sahel precipitation in ensembles of CMIP5 and CMIP6 simulations. Clim. Dyn. 55, 1385–1401. https://doi.org/10.1007/s00382-020-05332-0.

Monerie, P-A., Wilcox, L.J., Turner, A.G., 2022. Effects of anthropogenic aerosol and greenhouse gas emissions on Northern Hemisphere monsoon precipitation: mechanisms and uncertainty. J. Climate 1 (66). https://doi.org/10.1175/JCLI-D-21-0412.1.

Mousavi, S.V., Karami, K., Tilmes, S., et al., 2023. Future dust concentration over the Middle East and North Africa region under global warming and stratospheric aerosol intervention scenarios. Atmos. Chem. Phys. 23, 10677–10695. https://doi.org/10.5194/acp-23-10677-2023.

Mulcahy, J.P., Johnson, C., Jones, C.G., et al., 2020. Description and evaluation of aerosol in UKESM1 and HadGEM3-GC3.1 CMIP6 historical simulations. Geosci. Model Dev. 13, 6383–6423. https://doi.org/10.5194/gmd-13-6383-2020.

Müller, W.A., Jungclaus, J.H., Mauritsen, T., et al., 2018. A higher-resolution version of the Max Planck Institute Earth System Model (MPI-ESM1.2-HR). J. Adv. Model. Earth Syst. 10, 1383–1413. https://doi.org/10.1029/2017MS001217.

Munday, C., Savage, N., Jones, R.G., Washington, R., 2023. Valley formation aridifies East Africa and elevates Congo Basin rainfall. Nature 615, 276–279. https://doi.org/10.1038/s41586-022-05662-5.

Munday, C., Washington, R., 2017. Circulation controls on southern African precipitation in coupled models: the role of the Angola Low. J. Geophys. Res., Atmos. 122, 861–877. https://doi.org/10.1002/2016JD025736.

Munday, C., Washington, R., 2018. Systematic climate model rainfall biases over Southern Africa: links to moisture circulation and topography. J. Climate 31, 7533–7548. https://doi.org/10.1175/JCLI-D-18-0008.1.

Munday, C., Washington, R., 2019. Controls on the diversity in climate model projections of early summer drying over Southern Africa. J. Climate 32, 3707–3725. https://doi.org/10.1175/JCLI-D-18-0463.1.

Myhre, G., Shindell, D., Pongratz, J., 2014. Anthropogenic and natural radiative forcing. In: Intergovernmental Panel on Climate Change (Ed.), Climate Change 2013 – The Physical Science Basis: Working Group I Contribution to the Fifth Assessment Report of the Intergovernmental Panel on Climate Change. Cambridge University Press, Cambridge, pp. 659–740.

Nicholson, S.E., 2017. Climate and climatic variability of rainfall over eastern Africa. Rev. Geophys. 55, 590–635. https://doi.org/10.1002/2016RG000544.

Nicholson, S.E., Dezfuli, A.K., 2013. The relationship of rainfall variability in western equatorial Africa to the tropical oceans and atmospheric circulation. Part I: The boreal spring. J. Climate 26, 45–65. https://doi.org/10.1175/JCLI-D-11-00653.1.

Nikulin, G., Lennard, C., Dosio, A., et al., 2018. The effects of 1.5 and 2 degrees of global warming on Africa in the CORDEX ensemble. Environ. Res. Lett. 13, 65003. https://doi.org/10.1088/1748-9326/aab1b1.

O'Neill, B.C., Tebaldi, C., van Vuuren, D.P., et al., 2016. The Scenario Model Intercomparison Project (ScenarioMIP) for CMIP6. Geosci. Model Dev. 9, 3461–3482. https://doi.org/10.5194/gmd-9-3461-2016.

Ogega, O.M., Koske, J., Kung'u, J.B., et al., 2020. Heavy precipitation events over East Africa in a changing climate: results from CORDEX RCMs. Clim. Dyn. 55, 993–1009. https://doi.org/10.1007/s00382-020-05309-z.

Okumura, Y., Xie, S-P., 2004. Interaction of the Atlantic equatorial cold tongue and the African monsoon. J. Climate 17, 3589–3602. https://doi.org/10.1175/1520-0442(2004)017<3589:IOTAEC>2.0.CO;2.

Olusegun, C.F., Awe, O., Ijila, I., et al., 2022. Evaluation of dry and wet spell events over West Africa using CORDEX-CORE regional climate models. Model. Earth Syst. Environ. 8, 4923–4937. https://doi.org/10.1007/s40808-022-01423-5.

Ongoma, V., Chen, H., Gao, C., et al., 2018. Future changes in climate extremes over Equatorial East Africa based on CMIP5 multimodel ensemble. Nat. Hazards 90, 901–920. https://doi.org/10.1007/s11069-017-3079-9.

Osima, S., Indasi, V.S., Zaroug, M., et al., 2018. Projected climate over the Greater Horn of Africa under 1.5 °C and 2 °C global warming. Environ. Res. Lett. 13, 65004. https://doi.org/10.1088/1748-9326/aaba1b.

Palmer, P.I., Wainwright, C.M., Dong, B., et al., 2023. Drivers and impacts of Eastern African rainfall variability. Nat. Rev. Earth. Environ. 4, 254–270. https://doi.org/10.1038/s43017-023-00397-x.

Park, J-Y., Bader, J., Matei, D., 2015. Northern-hemispheric differential warming is the key to understanding the discrepancies in the projected Sahel rainfall. Nat. Commun. 6, 5985.

Park, J., Bader, J., Matei, D., 2016. Anthropogenic Mediterranean warming essential driver for present and future Sahel rainfall. Nat. Clim. Change 6, 941–945.

Pascale, S., Kapnick, S.B., Delworth, T.L., Cooke, W.F., 2020. Increasing risk of another Cape Town "Day Zero" drought in the 21st century. Proc. Natl. Acad. Sci. 117, 29495–29503. https://doi.org/10.1073/pnas.2009144117.

Pascale, S., Pohl, B., Kapnick, S.B., Zhang, H., 2019. On the Angola Low interannual variability and its role in modulating ENSO effects in Southern Africa. J. Climate 32, 4783–4803. https://doi.org/10.1175/JCLI-D-18-0745.1.

Pinto, I., Lennard, C., Tadross, M., et al., 2016. Evaluation and projections of extreme precipitation over southern Africa from two CORDEX models. Clim. Change 135, 655–668. https://doi.org/10.1007/s10584-015-1573-1.

Pohl, B., Camberlin, P., 2011. Intraseasonal and interannual zonal circulations over the Equatorial Indian Ocean. Theor. Appl. Climatol. 104, 175–191. https://doi.org/10.1007/s00704-010-0336-1.

Pohl, B., Macron, C., Monerie, P-A., 2017. Fewer rainy days and more extreme rainfall by the end of the century in Southern Africa. Sci. Rep. 7. https://doi.org/10.1038/srep46466.

Polson, D., Bollasina, M., Hegerl, G.C., Wilcox, L.J., 2014. Decreased monsoon precipitation in the Northern Hemisphere due to anthropogenic aerosols. Geophys. Res. Lett. 41, 6023–6029. https://doi.org/10.1002/2014GL060811.

Rodríguez-Fonseca, B., Mohino, E., Mechoso, C.R., et al., 2015. Variability and predictability of West African droughts: a review on the role of sea surface temperature anomalies. J. Climate 28, 4034–4060. https://doi.org/10.1175/JCLI-D-14-00130.1.

Roehrig, R., Bouniol, D., Guichard, F., et al., 2013. The present and future of the West African monsoon: a process-oriented assessment of CMIP5 simulations along the AMMA transect. J. Climate 26, 6471–6505. https://doi.org/10.1175/JCLI-D-12-00505.1.

Rong, X., Li, J., Chen, H., et al., 2021. The CMIP6 historical simulation datasets produced by the climate system model CAMS-CSM. Adv. Atmos. Sci. 38, 285–295. https://doi.org/10.1007/s00376-020-0171-y.

Rowell, D.P., 2003. The impact of Mediterranean SSTs on the Sahelian rainfall season. J. Climate 16, 849–862. https://doi.org/10.1175/1520-0442(2003)016<0849:TIOMSO>2.0.CO;2.

Rowell, D.P., 2019. An observational constraint on CMIP5 projections of the East African long rains and Southern Indian Ocean warming. Geophys. Res. Lett. 46, 6050–6058. https://doi.org/10.1029/2019GL082847.

Rowell, D.P., Chadwick, R., 2018. Causes of the uncertainty in projections of tropical terrestrial rainfall change: East Africa. J. Climate. https://doi.org/10.1175/JCLI-D-17-0830.1.

Saha, A., Ghosh, S., 2019. Can the weakening of Indian Monsoon be attributed to anthropogenic aerosols? Environ. Res. Commun. 1, 61006. https://doi.org/10.1088/2515-7620/ab2c65.

Saini, R., Wang, G., Yu, M., Kim, J., 2015. Comparison of RCM and GCM projections of boreal summer precipitation over Africa. J. Geophys. Res., Atmos. 120, 3679–3699. https://doi.org/10.1002/2014JD022599.

Sawadogo, W., Reboita, M.S., Faye, A., et al., 2021. Current and future potential of solar and wind energy over Africa using the RegCM4 CORDEX-CORE ensemble. Clim. Dyn. 57, 1647–1672. https://doi.org/10.1007/s00382-020-05377-1.

Schneider, T., Bischoff, T., Haug, G.H., 2014. Migrations and dynamics of the intertropical convergence zone. Nature 513, 45.

Séférian, R., Nabat, P., Michou, M., et al., 2019. Evaluation of CNRM Earth System Model, CNRM-ESM2-1: role of Earth system processes in present-day and future climate. J. Adv. Model. Earth Syst. 11, 4182–4227. https://doi.org/10.1029/2019MS001791.

Seland, Ø., Bentsen, M., Olivié, D., et al., 2020. Overview of the Norwegian Earth System Model (NorESM2) and key climate response of CMIP6 DECK, historical, and scenario simulations. Geosci. Model Dev. 13, 6165–6200. https://doi.org/10.5194/gmd-13-6165-2020.

Semmler, T., Danilov, S., Gierz, P., et al., 2020. Simulations for CMIP6 with the AWI Climate Model AWI-CM-1-1. J. Adv. Model. Earth Syst. 12, e2019MS002009. https://doi.org/10.1029/2019MS002009.

Seneviratne, S.I., Zhang, X., Adnan, M., et al., 2021. Weather and climate extreme events in a changing climate. Chapter, vol. 11.

Sherman, P., Gao, M., Song, S., et al., 2021. Sensitivity of modeled Indian monsoon to Chinese and Indian aerosol emissions. Atmos. Chem. Phys. 21, 3593–3605. https://doi.org/10.5194/acp-21-3593-2021.

Shi, X., Chen, X., Dai, Y., Hu, G., 2020. Climate sensitivity and feedbacks of BCC-CSM to idealized CO2 forcing from CMIP5 to CMIP6. J. Meteorol. Res. 34, 865–878. https://doi.org/10.1007/s13351-020-9204-9.

Shongwe, M.E., van Oldenborgh, G.J., van den Hurk, B.J.J.M., et al., 2009. Projected changes in mean and extreme precipitation in Africa under global warming. Part I: Southern Africa. J. Climate 22, 3819–3837. https://doi.org/10.1175/2009JCLI2317.1.

Soden, B.J., Held, I.M., 2006. An assessment of climate feedbacks in coupled ocean–atmosphere models. J. Climate 19, 3354–3360. https://doi.org/10.1175/JCLI3799.1.

Sorí, R., Nieto, R., Vicente-Serrano, S.M., et al., 2017. A Lagrangian perspective of the hydrological cycle in the Congo River basin. Earth Syst. Dyn. 8, 653–675. https://doi.org/10.5194/esd-8-653-2017.

Spinoni, J., Barbosa, P., Bucchignani, E., et al., 2021. Global exposure of population and land-use to meteorological droughts under different warming levels and SSPs: a CORDEX-based study. Int. J. Climatol. 41, 6825–6853. https://doi.org/10.1002/joc.7302.

Spinoni, J., Barbosa, P., De Jager, A., et al., 2019. A new global database of meteorological drought events from 1951 to 2016. J. Hydrol. Reg. Stud. 22, 100593. https://doi.org/10.1016/j.ejrh.2019.100593.

Stratton, R.A., Senior, C.A., Vosper, S.B., et al., 2018. A Pan-African convection-permitting regional climate simulation with the met office unified model: CP4-Africa. J. Climate 31, 3485–3508. https://doi.org/10.1175/JCLI-D-17-0503.1.

Sultan, B., Janicot, S., 2003. The West African monsoon dynamics. Part II: The "preonset" and "onset" of the summer monsoon. J. Climate 16, 3407–3427. https://doi.org/10.1175/1520-0442(2003)016<3407:TWAMDP>2.0.CO;2.

Swapna, P., Krishnan, R., Sandeep, N., et al., 2018. Long-term climate simulations using the IITM Earth System Model (IITM-ESMv2) with focus on the South Asian Monsoon. J. Adv. Model. Earth Syst. 10, 1127–1149. https://doi.org/10.1029/2017MS001262.

Swart, N.C., Cole, J.N.S., Kharin, V.V., et al., 2019. The Canadian Earth System Model version 5 (CanESM5.0.3). Geosci. Model Dev. 12, 4823–4873. https://doi.org/10.5194/gmd-12-4823-2019.

Taljaard, J.J., 1986. Change of rainfall distribution and circulation patterns over Southern Africa in summer. J. Climatol. 6, 579–592. https://doi.org/10.1002/joc.3370060602.

Tamoffo, A.T., Akinsanola, A.A., Weber, T., 2023a. Understanding the diversity of the West African monsoon system change projected by CORDEX-CORE regional climate models. Clim. Dyn. 61, 2395–2419. https://doi.org/10.1007/s00382-023-06690-1.

Tamoffo, A.T., Dosio, A., Weber, T., Vondou, D.A., 2023b. Dynamic and thermodynamic contributions to late 21st century projected rainfall change in the Congo Basin: impact of a regional climate model's formulation. Atmosphere (Basel) 14.

Tamoffo, A.T., Moufouma-Okia, W., Dosio, A., et al., 2019a. Process-oriented assessment of RCA4 regional climate model projections over the Congo Basin under 1.5 °C and 2 °C global warming levels: influence of regional moisture fluxes. Clim. Dyn. 53, 1911–1935. https://doi.org/10.1007/s00382-019-04751-y.

Tamoffo, A.T., Vondou, D.A., Pokam, W.M., et al., 2019b. Daily characteristics of Central African rainfall in the REMO model. Theor. Appl. Climatol. 137, 2351–2368. https://doi.org/10.1007/s00704-018-2745-5.

Tamoffo, A.T., Weber, T., Cabos, W., et al., 2024. Mechanisms of added value of a coupled global ocean-regional atmosphere climate model over Central Equatorial Africa. J. Geophys. Res., Atmos. 129, e2023JD039385. https://doi.org/10.1029/2023JD039385.

Tang, C., Morel, B., Wild, M., et al., 2019. Numerical simulation of surface solar radiation over Southern Africa. Part 2: projections of regional and global climate models. Clim. Dyn. 53, 2197–2227. https://doi.org/10.1007/s00382-019-04817-x.

Tatebe, H., Ogura, T., Nitta, T., et al., 2019. Description and basic evaluation of simulated mean state, internal variability, and climate sensitivity in MIROC6. Geosci. Model Dev. 12, 2727–2765. https://doi.org/10.5194/gmd-12-2727-2019.

Taylor, K.E., Stouffer, R.J., Meehl, G.A., 2012. An overview of CMIP5 and the experiment design. Bull. Am. Meteorol. Soc. 93, 485–498. https://doi.org/10.1175/BAMS-D-11-00094.1.

Thiam, M., Oruba, L., de Coetlogon, G., et al., 2024. Impact of the sea surface temperature in the North-Eastern tropical Atlantic on precipitation over Senegal. J. Geophys. Res., Atmos. 129, e2023JD040513. https://doi.org/10.1029/2023JD040513.

Tierney, J.E., Smerdon, J.E., Anchukaitis, K.J., Seager, R., 2013. Multidecadal variability in East African hydroclimate controlled by the Indian Ocean. Nature 493, 389–392. https://doi.org/10.1038/nature11785.

Ukkola, A.M., De Kauwe, M.G., Roderick, M.L., et al., 2020. Robust future changes in meteorological drought in CMIP6 projections despite uncertainty in precipitation. Geophys. Res. Lett. 47, e2020GL087820. https://doi.org/10.1029/2020GL087820.

Villamayor, J., Mohino, E., 2015. Robust Sahel drought due to the Interdecadal Pacific Oscillation in CMIP5 simulations. Geophys. Res. Lett. 42, 1214–1222. https://doi.org/10.1002/2014GL062473.

Voldoire, A., Saint-Martin, D., Sénési, S., et al., 2019. Evaluation of CMIP6 DECK experiments with CNRM-CM6-1. J. Adv. Model. Earth Syst. 11, 2177–2213. https://doi.org/10.1029/2019MS001683.

Volodin, E.M., Mortikov, E.V., Kostrykin, S.V., et al., 2017. Simulation of the present-day climate with the climate model INMCM5. Clim. Dyn. 49, 3715–3734. https://doi.org/10.1007/s00382-017-3539-7.

Volodin, E.M., Mortikov, E.V., Kostrykin, S.V., et al., 2018. Simulation of the modern climate using the INM-CM48 climate model. Russ. J. Numer. Anal. Math. Model. 33, 367–374. https://doi.org/10.1515/rnam-2018-0032.

Wainwright, C.M., Black, E., Allan, R.P., 2021. Future changes in wet and dry season characteristics in CMIP5 and CMIP6 simulations. J. Hydrometeorol. 22, 2339–2357. https://doi.org/10.1175/JHM-D-21-0017.1.

Wainwright, C.M., Marsham, J.H., Keane, R.J., et al., 2019. ‘Eastern African Paradox’ rainfall decline due to shorter not less intense Long Rains. npj Clim. Atmos. Sci. 2, 34. https://doi.org/10.1038/s41612-019-0091-7.

Wane, D., Coëtlogon, G.de, Lazar, A., et al., 2024. Atmospheric response to seasonal changes in sea surface temperature during the boreal summer in the Tropical Atlantic. Clim. Dyn. 62, 1597–1612. https://doi.org/10.1007/s00382-023-06968-4.

Wang, C., Kim, D., Ekman, A.M.L., et al., 2009. Impact of anthropogenic aerosols on Indian summer monsoon. Geophys. Res. Lett. 36. https://doi.org/10.1029/2009GL040114.

Wang, H., Xie, S-P., Kosaka, Y., et al., 2019. Dynamics of Asian summer monsoon response to anthropogenic aerosol forcing. J. Climate 32, 843–858. https://doi.org/10.1175/JCLI-D-18-0386.1.

Washington, R., James, R., Pearce, H., et al., 2013. Congo Basin rainfall climatology: can we believe the climate models? Philos. Trans. R. Soc. B Biol. Sci. 368, 20120296. https://doi.org/10.1098/rstb.2012.0296.

Wells, C.D., Kasoar, M., Bellouin, N., Voulgarakis, A., 2023. Local and remote climate impacts of future African aerosol emissions. Atmos. Chem. Phys. 23, 3575–3593. https://doi.org/10.5194/acp-23-3575-2023.

Westervelt, D.M., You, Y., Li, X., et al., 2020. Relative importance of greenhouse gases, sulfate, organic carbon, and black carbon aerosol for south Asian monsoon rainfall changes. Geophys. Res. Lett. 47, e2020GL088363. https://doi.org/10.1029/2020GL088363.

Wilcox, L.J., Allen, R.J., Samset, B.H., et al., 2022. The Regional Aerosol Model Intercomparison Project (RAMIP). Geosci. Model Dev. Discuss. 2022, 1–40. https://doi.org/10.5194/gmd-2022-249.

Wilcox, L.J., Highwood, E.J., Booth, B.B.B., Carslaw, K.S., 2015. Quantifying sources of intermodel diversity in the cloud albedo effect. Geophys. Res. Lett. 42, 1568–1575. https://doi.org/10.1002/2015GL063301.

Wilcox, L.J., Highwood, E.J., Dunstone, N.J., 2013. The influence of anthropogenic aerosol on multi-decadal variations of historical global climate. Environ. Res. Lett. 8, 24033. https://doi.org/10.1088/1748-9326/8/2/024033.

Woodward, S., Roberts, D.L., Betts, R.A., 2005. A simulation of the effect of climate change–induced desertification on mineral dust aerosol. Geophys. Res. Lett. 32. https://doi.org/10.1029/2005GL023482.

Worou, K., 2023. Past, present, and future impacts of oceanic internal modes of variability on the rainfall over the West African Guinea coast.

Worou, K., Goosse, H., Fichefet, T., et al., 2020. Interannual variability of rainfall in the Guinean Coast region and its links with sea surface temperature changes over the twentieth century for the different seasons. Clim. Dyn. 55, 449–470. https://doi.org/10.1007/s00382-020-05276-5.

Worou, K., Goosse, H., Fichefet, T., Kucharski, F., 2022. Weakened impact of the Atlantic Niño on the future equatorial Atlantic and Guinea Coast rainfall. Earth Syst. Dyn. 13, 231–249. https://doi.org/10.5194/esd-13-231-2022.

Wu, Y., Miao, C., Slater, L., et al., 2024. Hydrological projections under CMIP5 and CMIP6: sources and magnitudes of uncertainty. Bull. Am. Meteorol. Soc. 105, E59–E74. https://doi.org/10.1175/BAMS-D-23-0104.1.

Wyser, K., van Noije, T., Yang, S., et al., 2020. On the increased climate sensitivity in the EC-Earth model from CMIP5 to CMIP6. Geosci. Model Dev. 13, 3465–3474. https://doi.org/10.5194/gmd-13-3465-2020.

Yan, Y., Lu, R., Li, C., 2018. Relationship between the future projections of Sahel rainfall and the simulation biases of present South Asian and Western North Pacific rainfall in summer. J. Climate 32, 1327–1343. https://doi.org/10.1175/JCLI-D-17-0846.1.

Yang, W., Seager, R., Cane, M.A., Lyon, B., 2015. The annual cycle of East African precipitation. J. Climate 28, 2385–2404. https://doi.org/10.1175/JCLI-D-14-00484.1.

Yukimoto, S., Kawai, H., Koshiro, T., et al., 2019. The Meteorological Research Institute Earth System Model Version 2.0, MRI-ESM2.0: description and basic evaluation of the physical component. J. Meteorol. Soc. Japan Ser. II 97, 931–965. https://doi.org/10.2151/jmsj.2019-051.

Zhao, A., Ryder, C.L., Wilcox, L.J., 2022. How well do the CMIP6 models simulate dust aerosols? Atmos. Chem. Phys. 22, 2095–2119. https://doi.org/10.5194/acp-22-2095-2022.

Zhao, C., Liu, X., Ruby Leung, L., Hagos, S., 2011. Radiative impact of mineral dust on monsoon precipitation variability over West Africa. Atmos. Chem. Phys. 11, 1879–1893. https://doi.org/10.5194/acp-11-1879-2011.

Zhao, T., Dai, A., 2017. Uncertainties in historical changes and future projections of drought. Part II: model-simulated historical and future drought changes. Clim. Change 144, 535–548. https://doi.org/10.1007/s10584-016-1742-x.

Zhao, T., Dai, A., 2022. CMIP6 model-projected hydroclimatic and drought changes and their causes in the twenty-first century. J. Climate 35, 897–921. https://doi.org/10.1175/JCLI-D-21-0442.1.

Ziehn, T., Chamberlain, M.A., Law, R.M., et al., 2020. The Australian Earth System Model: ACCESS-ESM1.5. J. South Hemisph. Earth Syst. Sci.

Chapter 7

Detection and attribution of climate change impacts in Africa

Shingirai S. Nangombe[a], **Mohau J. Mateyisi**[b], **and Khetsiwe N. Khumalo**[c]
[a]*Danish Meteorological Institute, Copenhagen, Denmark,* [b]*Council for Scientific and Industrial Research, Pretoria, South Africa,* [c]*UNEP Copenhagen Climate Center, Copenhagen, Denmark*

7.1 Introduction

7.1.1 Background

The rising magnitude, intensity, and frequency of extreme rainfall events, including floods and droughts in various monsoon regions, have impacted the livelihoods of more than two-thirds of the global population (Nicholson et al., 2022; Biasutti, 2019; Hwang et al., 2013). In Africa, the impact of these extremes is compounded by high poverty levels in many countries, exacerbating the vulnerability to climate change extremes and posing significant challenges for adaptation and resilience efforts (IPCC Report, 2022).

Climate attribution is a process of evaluating and quantifying the relative contributions of causal factors associated with climate change and the physical characteristics of the observed events, such as the intensity, amplitude, and likelihood (Stott and Christidis, 2023; Bindoff et al., 2013). Specifically, climate-attribution science seeks to address the question of whether anthropogenic climate change has influenced the probability and intensity of observed extreme weather events and, if so, to what extent (Otto et al., 2020). Understanding the attribution of causal factors, whether human influence or natural climate variability, to the occurrence of these extreme events, is crucial. The findings of climate attribution studies empower scientists as well as the public and policymakers to link extreme weather experiences with the scientific understanding of anthropogenic climate change. There have been many attribution studies done on extreme events that occurred in various locales globally (e.g., Kimutai et al., 2023; Otto et al., 2023; Tradowsky et al., 2022; Kreienkamp et al., 2021; Nangombe et al., 2020; Uhe et al., 2018; Otto et al., 2018; Ma et al., 2017; Otto, 2015; Shiogama et al., 2013). However, in contrast to the global north, fewer studies have focused on Africa. This is despite the continent having experienced a higher frequency of these weather events and often having suffered severe impacts due to its limited capacity to cope. The poor adaptive capacity is largely

Aerosols and Precipitation Over Africa. https://doi.org/10.1016/B978-0-44-314050-1.00012-8

tied to the economic status of many countries (Adelekan et al., 2022; Ebi et al., 2014).

It was not until 2013 that the first climate model-based attribution study was done over Africa for a region in Southern Africa (Lott et al., 2013). The study focused on the severe drought that occurred in 2011, where it was concluded that the extreme rainfall deficit associated with this drought was attributed to both natural climate variability (i.e., a La Niña event) and a strong anthropogenic influence. Following the initial attribution study, a couple of related studies were conducted on parts of the continent with a focus on drought, flooding, and extreme-temperature events. For example, an anthropogenic influence was identified in the 2014 drought that affected East Africa (Herring et al., 2015). An attribution study of the 2016 Kenya drought concluded that natural variability was the main cause, while human-induced climate change was found to have made a limited contribution (Uhe et al., 2018). An analysis of floods in Kenya, i.e., the extremely heavy rainfall of October/November 2019, which left 100 people dead in Kenya, was mainly attributed to natural variability. Specifically, the heavy rain was linked to the Indian Ocean Sea Surface Temperatures (SSTs), which were quantified through the Dipole Mode Index (Nicholson et al., 2022).

In the West Africa monsoon region, an increase in the spatial and seasonal rainfall patterns in the Sahel was suggested to have been attributed to greenhouse gas (GHG) forcing (Biasutti, 2019). In contrast, the influence of the reflective aerosol emissions on the Intertropical Convergence Zone (ITCZ) was suggested to have contributed to the drying of the Sahel from the 1960s through to the 1980s (Hwang et al., 2013; Booth et al., 2012; Ackerley et al., 2011). According to Amouin et al. (2020), flood events that occur in June over the coastal areas of the West Africa Monsoon region are attributed to the natural variability in the climate system. Focusing on the April and May months, Lawal et al. (2016) concluded that there was little to no evidence of anthropogenic emissions' influence on the late onset of the 2015 rainfall season in Nigeria.

The change in precipitation trends in Africa can be influenced by pattern variations of aerosol concentration in the atmosphere (Paeth et al., 2009). Although aerosols can be from natural and anthropogenic sources, they are largely anthropogenic over the tropical African monsoon regions, where their major source is biomass burning (Paeth et al., 2009; Paeth and Feichter, 2006). The decreasing trend in rainfall over the northern African monsoon was attributed to aerosols, while that over the southern African monsoon seems to be attributed to the influence of GHG emissions (Ha et al., 2020; Undorf et al., 2018). Precipitation in the tropical regions, which include the West Africa and East Africa monsoon regions, has been shown to be influenced by anthropogenic sulfate aerosols (Ha et al., 2020; Hwang et al., 2013). Ha et al. (2020) attributed the rainfall changes in the climate scale over the African monsoon regions mainly to anthropogenic forcing. It is important to note that while precipitation change in tropical Africa is less sensitive to greenhouse-gas warming, there is a decreasing precipitation trend when the effect of aerosols from biomass burning is taken into account (Paeth and Feichter, 2006). Most available detection and attribution (D&A) studies conducted over Africa were based on precipitation extremes, as noted by the examples just cited (Wilhite, 2000; Winsemius et al., 2018). A point worth acknowledging is that confidence in precipitation-based attribution studies remains low in Africa, largely due to the limited observations that fail to parameterize the models (Biasutti, 2019).

This chapter covers the detection and attribution of extreme weather events that have occurred within and around monsoon regions in Africa. Its key objectives are to review and synthesize existing research on climate extremes attribution studies in Africa, explore the common methodologies used in detection and attribution studies, and present case studies on the attribution of specific climate extreme events that have occurred in some of the monsoon regions in Africa. The chapter opens with an overview of climate change attribution studies, gradually narrowing its focus to the African context. It progresses to discuss recent advancements in these studies, followed by an analysis of the two main methods employed in climate change detection and attribution studies. To exemplify climate attribution over Africa, the chapter then focuses on two case studies of past severe climate hazards that had severe negative consequences on people's livelihoods. The first case study focuses on an extreme temperature event around the North African monsoon region, while the second focuses on a drought event in the Southern African monsoon region. Finally, the chapter concludes by summarizing key findings and highlighting the challenges inherent in conducting detection and attribution studies in Africa.

7.2 Advances in climate-change attribution science

The advances in climate-change attribution science, like most climate science endeavors, are driven by: improvements in technology; development of modeling approaches; data storage and availability; and collaboration among scientific communities. Climate models have become increasingly sophisticated, allowing the incorporation of greenhouse gas emissions, solar radiation, atmospheric composition, changes in the land use patterns, and SSTs (Delworth et al., 2020; Gillett et al., 2016; Haarsma et al., 2016; Taylor et al., 2012). The emergence of frameworks for detection and attribution is one of the key developments in climate science, especially since extreme climate events are increasing (IPCC, 2021).

With the advent of global coordination on climate science, such as the World Climate Model Research Programme (WRCP, https://www.wcrp-climate.org/); Climate Model Intercomparison Project CMIP5 (Taylor et al., 2012) and CMIP6 (Eyring et al., 2016); Inter-Sectoral Impact Model Intercomparison Project (ISIMIP, Warszawski et al., 2014); and Detection and Attribution Model Intercomparison Project (DAMIP, Gillett et al., 2016); the simulations of the Earth's climate system have improved significantly. Such frameworks paved the way for the high quality and quantity of climate research and the sharing of data and methods. This led to substantial progress in climate change detection and attribution studies (Knutson et al., 2017). The free and open sharing of climate data and code on cloud-linked platforms such as Copernicus (Delworth et al., 2020), Earth System Grid Federation (ESGF, https://esgf.llnl.gov/nodes.html), and GitHub led to increased availability of climate data, thus bridging the climate data gaps in the detection and attribution studies. However, most attribution studies are currently limited to developed countries, which implies that knowledge gaps in this field are relatively large for developing countries. Scientific contributions towards the attribution of climate extremes stand a chance of providing essential information about these causes of significant damages and socioeconomic losses in places like Africa. Up-to-date, accurate assessment of the role of climate change on the continent is critical to avoid mal-adaptation that could result from limited or outdated scientific evidence underlying the challenges (Otto et al., 2020).

The latest Intergovernmental Panel on Climate Change (IPCC) Assessment Report (AR6) stated that scientific evidence of climate change threat to human well-being and the planet is unequivocal (IPCC Report, 2022; IPCC, 2021). The attribution of climatic events to these detected changes is of scientific and public interest. Fig. 7.1 depicts the findings on how scientific interest in climate change attribution and detection has grown over time. The nonlinear trend is reflective of the fact that global attribution research has lately received renewed interest among the climate change research community. The scientific developments on the subject matter were predominantly contributed by researchers affiliated with European institutions, followed by those in North America. When scientists from the developed Global North do studies in regions where they lack expertise, the framing and context of the studies may be less impactful and relevant compared to those led by locally knowledgeable scientists. There have been a few contributions from researchers in African-based institutions; however, these contributions are relatively low in number, considering the relative size of the continent. From Fig. 7.1b, Africa and South America are among the continents where the literature reflects a low participation in climate change detection and attribution. In Africa, this could be explained by limited access of researchers to high-quality observation data, poor research infrastructure, and unreliable internet services (Al-Zu'bi et al., 2022). This is despite Africa being a continent extremely vulnerable to climate change impacts, with 34 out of the 50 most climate-vulnerable countries located on the continent (ND-GAIN, 2016). However, advancements in satellite technology have made a lot of remote sensing model-derived data covering Africa available, where there is a dearth of observation data in most places. Such datasets are valuable in evaluating climate model outputs and for detection and attribution studies.

Upon conducting Network Analysis and examining a co-occurrence network by country, Kenya, South Africa, Ethiopia, and Ghana stand out among the African countries where attribution and detection studies have been most

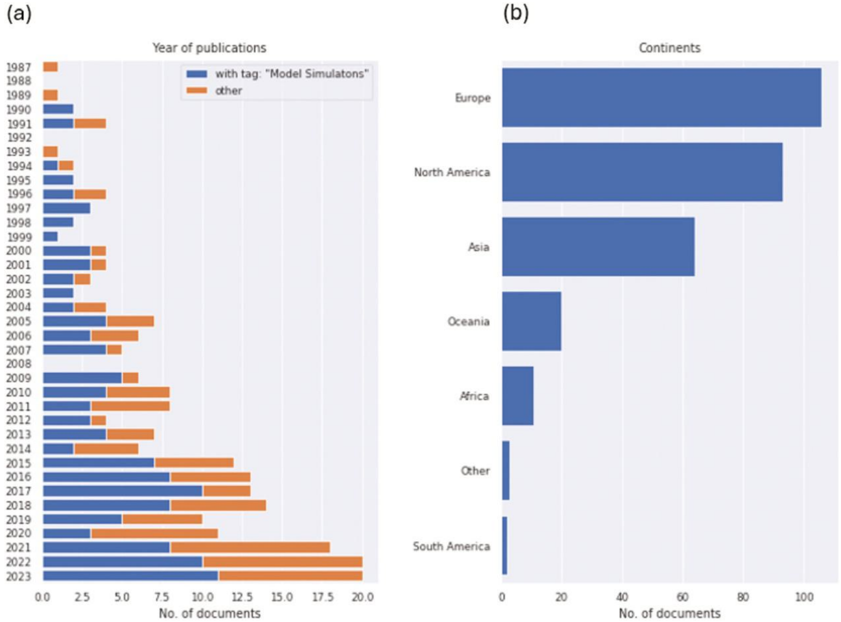

FIGURE 7.1 Summary of interest in climate-change detection and attribution published studies as per Scopus database (a) summarized by contributed articles per year and (b) contributed articles by condiment. The analysis was done using the Litstudy Python package (Heldens et al., 2022).

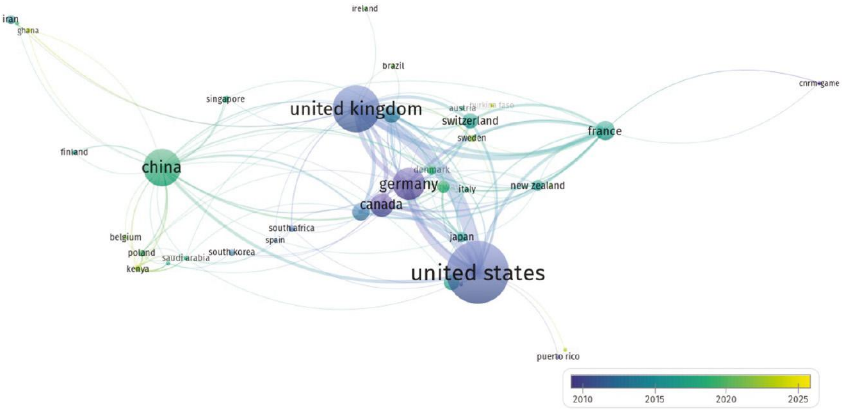

FIGURE 7.2 Co-occurrence network of climate-extremes attribution studies by country.

prevalent (see Fig. 7.2). In the figure, the thickness of the vertices is directly proportional to the number of articles published in collaboration with the countries represented by the nodes. Additionally, the size of each node corresponds to the number of papers contributed by the respective countries, with larger nodes indicating a higher number of published articles. The colors assigned to various clusters reflect the co-occurrence of countries in publications. Given that Africa is a geographically vast continent, spanning both the Southern and Northern Hemispheres, thereby experiencing diverse climate change impacts (Gemeda and Sima, 2015), there is a pressing need to devote more efforts to climate research in many other countries across Africa. Specifically, endeavors such as attribution studies hold significant potential to inform decision-makers about the merits of mitigation strategies.

The operational provision of climate attribution results through 'Operational Attribution' holds great potential for use in Africa. 'Operational Attribution' pertains to the routine production of rapid assessments regarding the influence of climate change on extreme weather events (Stott and Christidis, 2023). Significant advancements in the science of weather-event attribution and how it is effectively communicated have been notable through several efforts. Specifically, an international consortium of researchers devised a climate modeling approach for extreme-weather events detection and attribution (Stone et al., 2019). The World Weather Attribution group also came up with an effective and speedy way of conducting attribution assessments (Philip et al., 2020). European researchers have explored incorporating event attribution into climate services provisions (Otto et al., 2022), while in the UK, the Met Office has introduced rapid assessments of extreme events (Christidis, 2021). In the Global South, a collaborative effort in New Zealand has established an operational and largely automated system for rapid attribution of extreme-weather events (Tradowsky et al., 2022). Operational and coordinated services offering rapid attribution assessments can provide attribution information immediately after the occurrence of an extreme event when it is most needed. Therefore, countries in Africa can draw lessons from these efforts on how to operationalize extreme weather event attribution methods, thereby providing attribution results on such extreme events within days of occurrence. This information will enhance the public's understanding of how climate change is affecting their lives.

7.3 Main methods of climate-extremes attribution

In climate-extremes attribution studies, different approaches can be used. The particularly common methods are the event-driven forecast model-based approach (Tradowsky et al., 2023, 2022; Matte et al., 2022) and the climate model-based approach (Lott et al., 2013; Ma et al., 2017; Nangombe et al., 2020; F.E. Otto et al., 2023). Some scholars make use of both methods in the same study to evaluate anthropogenic influence in the occurrence of an extreme event (e.g., Kreienkamp et al., 2021; Otto et al., 2018; Uhe et al., 2018). Of note, no single classical approach provides satisfactory results that meet every researcher's preferences, but the different approaches can complement each other. This section provides brief overviews of these two approaches.

7.3.1 Forecast model-based method

Carrying out attribution studies on localized climate hazards such as extreme rainfall events is challenging (Matte et al., 2022). Specifically, global climate models struggle to simulate the magnitude, spatial extent, and timing of weakly forced convective events for the reasons explained in Matte et al. (2022) and Tradowsky et al. (2022). For example, when attributing flood hazards from smaller-scale phenomena like convective or orographic rainfall using global climate models, certain extrapolations and parameterization are necessary to infer attribution conclusions of these finer-scale attributes from broader-scale features. In addressing such occurrences, a more suitable approach is the forecast model-based method—a method that is used to analyze how anthropogenic climate change has impacted the severity or magnitude of an extreme event (Matte et al., 2022; Shepherd et al., 2018; Tradowsky et al., 2023).

This method, which can also be referred to as the "Storyline" extreme-event attribution method, involves simulating a particular extreme event under both factual and hypothetical counterfactual climate scenarios. Specifically, it delves into the impact of well-understood thermodynamic shifts on specific extreme events occurrences. This involves running simulations of a given extreme event under two distinct setups, each occurring within the same synoptic conditions. Specifically, when generating simulations used in this method, one setup employs a background field derived from a global model reflecting current climate conditions, while the other utilizes pre-industrialized background fields obtained by isolating and removing the influence of anthropogenic climate change to obtain hypothetical counterfactual conditions. The likelihood of occurrence under these true conditions is then compared to ascertain the anthropogenic influence in the severity of the extreme event of interest. This method is being used operationally in New Zealand, where it is semiautomated to carry out rapid attribution assessments of extreme events immediately after their occurrence in New Zealand (Tradowsky et al., 2022).

The forecast model method can measure the attributable change in local magnitude but lacks the capability to assess the likelihood of the event itself, which is a capability that is possessed by the climate model-based approach. While the forecast-model method does not draw conclusions regarding probabilities or the likelihood of extreme events occurring, it focuses on determining whether the severity of the hazard has shifted between a hypothesized natural world and the actual world. Although the forecast-based approach may appear simplistic at first glance, from a climate change attribution standpoint, the computational demands associated with generating high-resolution ensemble outputs for simulating such events present a significant challenge in Africa. Implementing this approach requires substantial computational power to execute the local area model effectively, in addition to a substantial amount of storage space required for the output data. Both requirements pose formidable challenges for most countries in Africa.

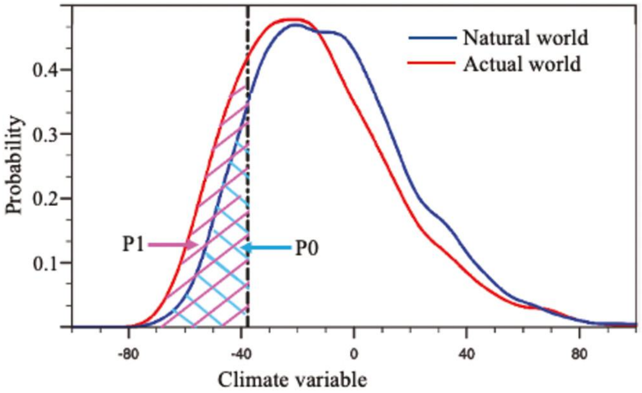

FIGURE 7.3 A sketch of the Probability Density Functions (PDF) of a climatic variable. PDF of a climate variable with and without the effect of anthropogenic influence on the climate represented in red and blue lines, respectively. The related probabilities (P1 and P0) of surpassing a prespecified observation value represented by a black vertical line are shown as hatched areas.

7.3.2 Climate model-based method

Apart from the forecast model-based approach in climate extremes attribution, one can use the climate model-based approach (Nangombe et al., 2020; Philip et al., 2018; Ma et al., 2017; Stott et al., 2004). The climate model-based method can attribute the frequency and likelihood of extreme events occurring under various climate scenarios, which the forecast model-based method cannot do. This method also uses existing global climate models that explicitly simulate the circulation patterns on a global scale and, hence, heavily rely on parameterized approximations to represent local conditions under which extreme events are experienced. It is worth mentioning that climate models are predominantly developed in developed nations and are optimized to accurately represent the climate of these nations, often at the expense of accurately capturing the climate of developing countries (James et al., 2018).

Two types of global models are principally used in climate-attribution studies using the climate-model-based approach, the type that simulates a "present" climate scenario with all the forcings present and the second that simulates a hypothetical world with only natural forcings without GHG emissions. In the Netherlands, the Royal Netherlands Meteorological Institute (KNMI) developed the Climate Explorer online platform, which used this method by incorporating the use of global climate models in analyzing trends and doing attribution studies by fitting statistical distributions for the estimation of anthropogenic signals (KNMI, 2022).

The climate model-based method uses the Fraction of Attributable Risk (FAR) and Probability Ratio (PR) techniques derived from the probability density functions (PDFs) to estimate the likelihood of anthropogenic emissions influencing the occurrence of extreme events. The key underlying concept of this method is shown in Fig. 7.3. PR represents the scale by which the likelihood of an event has changed under anthropogenic forcing, while FAR gives the fractional contribution of human activity to a particular event occurrence (i.e., the probability of an extreme event of magnitude represented by a vertical dashed line threshold occurring in the present climate (P1), compared with the probability of a similar event occurring in a hypothetical climate without anthropogenic influence (P0)). Thus, having computed the P0 and P1, results can be expressed as FAR, computed as 1-P0/P1, where a FAR value greater than 0.5 indicates a more than doubling of the probability attributed to human influence. The results can also be presented as a PR, also known as the Risk Ratio, expressed as P1/P0.

This method has largely been used on large-scale extreme events, but, with the improvement of spatial resolution of global models, there has been an increase in its use on local-scale events (Nangombe et al., 2020; Otto et al., 2023). It is worth mentioning here that the availability of such models with higher grid resolution remains limited. To employ this method, one uses available global models without running new simulations, making it the method of choice for climate-extreme attribution studies done over Africa where the availability of high-performance computers to run ensembles of high-resolution weather simulations is limited. Therefore, the following case studies presented in this chapter are based on the commonly used climate model-based method of extreme-event attribution.

7.4 Case studies of climate-hazards attribution in Africa

Natural and human systems are vulnerable to extreme weather and climate events. Consequently, as the climate continues to change due to anthropogenic influence, interest in how the changes and occurrence of extreme climate events fit within the context of climate change is also growing, as seen from the increase in many detection and attribution studies done under the World Weather Attribution program (https://www.worldweatherattribution.org/). Prolonged exposure to extremely high temperatures causes severe heat-related illness, including heat syncope, heat cramps, heat stroke, heat exhaustion, and even death in some cases (Kilbourne, 1999). This puts into context the need to investigate the contribution of anthropogenic emissions to the increasing occurrence and severity of at least one of the extreme-temperature events that occurred in Africa. A case of a record-breaking heat event that occurred around the North Africa monsoon (a monsoon region defined by He et al. (2023)) region is analyzed.

Out of the hydrometeorological hazards occurring across the world, drought ranks as one of the most severe in terms of economic loss and, consequently, the number of people it affects (Moccia et al., 2022). This is particularly problematic for Africa, where over a third of its population lives in severely drought-prone areas (Global Water Partnership – GWP, 2000). In Africa, millions of subsistence farmers depend on rain-fed agriculture in a climate system that exhibits strong natural variability (Engelbrecht and Engelbrecht, 2016). Thus, there is merit in investigating the contribution of anthropogenic emissions to the occurrence of droughts in Africa. The type of drought considered in this chapter is meteorological, defined as a prolonged lack of (or below normal) rainfall (Keyantash and Dracup, 2002). Scientific evidence incorporating attribution findings can help climate negotiators from Africa with evidence to push for more climate change mitigation action and present a justification for adaptation support, specifically access to "loss and damage" funds. Nevertheless, it should be noted that a particularly extreme climate event can occur due to internal natural variability and is hugely influenced by anthropogenic emissions. Thus, it remains impossible to fully attribute an extreme event entirely to human influence.

7.4.1 North Africa December–February 2009/2010 severe heat event

According to the World Meteorological Organization, a decadal analysis showed that global surface air temperature (SAT) averaged over the 2001–2010 decade was record-breaking since measurements began in 1850 (WMO, 2013). The global mean SAT for 2001–2010 was 0.47 °C ± 0.1 °C above the 1961–1990 average (WMO, 2013). Consequently, the decade was also the warmest on record for North Africa, reaching an alarming peak in 2010. Thus, a detection and attribution study is conducted in this section on the extremely high-temperature anomalies observed in December–February (DJF) of 2009/2010 over North Africa (NA, region shown by a black rectangle in Fig. 7.4a). This area covers the northern part of the North Africa monsoon region (He et al., 2023). Three observational gridded datasets are employed for the analysis of this extreme event and for model evaluation. These datasets are BEST v1 (Rohde et al., 2013), CRU TS4.0 (Harris et al., 2014), and GHCN v3 (Lawrimore et al., 2011). To estimate the relative contributions of anthropogenic emissions to the occurrence of this heat event, two global models are used, namely CAM5.1 (Stone et al., 2019) and MIROC5 (Shiogama et al., 2013). Two sets of simulations are considered. One set is forced by natural factors (All-Hist), while the other is forced is forced by a combination of natural and anthropogenic factors (All-Nat). The use of multiple gridded observational data and climate models is done as an attempt to overcome structural deficiency associated with the use of data from a single source. The attribution study done here follows a climate-model-based approach developed under the Detection and Attribution (D&A) framework (Stone et al., 2019). The Niño3.4 index and the North Atlantic Oscillation index (NAO) were used to explore to what extent this heat event was attributed to natural climate variability.

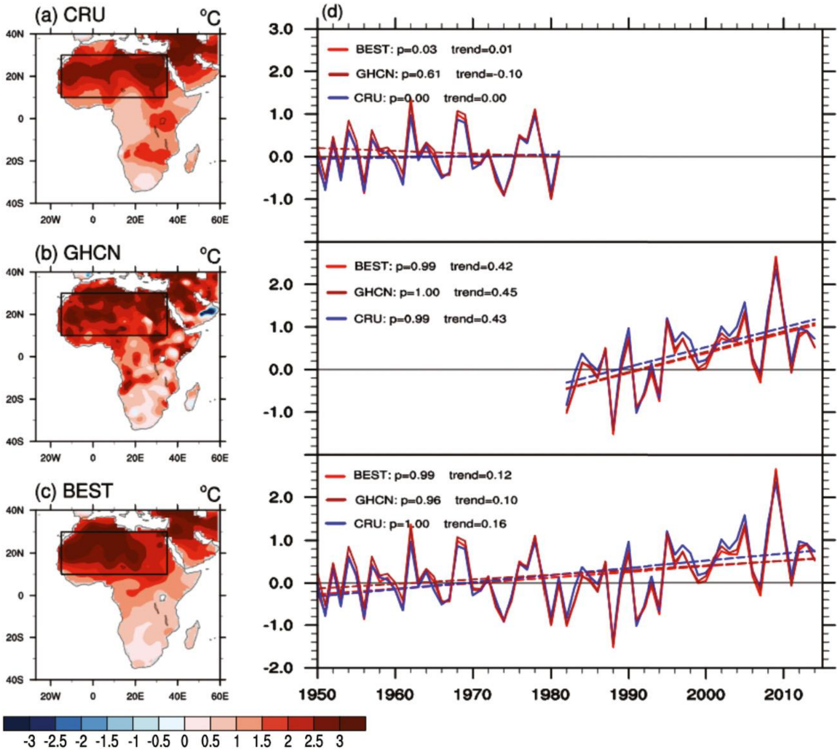

FIGURE 7.4 December–February averaged surface air temperature anomalies over North Africa. (a–c) Maps showing record-breaking 2009/2010 DJF surface air-temperature anomalies in North Africa derived from (a) CRU, (b) GHCN, and (c) BEST gridded observation datasets. (d) Maps showing time series DJF mean surface air temperature anomalies in the period (top) 1950–2015, (middle) 1983–2015, and (bottom) 1950–1983. The respective probabilities (1 minus p-value) and trend values per decade are given in the top left of each time series plot. The anomalies are relative to the 1961–1990 climatology.

7.4.1.1 Assessing the magnitude of the North Africa heat event

The DJF SAT anomalies over the period 1950–2015 over NA was record-breaking in 2009/2010 (Fig. 7.4). The weighted NA area averaged SAT anomaly for DJF 2009/2010 from the CRU, GHCN, and BEST datasets was 2.35 °C, 2.56 °C, and 2.66 °C, respectively (Fig. 7.4d). The results from the various datasets are consistent in showing the observed extremely high-temperature anomalies over NA, albeit with modest magnitude differences.

The same observational datasets were also used to analyze the trend of weighted NA areal average DJF SAT anomalies for 1950–2015 in Fig. 7.4d. The computed trends from CRU, GHCN, and BEST datasets are 0.12 °C, 0.10 °C, and 0.16 °C per decade, respectively, with all the trends being significant at a 95% confidence level. This long-term trend was then subdivided into two non-overlapping series, i.e., 1950–1983 and 1983–to 2015, with results show substantial differences in the magnitude of the trends for the two time series. For the latter, the trends are 0.42 °C, 0.45 °C, and 0.43 °C per decade, while, for the former, there is almost no trend, i.e., 0.01 °C, −0.10 °C, and 0 °C per decade from the three datasets, respectively. This implies that the positive trend in temperature in NA increased with time, becoming amplified after the 1980s.

7.4.1.2 Attribution of the North Africa December–February 2009/2010 severe heat event

7.4.1.2.1 Contribution of natural internal forcings to the North Africa heat-event occurrence

The DJF 2009/2010 magnitude of SAT, the middle (500 hPa) tropospheric level geopotential height (Z500), and Sea Surface Temperatures (SSTs) are shown in Fig. 7.5. The combination of mean SAT and the Z500 displayed in Fig. 7.5a indicates that the surface-heat event was associated with a high-pressure system in the middle levels. This consequently induced descending motion inhibiting cloudiness, thus providing ideal conditions for the formation of hot air at the surface. Furthermore, the season was associated with a strong El Niño, where SSTs of at least 1.5 °C were recorded in the Niño 3.4 region (Fig. 7.5b). This is consistent with observations from previous studies, which noted La Niña conditions at the beginning of 2009 transitioned into an El Niño phase in June and continued increasing into 2010 (e.g., Blunden et al., 2011; WMO, 2011). The El Nino phenomenon is one of the natural causes of climate change.

Climate in Africa north of the equator is modulated by the NAO, a feature of natural climate variability (Hoerling, 2010). Indeed, Fig. 7.5a depicts the status of the global middle-level geopotential height and SAT anomalies synonymous with negative NAO conditions (Hoerling, 2010; Hurrell et al., 2003; Moon et al., 2012). Furthermore, the results in Fig. 7.6 of the NA DJF SAT index regressed onto the 1000-mb air temperature and onto the Sea Level Pressure for the period 1950–2014 indicate that DJF SAT in NA is influenced by the NAO (Hoerling, 2010). Specifically, the SAT in the DJF season over NA is linearly related to conditions archetypical to the negative NAO, as highlighted by Hoerling (2010). From this, we can confirm that surface temperatures over NA during the DJF season are influenced by NAO conditions.

The DJF 2009/2010 season extreme heat event over NA coincided with a record-breaking negative NAO index of magnitude −2.49 (Fig. 7.7a). NAO in this period was negative and extreme, against the general overall upward trend of the NAO index since 1950. To demonstrate the proportional influence of NAO natural variability modes on SAT during DJF 2009/2010, we analyze the influence of NAO and its linear effect on surface temperatures in NA (Fig. 7.7b). The NAO explained most of the spatial pattern and intensity of surface temperature conditions observed in the Northern Hemisphere (Figs. 7.5a and 7.7b). Of note here is that not all the intensity of high temperatures observed in North Africa can be explained by NAO alone. Therefore, ENSO influence was assessed next.

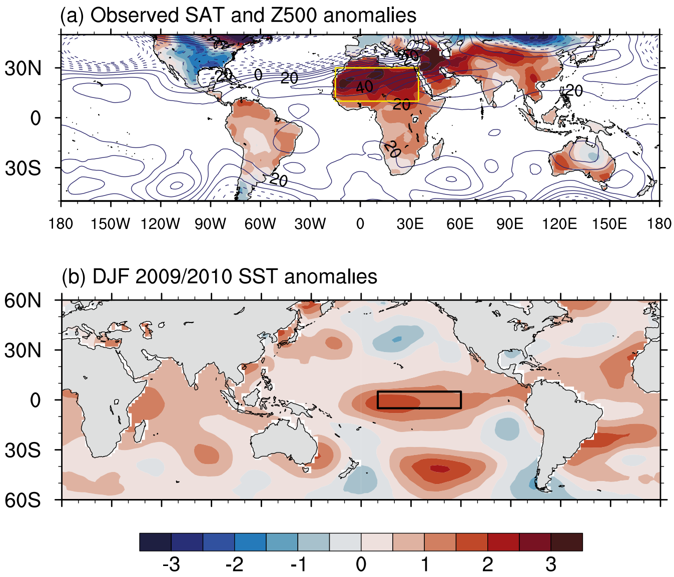

FIGURE 7.5 Oceanic and atmospheric temperature conditions in the December–February of 2009/2010. (a) Observed surface-air temperature anomalies (°C) and geopotential height anomalies (hPa) at 500 hPa level in December–February 2009/2010 (b) Sea-surface temperature anomalies in December–February 2009/2010. All anomalies are from 1961–1990 climatology. The boxes marked in (a) and (b) indicate the North Africa region and the Niño3.5 region, respectively.

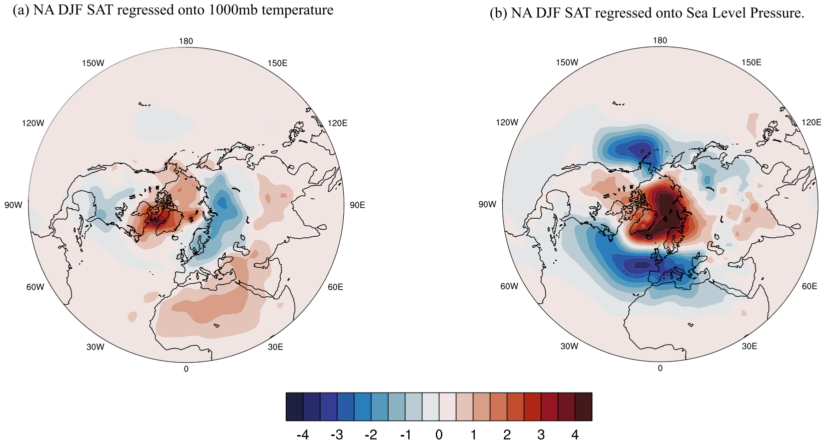

FIGURE 7.6 Influence of NAO on North Africa DJF surface air temperature. (a) North Africa's December to February surface-air temperature regressed on to the 1000mb air temperature from 1950 to 2014. (b) North Africa's December to February surface-air temperature regressed on sea level pressure from 1950 to 2014.

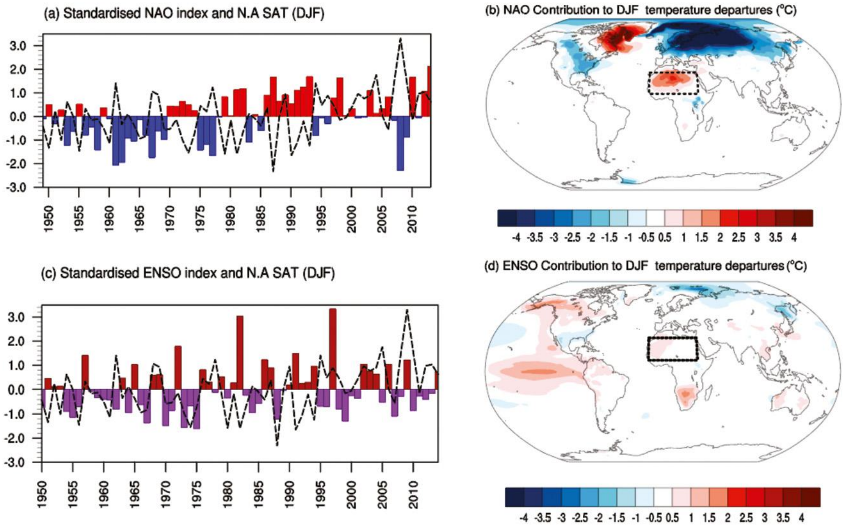

FIGURE 7.7 Influence of NAO and ENSO features on NA temperatures in DJF 2009/2010. (a, c) Time series of ENSO and NAO (bars) with overlaid NA SAT (lines) in DJF, respectively. (b, d) the relative components linearly related to the El Niño conditions and NAO conditions. The NAO impact is calculated by regressing the NAO index on the DJF 1000mb temperatures (1950–2010) and then scaling by the observed NAO seasonal value of −2.49 for 2009/2010, while the El Niño impact is calculated by regressing the index of Niño3.4 SST onto the DJF 1000-mb temperatures (1950–2014) and then scaling by the observed El Niño value of +1.6 °C for 2009/2010. Bars of ENSO positive (negative) departures are in red (blue), while those for NAO are in brown (purple). The 1000mb temperature used was derived from the NCEP-1 reanalysis dataset.

The DJF 2009/2010 season was also associated with a strong El Niño phenomenon. The contribution of El Niño to the DJF 2009/2010 season extreme heat event, which occurred over NA, could be informative in terms of determining which of the two natural climate features, El Nino or NAO, had the most influence in the occurrence of the heat event. The El Niño magnitude of that season was not record-breaking, but it was one of the highest—fitting into the list of the five strongest El Niños since 1950 for DJF (Fig. 7.7c). As was done for NAO, this El Niño was found to have influenced the pattern and intensity of this record-breaking heat event in North Africa, albeit with a lower influence than NAO (Figs. 7.5a and 7.7b, d). Although NAO and El Nino played a significant role in shaping temperature conditions during the DJF 2009/2010, it is improbable that the remarkable occurrence of this record-setting hot season over NA can be attributed solely to the NAO and El Nino effects. Thus, there is a strong possibility of external forcings, i.e., anthropogenic emissions, contributing to the occurrence of this event.

7.4.1.2.2 Contribution of anthropogenic external forcing

The preceding Section 7.4.1.2.1 discussed the potential influence of natural variability on the record-breaking temperature experienced over North Africa in DJF of 2009/2010. In this section, more exploration is done on how much other forcings influence the temperature climate in North Africa, specifically investigating the relative contribution of each component of anthropogenic forcings to the increasing temperature trend in Africa. A suite of 14 CMIP5 models with simulations forced by different anthropogenic and natural forcings is used here for the temperature trend attribution. The definitions of the model simulations used are as follows: ALL—simulations forced by a combination of natural forcings (solar radiation and volcanic aerosols) and anthropogenic forcings; ANT—simulations constituted by greenhouse gases and aerosol forcings; NAT—simulations forced by natural forcings only; AA— simulations forced by aerosols; and GHG—simulations forced by greenhouse gases. For a full list of these models and their respective specifications, see Peng et al. (2019). The trend is investigated for the 1951–2005 period, focusing on DJF (Fig. 7.8). In these models, simulations driven by natural and other external combined forcings are used to estimate the corresponding contribution to the increasing temperature trend. The analysis determines the extent to which different forcings were a factor in the intensity and trend of temperature in North Africa.

The simulations incorporating all forcings (ALL) demonstrate a pronounced DJF temperature increase over NA, signaling the combined influence of anthropogenic and natural factors (Fig. 7.8a). Comparing ANT and NAT simulations, the former exhibits the most significant temperature rise in NA, exceeding 1 °C, while in contrast, the impact of NAT remains negligible, with an insignificant increase of less than 0.2 °C (Fig. 7.8c, d). Further examination of the components of ANT reveals that GHG-based simulations contribute most substantially to the rising temperature trend, whereas AA-based simulations exhibit a significant negative effect, resulting in a cooling trend (Fig. 7.8b, e). Specifically, GHG simulations project a substantial temperature increase in NA, ranging between 1.4 °C and 1.8 °C, while by contrast, AA simulations suggest a cooling effect of magnitude ranging between −0.4 °C and −0.8 °C. This is corroborated by an earlier study that underscored the contrasting impacts of greenhouse gases and aerosols on temperature extremes, leading to a compensatory effect when both forcings are considered together (Paeth and Feichter, 2006).

The NA area-weighted averaged time series results for temperature anomalies spanning from 1951 to 2005 are illustrated in Fig. 7.8f. This figure includes time series of gridded observations and different sets of simulations driven by ALL, GHG, ANT, NAT, and AA forcings. The ‘ALL’ simulations-based trend aligns closely with that of the observations, exhibiting a correlation coefficient of 0.6, significant at the 99% level. Notably, the time series from ALL, ANT, GHG, and the observations depict an increase in temperature trends, which have become amplified from the 1980s onwards. This amplification is primarily attributed to the rising levels of greenhouse gases, as evidenced by the highest

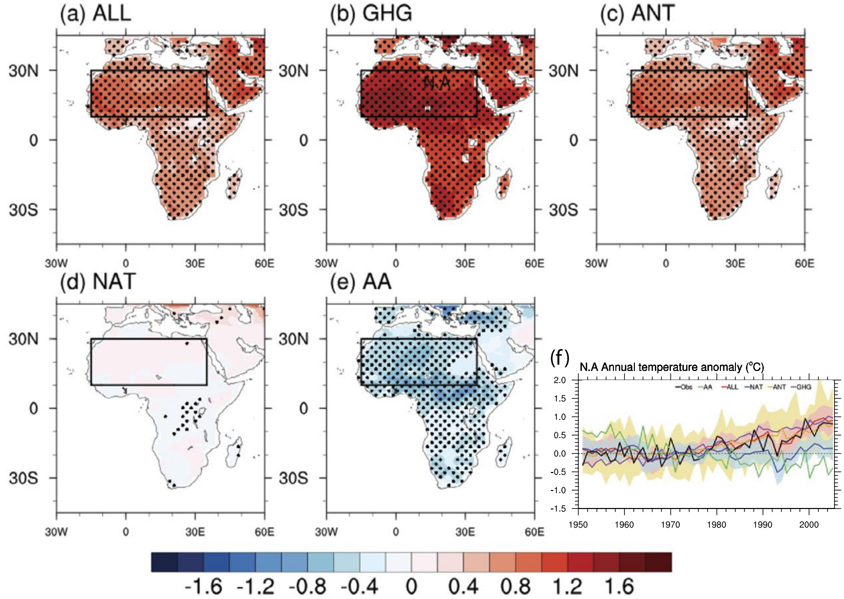

FIGURE 7.8 DJF temperature trend over the period 1951–2005 calculated from the CMIP5 multi-model mean simulations driven by (a) ALL forcings, (b) NAT forcings, (c) GHG forcings, (d) ANT forcings, and (e) AA forcings. (f) Time series of DJF temperature anomalies (°C) over North Africa. The yellow, pink, and blue shadings indicate the ±1 standard deviations of the model simulations driven by ANT, NAT, and ALL forcings, respectively. The anomalies in (f) are with respect to a 1961–1990 climatology and stippling in (a-e) indicates the grid points where the trends are statistically significant at the 90% level, and the units are in °C per 55 years.

temperature increase driven by GHGs (Fig. 7.8f). The substantial and increasing influence of anthropogenic emissions on temperature increases over NA is shown by a substantially higher and more increasing trend in the ANT-forced temperature time series than in the NAT-forced time series, particularly after the 1970s (Fig. 7.8f). Conversely, the time series from AA-forced simulations exhibit a declining temperature trend throughout the period 1951–2005.

To quantify the extent to which the DJF 2009/2010 extreme temperature event over NA is a result of anthropogenic climate change, i.e., to estimate the anthropogenic climate change proportion of risk in the occurrence of the extreme event, the CAM5.1 and MIROC5 models spanning 1959–2015 and 1960–2015, respectively, were utilized. The reliability of these model simulations for this case was tested against gridded observations and reanalysis data using empirical probability density functions (PDFs) of DJF mean temperature anomalies over NA from 1960 to 2014 (Fig. 7.9a, c). Comparing the PDFs of observational datasets with those of the CAM5.1 and MIROC5 All-Hist model simulations revealed a close match, suggesting that the DJF temperature simulations in NA align well with observations (Figs. 7.9a, c). This alignment (statistically significant distribution similarity) was confirmed using the two-

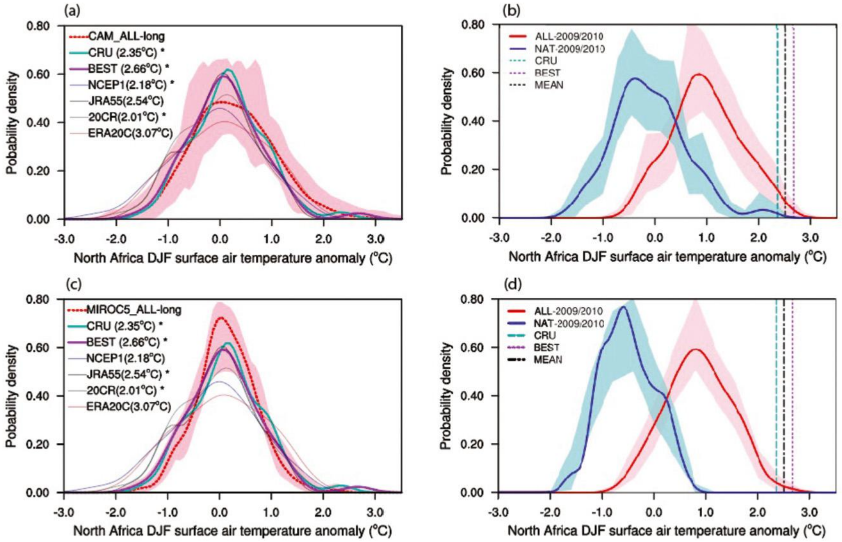

FIGURE 7.9 North African surface-air temperature anomalies. Probability density functions (PDFs) of December–February (DJF) mean SAT anomalies averaged over North Africa during 1960–2014 for observations, reanalysis, and ensemble mean of (a) CAM5.1 All-long and (c) MIROC5 All-long. The PDFs of DJF 2009/2010 mean SAT anomalies for the 100 members of CAM5.1 All-Hist and Nat-Hist in (b) and 60 members of MIROC5 All-Hist and All-Nat in (d), indicated by 'ALL-2009/2010. Reanalysis datasets NCEP1, JRA55, 20CR, and ERA20C in blue, black, sky-blue, and brown colored lines, respectively, are used. All-Hist, CRU, and BEST datasets in (a, c) are shown in bold dashed red, light green, and purple, respectively, where datasets with superscripts (*) depict a significant distribution similarity with All-long. All-Hist and Nat-Hist in (b, c) are denoted by red and blue lines, respectively, with pink and light blue shadings showing 10–90% confidence intervals. Dashed light green and purple vertical lines show observations from CRU and BEST, while the black is the average of the two.

sided Kolmogorov–Smirnov (KS) test, providing confidence in utilizing these model simulations in this case.

The PDFs of DJF 2009/2010 mean SAT anomalies averaged over NA, calculated from 100 (60) All-Hist members and 100 (60) Nat-Hist members of the CAM5.1 (MIROC5) model are shown in Fig. 7.9b, d. The substantial rightward shift of the All-Hist PDFs compared to Nat-Hist PDFs suggests an anthropogenic emission influence on the occurrence of this event (Fig. 7.9b, d). For quantification of the anthropogenic influence on this heat event occurrence, the CAM5.1 simulations estimate PR of 4.9 and 5.5 based on the CRU and BEST gridded observations, respectively, with corresponding FAR values of 80% and 82%. This can be expressed as "anthropogenic climate change is responsible for about 81% of the risk associated with this heat event which occurred in NA". On the other hand, MIROC5 simulations suggest that this event would not have occurred in the natural climate state but occurred in the current world with all anthropogenic and natural atmospheric forcings in play. This indicates a strong contribution of anthropogenic emissions to heat events in North Africa.

7.4.2 Case study 2: South Africa 2018 summer drought attribution

Here, we assess the anthropogenic influence on a severe drought event experienced during the 2018 austral summer in South Africa, situated in the southern part of the Southern Africa monsoon region. Although Southern Africa was historically not classified as a monsoon region, an updated definition now includes it within the global monsoon regions (Silvério and Grimm, 2022; Wang et al., 2020; Yim et al., 2014). The 2018 summer drought had profound consequences, causing a notable decline in maize crop yield, which is a crucial staple crop in South Africa (SADC RVAA, 2019). South Africa exports a substantial amount of maize, which it normally produces surplus (Simanjuntak et al., 2023). However, due to this drought, South Africa, together with Zambia, which is the main grain supplier in the region, experienced a decrease in the amount of maize exported, from 7.5 to 1.4 million tons (SADC RVAA, 2019). Consequently, food security in the region was compromised. The severity of this drought was exacerbated by severe water loss through the above-normal evapotranspiration experienced that season (Nangombe et al., 2020). Due to the widespread impact of this drought, this extreme event is another good example for conducting a detection and attribution study.

Here, a climate model with a large ensemble of simulations derived from the Seamless System for Prediction and Earth System Research (SPEAR) (Delworth et al., 2020) was used to assess the influence of anthropogenic climate change on the occurrence of the 2018 summer drought in South Africa. SPEAR data was specifically designed for climate prediction and projection on seasonal to multidecadal time scales (Delworth et al., 2020). The SPEAR MED version at a 50-km grid resolution was utilized in this case. These simulations encompass four 30-member ensembles, each representing different atmospheric compositions: (1) natural sources only (Nat-Hist); (2) natural plus anthropogenic sources (All-Hist); (3) future with high mitigation “Shared Socioeconomic Pathway” (SSP2-4.5); and (4) Future with low mitigation “Shared Socioeconomic Pathway” (SSP5-8.5). For further detailed information on the configuration of these model simulations, see Delworth et al. (2020). The climate model-based method of climate extremes attribution detailed in Section 7.3 is followed in this attribution case study.

7.4.2.1 Assessing the magnitude of the 2018 summer drought over South Africa

The 2018 summer drought experienced in South Africa was examined by first analyzing the first half of the rainfall season, i.e., October–December, and then the entire summer season from October to March. The reason for this was to determine if there was a late onset of the rainfall season that year, which of-

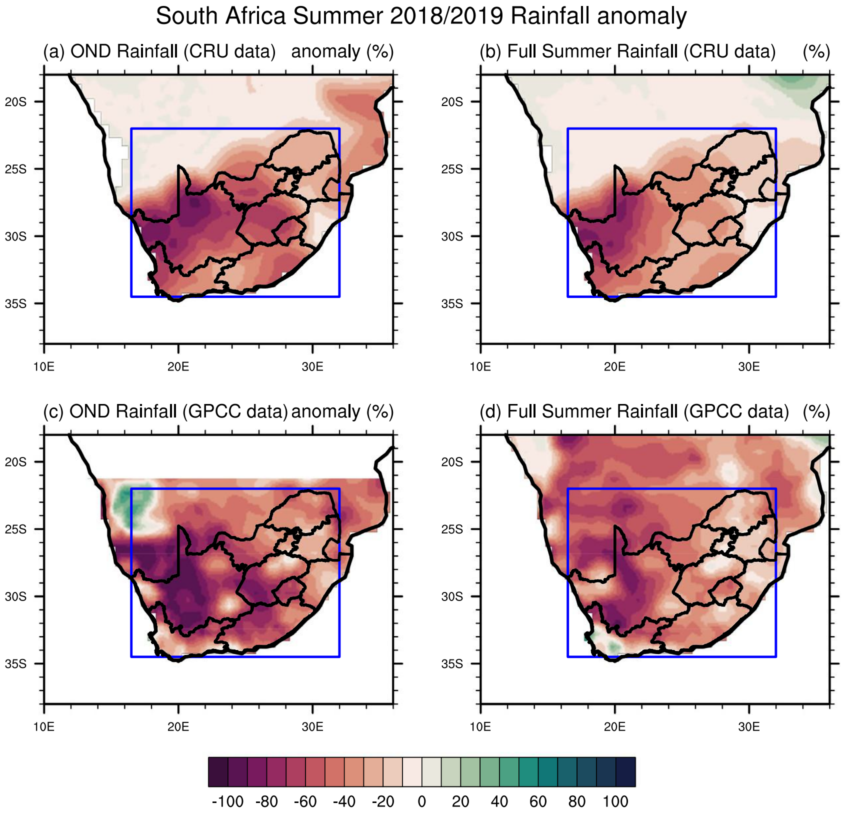

FIGURE 7.10 Summer 2018 droughts in South Africa. (a) and (c) are the October–December 2018 rainfall anomalies from CRU and GPCC gridded observational datasets, respectively, while (b) and (d) show the same but for the full October–March summer season. The anomalies are in % with respect to 1961–1990 climatology, and the blue boxes are the occurrence areas of the drought.

ten contributes to whether the season turns out to be a drought or a normal one (Dunning et al., 2018). During this first half of the 2018 summer season, rainfall was more than extremely (60%) below normal (Fig. 7.10a, c), resulting in reduced regional crop yield in most parts of Southern Africa, where livelihoods are primarily agriculture-based. The overall rainfall for the season turned out to be significantly below normal, with a total rainfall anomaly of more than 50% below normal in most areas, especially in the eastern parts of the country (Fig. 7.10b, d).

7.4.2.2 Attribution of the 2018 summer drought over South Africa

The period October to December 2018 was characterized by a notable reduction of the usual moisture influx over South Africa, coupled with diminished convection owing to a weakened tropical temperate trough (Ibebuchi, 2021).

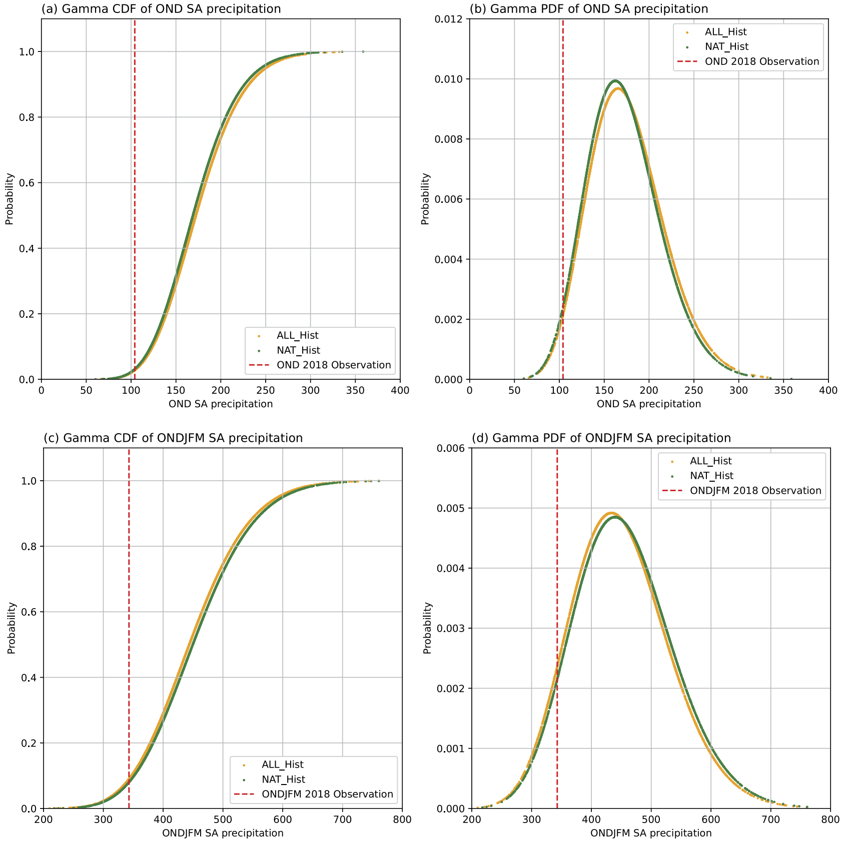

FIGURE 7.11 Cumulative and probability density functions for area-averaged future precipitation over South Africa accumulated in (a) Oct–Dec 2018 and (b) Oct–Mar 2018/2019 under All-Hist (orange) and Nat-Hist (green) climate scenarios. The vertical red lines are the thresholds for the 2018/2019 drought.

This departure from the norm contrasted with the typical northeasterly moisture transport originating from the tropical Indian Ocean during this time of the year (Nangombe et al., 2020). Such circumstances are commonly experienced during El Niño occurrence, suggesting that natural climate variability contributed to the occurrence of this drought.

7.4.2.2.1 Estimating the anthropogenic influence on the SA 2018 drought occurrence

The Gamma distribution was used to estimate the probabilities of the drought occurring in different climates. Precipitation distributions are well-fitted by the gamma distributions (Martinez-Villalobos and Neelin, 2019). This distribution has also been used in past extreme precipitation studies over Southern

TABLE 7.1 Probabilities of the 2018 drought occurring under different climate scenarios, estimated by the gamma distribution.

Hazard	Probability: Natural* world (%)	Probability: Current world (%)	Probability: SSP2-45 scenario (%)	Probability: SSP5-85 scenario (%)
Early Summer (Oct-Dec) 2018	**3%**	**3%**	**2%**	**3%**
Full Summer (Oct-Mar) 2018	**7%**	**9%**	**8%**	**9%**

Africa (Bellprat et al., 2015; Husak et al., 2007). The cumulative density functions (CDF) and PDFs of precipitation averaged over South Africa (marked in Fig. 7.10) for the first half and the full summer season are depicted in Fig. 7.11. The area under the curves from the left tail bounded by the vertical line depicts the magnitude of probabilities of a drought event occurring under the All-Hist and Nat-Hist climates. Specifically, the CDF and PDF curves drawn from the October–December and October–March period averaged over South Africa under All-Hist and Nat-Hist climate are shown in Fig. 7.11a, b. There are minimal differences in the All-Hist climate curves compared to the Nat-Hist climate curves. For example, the probability of the October–March 2018/2019 drought occurring under All-Hist and Nat-Hist climates is 9% and 7%, respectively (Table 7.1). Thus, this suggests that there is a slight anthropogenic emissions influence on the occurrence of this drought event. This finding relates to the one by Ha et al. (2020) who concluded that the decreasing trend in rainfall in the Southern Africa monsoon region can be attributed to GHG emissions. However, the small influence of anthropogenic emissions in this drought's occurrence suggests that natural variability may have also played a role. The El Nino at play during this period (Johnson et al., 2019), likely contributed substantially to the occurrence of this drought. The results here show that anthropogenic emissions do not always have a strong influence on increasing the intensity of all climate hazards.

7.4.2.2.2 Assessing the likelihood of the SA 2018 drought in the future

To demonstrate the future climates of the areas covered by the droughts under various climate scenarios, Fig. 7.12 depicts CDF and PDF curves of area-averaged Oct–Dec and Oct–Mar rainfall generated for the drought area marked in Fig. 7.10. We found leftward shifts of the SSP5-8.5 CDF and PDF curves relative to the SSP2-4.5 CDF and PDF curves. This implies that rainfall magnitude will be less under the SSP5-8.5 future scenario than under the SSP2-4.5 scenario for the areas where the drought occurred. Thus, it implies that the magnitude and likelihood of droughts will be higher under the SSP5-8.5 climate than under the SSP2-4.5 climate. The probabilities of droughts resembling both the October–December 2018 and the October–March 2018 drought in South Africa

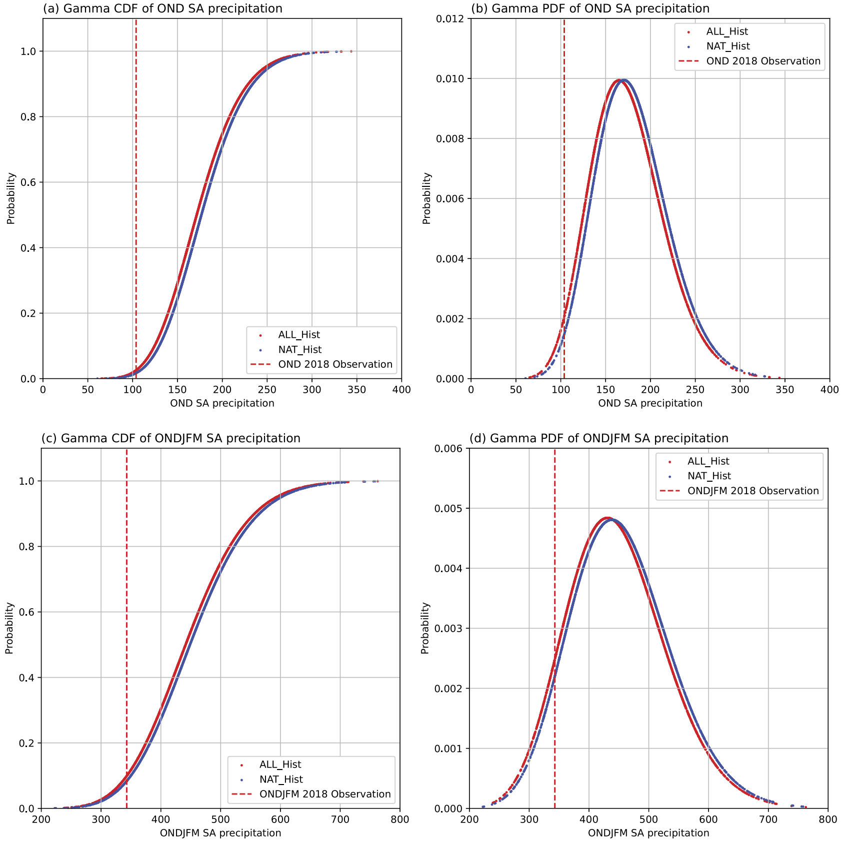

FIGURE 7.12 Cumulative and probability density functions for area-averaged future precipitation over South Africa accumulated over (a) October–December 2018 and (b) October–March 2018/2019 under SSP5-8.5 (red) and SSP2-4.5 (blue) climate scenarios. The vertical red lines are the thresholds for the 2018 drought.

occurring under low and high mitigation future scenarios are shown in Table 7.1. Specifically, the probability of the October–March 2018/2019 drought occurring under low mitigation scenario (SSP5-8.5) and high mitigation scenario (SSP2-4.5) is 9% and 8%, respectively. Although there is a small difference in the odds of this drought occurring under low and high mitigation scenarios, advocating for heightened global mitigation endeavors to curtail global warming still holds merit in mitigating the occurrence of these kinds of hazards.

Due to the large geographical size of South Africa, diverse topography, and influence of the warm Agulhas current in the Indian Ocean and the cool Benguela current in the Atlantic Ocean, the country is characterized by various climate zones based on the Köppen–Geiger classification (Beck et al., 2018). Using this classification, we classified the country into five regions, i.e.,

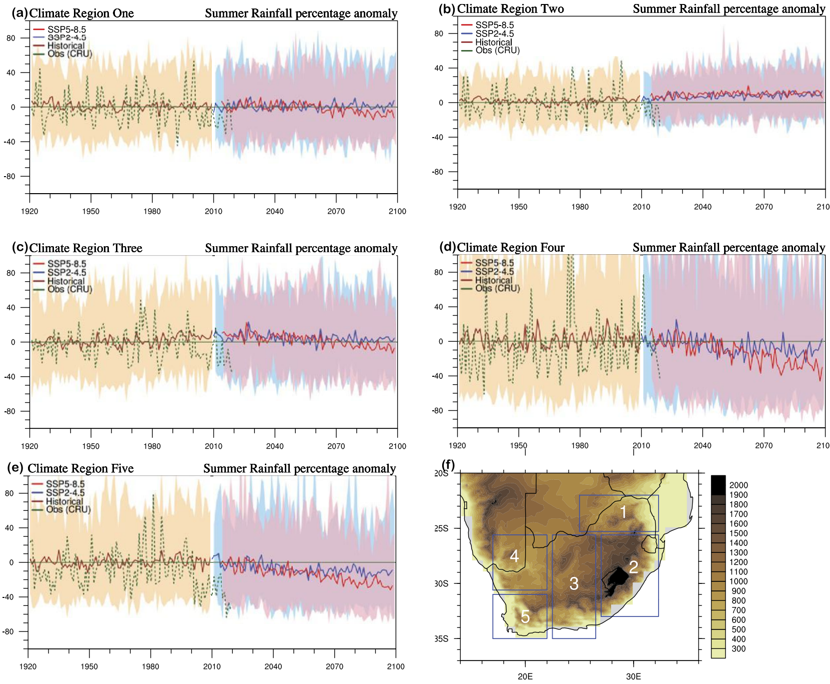

FIGURE 7.13 Precipitation time series for the climate zones in South Africa based on All-Hist (brown), CRU observations (green), SSP2.4.5 (blue), and SSP5-8.5 (red) datasets in summer. The cream, sky-blue and gray shading show the model spread of the All-Hist, SSP2.4.5, and SSP5-8.5 time series, respectively. The anomalies are from a 1961–1990 baseline, and (e) shows the climate zones used overlaid on the topography.

region 1—semiarid and hot summers; region 2—heavy rain and cool to hot summers; region 3—cold and semi-arid; region 4—hot and arid; region 5—winter rain and cold temperatures. We, therefore, analyzed precipitation trends averaged over these five regions of South Africa under different climate scenarios. These five climatic zones shown in Fig. 7.13f are derived from the Köppen climate classification (Beck et al., 2018). Understanding these zones is crucial for anticipating the impact of climate change across the country. Future climates over these regions may respond differently to anthropogenic climate change. For instance, arid regions may experience worsened droughts, while areas with year-round rainfall could face increased flooding risks or less rain. The rainfall average for each zone is based on the October to March summer season using SPEAR-based model ensembles and CRU gridded observations covering the period 1920–2100.

The rainfall time series averaged over South Africa's five climate regions under SSP2-4.5 and SSP5-8.5 scenarios vary (Fig. 7.13). The low mitigation SSP5-8.5 based time series has a higher decreasing trend compared to the high mitigation SSP2-4.5 scenario one. The time series under these two scenarios exhibit a decrease in future precipitation in all the regions except region 2, with the two future-based time series diverging as they approach the end of the century. Thus, the model suggests that anthropogenic emissions will be a contributing factor to the decrease in rainfall towards the end of the century, especially in regions 4 and 5 (Fig. 7.13d, e). For region 2, the time series maintains a slightly positive trend up to the end of the century for all the future scenarios. However, this result is marked by high uncertainty, as depicted by the wide model spread of the simulations. Region 2 receives the highest rainfall in the country, hence, more precipitation in the future might bring flooding challenges to the area. Arid regions 4 and 5 have a substantially decreasing precipitation trend in the future compared to the other zones, hence, there is a greater likelihood of droughts worsening the water security situation in the western half of the country.

7.5 Conclusion

In laying the groundwork for a discussion on climate attribution in Africa, revisiting the methodologies employed and highlighting their strengths is essential. From the reviewed literature, two predominant methods emerge in attribution studies: the forecast model-based- and climate model-based methods. The forecast model-based approach aims to discern how the magnitude of specific extreme events can be attributed to anthropogenic climate change. Conversely, the climate model-based approach focuses on determining the probability of certain events occurring under anthropogenic climate change compared to natural climate variability.

Two case studies were carried out, and detection and attribution studies were done using the climate model-based method. The approach is used to evaluate the likely influences of natural climate variability and/or anthropogenic emissions in the occurrence of two severe climate hazard events in the North Africa and Southern Africa monsoon regions. We used the climate model-based method in both case studies instead of employing the forecast model-based approach for one of them primarily because we lacked access to the high computational resources required for the latter. Nonetheless, the two case studies focus on hazards that occurred in two monsoon regions in Africa: One covers a temperature extreme event, while the other covers a precipitation event. Specifically, the two cases were the record-breaking December to February 2009/2010 hot season in North Africa (Fig. 7.4) and the severe 2018/2019 summer drought in South Africa (Fig. 7.10). For the former, North Africa experienced a significant surface air temperature anomaly of magnitude 2.5 °C above normal. The attribution analysis showed that the occurrence of this event can be attributed to the natural stochastic positive middle-level high-pressure anomalies, reinforced by a strong El Niño and a record-breaking negative North Atlantic Oscillation index (Figs. 7.5 and 7.7). While these natural variability modes played a substantial role in this event, anthropogenic climate change forcings amplified its likelihood by almost five-fold, and 79% of this heat event is attributable to anthropogenic influence. The findings presented here indicate that greenhouse gases and all anthropogenic forcings combined exert the strongest influence on the increase in temperature over North Africa, while the influence from natural variability is comparatively minimal (Fig. 7.8). This underscores that anthropogenic factors drive temperature in North Africa to increase more rapidly than natural variability. Conversely, aerosol forcings induce a cooling effect, particularly towards the tropics (Fig. 7.8), where wildfires are prevalent.

For the South Africa case study, the country experienced a severe rainfall deficit in the 2018/2019 summer season, where over 50% of below-normal rainfall was recorded (Fig. 7.10). The detection and attribution study we conducted on this drought event suggested that anthropogenic emissions played a role, though minimal, in its occurrence. El Nino played a major role in the occurrence of this drought. In the future, similar drought hazards in South Africa are projected to recur slightly more frequently under a low mitigation scenario than under a high mitigation scenario (Table 7.1, Fig. 7.12), emphasizing the importance of global mitigation efforts to alleviate these risks. Additionally, examining the influence of anthropogenic emissions on climate across different climatic regions within the same Southern African country reveals varied impacts on precipitation trends (Fig. 7.13), highlighting the need for region-specific adaptation strategies. We classified South Africa into 5 climatic regions. Region 2 currently receives the highest rainfall and is experiencing an increasing trend, posing potential flooding challenges from the projected future precipitation increase. Conversely, hot and arid regions 4 and 5 are experiencing significant decreases in rainfall. This could worsen water challenges in these regions. The differing effects of anthropogenic emissions on precipitation are observed across all five regions; particularly, a decline in precipitation is pronounced in regions 4 and 5, highlighting the varied impacts within the same country.

Understanding the impact of climate change on precipitation patterns in Africa is crucial for effective mitigation and adaptation strategies. However, confidence in precipitation-based attribution studies remains low due to significant uncertainty arising from various factors, including limitations in observational data quality (Otto et al., 2013), challenges in modeling precipitation processes (Jenkins et al., 2002; Wu et al., 2020), and difficulties in accurately attributing specific events to anthropogenic influences (Hulme, 2014; Sonali and Nagesh Kumar, 2020). Climate models sensitive to carbon dioxide play a key role in attribution methods for climate extremes, but their reliance on parameterized approximations and the computational demands associated with high-resolution modeling present significant challenges (Gillett et al., 2016), particularly in African countries where resources are often limited. Moreover, limited investment in climate research and infrastructure within Africa further constrains attribution studies, with many being conducted by institutions outside the continent. Despite these challenges, attribution studies are essential for informing policy decisions and enhancing resilience to climate-related risks in Africa.

Overall, the attribution of extreme climate events in Africa is vital for understanding and mitigating their impacts on society. Policy formulation should integrate insights from climate-model oriented and weather forecast-oriented attribution studies to effectively address climate risks. Building research infrastructure and capacity for dynamic modeling is essential to obtain credible estimates of potential climate risks and inform adaptation strategies across Africa. Collaboration and investment in automated systems, as witnessed in other regions like New Zealand, can further enhance capabilities in climate research and risk assessment in Africa.

References

Ackerley, D., Booth, B.B.B., Knight, S.H.E., Highwood, E.J., Frame, D.J., Allen, M.R., Rowell, D.P., 2011. Sensitivity of Twentieth-Century Sahel rainfall to sulfate aerosol and CO2 forcing. Journal of Climate. https://doi.org/10.1175/JCLI-D-11-00019.1.

Adelekan, I.O., Simpson, N.P., Totin, E., Trisos, C.H., 2022. IPCC Sixth Assessment Report (AR6): Climate Change 2022-Impacts, Adaptation and Vulnerability: Regional Factsheet Africa.

Al-Zu'bi, M., Dejene, S.W., Hounkpè, J., Kupika, O.L., Lwasa, S., Mbenge, M., Mwongera, C., Ouedraogo, N.S., Touré, N.E., 2022. African perspectives on climate change research. Nature Climate Change 12 (12), 1078–1084.

Amouin, J., Kouadio, K.Y., Kacou, M., Djakouré, S., Ta, S., 2020. Diagnosis of the causes of the rain flooding in June in the West Africa coastal area. Atmospheric and Climate Sciences 11 (01), 11.

Beck, H.E., Zimmermann, N.E., McVicar, T.R., Vergopolan, N., Berg, A., Wood, E.F., 2018. Present and future Köppen–Geiger climate classification maps at 1-km resolution. Scientific Data 5. https://doi.org/10.1038/sdata.2018.214.

Bellprat, O., Lott, F.C., Gulizia, C., Parker, H.R., Pampuch, L.A., Pinto, I., Ciavarella, A., Stott, P.A., 2015. Unusual past dry and wet rainy seasons over Southern Africa and South America from a climate perspective. Weather and Climate Extremes 9, 36–46.

Biasutti, M., 2019. Rainfall trends in the African Sahel: characteristics, processes, and causes. Wiley Interdisciplinary Reviews: Climate Change 10 (4), e591.

Bindoff, N.L., Stott, P.A., AchutaRao, K.M., Allen, M.R., Gillett, N., Gutzler, D., Hansingo, K., Hegerl, G., Hu, Y., Jain, S., Mokhov, I.I., Overland, J., Perlwitz, J., Sebbar, R., Zhang, X., 2013. Detection and Attribution of Climate Change: From Global to Regional. In Climate Change 2013: The Physical Science Basis. Contribution of Working Group I to the Fifth Assessment Report of the Intergovernmental Panel on Climate Change, pp. 867–952.

Blunden, J., Arndt, D.S., Baringer, M.O., 2011. State of the climate in 2010. Bulletin of the American Meteorological Society 92 (6), S1–S236.

Booth, B.B., Dunstone, N.J., Halloran, P.R., Andrews, T., Bellouin, N., 2012. Aerosols implicated as a prime driver of twentieth-century North Atlantic climate variability. Nature 484 (7393), 228–232.

Christidis, N., 2021. Using CMIP6 multi-model ensembles for near real-time attribution of extreme events. Hadley Centre Technical Note, 107.

Delworth, T.L., Cooke, W.F., Adcroft, A., Bushuk, M., Chen, J.H., Dunne, K.A., Ginoux, P., Gudgel, R., Hallberg, R.W., Harris, L., Harrison, M.J., Johnson, N., Kapnick, S.B., Lin, S.J., Lu, F., Malyshev, S., Milly, P.C., Murakami, H., Naik, V., et al., 2020. SPEAR: the next generation GFDL modeling system for seasonal to multidecadal prediction and projection. Journal of Advances in Modeling Earth Systems 12 (3). https://doi.org/10.1029/2019MS001895.

Dunning, C.M., Black, E., Allan, R.P., 2018. Later wet seasons with more intense rainfall over Africa under future climate change. Journal of Climate. https://doi.org/10.1175/JCLI-D-18-0102.1.

Ebi, K.L., Ndebele-Murisa, M.R., Newsham, A.J., Schleyer, M., 2014. IPCC WGII AR5 Chapter 22. Africa.

Engelbrecht, C.J., Engelbrecht, F.A., 2016. Shifts in Köppen-Geiger climate zones over southern Africa in relation to key global temperature goals. Theoretical and Applied Climatology 123 (1–2). https://doi.org/10.1007/s00704-014-1354-1.

Eyring, V., Bony, S., Meehl, G.A., Senior, C.A., Stevens, B., Stouffer, R.J., Taylor, K.E., 2016. Overview of the Coupled Model Intercomparison Project Phase 6 (CMIP6) experimental design and organization. Geoscientific Model Development. https://doi.org/10.5194/gmd-9-1937-2016.

Gemeda, D.O., Sima, A.D., 2015. The impacts of climate change on African continent and the way forward. Journal of Ecology and the Natural Environment 7 (10), 256–262.

Gillett, N.P., Shiogama, H., Funke, B., Hegerl, G., Knutti, R., Matthes, K., Santer, B.D., Stone, D., Tebaldi, C., 2016. The detection and attribution model intercomparison project (DAMIP v1. 0) contribution to CMIP6. Geoscientific Model Development 9 (10), 3685–3697.

Global Water Partnership – GWP, 2000. Towards water security: a framework for action. In: GWP.

Ha, K.-J., Kim, B.-H., Chung, E.-S., Chan, J.C., Chang, C.-P., 2020. Major factors of global and regional monsoon rainfall changes: natural versus anthropogenic forcing. Environmental Research Letters 15 (3), 034055.

Haarsma, R.J., Roberts, M.J., Vidale, P.L., Senior, C.A., Bellucci, A., Bao, Q., Chang, P., Corti, S., Fučkar, N.S., Guemas, V., 2016. High resolution model intercomparison project (HighResMIP v1. 0) for CMIP6. Geoscientific Model Development 9 (11), 4185–4208.

Harris, I., Jones, P.D., Osborn, T.J., Lister, D.H., 2014. Updated high-resolution grids of monthly climatic observations—the CRU TS3.10 dataset. International Journal of Climatology 34 (3), 623–642. https://doi.org/10.1002/joc.3711.

He, J., Sun, W., Wang, J., Wang, B., Liu, J., 2023. Strength of the North African monsoon in the Last Interglacial and under future warming. Atmospheric and Oceanic Science Letters 16 (3), 100320.

Heldens, S., Sclocco, A., Dreuning, H., van Werkhoven, B., Hijma, P., Maassen, J., van Nieuwpoort, R.V., 2022. Litstudy: a Python package for literature reviews. SoftwareX 20, 101207.

Herring, S.C., Hoerling, M.P., Kossin, J.P., Peterson, T.C., Stott, P.A., 2015. Explaining extreme events of 2014 from a climate perspective. Bulletin of the American Meteorological Society 96 (12), S1–S172. https://doi.org/10.1175/BAMS-ExplainingExtremeEvents2014.1.

Hoerling, M., 2010. Understanding the mid-Atlantic snowstorms during the winter of 2009-2010. Expert assessment report of the National Oceanic and Atmospheric Administration. NOAA, p. 16. http://www.esrl.noaa.gov/psd/csi/images/NOAA_AttributionTeam_SnowstormReport.pdf.

Hulme, M., 2014. Attributing weather extremes to 'climate change': a review. Progress in Physical Geography 38 (4), 499–511.

Hurrell, J.W., Kushnir, Y., Ottersen, G., Visbeck, M., 2003. An overview of the North Atlantic oscillation. In: Geophysical Monograph Series. https://doi.org/10.1029/134GM01.

Husak, G.J., Michaelsen, J., Funk, C., 2007. Use of the gamma distribution to represent monthly rainfall in Africa for drought monitoring applications. International Journal of Climatology: A Journal of the Royal Meteorological Society 27 (7), 935–944.

Hwang, Y.-T., Frierson, D.M., Kang, S.M., 2013. Anthropogenic sulfate aerosol and the southward shift of tropical precipitation in the late 20th century. Geophysical Research Letters 40 (11), 2845–2850.

Ibebuchi, C.C., 2021. Revisiting the 1992 severe drought episode in South Africa: the role of El Niño in the anomalies of atmospheric circulation types in Africa south of the equator. Theoretical and Applied Climatology 146 (1), 723–740.

IPCC, 2021. Climate Change 2021—The Physical Science Basis—Summary for Policymakers. Climate Change 2021: The Physical Science Basis.

IPCC Report, I., 2022. Climate change 2022: Impacts, Adaptation and Vulnerability. Summary for policymakers. Contribution of Working Group II to the Sixth Assessment Report of the Intergovernmental Panel on Climate Change. *United Nations Environment Programme UNEP*, *AR6*.

James, R., Washington, R., Abiodun, B., Kay, G., Mutemi, J., Pokam, W., Hart, N., Artan, G., Senior, C., 2018. Evaluating climate models with an African lens. Bulletin of the American Meteorological Society 99 (2), 313–336.

Jenkins, G.S., Adamou, G., Fongang, S., 2002. The challenges of modeling climate variability and change in West Africa. Climatic Change 52 (3), 263–286.

Johnson, N.C., L'Heureux, M.L., Chang, C., Hu, Z., 2019. On the delayed coupling between ocean and atmosphere in recent weak El Niño episodes. Geophysical Research Letters 46 (20), 11416–11425.

Keyantash, J., Dracup, J.A., 2002. The quantification of drought: an evaluation of drought indices. Bulletin of the American Meteorological Society 83 (8), 1167–1180.

Kilbourne, E.M., 1999. The spectrum of illness during heat waves. American Journal of Preventive Medicine. https://doi.org/10.1016/S0749-3797(99)00016-1.

Kimutai, J., Barnes, C., Zachariah, M., Philip, S., Kew, S., Pinto, I., Wolski, P., Koren, G., Vecchi, G., Yang, W., Li, S., 2023. Human-induced climate change increased drought severity in Horn of Africa.

KNMI, 2022. KNMI Climate Explorer. Royal Netherlands Meteorological Institute. https://climexp.knmi.nl/. (Accessed 12 May 2024).

Knutson, T., Kossin, J., Mears, C., Perlwitz, J., Wehner, M., 2017. Detection and attribution of climate change.

Kreienkamp, F., Philip, S.Y., Tradowsky, J.S., Kew, S.F., Lorenz, P., Arrighi, J., Belleflamme, A., Bettmann, T., Caluwaerts, S., Chan, S.C., 2021. Rapid attribution of heavy rainfall events leading to the severe flooding in Western Europe during July 2021. In: World Weather Attribution.

Lawal, Kamoru A., Abatan, Abayomi A., Angélil, Oliver, Olaniyan, Eniola, Olusoji, Victoria H., Oguntunde, Philip G., Lamptey, Benjamin, et al., 2016. 13. The late onset of the 2015 wet season in Nigeria. Bulletin of the American Meteorological Society 97 (12), S63–S69.

Lawrimore, J.H., Menne, M.J., Gleason, B.E., Williams, C.N., Wuertz, D.B., Vose, R.S., Rennie, J., 2011. An overview of the Global Historical Climatology Network monthly mean temperature data set, version 3. Journal of Geophysical Research. Atmospheres 116 (D19).

Lott, F.C., Christidis, N., Stott, P.A., 2013. Can the 2011 East African drought be attributed to human-induced climate change? Geophysical Research Letters 40 (6), 1177–1181. https://doi.org/10.1002/grl.50235.

Ma, S., Zhou, T., Stone, D.A., Angélil, O., Shiogama, H., 2017. Attribution of the July-August 2013 heat event in Central and Eastern China to anthropogenic greenhouse gas emissions. Environmental Research Letters 12 (5). https://doi.org/10.1088/1748-9326/aa69d2.

Martinez-Villalobos, C., Neelin, J.D., 2019. Why do precipitation intensities tend to follow gamma distributions? Journal of the Atmospheric Sciences 76 (11), 3611–3631.

Matte, D., Christensen, J.H., Feddersen, H., Vedel, H., Nielsen, N.W., Pedersen, R.A., Zeitzen, R.M., 2022. On the potentials and limitations of attributing a small-scale climate event. Geophysical Research Letters 49 (16), e2022GL099481.

Moccia, B., Mineo, C., Ridolfi, E., Russo, F., Napolitano, F., 2022. SPI-based drought classification in Italy: influence of different probability distribution functions. Water 14 (22), 3668.

Moon, J.-Y., Wang, B., Ha, K.-J., 2012. MJO modulation on 2009/10 winter snowstorms in the United States. Journal of Climate 25 (3), 978–991.

Nangombe, S., Zho, T., Zhang, L., Zhang, W., 2020. Attribution of the 2018 October–December drought over south southern Africa. Bulletin of the American Meteorological Society. https://doi.org/10.1175/BAMS-D-19-0179.1.

ND-GAIN, 2016. Rankings |ND-GAIN country index. https://gain.nd.edu/our-work/country-index/rankings/.

Nicholson, S.E., Fink, A.H., Funk, C., Klotter, D.A., Satheesh, A.R., 2022. Meteorological causes of the catastrophic rains of October/November 2019 in equatorial Africa. Global and Planetary Change 208, 103687.

Otto, F.E., Kew, S., Philip, S., Stott, P., Oldenborgh, G.J.V., 2022. How to provide useful attribution statements: lessons learned from operationalizing event attribution in Europe. Bulletin of the American Meteorological Society 103 (3), S21–S25.

Otto, F.E.L., 2015. Climate change: attribution of extreme weather. Nature Geoscience 8 (8), 581–582. https://doi.org/10.1038/ngeo2484.

Otto, F.E.L.L., Jones, R.G., Halladay, K., Allen, M.R., 2013. Attribution of changes in precipitation patterns in African rainforests. Philosophical Transactions of the Royal Society B: Biological Sciences 368 (1625), 20120299. https://doi.org/10.1098/rstb.2012.0299.

Otto, F.E.L., Wolski, P., Lehner, F., Tebaldi, C., Van Oldenborgh, G.J., Hogesteeger, S., Singh, R., Holden, P., Fučkar, N.S., Odoulami, R.C., New, M., 2018. Anthropogenic influence on the drivers of the Western Cape drought 2015–2017. Environmental Research Letters. https://doi.org/10.1088/1748-9326/aae9f9.

Otto, F.E., Zachariah, M., Saeed, F., Siddiqi, A., Kamil, S., Mushtaq, H., Arulalan, T., AchutaRao, K., Chaithra, S.T., Barnes, C., 2023. Climate change increased extreme monsoon rainfall, flooding highly vulnerable communities in Pakistan. Environmental Research: Climate 2 (2), 025001.

Otto, F., Harrington, L., Schmitt, K., Philip, S., Sarah, K., 2020. Challenges to understanding extreme weather changes in lower income countries. Bulletin of the American Meteorological Society 101 (10), E1851–E1860. https://doi.org/10.1175/BAMS-D-19-0317.1.

Paeth, H., Born, K., Girmes, R., Podzun, R., Jacob, D., 2009. Regional climate change in tropical and Northern Africa due to greenhouse forcing and land use changes. Journal of Climate 22 (1), 114–132. https://doi.org/10.1175/2008JCLI2390.1.

Paeth, H., Feichter, J., 2006. Greenhouse-gas versus aerosol forcing and African climate response. Climate Dynamics 26, 35–54.

Peng, D., Zhou, T., Zhang, L., Zou, L., 2019. Detecting human influence on the temperature changes in Central Asia. Climate Dynamics 53, 4553–4568.

Philip, S., Kew, S.F., van Oldenborgh, G.J., Otto, F., O'Keefe, S., Haustein, K., King, A., Zegeye, A., Eshetu, Z., Hailemariam, K., Singh, R., Jjemba, E., Funk, C., Cullen, H., 2018. Attribution analysis of the Ethiopian drought of 2015. Journal of Climate 31 (6), 2465–2486. https://doi.org/10.1175/JCLI-D-17-0274.1.

Philip, S., Kew, S., van Oldenborgh, G.J., Otto, F., Vautard, R., van Der Wiel, K., King, A., Lott, F., Arrighi, J., Singh, R., 2020. A protocol for probabilistic extreme event attribution analyses. Advances in Statistical Climatology, Meteorology and Oceanography 6 (2), 177–203.

Rohde, R., Muller, R., Jacobsen, R., Perlmutter, S., Mosher, S., 2013. Berkeley Earth temperature averaging process. Geoinformatics & Geostatistics: An Overview 01 (02). https://doi.org/10.4172/2327-4581.1000103.

SADC RVAA, 2019. SADC 2019 Synthesis Report on the State of Food and Nutrition Security and Vulnerability in Southern Africa.

Shepherd, T.G., Boyd, E., Calel, R.A., Chapman, S.C., Dessai, S., Dima-West, I.M., Fowler, H.J., James, R., Maraun, D., Martius, O., 2018. Storylines: an alternative approach to representing uncertainty in physical aspects of climate change. Climatic Change 151, 555–571.

Shiogama, H., Wehner, M., Min, S.-K., Zwiers, F., Tung, Y.-S., Zhang, X., 2013. Multimodel detection and attribution of extreme temperature changes. Journal of Climate 26 (19), 7430–7451. https://doi.org/10.1175/jcli-d-12-00551.1.

Silvério, K.C., Grimm, A.M., 2022. Southern African monsoon: intraseasonal variability and monsoon indices. Climate Dynamics 58 (3), 1193–1220.

Simanjuntak, C., Gaiser, T., Ahrends, H.E., Ceglar, A., Singh, M., Ewert, F., Srivastava, A.K., 2023. Impact of climate extreme events and their causality on maize yield in South Africa. Scientific Reports 13 (1), 12462.

Sonali, P., Nagesh Kumar, D., 2020. Review of recent advances in climate change detection and attribution studies: a large-scale hydroclimatological perspective. Journal of Water and Climate Change 11 (1), 1–29.

Stone, D.A., Christidis, N., Folland, C., Perkins-Kirkpatrick, S., Perlwitz, J., Shiogama, H., Wehner, M.F., Wolski, P., Cholia, S., Krishnan, H., 2019. Experiment design of the International CLIVAR C20C+ Detection and Attribution project. Weather and Climate Extremes 24, 100206.

Stott, P.A., Christidis, N., 2023. Operational attribution of weather and climate extremes: what next? Environmental Research: Climate 2 (1), 013001.

Stott, P.A., Stone, D.A., Allen, M.R., 2004. Human contribution to the European heatwave of 2003. Nature 432 (7017), 610–614. https://doi.org/10.1038/nature03089.

Taylor, K.E., Stouffer, R.J., Meehl, G.A., 2012. An overview of CMIP5 and the experiment design. Bulletin of the American Meteorological Society 93 (4), 485–498. https://doi.org/10.1175/BAMS-D-11-00094.1.

Tradowsky, J.S., Bird, L., Kreft, P.V., Rosier, S.M., Soltanzadeh, I., Stone, D.A., Bodeker, G.E., 2022. Toward near-real-time attribution of extreme weather events in Aotearoa New Zealand. Bulletin of the American Meteorological Society 103 (3), S105–S110.

Tradowsky, J.S., Bodeker, G.E., Noble, C.J., Stone, D.A., Rye, G.D., Bird, L.J., Herewini, W.I., Rana, S., Rausch, J., Soltanzadeh, I., 2023. A forecast-model-based extreme weather event attribution system developed for Aotearoa New Zealand. Environmental Research: Climate 2 (4), 045008.

Uhe, P., Philip, S., Kew, S., Shah, K., Kimutai, J., Mwangi, E., van Oldenborgh, G.J., Singh, R., Arrighi, J., Jjemba, E., 2018. Attributing drivers of the 2016 Kenyan drought. International Journal of Climatology 38, e554–e568.

Undorf, S., Polson, D., Bollasina, M.A., Ming, Y., Schurer, A., Hegerl, G.C., 2018. Detectable impact of local and remote anthropogenic aerosols on the 20th century changes of West African and South Asian monsoon precipitation. Journal of Geophysical Research. Atmospheres 123 (10), 4871–4889.

Wang, B., Biasutti, M., Byrne, M.P., Castro, C., Chang, C.-P., Cook, K., Fu, R., Grimm, A.M., Ha, K.-J., Hendon, H., 2020. Monsoons climate change assessment. Bulletin of the American Meteorological Society, 1–60.

Warszawski, L., Frieler, K., Huber, V., Piontek, F., Serdeczny, O., Schewe, J., 2014. The inter-sectoral impact model intercomparison project (ISI–MIP): project framework. Proceedings of the National Academy of Sciences 111 (9), 3228–3232.

Wilhite, D.A., 2000. Chapter I Drought as a natural hazard: concepts and definitions. In: Drought: A Global Assessment.

Winsemius, H.C., Jongman, B., Veldkamp, T.I., Hallegatte, S., Bangalore, M., Ward, P.J., 2018. Disaster risk, climate change, and poverty: assessing the global exposure of poor people to floods and droughts. Environment and Development Economics 23 (3), 328–348.

WMO, 2011. WMO Statement on the status of the global climate in 2010 (WMO-No. 1074, p. 20). World Meteorological Organization. https://library.wmo.int/idurl/4/56348.

WMO, 2013. The global climate 2001–2010: a decade of climate extremes. WMO-No. 1103, 119.

Wu, M., Nikulin, G., Kjellström, E., Belušić, D., Jones, C., Lindstedt, D., 2020. The impact of regional climate model formulation and resolution on simulated precipitation in Africa. Earth System Dynamics 11 (2), 377–394.

Yim, S.-Y., Wang, B., Liu, J., Wu, Z., 2014. A comparison of regional monsoon variability using monsoon indices. Climate Dynamics 43, 1423–1437.

Index

DEVELOPMENTS IN WEATHER AND CLIMATE SCIENCE 7

SERIES EDITOR: PAUL D. WILLIAMS

AEROSOLS AND PRECIPITATION OVER AFRICA

Progress, Challenges, and Prospects

This book unravels the complex interplay between airborne particles and precipitation patterns across the vast African continent.

Aerosols and Precipitation Over Africa is an essential exploration of the relationship between atmospheric aerosols and precipitation over Africa's climatically diverse regions. The book begins by examining the sources, properties, and distribution of aerosols over Africa. It then examines the effect of aerosols on the West African monsoon and the climate of the tropical Atlantic. The observation and modeling of precipitation distribution and recent cloud trends is explored. Later chapters discuss projected changes in precipitation and expected climate-change impacts.

This book is a valuable resource for environmental researchers, academics, policymakers, and anyone interested in understanding the latest developments in aerosols and precipitation over Africa.

Key features:

- Provides detailed regional/subregional insights and impacts of aerosols and precipitation on local climate
- Encompasses findings from both observations and climate models
- Looks to the future changes and coming challenges in aerosol and precipitation over Africa

About the Editors:

Dr. Akintomide A. Akinsanola is a Professor of Climate Science in the Department of Earth and Environmental Sciences at the University of Illinois Chicago. He also holds a joint appointment in the Environmental Science Division of Argonne National Laboratory. His research focuses on utilizing various Earth system models and observations to better understand climate dynamics, particularly processes that impact tropical and midlatitude climates.

Dr. Adeyemi A. Adebiyi is a Professor of Atmospheric Science in the Department of Life and Environmental Sciences at the University of California Merced. His research focuses on understanding the impacts of atmospheric aerosols on the regional and global climate, including the impacts of aerosols on radiation, clouds, and meteorology.

RMetS
Royal Meteorological Society

ISBN 978-0-443-14050-1

9 780443 140501

ELSEVIER

elsevier.com/books-and-journals